Technical Physics Letters, Vol. 26, No. 8, 2000, pp. 645–646. Translated from Pis'ma v Zhurnal Tekhnicheskoĭ Fiziki, Vol. 26, No. 15, 2000, pp. 1–5.

Effect of the Ion-Beam-Induced Getters on the Parameters of Neutron-Irradiated GaAs Heterostructures

S. V. Obolenskiĭ and V. D. Skupov

Nizhegorodskiĭ State University, Nizhniĭ Novgorod, Russia

Received February 28, 2000

Abstract—It was found that the negative influence of neutron irradiation on the parameters of Schottky-gate field-effect transistors based on epitaxial GaAs heterostructures can be markedly reduced by preliminarily implanting the heterostructures with Ar ions from the side of a substrate. The effect is explained by the far-range gettering of impurities and defects from the active transistor regions in the course of the neutron irradiation, which suppresses the formation of irradiation-induced deep energy levels. © *2000 MAIK "Nauka/Interperiodica".*

Theoretically, the electrical and functional characteristics of discrete devices and integrations based on GaAs must exhibit a higher stability with respect to the action of high-energy corpuscular and photon beams as compared to the properties of silicon-based analogs [1]. There is some experimental evidence that confirms this hypothesis, but a high level of defectness in single crystals and epitaxial layers of GaAs frequently levels off the advantage of GaAs over Ge.

Recently [2], we demonstrated that bombardment of the substrate in epitaxial GaAs heterostructures at room temperature with medium-energy ions from the side of a substrate produces a long-range effect improving the parameters of Schottky-gate field-effect transistors based on these heterostructures. The character of the changes in the parameters of transistors suggested that the ion bombardment reduced the concentration of crystallographic defects detrimentally affecting the mobility and concentration of charge carriers in the active layers of transistor. Therefore, it would be natural to expect that this pretreatment may also improve the radiation stability of devices based on the ion-bombarded heterostructures. The purpose of this work was to study the long-range gettering effect of the preliminary ion-beam treatment on the electrical characteristics of GaAs transistor heterostructures subject to subsequent neutron irradiation.

The experiments were performed on n^+nn^- transistors with a gate width of 0.5 μm. The structure design and preparation technology were described elsewhere [2]. Before cutting into separate transistor structures, the sample wafers with transistors were thinned to 100 μm and irradiated from the substrate side with 90-keV argon ions to a total ion dose of 5×10^{15} cm^{-2} at an ion beam current density not exceeding 0.5 μA/cm^2. Only half of the wafer surface was exposed to the ion beam, while the other half was shielded by a titanium mask. Upon cutting, the nonpackaged transistors were exposed to a pulsed neutron radiation with an average particle energy of 1 MeV, a pulse duration of less than 1 ms, and a maximum fluence of 10^{15} cm^{-2} per pulse. Changes in the parameters of transistors were judged by their current–voltage (*I–V*) characteristics measured on an L2-56 instrument. In addition, the parameters of transistors were calculated within the framework of a theoretical model [3] using the values of electron gas parameters in the active layers of analogous transistors determined in [2].

The results of our measurements demonstrated that the character of degradation of the *I–V* curves of the neutron-irradiated transistors was qualitatively the same for the control samples (not implanted with argon) and the pretreated structures with getters formed by the ion bombardment (Fig. 1). However, the rate of degradation of the latter structures was only about half that of the control samples with the same neutron fluence (Fig. 1a). As seen from Fig. 1b, the neutron irradiation led to an increasing channel resistance in the transistors of both groups, but the ion-beam-induced gettering markedly reduced this effect. Moreover, the pretreated devices showed no residual conductivity in the source–drain chain at large negative voltages on the gate (Fig. 1b). This conductivity is determined by resistances of the buffer layer and the substrate at their epitaxial contact boundary [4]. The absence of the residual conductivity confirms the fact [2] that the concentration gradient of the donor distribution profile at the nn^- interface increases upon ion bombardment from the substrate side. As a result, the drain current becomes a linear function of the gate potential in the cut-off voltage region. The linearity was retained upon neutron irradiation of the ion-beam-gettered transistor structures, although the cut-off voltage of these transistors (as well as that of the control samples) somewhat decreased.

The preliminary gettering markedly decreases the rate of the neutron-fluence-dependent degradation of

1063-7850/00/2608-0645$20.00 © 2000 MAIK "Nauka/Interperiodica"

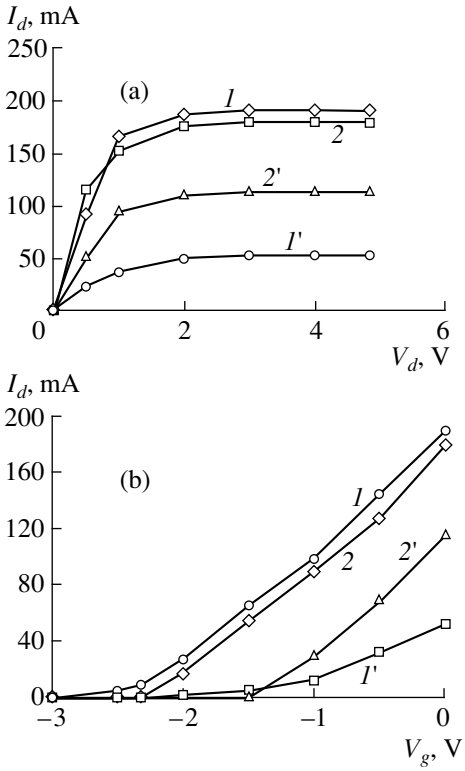

Fig. 1. The plots of drain current I_d (a) versus drain voltage V_d at a gate voltage $V_g = 0$ V and (b) versus the gate voltage at $V_d = 5$ V for the GaAs field-effect transistors (*1*, *2*) before and (*1*', *2*') after neutron irradiation to a fluence of $D_n = 1 \times 10^{15}$ cm^{-2}: (*1*, *1*') control samples (not implanted with argon); (*2*, *2*') samples gettered by the preliminary ion-beam treatment; solid lines show the results of model calculations.

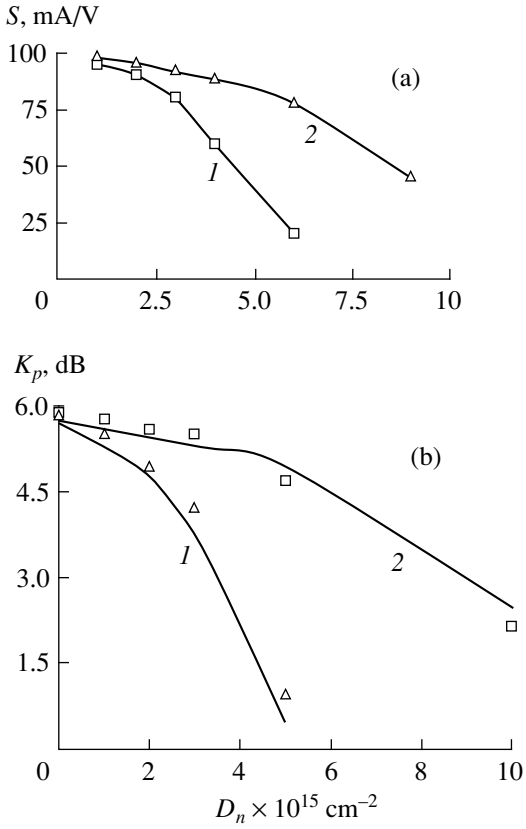

Fig. 2. The plots of (a) the *I–V* curve slope *S* and (b) power gain coefficient K_p versus neutron fluence for the GaAs field-effect transistors based on (*1*) control (not implanted with argon) and (*2*) ion-beam-gettered heterostructures.

the transistor *I–V* curve slope and the power gain factor (Fig. 2). Note a good coincidence of the experimental data and the values calculated by the model [3] using the parameters from [2] for the transistors before and after neutron irradiation. This coincidence, on the one hand, confirms validity of the model concepts [3] and, on the other hand, proves the possibility for effectively increasing the radiation stability of GaAs transistors by means of ion-beam-induced gettering.

In our opinion, the above results indicate that the preliminary ion irradiation accelerates the rearrangement of the components of the impurity–defect composition in each layer of the transistor heterostructure and boundary regions. This leads, in particular, to a decrease in the concentration of background impurities and antistructural defects responsible for the deep level formation in the course of neutron irradiation [5]. These impurities and defects are gettered by extended defects of the dislocation type and by the free surface. We believe that the rearrangement process is initiated and driven by elastic waves generated in the ion stopping region and at the inner boundaries of a multilayer structure irradiated from the substrate side [2, 6]. Future investigations with the use of deep-level spectroscopy have to specify the processes responsible for the ion-beam-induced increase in the stability of GaAs field-effect transistors with respect to subsequent neutron irradiation.

REFERENCES

1. R. Zulig, in *VLSI Electronics*, Vol. 10: *Surface and Interface Effects in VLSI*; Vol. 11: *GaAs Microelectronics*, ed. by N. Einspruch (Academic, New York, 1985; Mir, Moscow, 1988).
2. S. V. Obolenskiĭ, V. D. Skupov, and A. G. Fefelov, Pis'ma Zh. Tekh. Fiz. **25** (16), 50 (1999) [Tech. Phys. Lett. **25**, 655 (1999)].
3. N. V. Demarina and S. V. Obolenskiĭ, Microelectron. Reliab. **39**, 1247 (1999).
4. M. Shur, *GaAs Devices and Circuits* (Plenum, New York, 1987; Mir, Moscow, 1991).
5. V. A. Novikov and V. V. Peshev, Fiz. Tekh. Poluprovodn. (St. Petersburg) **32** (4), 411 (1998) [Semiconductors **32**, 366 (1998)].
6. P. V. Pavlov, Yu. A. Semin, V. D. Skupov, and D. I. Tetel'baum, Fiz. Tekh. Poluprovodn. (Leningrad) **20** (5), 503 (1986) [Sov. Phys. Semicond. **20**, 315 (1986)].

Translated by P. Pozdeev

Technical Physics Letters, Vol. 26, No. 8, 2000, pp. 647–649. Translated from Pis'ma v Zhurnal Tekhnicheskoĭ Fiziki, Vol. 26, No. 15, 2000, pp. 6–11.

Mechanisms of Formation and Charge States of Intrinsic Defects in Lead Telluride Films

M. A. Ruvinskiĭ, D. M. Freik, B. M. Ruvinskiĭ, and V. V. Prokopiv

Physicochemical Institute, Stefanik Carpathian University, Ivano-Frankivsk, Ukraine

Received January 11, 2000

Abstract—A crystallochemical model of the vapor-phase epitaxy of lead telluride films is suggested. The model is based on the simultaneous formation of singly- and doubly-charged Frenkel defects in the cationic sublattice. The results of numerical calculations based on this model are in good agreement with the known experimental data. © *2000 MAIK "Nauka/Interperiodica".*

1. It is well known [1–4] that compositional changes within the homogeneity range of lead chalcogenides provide a control of the electric properties of the films of these compounds, including the type of conductivity and the charge carrier concentration. However, there is still no commonly accepted opinion about the prevalent type of intrinsic defects in $A^{IV}B^{VI}$ compounds and their charge state [4–7].

2. In order to interpret the dependence of the charge carrier concentration on various growth parameters (including the partial pressure P_{Te_2} of tellurium vapors in the growth zone [8]) in lead telluride films grown from the vapor phase by the hot-wall method, we suggest the first model describing disorder in the metal sublattice by the Frenkel mechanism with the simultaneous formation of singly- and doubly-charged defects (interstitial lead ions, Pb_i^{2+} and Pb_i^{+}, and lead vacancies, V_{Pb}^{2-} and V_{Pb}^{-}).

3. Using the methods suggested in [9], the source–vapor and vapor–condensate equilibria can be described by the following quasichemical reactions:

$$PbTe^{S} \rightleftarrows Pb^{V} + (1/2)Te_2^{V}, \quad K_{PbTe}(T_e) = P_{Pb}P_{Te_2}^{1/2}; \quad (1)$$

$$Pb^{V} \rightleftarrows Pb_i^{+} + e^{-}, \quad K'_{Pb,V}(T_s) = [Pb_i^{+}]nP_{Pb}^{-1}; \quad (2)$$

$$(1/2)Te_2^{V} \rightleftarrows V_{Pb}^{-} + Te_{Te}^{0} + h^{+}, \quad K'_{Te,V}(T_s) = [V_{Pb}^{-}]pP_{Te_2}^{-1/2}; \quad (3)$$

$$Pb^{V} \rightleftarrows Pb_i^{2+} + 2e^{-}, \quad K''_{Pb,V}(T_s) = [Pb_i^{2+}]n^2P_{Pb}^{-1}; \quad (4)$$

$$(1/2)Te_2^{V} \rightleftarrows V_{Pb}^{2} + Te_{Te}^{0} + 2h^{+}, \quad K''_{Te_2,V}(T_s) = [V_{Pb}^{2-}]p^2P_{Te_2}^{-1/2}. \quad (5)$$

Equation (1) characterizes equilibrium in the source–vapor system during the decomposition of lead telluride in the evaporator at the evaporation temperature T_e. Reactions (2)–(5) define the vapor–condensate equilibrium responsible for the formation of intrinsic defects at the substrate temperature T_s.

The intrinsic conductivity and the ionization of Frenkel defects are described by Eqs. (6) and (7)–(10):

$$\text{"0"} \rightleftarrows e^{-} + h^{+}, \; K_i(T_s) = np; \quad (6)$$

$$\text{"0"} \rightleftarrows V_{Pb}^{-} + Pb_i^{+}, \; K'_F(T_s) = [V_{Pb}^{-}][Pb_i^{+}]; \quad (7)$$

$$\text{"0"} \rightleftarrows V_{Pb}^{2-} + Pb_i^{2+}, \; K''_F(T_s) = [V_{Pb}^{2-}][Pb_i^{2+}]; \quad (8)$$

$$\text{"0"} \rightleftarrows V_{Pb}^{-} + Pb_i^{2+} + e^{-}, \; K_F^{(e)}(T_s) = [V_{Pb}^{-}][Pb_i^{2+}]n; \quad (9)$$

$$\text{"0"} \rightleftarrows V_{Pb}^{2-} + Pb_i^{+} + h^{+}, \quad K_F^{(h)}(T_s) = [V_{Pb}^{2-}][Pb_i^{+}]p; \quad (10)$$

$$K_j = K_{0j}\exp(-\Delta H/kT).$$

The general condition of electroneutrality has the

Table

Reaction constant	K_0	ΔH, eV
K_{PbTe}, $Pa^{3/2}$	1.4×10^{18}	3.51
$K'_{Pb,V}$, $cm^{-6}\,Pa^{-1}$	5.5×10^{30}	–1.01
$K'_{Te_2,V}$, $cm^{-6}\,Pa^{-1/2}$	1.2×10^{38}	0.25
$K''_{Pb,V}$, $cm^{-9}\,Pa^{-1}$	1.9×10^{51}	–0.87
$K''_{Te_2,V}$, $cm^{-9}\,Pa^{-1/2}$	1.0×10^{59}	0.39

1063-7850/00/2608-0647$20.00

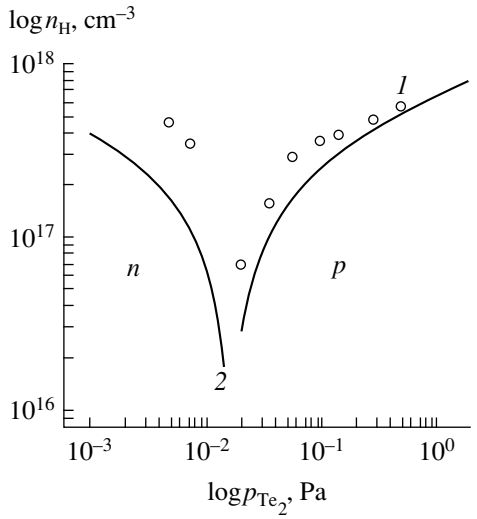

Fig. 1. The concentration of charge carriers in lead telluride films as function of the partial pressure of tellurium vapors: (*1*) experiment [8]; (*2*) calculation by Eqs. (12) and (13). The substrates were the (111) cleavages of BaF_2 crystals (T_e = 833 K; T_s = 653 K).

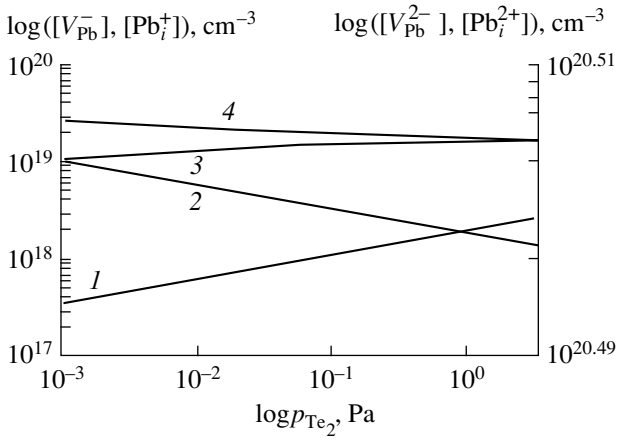

Fig. 2. Calculated concentrations of charged defects in lead telluride films as functions of the partial pressure of tellurium vapors: (*1*) [V_{Pb}^{-}], (*2*) [Pb_i^{+}], (*3*) [Pb_i^{2+}], (*4*) [V_{Pb}^{2-}] (T_e = 833 K; T_s = 653 K).

form

$$p + [Pb_i^{+}] + 2[Pb_i^{2+}] = n + [V_{Pb}^{-}] + 2[V_{Pb}^{2-}]. \quad (11)$$

According to Eqs. (1)–(11), the carrier concentration n can be determined in terms of the equilibrium constants of the quasichemical reactions and pressure P_{Te_2} using the equation

$$An^4 + Bn^3 - Cn - D = 0, \quad (12)$$

where

$$A = 2K''_{Te_2,V}K'_F P_{Te_2}^{1/2}(K_{PbTe}K'_{Pb,V}K'_{Te_2,V}K_i)^{-1},$$

$$B = 1 + K'_F P_{Te_2}^{1/2}(K_{PbTe}K'_{Pb,V})^{-1},$$

$$C = K_i + K_{PbTe}K'_{Pb,V}P_{Te_2}^{-1/2}, \quad D = 2K_{PbTe}K''_{Pb,V}P_{Te_2}^{-1/2}.$$

The charge carrier concentration determined from the Hall effect n_H is

$$n_H = n - p = n - K_i n^{-1}. \quad (13)$$

Using this model, it is also possible to determine the concentration of charged defects.

4. The intrinsic conductivity constant K_i was determined with due regard for the temperature dependence of the bandgap $E_g(T)$ and the effective mass of the density of states $m(T)$ [10] as

$$K_i(T) = N_C N_V \exp(-E_g/kT), \quad (14)$$

where

$$N_C = N_V = 2(mkT/2\pi\hbar^2)^{3/2},$$

$$\begin{cases} m(T) = g_C^{3/2}K^{1/3}0.048m_0\sqrt{T/300}, \\ g_C = 4, \quad K = m_\parallel/m_\perp = 9 \quad (T \geq 300\ \text{K}); \end{cases}$$

$$E_g = 0.217 + 4.5\times10^{-4}(T - 77)\ (\text{eV}) \quad (T \geq 77\ \text{K}).$$

The K'_F constant was determined from the equilibrium condition

$$K'_F(T_s) = K_{PbTe}(T_s)K'_{Pb,V}(T_s)K'_{Te_2,V}(T_s)K_i^{-1}(T_s). \quad (15)$$

For the ideal vapor, we have

$$K_{PbTe}(T_s) = K_{PbTe}(T_e)(T_s/T_e)^{3/2}.$$

The reaction constants K_{PbTe}, $K'_{Pb,V}$, $K'_{Te_2,V}$, $K''_{Pb,V}$, and $K''_{Te_2,V}$ were taken from [2, 11] (see table).

5. The experimental and the calculated dependences of the defect and charge carrier concentrations in PbTe films as functions of the partial pressure P_{Te_2} of tellurium vapors in the growth zone are shown in Figs. 1 and 2. It is seen from Fig. 2 that the concentrations of doubly-charged defects [Pb_i^{2+}] and [V_{Pb}^{2-}] in the films are considerably higher than the concentrations of singly-charged defects. This is consistent with the qualitative tendency to the prevailing formation [12, 13] of multiply charged vacancies and interstitials capable of multiple ionization in the presence of rather shallow acceptor and donor levels [12, 13]. However, because of partial compensation of the doubly-charged defects, an important role in the change of the charge carrier concentration in PbTe films (dependent on various growth factors) is also played by singly-charged defects—Pb_i^{+} and V_{Pb}^{-} (Fig. 2). Upon increasing the tellurium-vapor pressure P_{Te_2}, the electron concentra-

tion first decreases, then the conductivity changes from the *n*- to the *p*-type and the hole concentration increases (Fig. 1). This corresponds to an increase of the concentration of singly-charged acceptor lead vacancies [V_{Pb}^{-}] and a decrease of the concentration of singly-charged donor lead interstitials [Pb_i^{+}] (Fig. 1).

Thus, it can be stated that the equilibrium state of the defect subsystem in PbTe films is rather complicated. The experimental results can be satisfactorily interpreted only assuming that singly- and doubly-charged defects simultaneously exist in the cationic sublattice.

REFERENCES

1. N. Kh. Abrikosov and L. E. Shelimova, *Semiconductor Materials Based on $A^{IV}B^{VI}$ Compounds* (Nauka, Moscow, 1975).
2. V. P. Zlomanov, *P–T–X Diagrams of Two-Component Systems* (Mosk. Gos. Univ., Moscow, 1980).
3. Yu. I. Ravich, B. A. Efimova, and I. A. Smirnov, *Semiconducting Lead Chalcogenides* (Nauka, Moscow, 1968; Plenum, New York, 1970).
4. N. J. Parada and G. W. Pratt, Phys. Rev. Lett. **22**, 180 (1969).
5. M. Schenk, H. Berger, and A. Kimakov, Cryst. Res. Technol. **23** (1), 77 (1988).
6. D. M. Zayachuk and V. A. Shenderovs'kiĭ, Ukr. Fiz. Zh. **36** (11), 1692 (1991).
7. D. M. Freik, V. V. Prokopiv, A. V. Nych, *et al.*, Mater. Sci. Eng. B **48**, 226 (1997).
8. A. Lopez-Otero, Appl. Phys. Lett. **26** (8), 470 (1975).
9. F. A. Kröger, *The Chemistry of Imperfect Crystals* (Wiley, New York, 1964; Mir, Moscow, 1969).
10. T. S. Moss, G. J. Burrell, and B. Ellis, *Semiconductor Opto-Electronics* (Butterworths, London, 1973; Mir, Moscow, 1976).
11. A. M. Gas'kov, V. P. Zlomanov, and A. V. Novoselova, Izv. Akad. Nauk SSSR, Neorg. Mater. **15** (8), 1476 (1979).
12. F. A. Kröger, J. Phys. Chem. Solids **26**, 1717 (1965).
13. V. L. Vinetskiĭ and G. A. Kholodar', *Statistical Interaction of Electrons and Holes in Semiconductors* (Naukova Dumka, Kiev, 1969).

Translated by L. Man

Technical Physics Letters, Vol. 26, No. 8, 2000, pp. 650–653. Translated from Pis'ma v Zhurnal Tekhnicheskoĭ Fiziki, Vol. 26, No. 15, 2000, pp. 12–20.

Longitudinal Self-Focusing of an Electron Bunch under Coherent Emission Conditions

N. S. Ginzburg, Yu. V. Novozhilova, R. M. Rozental', and A. S. Sergeev

Institute of Applied Physics, Russian Academy of Sciences, Nizhniĭ Novgorod, 603600 Russia

Received March 10, 2000

Abstract—The longitudinal motion of an electron bunch with a length much smaller than its wavelength is studied theoretically under coherent emission conditions. It is demonstrated that the bunch can be focused under the action of a longitudinal component of the ponderomotive force of the radiation fields. This mechanism is operative when a bunch moves parallel to metallic surfaces partly reducing the space-charge forces. © *2000 MAIK "Nauka/Interperiodica".*

1. The creation of short electron bunches stable with respect to Coulomb repulsion is a task of practical significance [1–3]. This study demonstrates that certain progress toward solving the problem can be made by using the ponderomotive force exerted by radiation fields. Specifically, a transverse oscillation velocity should be imparted to the electrons in a bunch so that the radiation fields thus produced would focus the bunch in the longitudinal direction. The oscillatory motion may represent a cyclotron gyration of particles in a uniform longitudinal magnetic field. Alternatively, the oscillations may be caused by an external electromagnetic field or a nonuniform magnetostatic field (such as that in an undulator).

The ponderomotive interaction between two particles oscillating in phase is attractive if the distance between particles is shorter than half of the radiation wavelength [4]. Naturally, the ponderomotive force depends on the magnitude of the transverse oscillation velocity. However, even at relativistic velocities, the force is weaker than the Coulomb repulsion of the particles. It is therefore necessary to partly neutralize the action of the space charge. This can be achieved if the bunch moves parallel to metallic surfaces.

The present study addresses the longitudinal electron focusing under the conditions of cyclotron radiation emission. First, we analyze the simplest one-dimensional model that represents the electron ensemble as a layer extending to infinity along both of the transverse coordinate axes, assuming that the space-charge forces are partly reduced. Then we proceed to a bunch of electrons gyrating in a uniform magnetic field between two conducting planes. Based on the particle-in-cell simulation with a two-dimensional version of the KARAT code, we demonstrate that the bunch can be contracted in the longitudinal direction.

2. Consider a one-dimensional model. Let there be a layer of electrons gyrating in a uniform magnetic field ($\mathbf{H}_0 = H_0\mathbf{z}_0$) that is directed perpendicularly to the boundaries of the layer. The width of the layer is denoted by b. All of the electrons have the same initial phase of cyclotron gyration, so that the transverse momentum of an electron can be represented as $p_+ = p_x + ip_y = p_\perp \exp(i\omega_H t)$, where $\omega_H = eH_0/mc\gamma_0$ is the gyromagnetic frequency with γ_0 being the initial value of the relativistic factor. Let us divide the layer into a finite number of sheets of charge (macroelectrons) differing in the longitudinal coordinate z', so as to analyze the dynamics of the layer. For each sheet of charge, the surface current density is $j_+ = j_x + ij_y = j_0 \exp(i\omega_H t)$, where $j_0 = \sigma v_\perp$ with σ being the surface charge density and $v_\perp = p_\perp/m\gamma$, the transverse velocity. The field generated by a sheet is a circularly polarized plane wave

$$E_+ = E_x + iE_y = E_0 \exp(i\omega_H t) \tag{1}$$

with the amplitude

$$E_0(z, t) = -\frac{2\pi}{c} j_0(z', t - |z - z'|/c), \tag{2}$$

where $j_0(z', t - |z - z'|/c)$ is the surface current density amplitude taken at a retarded time instant

$$j_0(z', t - |z - z'|/c) = \sigma v_\perp(z', t) \exp(-i\omega_H |z - z'|/c). \tag{3}$$

In Eq. (3), the characteristic time of the bunch focusing is assumed to be much greater than the time lag b/c across the layer; in other words, the longitudinal motion is assumed to be weakly relativistic. In a plane wave, the magnetic field is $H_+ = H_x + iH_y = iE_+$. Accordingly, the longitudinal ponderomotive force with which one sheet of charge acts upon a unit area of another sheet that lies at the distance $|z - z'|$ is expressed as

$$F_z^{\text{pond}} = -(2\pi\sigma^2 v_\perp(z, t) v_\perp(z', t)/c^2) \times \operatorname{sgn}(z - z') \cos((z - z')\omega_H/c). \tag{4}$$

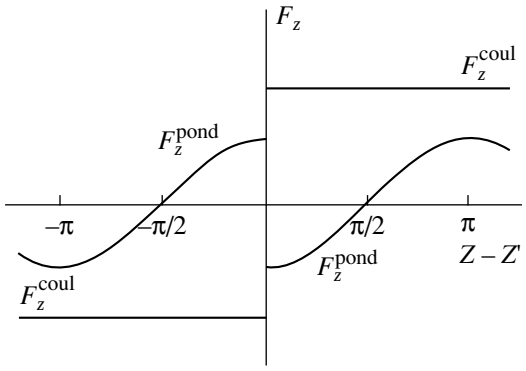

Fig. 1. The interaction of macroelectrons in a one-dimensional model: the longitudinal components of the Coulomb and ponderomotive forces vs. the distance between sheets of charge.

Figure 1 demonstrates that F_z^{pond} changes its sign. Note that F_z^{pond} is an attractive force if the distance is less than half the wavelength. Also shown in Fig. 1 is the longitudinal component of the Coulomb force $F_z^{coul} = 2\pi\sigma^2 \operatorname{sgn}(z - z')$, which is a repulsive force for any distance between the planes. Since the Coulomb force surpasses the ponderomotive force (Fig. 1), the former must be partly neutralized so that longitudinal focusing is possible. This can be achieved by introducing an ion background or metallic surfaces parallel to which the bunch would move.

Suppose the space-charge force is partly reduced, the degree of the reduction being evaluated by the factor $r < 1$. Let us describe the motion in terms of the Lagrangian variables, with which the position of each plane of charge (macroparticle) $Z_\alpha(Z_0, \tau)$ and its velocity are functions of the time τ and the initial coordinate Z_0 (it is assumed that the transverse electron motion is relativistic and the longitudinal motion is weakly relativistic.) Then the equations of motion for the macroelectrons are as follows:

$$\frac{d^2 Z_\alpha}{d\tau^2} = \operatorname{Re}\left(i\bar{p}_{\perp_\alpha} \frac{\partial a^*}{\partial Z}\bigg|_{Z = Z_\alpha} \right) + Ir \int_0^B \operatorname{sgn}(Z_\alpha - Z_{\alpha'}) dZ_{0_{\alpha'}}, \tag{5a}$$

$$\frac{d\bar{p}_{\perp_\alpha}}{d\tau} = i\bar{p}_{\perp_\alpha}\left(1/\sqrt{1 - \beta_{\perp_0}^2 + \left|\bar{p}_{\perp_\alpha}\right|^2} - 1\right) - a, \tag{5b}$$

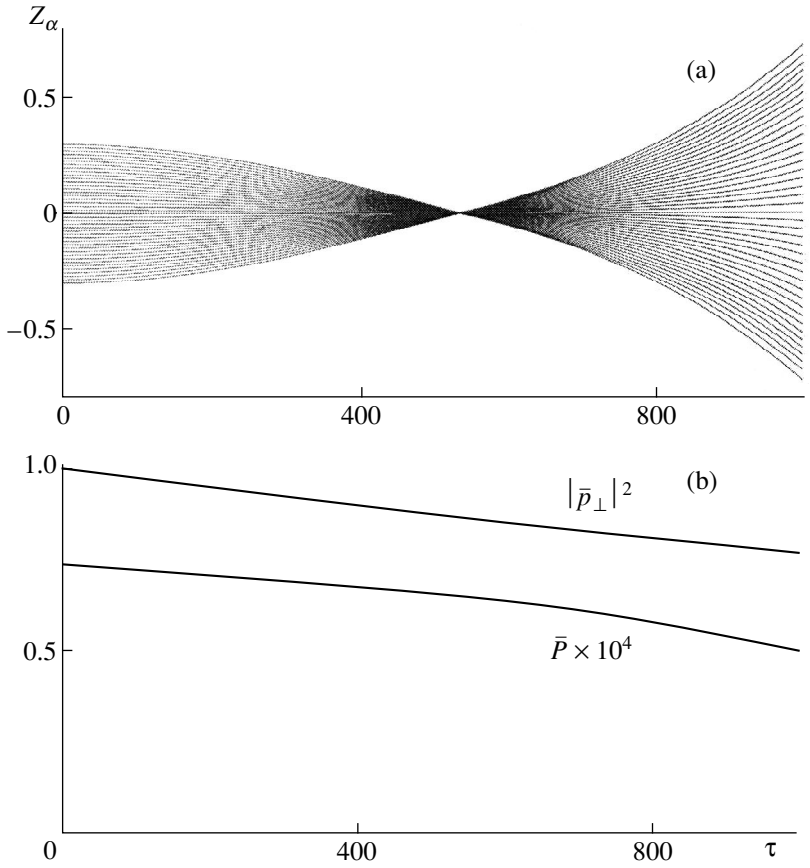

Fig. 2. Time variation of (a) the longitudinal coordinates of macroelectrons and (b) the mean-square transverse momentum and the radiation power at $I = 10^{-4}$, $\beta_\perp^2 = 0.8$, $B = 0.6$, and $r = 0.7$.

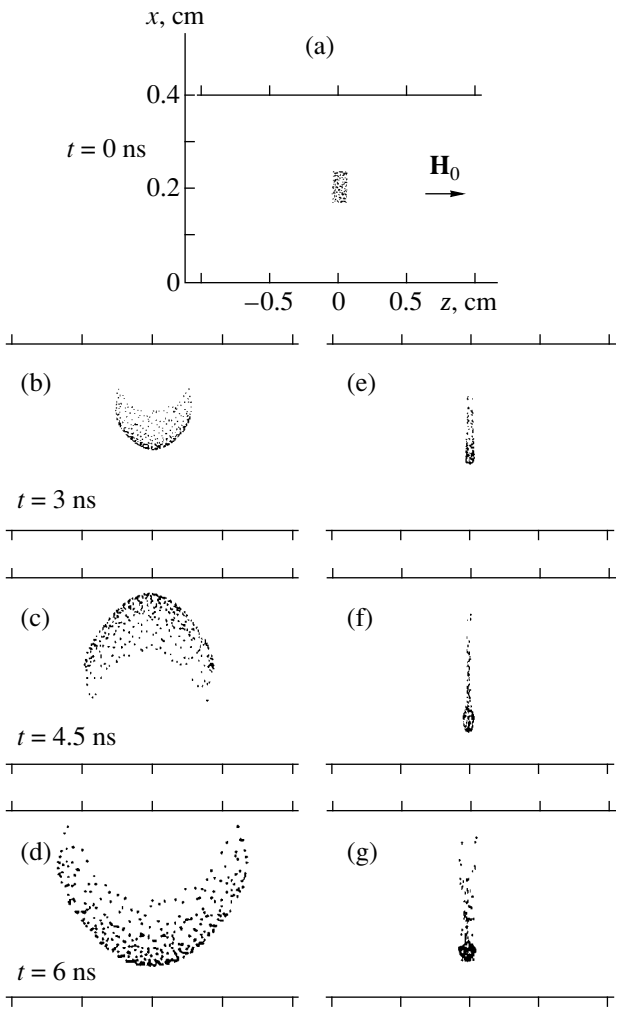

Fig. 3. Particle-in-cell simulation of longitudinal focusing: (a) initial configuration of a bunch; (b, c) evolution of the bunch with neglect of the emission; (d, e) evolution of the bunch under the action of the radiation field. The initial density of the bunch is 10^{10} cm^{-3}, the electron energy is 1 MeV, and the magnetic flux density is 3 T.

where

$$a(Z,\tau) = I\int_0^B \bar{p}_{\perp_{\alpha'}} \exp(-i|Z - Z_{\alpha'}|)/\sqrt{1-\beta_{\perp_0}^2 + |\bar{p}_{\perp_{\alpha'}}|^2}\, dZ_{0_{\alpha'}} \quad (5c)$$

is the radiation amplitude. Equations (5) employ the following dimensionless quantities: $a = eE_0/(mc\gamma_0\omega_H)$, $Z = \omega_H z/c$, $\tau = \omega_H t$, $\bar{p}_\perp = p_\perp/(mc\gamma_0)$, $B = b\omega_H/c$, $I = \omega_p^2/2\omega_H^2$, and $\omega_p = \sqrt{4\pi e^2 n/m\gamma_0}$, where ω_p denotes the relativistic plasma frequency.

According to Eq. (5c), for a given charge per unit area, the radiation amplitude attains its maximum $a = IB$ when the layer width is much smaller than the wavelength: $B \ll 1$. Then, Eq. (5a) gives the following condition for neutralization of the Coulomb repulsion by the radiative attraction:

$$r < \beta_\perp^2. \quad (6)$$

Figure 2a shows the trajectories of macroelectrons in the case where condition (6) is met at the initial moment of time τ. Figure 2b depicts the radiation power $W = |a|^2_{Z=0} + |a|^2_{Z=B}$ and the mean-square transverse momentum of the macroparticles for the same parameters. Comparing the two figure panels with each other shows that effective coherent emission from the layer with a pronounced longitudinal self-focusing takes place for $\tau \le 800$. As τ increases further, the self-focusing changes to expansion of the layer. The reason is that the transverse momentum decreases during the emission to reduce the ponderomotive force which is proportional to the squared momentum.

3. For a two-dimensional model, the longitudinal self-focusing was demonstrated using a particle-in-cell simulation with the help of the KARAT code that directly embodies Maxwell's equations together with the equations of motion. The bunch was assumed to move between two metallic planes reducing the Coulomb repulsion (Fig. 3). Figure 3a shows the initial configuration of the bunch with a density of 10^{10} cm^{-3} and the dimensions 1 and 0.5 mm along the *z*- and the *x*-axis, respectively. The electrons gyrate under the action of a uniform magnetic field oriented along the *z*-axis and having a magnetic flux density of 3 T. The initial energy of the electrons is 1 MeV. Figures 3b–3d show how the bunch expands due to the Coulomb interaction, the emission fields being ignored. Figures 3e–3g present configurations of the bunch experiencing the focusing action of the radiation at various time instants. Comparing the figures suggests that the bunch undergoes contraction during an initial stage of the process, accompanied by the emission from oscillating electrons. Then, the radiation power and the mean transverse velocity decrease (Fig. 4) to attenuate the ponderomotive force. This results in expansion of the bunch.

4. It should be emphasized that the above analysis applies to a bunch moving as a whole with a translational velocity $v_{\|0}$ and that the process has been studied in the intrinsic frame of reference *K*' moving with the unperturbed translational velocity. For the laboratory frame of reference *K*, the Lorentz transformations give the following expressions of the electron transverse velocity, energy, and concentration, respectively: $v_\perp = v'_\perp \gamma_\|$, $\gamma = \gamma'\gamma_\|$, and $n = n'\gamma_\|$, where ($\gamma_\| = 1/\sqrt{1-\beta_{\|0}^2}$). For example, at $v_{\|0} = 0.98c$, the bunch dealt with in Section 3 has an energy of 7.5 MeV, the pitch factor $\beta_\perp/\beta_\| = 0.2$, and a concentration of 5×10^{10} cm^{-3} (the current density being ~250 A/cm^2). Note that the Lorentz (relativistic) time dilation must be allowed for as well: if the time to focus $\Delta\tau'$ is 3 ns in the intrinsic frame, then the corresponding value in the laboratory frame is $\Delta\tau =$

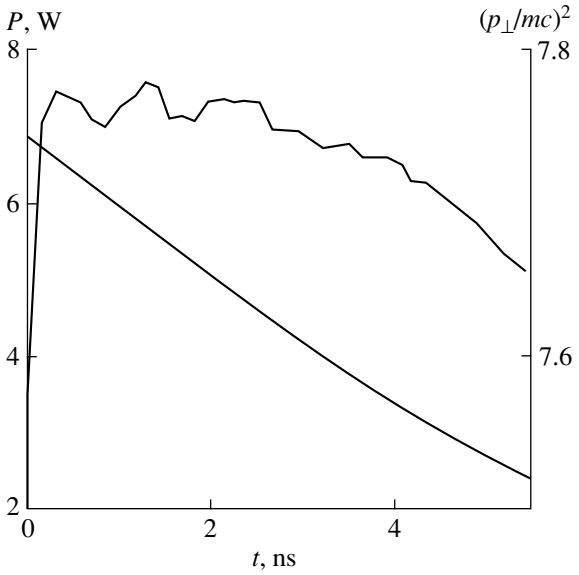

Fig. 4. Time variation of the mean-square transverse momentum and the radiation power. The values of parameters are as in Fig. 3.

$\Delta\tau'\gamma_{\|} \approx 15$ ns. During this time, the bunch having a translational velocity close to the velocity of light will travel ~4.5 m.

5. In conclusion, note that there must be no decrease in the transverse oscillation velocity during coherent emission if the electrons perform forced oscillations, being exposed to external time-dependent fields. Consider, for example, the motion inside a capacitor. The process obeys Eqs. (5a) and (5c), where the amplitude of the transverse momentum is a constant proportional to the amplitude of the capacitor field. Remarkably, the self-focusing and coherent emission in this model system will continue indefinitely, provided condition (6) is met. Also interesting is the case where the oscillations are excited by a traveling electromagnetic pump wave. Then, the longitudinal self-focusing and coherent emission (scattering) must be accompanied by acceleration of the bunch as a whole due to the longitudinal momentum imparted by the pump wave. An opposite effect must occur when a short bunch moves in a variable undulator field. Then, the bunch would be retarded as a whole and the self-focusing would provide for the coherent emission.

This study was supported by the Russian Foundation for Basic Research, project no. 98-02-17308.

REFERENCES

1. Ya. B. Faĭnberg, A. K. Berezin, V. A. Balakirev, *et al.*, in *Relativistic High-Frequency Electronics*, ed. by A. V. Gaponov-Grekhov (Inst. Prikl. Fiz. Ross. Akad. Nauk, Nizhniĭ Novgorod, 1993), Vol. 7, p. 104.
2. P. Chen, J. M. Dawson, R. Huff, and T. Katsouleas, Phys. Rev. Lett. **54** (7), 692 (1985).
3. J. B. Rosenzweig, Phys. Rev. Lett. **58** (6), 555 (1987).
4. N. S. Ginzburg and A. S. Sergeev, Pis'ma Zh. Éksp. Teor. Fiz. **54** (8), 445 (1991) [JETP Lett. **54**, 446 (1991)].

Translated by A. Sharshakov

Technical Physics Letters, Vol. 26, No. 8, 2000, pp. 654–655. Translated from Pis'ma v Zhurnal Tekhnicheskoĭ Fiziki, Vol. 26, No. 15, 2000, pp. 21–25.

Photo EMF Observed upon the Laser Resonance Excitation of Sodium Vapors

N. A. Gorbunov* and T. Stacewicz**

** Institute of Physics, St. Petersburg State University, St. Petersburg, Russia*

*** Institute of Experimental Physics, Warsaw University, Hoza 69, 00-689 Warsaw, Poland*

Received March 16, 2000

Abstract—A method of the direct light-to-electric energy conversion in photoplasma is proposed. The photo emf was observed in experiments on the pulsed laser excitation of sodium vapors. It is demonstrated that the separation of charged particles in the plasma is caused by the inhomogeneous distribution of resonance-excited atoms in the direction of optical excitation. *© 2000 MAIK "Nauka/Interperiodica".*

Optical radiation can be detected using the light-induced changes of conductivity in semiconductors [1] and in the electric discharge plasma (optogalvanic effect) [2]. The effect of the photo emf generation in semiconductors was also comprehensively studied and found wide practical applications in the light-to-electric energy converters. The phenomenon of the photo emf generation in plasma is not as well studied.

A potential difference between points in the illuminated gas medium arises in two stages: first, the formation of charged particles (photionization); second, separation of these charges in space.

The light-induced plasma formation in metal vapors is extensively studied both theoretically and experimentally (see, for example, [3–5]). Resonance absorption of the incident light quanta leads to maximum ionization of the medium. Effective absorption of the resonance quanta is followed by ionization mainly caused by the processes involving electrons heated in superelastic collisions with the optically excited atoms.

The studies of mechanisms of the photoinduced potential difference generation were stimulated by interest in the direct light-to-electric energy conversion in photoplasma. Dunning and Palmer [6] proposed a method of solar energy conversion in photoplasma based on the MHD transformation. The laser energy conversion into electricity in a thermoemission converter employing a CO_2 laser for the plasma initiation were experimentally studied in [7, 8]. The mechanism of charge separation upon resonance optical excitation is less elaborate. Brandenberg [9] observed a photo emf in the microwave discharge in krypton upon illuminating the cell perpendicularly to its axis by laser light with a wavelength of 785.5 nm ($1s3$–$2p3$ transition). A mechanism of the photo emf generation in this system (the potential difference was about 0.1 V at a laser power of about 1 mW) is related to violation of the discharge symmetry caused by the light-induced changes of the Kr metastable state ($1s3$) density.

We have generated a photo emf by resonance pulsed laser irradiation of sodium vapors. A glass tube with the vapors had a length of $L = 70$ mm and an inner diameter of $d = 20$ mm. Cylindrical kovar electrodes welded at the ends of the tube measured the electric current. Sapphire windows on the electrode edges allowed for the input of the laser beam. A heater controlled the density of the sodium vapors.

A pulsed tunable laser with the spectral half-width of about 0.5 Å provided the resonance excitation of sodium vapors (resonance transitions $3S$–$3P_{1/2, 3/2}$). The energy of the laser pulse amounted to 20 mJ at a pulse duration of about 7 ns and a repetition rate of 10 Hz. An HP54220 A digital oscilloscope measured the voltage U across the measuring resistor $R = 50\ \Omega$ connected in series with the gas cell and a testing constant voltage (φ) source.

Figure 1a shows the plots of voltage U versus time at $[Na] = 3 \times 10^{14}$ cm^{-3} and $\varphi = 0$. Curve *1* refers to the case when the wavelength corresponding to the maximum laser power is centered at the sodium $3S_{1/2}$–$3P_{3/2}$ absorption band. Consider the qualitative interpretation of this phenomenon. In the case under consideration, the laser power density is insufficient for homogeneous optical saturation of the resonance transition over the entire cell length. The light energy is absorbed within a few millimeters near the input window. This leads to inhomogeneous distribution of the excited atoms along the cell axis and, consequently, to inhomogeneous plasma formation. Plasma emission mainly concentrates in a narrow layer near the input window. An excess of positive ions related to the diffusion outflow of more mobile electrons gives rise to a positive potential in this region. The resulting ambipolar potential difference $\Delta\phi \approx (T_e/e)/\ln(n_1/n_2)$ depends on the electron temperature (T_e) and the charged particle densities n_1 and n_2 in both ends of the cell [10].

1063-7850/00/2608-0654$20.00 © 2000 MAIK "Nauka/Interperiodica"

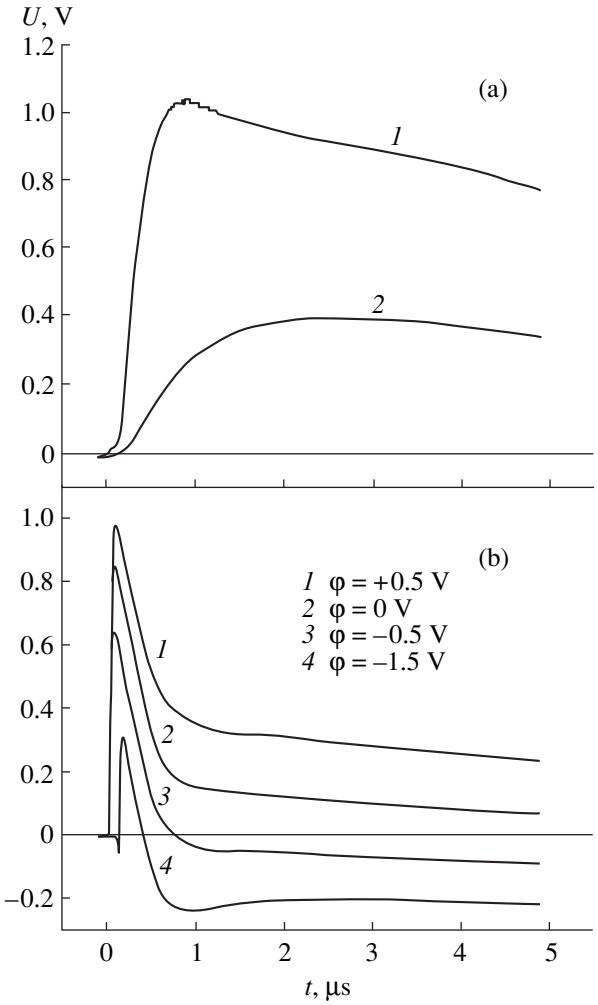

Fig. 1. The plots of voltage versus time measured in a cell filled with (a) sodium vapors and (b) sodium–helium mixture. See the test for explanation.

The value of the photocurrent in the external circuit depends on the relationship between the load resistance and the internal resistance of the photo emf source. It is seen that the photocurrent reaches its maximum value in ~1 μs after the laser pulse termination, which coincides with the time instant when the electron density reaches a maximum [5]. The subsequent decay is caused by the T_e relaxation and spatial blurring of the primary ionization zone due to the resonance radiation transfer. A shift of the laser wavelength by ~1 Å toward the absorption band wing leads to decreasing photo emf (Fig. 1a, curve *2*). This was explained by a more homogeneous excitation of the sodium vapors along the laser beam, as confirmed by observations of the plasma emission.

Figure 1b shows the plots of voltage versus time for a mixture of a sodium vapors ([Na] ≈ 10^{15} cm^{-3}) and helium ([He] = 7×10^{17} cm^{-3}) at various constant bias voltages. In contrast to the case of pure sodium and φ = 0, we observe shortening of the photoinduced voltage pulses. The voltage U reaches its maximum value 0.2 μs after termination of the exciting laser pulse. This coincides with the characteristic time of relaxation of the electron temperature T_e caused by collisions with helium atoms. The consequent deionization regime terminates the growth of the charged particles concentration in the plasma. Shortening of the photo emf decay time in comparison with the case of pure sodium is explained by increasing rates of the T_e relaxation and the resonance radiation transfer caused by the buffer gas influence.

An external field leads to increasing load current, provided the electron drift direction in this field coincides with the ambipolar diffusion direction (Fig. 1b, curve *1*). In the opposite case (Fig. 1b, curves *3* and *4*), the load current depends on the difference between the photo emf and the bias voltage. The maximum photo emf measured by the compensation method was $\Delta\varphi_{max} \sim 3$ V.

Thus, the inhomogeneous photo-excitation of atoms in a gas-filled cell leads to generation of the photo emf. This effect is similar to the Dember emf generation upon inhomogeneous excitation of a uniform semiconductor [1]. In contrast to the case of semiconductors, the photo emf in plasma exhibits a resonance character with respect to the excitation wavelength.

The authors are grateful to L. D. Tsendin for helpful discussions.

This work was supported by the KBN grant (Poland).

REFERENCES

1. V. L. Bonch-Bruevich and S. G. Kalashnikov, *The Physics of Semiconductors* (Nauka, Moscow, 1990).
2. V. N. Ochkin, N. G. Preobrazhenskiĭ, and N. Ya. Shaparev, *Optogalvanic Effect in Ionized Gases* (Nauka, Moscow, 1991).
3. I. M. Beterov, A. V. Eletskiĭ, and B. M. Smirnov, Usp. Fiz. Nauk **155** (2), 265 (1988) [Sov. Phys. Usp. **31**, 535 (1988)].
4. V. A. Kas'yanov and A. N. Starostin, in *Chemistry of Plasma*, ed. by B. M. Smirnov (Énergoatomizdat, Moscow, 1990), Vol. 16, pp. 67–97.
5. N. N. Bezuglov, A. N. Klyucharev, and T. Stasevich, Opt. Spektrosk. **77** (3), 342 (1994) [Opt. Spectrosc. **77**, 304 (1994)].
6. G. J. Dunning and A. J. Palmer, J. Appl. Phys. **52** (12), 7086 (1981).
7. R. W. Thompson, E. J. Manista, and D. L. Alger, Appl. Phys. Lett. **32** (10), 610 (1978).
8. E. J. Britt, N. S. Rasor, G. Lee, and K. W. Billman, Appl. Phys. Lett. **33** (5), 385 (1978).
9. J. R. Brandenberg, Phys. Rev. A **36** (1), 76 (1987).
10. V. A. Rozhanskiĭ and L. D. Tsendin, *Collisional Transfer in a Partially Ionized Plasma* (Énergoatomizdat, Moscow, 1988).

Translated by A. Chikishev

Technical Physics Letters, Vol. 26, No. 8, 2000, pp. 656–658. Translated from Pis'ma v Zhurnal Tekhnicheskoĭ Fiziki, Vol. 26, No. 15, 2000, pp. 26–31.

Transients in an Autostochastic Oscillator with Delayed Feedback

É. V. Kal'yanov

Institute of Radio Engineering and Electronics, Russian Academy of Sciences, Fryazino, Moscow oblast, Russia

Received February 4, 2000

Abstract—A numerical analysis of the turn-on transients in an autostochastic oscillator with delayed feedback is reported. Dependence of the transients on the intensity of chaotic initial conditions is studied. It is demonstrated that the chaotic oscillations may switch from one basin of attraction to another. © *2000 MAIK "Nauka/Interperiodica".*

Delayed-feedback oscillators (DFOs) are widely employed as models in various areas of scientific inquiry [1–5]. Nevertheless, the dynamics of DFOs is still poorly understood due to its complicated nature. In particular, little is known about the transients observed under chaotic conditions at large feedback delays. The processes must differ from those occurring in oscillators with a zero delay. Chaos is the factor that seriously complicates the transients in DFOs. On the other hand, the understanding of chaotic transients and ways to reduce them is necessary in some cases, e.g., when using autostochastic DFOs for communications based on deterministic chaos [6].

It is pertinent to note that the very concept of transient in its conventional sense seems to apply to regular operation only. A chaotic oscillation can hardly be treated as a steady process because its state varies continuously. In fact, the chaotic operation of a DFO may be considered as a kind of "transient" state [7]. On the other hand, there is a noticeable growth in the oscillation magnitude once a chaotic regime has been turned on, just as in a regular operation mode. Furthermore, the maximum fluctuations of the chaotic oscillation eventually become bounded from above so that the oscillation reaches some kind of saturation. It is therefore possible to define the buildup time of a chaotic oscillation under certain conditions. This paper presents the results of simulating the turn-on transients accompanying the excitation of chaotic oscillations in a DFO described by fairly general delay equations.

The DFO under study is a closed loop comprised of a nonlinear amplifier, first- and a second-order filters, a delay line, and a differentiating circuit. The simulation is based on a set of nonlinear difference–differential equations using a third-order approximation of the amplifier nonlinearity. The equations are as follows:

$$\begin{aligned} \dot{x} &= y, \\ \dot{y} + (\omega/Q)y + \omega^2 x &= \omega^2\{B[(1-z^2)/\delta][x(t-\tau)-z]\}, \\ \delta\dot{z} + z &= x(t-\tau), \end{aligned} \tag{1}$$

where x, y, and z are the time-dependent variables; the dot denotes differentiation with respect to the time t; ω and Q are the natural frequency and the Q-factor of the second-order filter, respectively; δ is the time constant of the first-order filter; τ is the feedback delay; and B is the gain parameter.

In contrast to the zero-delay case [8], the initial conditions cannot be considered independent of time (constant) when dealing with the turn-on transients in DFOs. Circulating in the loop, an initial disturbance (in a real system, arising from noise oscillations of various origin) keeps acting upon the DFO in a random fashion. It is therefore necessary to specify initial conditions in the form of time-dependent noise (or noise-like) oscillations. To obtain reproducible results, it is expedient to construct the initial conditions from a solution to a system of equations describing systems with chaotic behavior. In particular, it is convenient to use the chaotic solutions to relatively simple nonlinear Rössler equations:

$$\begin{aligned} \dot{u} &= -v - w, \\ \dot{v} &= u + \alpha v, \\ \dot{w} &= -\beta w + uv + \sigma, \end{aligned} \tag{2}$$

where u, v, and w are the time-dependent variables, whereas α, β, and σ are constants [9]. At $\alpha = 0.3$, $\beta = 8.5$, and $\sigma = 0.4$, the solutions to Eqs. (2) are chaotic with a funnel-shaped attractor [1]; the spectrum has no regular components.

1063-7850/00/2608-0656$20.00

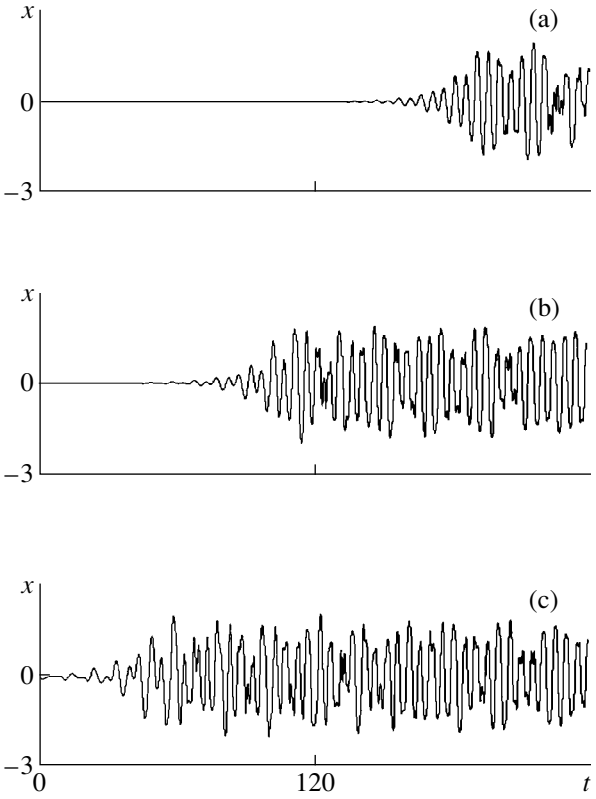

Fig. 1. Waveforms of growing oscillations for different intensities of the initial chaotic conditions $\gamma = 0.000001$ (a); 0.001 (b); 0.1 (c).

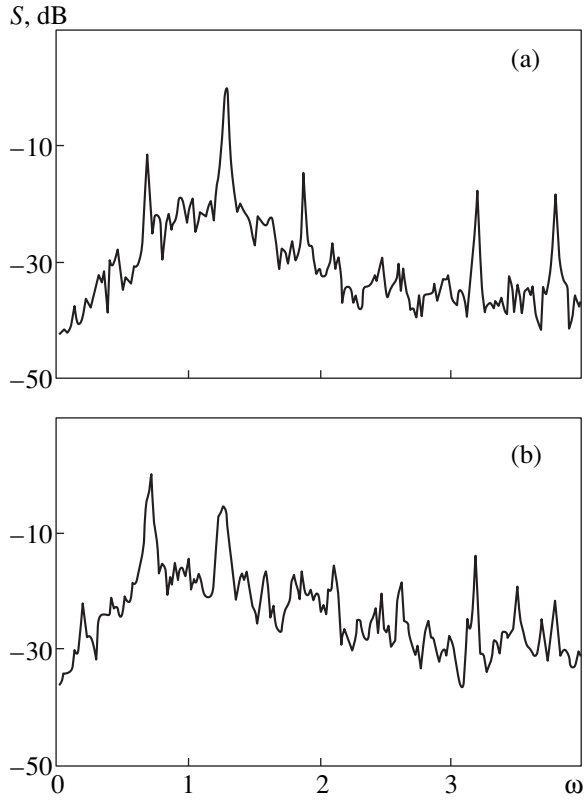

Fig. 2. Power spectrum densities for different intensities of the initial chaotic conditions $\gamma = 0.000001$ (a); 0.001 (b).

In connection with the above considerations, the initial conditions for x, y, and z in Eqs. (1) are determined by $\gamma u(t)$, $\gamma v(t)$, and $\gamma w(t)$, respectively, where $u(t)$, $v(t)$, and $w(t)$ constitute a solution to Eqs. (2) with constants indicated above. The coefficient γ makes it possible to control the intensity of the chaotic oscillations representing the initial conditions for system (1). To eliminate transients in the solution to Eqs. (2), the initial conditions are set as follows: $u(0) = 5.536877$, $v(0) = -1.617695$, and $w(0) = 0.1127826$. These values of u, v, and w are attained after a sufficiently long time from the beginning of oscillation. The numerical analysis employed a fourth-order Runge–Kutta method with a step size of 0.05. The parameters of Eqs. (1) were fixed at the following values: $Q = 1$, $B = 2.9$, $\omega = 1$, and $\delta = 0.1$.

The results of numerically solving Eqs. (1) with the initial conditions specially selected as described above support our expectation that oscillations in the DFO arise with a lag increasing with τ. This phenomenon occurs in both regular and chaotic operation modes.

Now consider the effect of changes in γ. Figure 1 shows the excitation of chaotic oscillations for three values of γ at a delay of $\tau = 9.4$. If γ is very small ($\gamma = 0.000001$, see Fig. 1a), then the oscillation reaches an appreciable magnitude only after a sufficiently long time ($t \in [0, 140]$). This interval may be called the quiescent time, its length being denoted by T. As the γ value increases, the quiescent time drops: $T = 80$ for $\gamma = 0.0001$ and $T = 45$ for $\gamma = 0.001$ (Fig. 1b). In fact, T is virtually zero for $\gamma = 0.1$ (Fig. 1c). Thus, one should raise γ so as to reduce the quiescent time and increase the buildup rate of a chaotic oscillation.

Remarkably, the power spectrum density distribution in a "steady-state" oscillation regime (set in after the time $t \in [0, 2400]$ for $\tau = 9.4$) depends on γ for a given τ. By taking various values of γ, we discovered two different shapes of the spectrum S, which are shown in Fig. 2. The spectrum in Fig. 2a is obtained for $\gamma = 0.000001$ and that in Fig. 2b, for $\gamma = 0.001$ (the delay τ being fixed at 9.4). Note that the low-frequency part has more power in the latter case. For $\gamma = 0.8$, the spectrum is as in Fig. 2b, whereas for $\gamma = 0.0001$, 0.01, or even 1, the spectrum is as in Fig. 2a.

A change in the spectrum of oscillations in the chaotic mode observed in Fig. 2b suggests that the oscillations may go to another basin of attraction (corresponding to lower frequencies). In other words, the intensity of the chaotic initial conditions may determine the basin of attraction where a chaotic oscillation will be excited.

To sum up, this study has demonstrated that the turn-on transients in an autostochastic DFO may take a

considerable time that increases with the feedback delay. To reduce the transient time, one should increase the magnitude of the chaotic initial conditions. In practice, this can be achieved with an amplifier possessing a high level of internal noise. On the other hand, it should be borne in mind that the chaotic oscillation may switch from one basin of attraction to another.

This study was supported by the Russian Foundation for Basic Research (project no. 98-02-16722).

REFERENCES

1. Yu. I. Neimark and P. S. Landa, *Stochastic and Chaotic Oscillations* (Nauka, Moscow, 1987; Kluwer, Dordrecht, 1992).
2. L. Glass and M. Mackey, *From Clocks to Chaos. The Rhythms of Life* (Princeton Univ. Press, Princeton, 1988; Mir, Moscow, 1991).
3. V. Ya. Kislov, Radiotekh. Élektron. (Moscow) **38** (10), 1783 (1993).
4. É. V. Kal'yanov, Pis'ma Zh. Tekh. Fiz. **21** (16), 71 (1995) [Tech. Phys. Lett. **21**, 665 (1995)].
5. A. Yu. Loskutov, A. V. Mushenkov, A. I. Odintsov, *et al.*, Kvantovaya Élektron. (Moscow) **29** (2), 127 (1999).
6. L. M. Pecora, T. L. Caroll, G. A. Johnson, *et al.*, Chaos **7** (4), 520 (1997).
7. E. A. Kotyrev and L. E. Pliss, Radiotekh. Élektron. (Moscow) **10** (9), 1628 (1965).
8. A. O. Maksimov and E. V. Sosedko, Pis'ma Zh. Tekh. Fiz. **25** (17), 1 (1999) [Tech. Phys. Lett. **25**, 675 (1999)].
9. O. E. Rossler, Phys. Lett. A **57** (5), 397 (1976).

Translated by A. Sharshakov

Technical Physics Letters, Vol. 26, No. 8, 2000, pp. 659–661. Translated from Pis'ma v Zhurnal Tekhnicheskoĭ Fiziki, Vol. 26, No. 15, 2000, pp. 32–38.

Effect of Shock Waves Outgoing from Partly Blocked Channel upon an Obstacle

T. V. Bazhenova, T. A. Bormotova, V. V. Golub, S. A. Novikov, and S. B. Shcherbak

Institute of Thermal Physics of Extremal States, Department of the Institute of High Temperatures, Russian Academy of Sciences, Moscow, Russia

Received January 18, 2000

Abstract—Partial channel blocking affects the relative contributions of shock waves and concurrent jet flow. This results in decreasing or increasing the dynamic shock-wave action upon an obstacle, depending on the duration of action and the Mach number. © *2000 MAIK "Nauka/Interperiodica".*

Description of the effect of shock waves outgoing from a partly blocked channel upon an obstacle is a complex problem of gas dynamics. For large Mach numbers of the shock wave, the wave–obstacle interaction is determined by the shock-wave action, while small M values imply a dominating role of the cocurrent jet flow. Intermediate cases feature an interplay of the two processes. We have studied the effect of partial channel blocking on the relative contributions of two flow components. Partial blocking of the channel may enhance the diffracted shock wave action upon the obstacle because the initial pressure drop in the wave increases reaching a level intermediate between the values for the incident and reflected waves.

The action of a weak diffracted shock wave outgoing from a round open channel upon an obstacle was experimentally studied in by Panov *et al.* [1]. Serova [2] performed a numerical calculation for the early stage of this process and obtained an isobar field coinciding with the experimental configuration of the incident and reflected waves. The effect of a weak diffracted shock wave with an obstacle was also studied in the context of finding the optimum shape for a car muffler [3, 4]. Yu and Gronig [5] showed that attenuation of a diffracted shock wave outgoing from an axisymmetric channel can be decreased by placing a coaxial cylindrical insert at the tube output. It was recommended to use this output channel geometry to enhance the shock wave action upon processed surfaces. The effect of partial blocking of the channel output upon the shock wave–obstacle interaction was not studied.

Our experiments were performed in a shock-wave tube with a 40×40 cm^2 cross section connected to a cylindrical vacuum chamber with a diameter of 80 cm and a length of 120 cm. The shock-wave tube end was closed with a flange carrying a channel with a circular cross section (diameter $d = 20$ mm; length $l = 100$ mm) situated inside the tube. The tube edge could be additionally shielded with a diaphragm having a $0.5d$ hole in the middle. The shock-wave tube edge with the flange (mounted perpendicularly to the tube walls) was arranged within the visual field of plane-parallel windows of a pressure chamber. A flat obstacle could be mounted at a variable distance from the shock-wave tube edge. The flow patterns were visualized by an IAB-451 shadowing instrument and registered with a high-speed VSK-5 camera.

The corresponding nonautomodel diffraction problem was numerically modeled by solving the Euler equations using the Godunov method with second-order accuracy. A difference scheme, based on the integral form of the conservation laws, was constructed by the finite volume method. We have employed the first-order-accuracy monotonic schemes in terms of the Godunov and Steger–Warming spatial coordinates, the related second-order schemes, and the Chakravarti–Harten schemes constructed using a similar approach. The second-order schemes were constructed using the total variation diminishing (TVD) concept. The boundary conditions were selected in accordance with the system geometry, taking into account the possibility of partial channel blocking and mounting an obstacle at a certain distance from the tube edge. The field of flow parameters was calculated for a given Mach number of the incident shock wave, taking into account partial reflection of the shock wave from the diaphragm. The results of calculations were represented in dimensionless coordinates normalized to the parameters (density ρ_0 and pressure p_0) of unperturbed gas in the pressure chamber. Distances are expressed in units of the tube diameter d. The dimensionless time t is related to the current time τ by the formula $t = \dfrac{\tau}{d}\sqrt{\dfrac{p_0}{\rho_0}}$.

We have obtained the Toepler patterns describing diffraction of the shock waves with $1.15 < M_0 < 5$ and their interaction with the obstacle. The experimental data describing propagation of the diffracted wave front along the symmetry axis was compared to the results of numerical calculations, where the shock-wave front

1063-7850/00/2608-0659$20.00

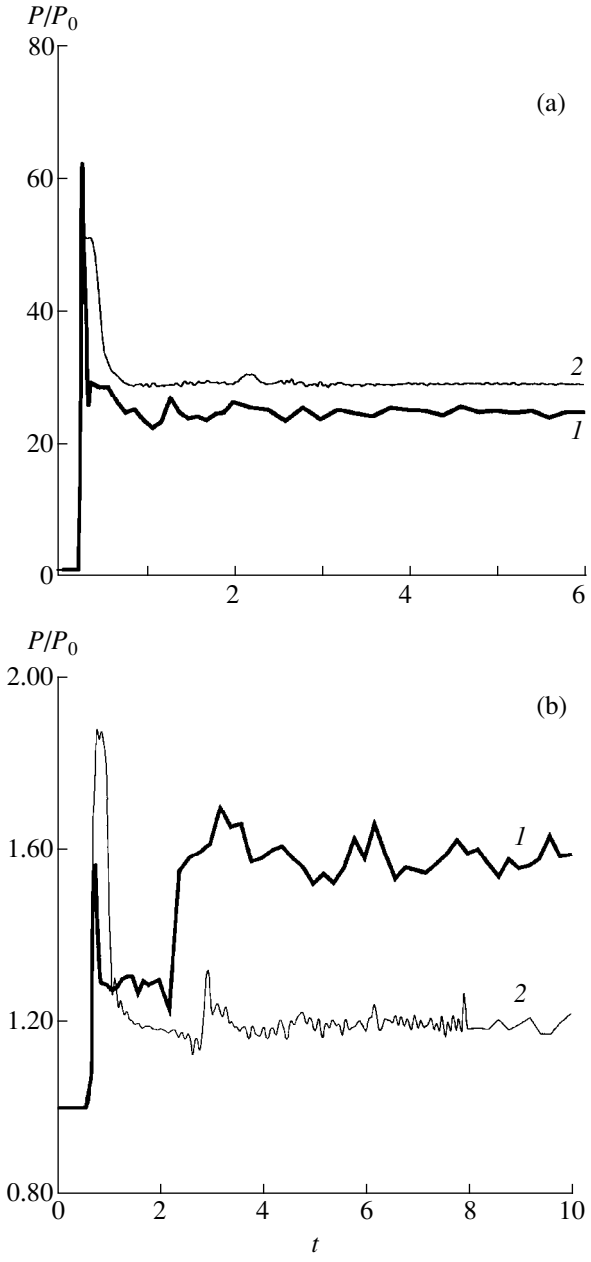

Fig. 1. Time variation of the relative pressure produced by a shock wave with $M_0 = 3$ (a) and 1.15 (b) at the obstacle mounted at a distance of 0.5*d* in front of the channel output: (*1*) channel partly blocked by a diaphragm with a hole diameter of 0.5*d*; (*2*) open channel (*d* is the channel diameter).

position was determined as the coordinate of the point with maximum density gradient (this very point is registered on the experimental Toepler patterns). The results of numerical calculations showed a satisfactory coincidence with the experimental data. We have also compared the time variation of the pressure at the obstacle, determined by numerical calculations, with the data measured for the shock waves outgoing from the open or partly blocked channel with $M_0 = 1.15$ (a weak shock wave with subsonic flow behind) and $M_0 = 3$ (a strong shock wave with supersonic flow behind). The distance between the channel edge and the obstacle was varied from 0.2*d* to 1.5*d*.

Figure 1 shows time variation of the pressure at the center of the obstacle (plate) mounted at a distance of 0.5*d* from the channel edge. Data are presented for a shock wave with $M_0 = 3$ or 1.15 outgoing from the open channel or a channel blocked with a diaphragm (hole diameter, 0.5*d*). For $M_0 = 3$ (Fig. 1a), the diffracted shock wave produces an initial pressure jump followed by a rapid drop, which is similar to the reflection of a spherical shock wave. When a boundary between the outgoing flow and the flow of the unperturbed gas behind the diffracted wave comes to the obstacle, the pressure exhibits the second increase. Then, a quasistationary state is established at the center of the plate. As seen, the second pressure pulse is insignificant as compared to the pressure level observed at the instant of the shock wave reflection. With the diaphragm installed, the pressure at the obstacle decreases but the character of pressure variation remains the same as for the open channel. This result agrees with our previous data [6] showing that a reflecting nozzle mounted at the edge of a channel decreases the pressure at the obstacle.

When the same obstacle is exposed to a weak shock wave (Fig. 1b), the diaphragm favors an increase in the amplitude and duration of the shock wave action. Here, in contrast to the case of a diffracted wave outgoing from the open channel, the pressure on the obstacle mostly increases at a later stage of the interaction featuring retardation of the cocurrent flow rather than upon the diffracted wave reflection. Similar patterns of pressure variation were observed when the obstacle was mounted at other distances from the channel edge.

In order to compare the effects of shock waves outgoing from an open and partly blocked channel, we have calculated the ratio of pressure pulse intensities developed in the two cases at various time instants (Fig. 2). The pulse intensity ratio varies with time in the same manner for all distances from the channel edge to obstacle (from 0.2*d* to 1.5*d*). In the first stage of the shock wave–obstacle interaction, the shock wave outgoing from a partly blocked channel produces a pressure pulse 15–20% smaller as compared to that in the case of open channel. Subsequently, the pressure pulse of a shock wave outgoing from a partly blocked channel increases and becomes greater than that of a similar wave from the open channel. Upon reaching a quasistationary state, the excess pressure reaches 25%.

The results of our experiments and calculations showed that the partial channel blocking may either decrease or increase the dynamic action of shock waves upon the obstacle, depending on the duration of action and the Mach number. When the Mach number is small, the shock wave dominates in the first stage of interaction and the cocurrent jet wave, in the second stage. When a diaphragm with the 0.5*d* hole is mounted at the tube edge, the shock wave exhibits partial reflection

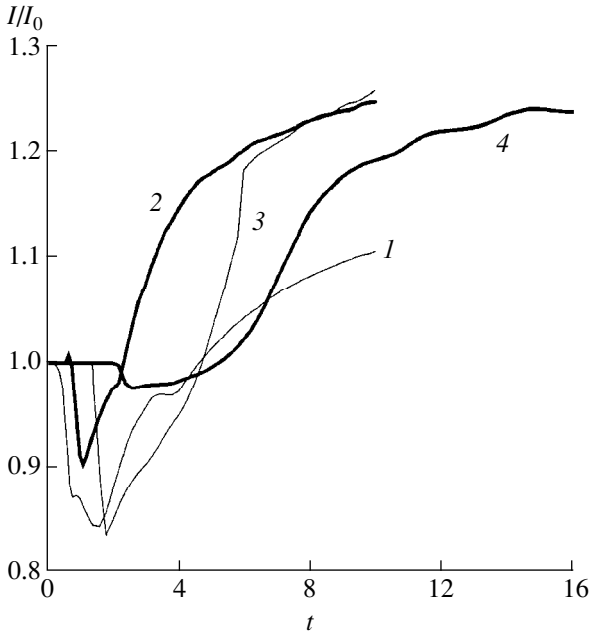

Fig. 2. Time variation of the ratio of pressure pulse intensities for the shock waves with $M_0 = 1.15$ outgoing from the partly blocked channel (I) (diaphragm hole diameter $0.5d$) and the open channel (I_0). The pressure was determined at a flat obstacle spaced by (*1*) $0.2d$, (*2*) $0.5d$, (*3*) $1.0d$, and (*4*) $1.5d$ from the channel output edge.

from the diaphragm and the central part is diffracted into the open space. A distance of $1.0d$ to the obstacle is equivalent to two diameters of hole in the diaphragm. Attenuation of the diffracted shock wave intensity is calibrated by the hole diameter. In this first stage, the intensity of the shock wave outgoing from the partly blocked channel is smaller than the intensity of a wave from the open channel at the same distance. In the following, the reflected part of the shock wave significantly affects parameters of the flow behind the wave front. This perturbation is transferred toward the symmetry axis (with the velocity of sound) and in the direction of the primary shock wave propagation (with the flow velocity). This results in increasing pressure at the flat obstacle mounted in front of the channel output. As a result, the pressure pulse at the obstacle produced by the shock wave coming from the partly blocked channel exceeds the level observed for the wave outgoing from the open channel.

This phenomenon can be used to control the shock-wave pressure pulse developed at the obstacle by changing the channel output geometry.

The work was partly supported by the Russian Foundation for Basic Research.

REFERENCES

1. B. Yu. Panov, A. I. Starshinov, and E. A. Ugryumov, Gazodin. Teploobmen **1**, 108 (1970).
2. V. D. Serova, Gazodin. Teploobmen **6**, 121 (1981).
3. K. Phan and J. Stollery, in *Proceedings of the 14th International Symposium on Shock Tubes and Shock Waves, Sydney, 1983*, pp. 519–525.
4. S. Matsumura, O. Onodera, and K. Takayama, in *Proceedings of the 19th International Symposium on Shock Waves, Marseille, 1993*, ed. by R. Brun and L. Z. Dumitrescu (Springer Verlag, Berlin, 1995), Vol. 3, pp. 367–372.
5. Q. Yu and H. Gronig, Shock Waves **6** (5), 249 (1996).
6. T. V. Bazhenova, V. V. Golub, T. A. Bormotova, *et al.*, Izv. Akad. Nauk, Mekh. Zhidk. Gaza, No. 4, 110 (1999).

Translated by P. Pozdeev

Technical Physics Letters, Vol. 26, No. 8, 2000, pp. 662–665. Translated from Pis'ma v Zhurnal Tekhnicheskoĭ Fiziki, Vol. 26, No. 15, 2000, pp. 39–47.

Transformation of the Electronic Structure of Fullerene C_{60} Caused by Complex Formation in *N*-Methylpyrrolidone Solutions

Yu. F. Biryulin, N. P. Evlampieva, E. Yu. Melenevskaya, V. N. Bocharov, V. N. Zgonnik, and E. I. Ryumtsev

Ioffe Physicotechnical Institute, Russian Academy of Sciences, St. Petersburg, Russia
Institute of Physics, St. Petersburg State University, St. Petersburg, Russia
Institute of Macromolecular Compounds, Russian Academy of Sciences, St. Petersburg, 199004 Russia
Received March 29, 2000

Abstract—Evolution of the electronic absorption and photoluminescence spectra of the fullerene C_{60} solutions with various concentrations in a polar solvent (*N*-methylpyrrolidone) was studied. Comparison with the electrooptical properties of these solutions shows that a slow (associative) fullerene–solvent interaction mechanism is operative at large (nearly saturating) concentrations (1×10^{-3} g/cm^3), whereas the solutions of relatively low concentration (less than 5×10^{-4} g/cm^3) exhibit fast complex formation between fullerene and the solvent molecules. The latter interaction significantly changes the electronic structure of fullerene. © *2000 MAIK "Nauka/Interperiodica".*

A specific property of fullerene C_{60} is its ability to form complexes of the donor–acceptor type with various organic and inorganic electron donors in solvents [1]. It was recently demonstrated that fullerene C_{60} exhibits the donor–acceptor interaction not only with the known complex-forming substances (e.g., tetrafulvalenes [2] and calixarenes [3]) but also with the conventional organic solvents to form complexes with a certain number of the solvent molecules [1, 4, 5]. Masin *et al.* [4, 5] used NMR spectroscopy to determine the parameters of the crystal lattice of the $C_{60} \cdot 4C_6H_6$ and $C_{60} \cdot C_6H_5(CH_3)$ complexes obtained by slow evaporation of the C_{60} solutions in benzene and toluene, respectively, at room temperature.

Based on the results presented below, we conclude that fullerene C_{60} forms complexes with the molecules of one more solvent: polar cyclic organic compound *N*-methylpyrrolidone.

Recent hydrodynamic and electrooptical studies [6] of C_{60} solutions in *N*-methyl-pyrrolidone (MP) and *N*-methylmorpholine revealed changes in the properties of these solutions caused by slowly developing aggregation process and showed a special role of the solvents in this process. The purpose of this work was to study in further detail the interaction of MP as the solvent with fullerene C_{60} by optical methods.

We measured and analyzed the electronic absorption and photoluminescence spectra of C_{60} solutions in MP prepared various methods and traced evolution of the spectra with time. The changes of the spectral characteristics were compared to changes of the electrooptical properties (birefringence in the electric field) for various concentrations and storage times of the C_{60} solutions in MP.

EXPERIMENTAL

The electronic absorption spectra of C_{60} solutions in MP were measured in the 220–900 nm spectral range on a Specord M40 spectrophotometer employing 2-mm- and 1-cm-thick cells.

A modulated argon laser (wavelength, 488 nm; modulation frequency, 135 Hz, power, less than 100 mW) excited the photoluminescence (PL) of the solutions. Detection system used an FEU-62 wideband photomultiplier tube (detection range, 280–1200 nm) and a lock-in amplifier.

Electrooptical experiments used a pulsed electric field with a rectangular pulse duration of 40 μs. A photoelectric detection system employed a low-frequency modulation of the elliptically polarized light to measure the electric-field-induced birefringence of the sample solutions [7].

The spectral and electrooptical measurements were carried out at room temperature.

The experiments were performed with commercial fullerene C_{60} of the 99 mass % grade produced by the "Fullerenovye Tekhnologii" company (Fullerene Technologies Ltd., Russia).

The initial solutions were prepared by dissolving C_{60} in MP for two days to a maximum concentration of $c_1 = 0.1 \times 10^{-2}$ g/cm^3 [6]. Then, a part of the solution

1063-7850/00/2608-0662$20.00 © 2000 MAIK "Nauka/Interperiodica"

with the initial concentration c_1 was diluted with MP to obtain a series of solutions for the optical studies with the concentrations $c_2 = 0.8c_1$, $c_3 = 0.6c_1$, $c_4 = 0.5c_1$, $c_5 = 0.2c_1$, and $c_6 = 0.1c_1$.

RESULTS AND DISCUSSION

The PL studies of the C_{60} solutions in MP at various concentrations and storage times revealed a sharp variation of the PL characteristics at certain concentrations, which were indicative of changes in the electronic structure of fullerene.

Figures 1a and 1b show the pattern of changes in the PL spectra at the concentrations c_1 and $c_6 = 0.01 \times 10^{-2}$ g/cm^3, respectively, over a time interval of 38 days. The concentrated solution (Fig. 1a) exhibits no significant changes in shape of the PL spectrum after a one-month storage, but shows an approximately threefold increase in the quantum efficiency (radiative recombination yield). The PL spectrum of the diluted solution ($c_1/10$) shows substantial qualitative changes. The spectrum measured immediately or two days after preparation exhibits a maximum at 1.65 eV and resembles a PL spectrum of the fullerene C_{60} solution in toluene [8]. A fifteen-day storage leads to a several-fold increase in the PL intensity, a substantial broadening of the spectrum, and a high-energy shift of its maximum by 0.4–0.5 eV (Fig. 1b). The two weeks that follow the sharp transformation bring virtually no changes in the spectrum shape.

Thus, the results of the PL studies show that the time evolution of the intermolecular interactions in the fullerene solutions in MP substantially depends on the solution concentration. A conventional associative mechanism dominates at high fullerene concentrations: in the first days, the PL spectrum exhibits virtually no differences from the spectrum of the molecular fullerene [8] and then some slow changes proceed in time with increasing intermolecular interactions (Fig. 1a). A different, rather fast (taking from several days to several hours) process causes drastic changes in the electronic structure of fullerene in the diluted solution ($c = 0.1c_1$, Fig. 1b) and gives rise to the recombination transitions that substantially differ from those typical of isolated C_{60}.

We studied optical absorption of the C_{60} solutions in MP in the UV range at a concentration of ~$(0.005–0.006) \times 10^{-2}$ g/cm^3. A characteristic C_{60} absorption band at 330 nm [9] shows up only in the spectra of solutions prepared immediately prior to the measurement and then slowly "disappears" with time. The rate of the spectral changes depends on the concentration of the initial stock solution from which the sample was prepared. Figure 2 shows evolution of the UV absorption spectrum of a C_{60} solution in MP with a concentration of 0.005×10^{-2} g/cm^3 prepared by diluting the c_1 solution immediately before the measurements. It is seen

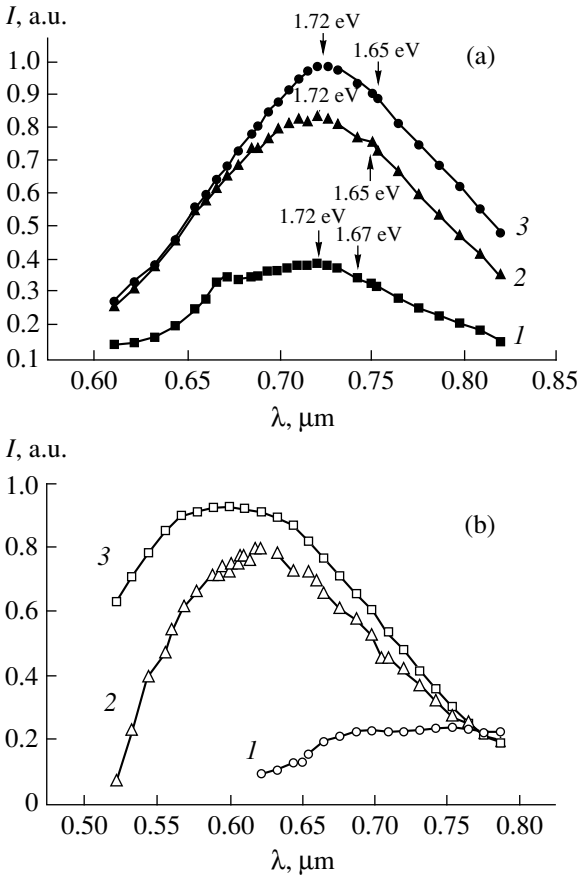

Fig. 1. Time evolution of the PL spectra of the C_{60} solutions in MP with the concentrations (a) 0.1×10^{-2} g/cm^3 and (b) 0.01×10^{-2} g/cm^3: the spectra are measured (*1*) 2, (*2*) 15, and (*3*) 38 days after preparation.

that the C_{60} absorption maximum completely disappears in three days. In contrast, solutions prepared from the initial solution of lower concentration ($c \le 0.5c_1$) exhibit a faster evolution of the absorption spectra: changes similar to those shown in Fig. 2 occur within several hours.

The C_{60} solutions in MP demonstrate rather unusual spectral changes. The formation of the C_{60} solvates in various solvents normally leads to a high-energy shift of the UV absorption edge by approximately 0.1 eV as compared to the absorption of individual C_{60} [10]. The character of the UV absorption spectra of the C_{60} solutions in MP does not comply with the conventional solvation of C_{60} by solvent molecules and indicates a transition of C_{60} in this solvent into a state with a new electronic structure of the optical transitions. The solutions of high ($c \sim 0.1 \times 10^{-2}$ g/cm^3) and low ($c \le 0.05 \times 10^{-2}$ g/cm^3) concentrations exhibit slow and very fast fullerene state transformations, respectively.

Qualitative changes of the fullerene interaction with MP molecules during serial dilution are additionally confirmed by experimental results on the pulsed-

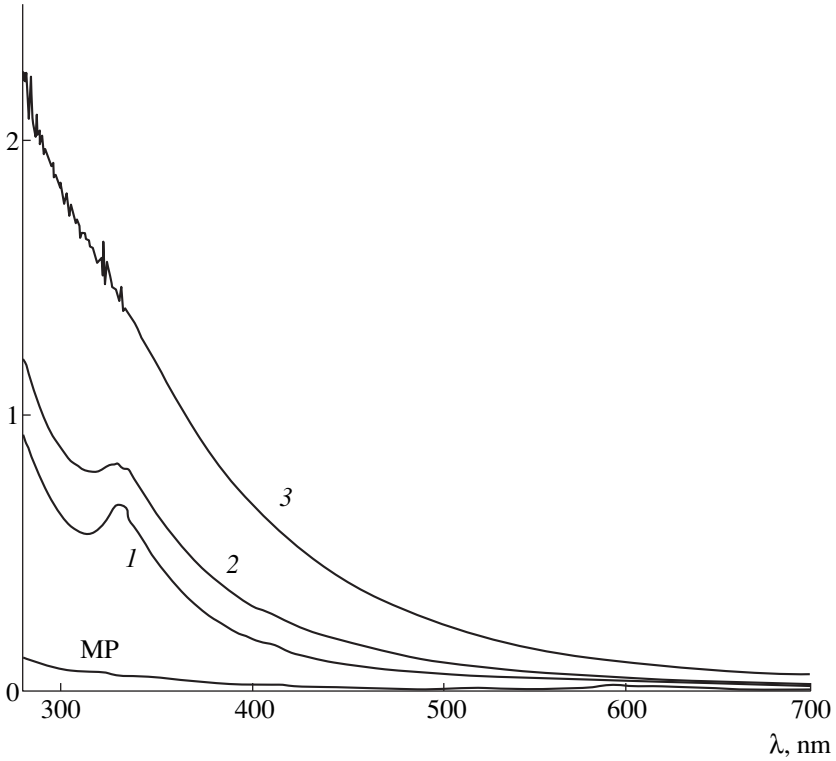

Fig. 2. Time evolution of the UV absorption spectra of a C_{60} solution in MP with the concentration 0.005×10^{-2} g/cm^3: the spectra were measured (*1*) immediately after dilution of the initial solution with the concentration 0.1×10^{-2} g/cm^3; (*2*) 4 hours later; (*3*) three days later. (MP) absorption spectrum of the solvent.

electric-field-induced birefringence of the C_{60} solutions in MP.

Figure 3 shows the change in sign of the electrooptical effect at a concentration of $(0.05–0.06) \times 10^{-2}$ g/cm^3, which proves modification of the solution properties.

High symmetry of the C_{60} molecule suggests its optical isotropy. Then the observed negative electrooptical effect (the absolute birefringence being smaller than that of the solvent) can be explained by the fact that a part of the solvent molecules bound to (or associated with) C_{60} molecules are not involved into the electric-field-induced orientation. The change of sign of the electrooptical effect points to different involvement of the polar solvent molecules into the field-induced orientation at a concentration lower and higher than 0.05×10^{-2} g/cm^3. The positive effect at a concentration of about 0.05×10^{-2} g/cm^3 can be related to the formation of a polar asymmetric complex of C_{60} with MP molecules. The orientation of these complexes in the electric field accounts for the larger absolute value of the electrooptical effect in comparison with that in the case of pure MP.

Figure 4 compares the optical absorption spectra of the solutions of C_{60} and the C_{60}–MP complex (obtained by vacuum evaporation of MP) in methylene chloride. The spectrum of the complex retains the main spectral features of the C_{60} absorption in the UV range and exhibits additional weak absorption bands peaked at 435 and 460 nm similarly to the C_{60} complex with poly(vinylpyrrolidone)—a polymeric analog of MP [10].

Summarizing the results of the studies of the C_{60} solutions in MP we arrive at the following conclusions on the character of the fullerene-solvent interaction and its kinetics upon serial dilution.

(1) MP molecules are strongly associated with C_{60} molecules at a near-saturation concentration of about

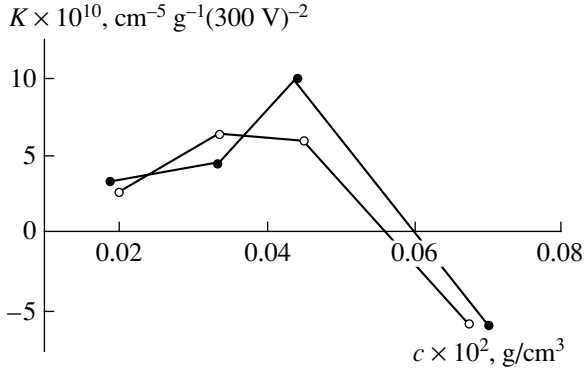

Fig. 3. Plots of the specific (per fullerene unit mass) electrooptical constant K versus C_{60} concentration measured during serial dilution of the C_{60} solution in MP. The curves belong to two independently prepared samples.

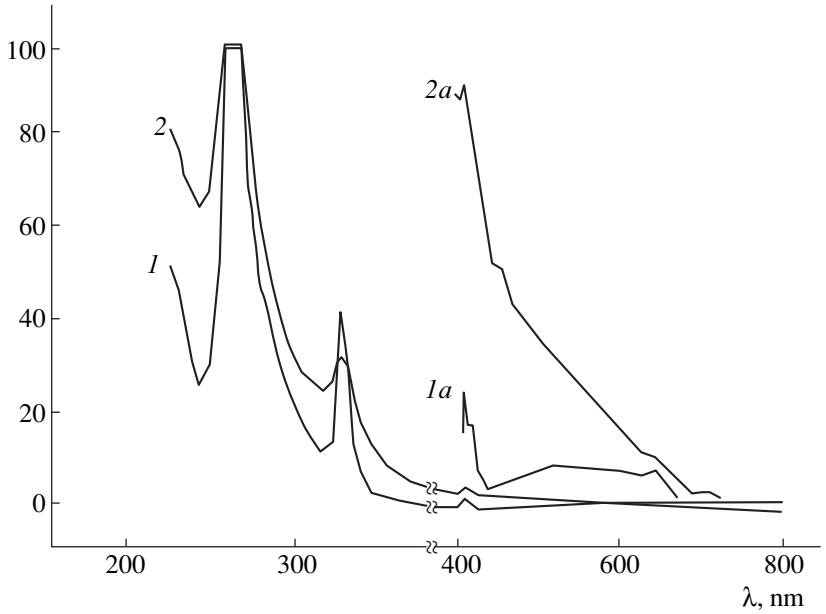

Fig. 4. The optical absorption spectra of (*1*) C_{60} and (*2*) C_{60}–MP complex solutions in methylene chloride; curves (*1a*) and (*2a*) show the long-wavelength parts of the corresponding spectra scaled by the factors 5 and 10, respectively.

0.1×10^{-2} g/cm^3. The character of the fullerene–MP interaction changes with time and depends on the initial solution concentration.

(2) Serial dilution of the solutions down to a concentration of $(0.05–0.06) \times 10^{-2}$ g/cm^3 leads to sharp changes of their spectral, optical, and electrooptical characteristics, which indicates the transition of C_{60} into the state with a new electronic structure, presumably due to a fullerene complex formation with MP. The PL spectra of the solutions exhibit a high-energy shift of the maximum by ~0.4–0.5 eV, while bands characteristic of C_{60} disappear from the electronic absorption spectra.

(3) The C_{60}–MP complex extracted from solution and dissolved in methylene chloride retains all features of the C_{60} absorption spectrum and exhibits additional peaks at 435 and 460 nm typical of the C_{60}–poly(vinylpyrrolidone) complex. Hence, C_{60} molecules interact with the heterocycles of these compounds in the same way.

This work was supported by the Russian Interdisciplinary Scientific–Technical Program “Fullerenes and Atomic Clusters” (project no. 98076) and the Russian Federal Program “Integration” (project no. 7-326.38).

REFERENCES

1. D. V. Konarev and R. N. Lyubovskaya, Usp. Khim. **68** (1), 23 (1999).
2. A. Izuoka, T. Tachikawa, T. Sugawara, *et al.*, J. Chem. Soc. Chem. Commun. 1472 (1995).
3. T. Suzuki, K. Nakashima, and S. Shinkai, Chem. Lett. 699 (1994).
4. F. Masin, A.-S. Grell, I. Messari, and G. Gusman, Solid State Commun. **106** (1), 59 (1998).
5. A.-S. Grell, I. Messari, P. Pirotte, *et al.*, in *Molecular Nanostructures: Proceedings of the International Winterschool on Electronic Properties of Novel Materials, 1998*, ed. by H. Kuzmany [AIP Conf. Proc. **442**, 28 (1999)].
6. N. P. Evlampieva, S. G. Polushin, N. P. Lavrenko, *et al.*, Zh. Fiz. Khim. **74** (7), 1282 (2000).
7. V. N. Tsvetkov, in *Rigid-Chain Polymer Molecules* (Nauka, Leningrad, 1986), Ch. 7.
8. Yu. F. Biryulin, L. V. Vinogradova, and V. N. Zgonnik, Pis’ma Zh. Tekh. Fiz. **24** (22), 71 (1998) [Tech. Phys. Lett. **24**, 896 (1998)].
9. V. N. Bezmel’nitsyn, A. V. Eletskiĭ, and M. V. Okun’, Usp. Fiz. Nauk **168** (11), 1195 (1998) [Phys. Usp. **41**, 1091 (1998)].
10. V. N. Zgonnik, L. V. Vinogradova, E. Yu. Melenevskaya, *et al.*, Zh. Prikl. Khim. **70** (9), 1538 (1997).

Translated by A. Chikishev

Technical Physics Letters, Vol. 26, No. 8, 2000, pp. 666–667. Translated from Pis'ma v Zhurnal Tekhnicheskoĭ Fiziki, Vol. 26, No. 15, 2000, pp. 48–52.

Medium-Frequency (f < 1 MHz) Oscillations in a Quadrupole Electric-Discharge Galathea Trap ("String-Bag")

A. I. Morozov, A. I. Bugrova, A. S. Lipatov, and V. K. Kharchevnikov

Kurchatov Institute of Atomic Energy, State Scientific Center of the Russian Federation, Moscow, Russia
Moscow Institute of Radio Engineering, Electronics, and Automatics, Moscow, Russia

Received March 22, 2000

Abstract—Two oscillation modes ($f_1 \sim 25$ kHz, $f_2 \sim 250$ kHz) experimentally observed in an electric-discharge galathea trap of the quadrupole type ("string-bag") are described and the nature of these oscillations is discussed. © *2000 MAIK "Nauka/Interperiodica".*

1. Previously [1–3], we have described a quadrupole ("string-bag") variant of the multipole electric-discharge galathea trap (EDT-M). For convenience, Fig. 1 reproduces a schematic diagram of this device and shows a radial distribution of the magnetic field z-component in the plane $z = 0$.

The discharge and plasma parameters of the "string-bag" trap reported in [1–3] represented time-averaged characteristics, while oscillations possible in the system were only briefly mentioned in [4]. Below, we will present experimental data on the medium-frequency (f < 1 MHz) oscillations observed in a quadrupole trap operating in the "barrier" mode (this regime, realized by placing a cathode in the region of zero magnetic field, was previously referred to as a "discharge with mantle" [1, 2]) and suggest the most probable interpretation.

The experiments were performed using an EDT-M device of the "string-bag" type operated in the following regime: working gas, xenon; gas flow rate $\dot{m}$ = 2 mg/s; discharge voltage U_p = 200 V; discharge current J_p = 200 mA; barrier field strength H_1 = 20 Oe; residual air pressure, $\sim 2 \times 10^{-4}$ Torr. Under these conditions, the plasma was characterized by a maximum electron temperature of $T_{e\,\max} \sim 20$ eV, a maximum charge density of $n_{\max} \sim 9 \times 10^{10}$ cm^{-3}, and a minimum potential well depth of $|\varphi_{\min}| \sim 50$ V.

2. Oscillograms of the discharge current $J_1^{\sim}$ reveal the presence of quite regular oscillations (Fig. 2) with the frequencies $f_1 \sim 25$ kHz, $f_2 \sim 250$ kHz.

3. Oscillations with the frequency f_1 represent, as suggested previously [3], a "reset" wave process preventing the trap from overfilling in the course of continuous ionization of supplied gas. The accumulated plasma reaches a threshold of the magnetohydrodynamic instability (Ohkawa's surface [5]) and is convectively ejected from the trap. This hypothesis is confirmed by the following facts.

(a) The frequency f_1 is close to the inverse time of ion accumulation in the trap: $f_1 \sim \frac{1}{\tau} = n_0\langle\sigma V\rangle \sim 30$ kHz, where $n_0 \sim 3 \times 10^{12}$ cm^{-3} is the xenon concentration in the working chamber and $\langle\sigma V\rangle \sim 10^{-8}$ cm^3/s. The presence of a tube supplying xenon weakly changes the discharge parameters as compared to those in the system without tube operating under the same gas pressure.

(b) The ion and electron currents to the probes exhibit synchronous oscillations with the relative amplitudes ($J^{\sim}/J^{\parallel}$), being close on the experimental accuracy scale of ~30% (Fig. 3).

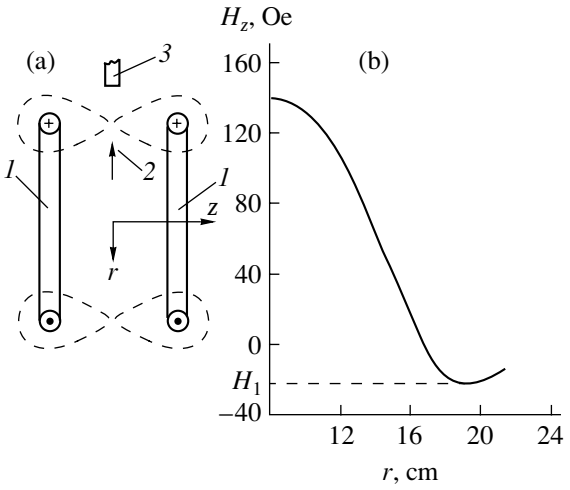

Fig. 1. (a) Schematic diagram of the quadrupole electric-discharge trap: (*1*) magnetic coils; (*2*) cathode; (*3*) xenon inlet tube; (b) radial distribution of the magnetic field H_z (r, z = 0); H_1 is the barrier field.

1063-7850/00/2608-0666$20.00 © 2000 MAIK "Nauka/Interperiodica"

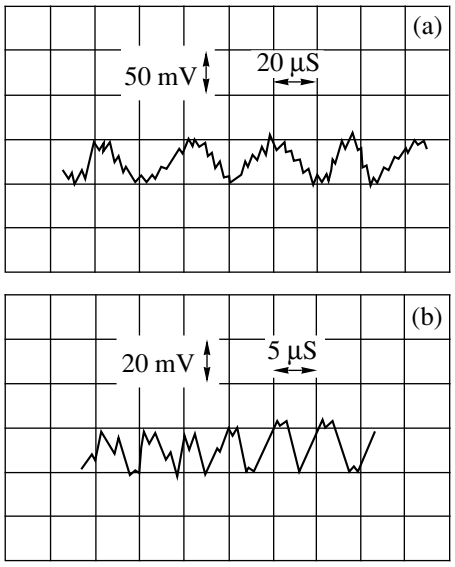

Fig. 2. Oscillograms of the discharge current oscillations: (a) 20-μs scale; (b) 5-μs scale with the low-frequency component suppressed.

(c) The relative amplitude of oscillations of the probe currents increases when the probes are moved from the plasma column center to the periphery.

(d) The ion current minima measured with a probe placed inside the plasma volume coincide with the maxima of ion current ejected from the trap, the latter measured by a probe oriented along the radius.

4. Direct experiments with oriented probes showed that the flux of ions ejected from the trap has both radial and azimuthal velocity components. The latter component is apparently related to an azimuthal electric field, which was experimentally detected and explained by azimuthal dependence of the reset wave field.

5. As for the oscillations with the frequency f_2, there are rather few experimental data on this phenomenon. However, taking into account a regular character of these oscillations, their electron and ion energy scale ($T_e \sim T_i \sim 20$ eV), and the transverse size of the plasma volume, we may suggest that these oscillations represent an ion-acoustic volume "resonance." Indeed, the wavelength of these oscillations can be calculated by the formula

$$\lambda = \frac{c_3}{f_2} = \sqrt{\frac{k(T_e + T_i)}{M}}\frac{1}{f_2} \approx 3 \text{ cm},$$

where $T_e = T_i = 20$ eV, $M \sim 2 \times 10^{-22}$ g is the xenon ion mass, and $f_2 = 200$ kHz. This λ value, being close to the effective transverse size of the plasma volume, is in our opinion a strong evidence for the above suggestion.

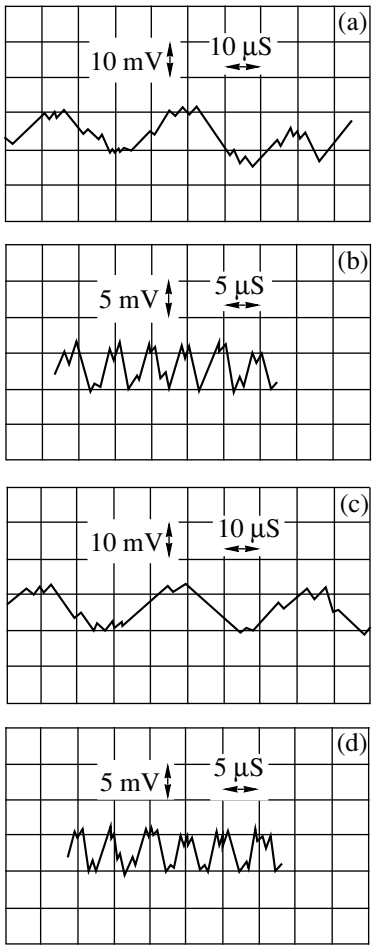

Fig. 3. Oscillograms of the (a, b) ion and (c, d) electron probe current oscillations: (a, c) 20-μs scale; (b, d) 5-μs scale with the low-frequency component suppressed.

The work was supported by the Ministry of Atomic Energy of the Russian Federation.

REFERENCES

1. A. I. Bugrova, A. S. Lipatov, A. I. Morozov, and V. K. Kharchevnikov, Pis'ma Zh. Tekh. Fiz. **18** (8), 1 (1992) [Sov. Tech. Phys. Lett. **18**, 242 (1992)].
2. A. I. Bugrova, A. S. Lipatov, A. I. Morozov, and V. K. Kharchevnikov, Fiz. Plazmy **19** (12), 1411 (1993) [Plasma Phys. Rep. **19**, 741 (1993)].
3. A. I. Morozov and V. V. Savel'ev, Usp. Fiz. Nauk **168** (11), 1153 (1998) [Phys. Usp. **41**, 1049 (1998)].
4. A. I. Bugrova, A. S. Lipatov, A. I. Morozov, and V. K. Kharchevnikov, in *Proceedings of the XXVI Zvenigorod Conference on Plasma Physics and CTR, Zvenigorod, 1999*, Vol. 18, p. 83.
5. H. G. Voorhies and T. Ohkawa, Phys. Fluids **11** (7), 1572 (1968).

Translated by P. Pozdeev

Technical Physics Letters, Vol. 26, No. 8, 2000, pp. 668–670. Translated from Pis'ma v Zhurnal Tekhnicheskoĭ Fiziki, Vol. 26, No. 15, 2000, pp. 53–57.

Calculation of Correlations in the Surface Structure of Solids

S. M. Mursalov, N. V. Bodyagin, and S. P. Vikhrov

Ryazan State Radioengineering Academy, Ryazan, Russia

Received November 16, 1999

Abstract—Methods for the calculation of correlations in the surface structure of solids are analyzed. A new approach is proposed based on determination of the mean reciprocal information for two-dimensional systems. The approach is applied to interpretation of the results of experimental investigation of the surface of amorphized hydrogenated silicon. © *2000 MAIK "Nauka/Interperiodica".*

The existing methods used for investigations of the order in solid materials and the mechanisms and dynamics of growth processes have significant drawbacks, and the task of studying these systems is still far from being solved [1]. This situation necessitates the development of alternative approaches. A possible variant is offered by the methods of nonlinear dynamics, since a substance in the course of solidification can be considered as a nonlinear self-organizing system [2, 3].

An important characteristic of nonlinear systems is their mean reciprocal information (MRI). It is this information—rather than distribution functions, autocorrelation function, and Fourier spectra—that characterizes correlations in chaotic nonlinear systems. Moreover, the search of local MRI minimum is an important stage in the procedure of embedding and calculating the system attractor dimensionality [4].

The reciprocal information is determined as the amount of information about the random function value at point A that becomes known when we know the function value at point B. Let D be the domain of definition of a random function and *Z*, the codomain; P_X, the probability distribution density at a point X (as a function on Z); and P_{XY}, the joint probability distribution density at the points X and Y (as function on Z^2). The reciprocal information $I_{AB}(z_1, z_2)$ for a given pair of the known and predicted values is calculated by the following formula:

$$I_{AB}(z_1, z_2) = \log\left[\frac{P_{AB}(z_1, z_2)}{P_A(z_1)P_B(z_2)}\right]. \quad (1)$$

Here and below, the logarithm is binary and the values are expressed in bits.

According to Eq. (1), the reciprocal information is defined as a function on Z^2 and has non-negative values (since $P_{AB} \geq P_A P_B$). The mean reciprocal information is determined as the mean expected value of reciprocal information for a given pair of points by integrating over Z^2:

$$I(A, B) = \int_{Z^2} P_{AB}(z_1, z_2)\log\left[\frac{P_{AB}(z_1, z_2)}{P_A(z_1)P_B(z_2)}\right]dz_1 dz_2. \quad (2)$$

Thus, MRI is a function defined on D^2, adopting non-negative values.

Let us consider the case when D is a rectangular domain and a random function is the surface relief of a material studied. We assume that the surface properties are invariant relative to the origin of the frame; this implies that we will study various convolutions of the $I(A, B)$ function.

Let R be a domain of non-negative real values and $L = L(r)$ be the MRI defined on R as function of the distance on D determined as a convolution of $I(A, B)$ over circles with a radius r. The physical meaning of L is the average amount of information which the known function value at a given point carries about the values at a distance r. The $L(r)$ value is calculated using methods of numerical integration, by constructing multidimensional histograms on $D \times D \times R$, followed by summing over equal distances.

Figure 1 shows typical shapes of $L(r)$ for various two-dimensional objects. Here, curve *1* refers to a signal of the type $A(x, y) = \sin(wx) + \cos(wy)$; curve *2*, to the surface of amorphized hydrogenated silicon (*a*-Si:H) film; and curve *3*, to a random two-dimensional noise.

The *a*-Si:H films were deposited from a glow discharge in 100% silane (discharge parameters: power, 50 mW/cm^2; pressure, 70 Pa; silane flow rate, 200 cm^3/s) onto substrates heated to various temperatures. The MRI were calculated using the sample surface profile measured by the method of atomic force microscopy. The profile height was determined at discrete points and measured from a certain level considered as the zero level.

1063-7850/00/2608-0668$20.00 © 2000 MAIK "Nauka/Interperiodica"

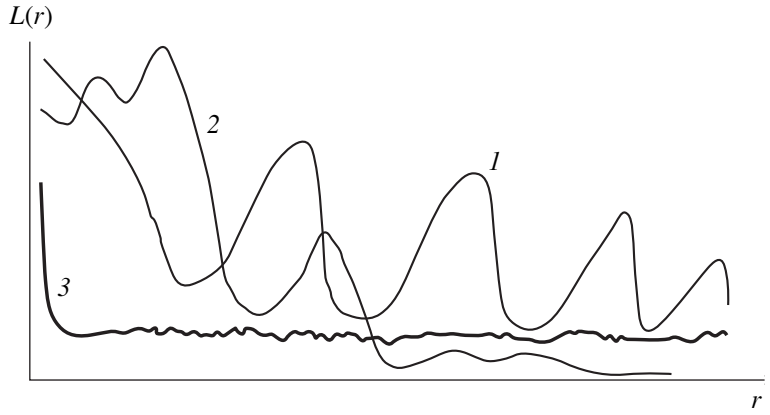

Fig. 1. The typical shapes of $L(r)$ curves for various two- dimensional objects (see the text for explanation).

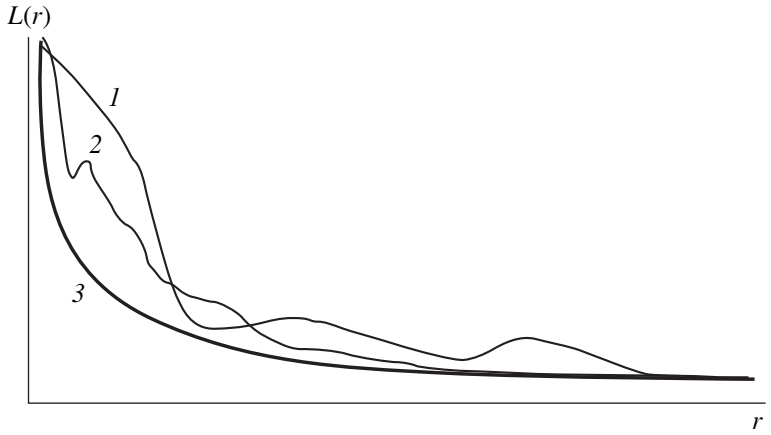

Fig. 2. The shapes of normalized $L(r)$ curves for the same two- dimensional objects as in Fig. 1.

The shapes of MRI curves presented in Fig. 1 poses serious questions. In particular, curve *1* exhibits poorly pronounced periodicity, while curve *3* (noise) reveals no expected random uniform signal. A reason for these discrepancies is specific to the systems with dimensionalities greater than unity: the quality of statistics is significantly different for various distances. Indeed, this quality is directly determined by the size of a sample set. For the two-dimensional case, this size is directly proportional to the circle length with a radius equal to the argument $(2\pi r)$.

In the case of studying a real sample, this effect is manifested by the incorrect selection of the MRI minimum or its absence, which results in an attractor being poorly "developed" in space.

The variable quality of statistics can be correctly taken into account using the MRI normalization calculated by Eq. (2). The normalization factor can be represented by the quantity $L_3(r) = \dfrac{\log(1+r)}{r}$ describing the MRI plot for a random two-dimensional noise (Fig. 1, curve *3*). Here, the normalized MRI is determined as

$$L_N(r) = \frac{r}{\log(1+r)} L(r). \qquad (3)$$

Figure 2 shows the plots of normalized MRI calculated for various two-dimensional structures under the same initial conditions as those used in Fig. 1. Apparently, the normalized MRI adequately reflects spatial correlations in the systems studied. Indeed, the MRI for $A(x, y) = \sin(wx) + \cos(wy)$ exhibits a clearly pronounced sinusoidal shape. The MRI of a random noise, as expected, is uniform. The MRI for an *a*-Si:H sample surface has a distinct minimum not coinciding with that observed in Fig. 1. The distances for which the MRI function exhibits maxima are approximately equal to the size of inhomogeneities (islands) on the *a*-Si:H surface. The same pattern is observed for *a*-Si:H samples deposited at different substrate temperatures. The character of the MRI variation is highly sensitive toward the conditions of film deposition. A more detailed analysis of the physical meaning of the MRI curve and the

effects of technological parameters on this function is a subject of special investigation.

Thus, the proposed approach based on the MRI calculation can provide for an adequate description of correlations in spatially distributed two-dimensional systems.

REFERENCES

1. A. A. Aĭvazov, B. G. Budagyan, S. P. Vikhrov, and A. I. Popov, *Disordered Semiconductors: Learning Aid* (Mosk. Énerg. Inst., Moscow, 1995).
2. G. Nicolis and I. Prigogine, *Exploring Complexity* (Freeman, New York, 1989; Mir, Moscow, 1990).
3. A. A. Aivazov, N. V. Bodyagin, and S. P. Vikhrov, in *Materials Research Society USA, Spring Meeting Proceedings, 1996*, Vol. 420, pp. 145–151.
4. H. D. I. Abarbanel, R. Brown, J. J. Sidorovich, and L. S. Tsimiring, Rev. Mod. Phys. **65** (4), 1331 (1993).

Translated by P. Pozdeev

Technical Physics Letters, Vol. 26, No. 8, 2000, pp. 671–674. Translated from Pis'ma v Zhurnal Tekhnicheskoĭ Fiziki, Vol. 26, No. 15, 2000, pp. 58–64.

Dynamic Characteristics of Chaotic Processes Determined from Point Process Analysis

A. N. Pavlov and V. S. Anishchenko

Saratov State University, Saratov, Russia

e-mail: wadim@chaos.ssu.runnet.ru

Received April 4, 2000

Abstract—The capability of calculating the highest Lyapunov index during analysis of the so-called point processes [1] is analyzed. Two mathematical models describing the generation of pulses by receptor neurons are considered and the conditions are established for which the dynamic characteristics of chaotic oscillations, determined from the output sequence of pulses, are retained during linear transformations of the neuron input signal. © *2000 MAIK "Nauka/Interperiodica".*

The study of information processing in living organisms is a currently important task of natural sciences. Solving this task encounters a large variety of particular problems, including the question of how are data coded by the nerve cells. Each cell (receptor neuron) is essentially a threshold device transforming a complex input signal $S(t)$ into a sequence of identical pulses (spikes) registered at the output (Fig. 1a). Since the shape of the output pulses is independent of the external factors, all information about the input signal $S(t)$ must be converted into the length of time intervals between output pulses—interspike intervals (ISIs) [2, 3].

In how much detail can the input signal be characterized upon analysis of the output sequence of spikes? In recent years, this problem has drawn the attention of researchers in connection with the problem of dynamic system (DS) reconstruction. In order to apply reconstruction methods to analysis of the point processes (where the information is carried in the form of times of various events), it is necessary to answer the question formulated by Sauer [1]: can the output ISI sequence determine the state of a system if the input signal is deterministic and generated by the DS with small-scale dynamics?

An answer to this question was also originally given by Sauer [1], according to which an ISI set can be considered as points of a new coordinate of state, in using which it is possible to characterize the small-scale dynamics at the input. Then, Sauer [4] proved the embedding theorem for time intervals, thus extending rigorous mathematical formalism developed by Takens [5] to the case of point processes. The possibilities of reconstruction were investigated by numerical methods in [6–9].

By now, various models have been developed to describe the process of spike generation, including the rather popular (and biologically justified) "integrate-and-fire" (IF) and "threshold crossing" (TC) models [8]. Within the framework of the IF model, the $S(t)$ signal is frequently represented by a function of variables of the small-scale dynamic system. A set of times T_i corresponding to the moments of spike generation (Fig. 1a) is determined from the equation

$$\int_{T_i}^{T_{i+1}} S(t)dt = \theta, \quad I_i = T_{i+1} - T_i, \tag{1}$$

where θ is the threshold level and I_i are the time intervals (IF ISIs). The integral value is reset to zero on reaching the threshold.

The TC model introduces a threshold level Θ determining the equation of a secant plane $S = \Theta$, where $S(t)$ is considered as a DS coordinate. The spike production corresponds to the time instants when the threshold level is crossed by the signal $S(t)$ in one direction (e.g., upward). From the standpoint of the DS theory, the time intervals between spikes (TC ISIs) represent the times of phase trajectory return to the secant plane.

In this work, we attempted to answer the question as to how the threshold level and the ISI sequence structure affect the results of the reconstruction. The conversion of a continuous input signal into a sequence of spikes is a nonlinear transformation. Moreover, this transformation is accompanied by a partial loss of information about the external factor (in particular, about the signal shape in the TC model). Can we still calculate characteristics of the input signal using the ISI sequence and what are the necessary conditions providing for this possibility?

The study was focused on calculating the highest Lyapunov index λ_1, which is apparently the most informative invariant of a complex dynamic process. Below, we will discuss the conditions under which the λ_1 value can be determined from analysis of a point process.

1063-7850/00/2608-0671$20.00 © 2000 MAIK "Nauka/Interperiodica"

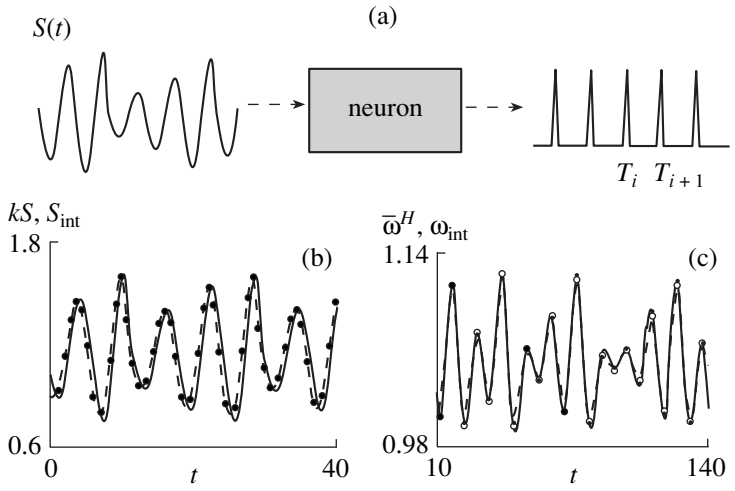

Fig. 1. (a) A schematic diagram illustrating the input signal conversion by a receptor neuron. (b) A linear transformation of the input signal: solid curve, $\frac{1}{\theta}S(t)$; dashed curve, $S_{\text{int}}(t)$ interpolation; points, $1/I_i(T_i)$ values. (c) The values of instantaneous frequency $\bar{\omega}^H(T_i)$ (according to Hilbert) corresponding to the threshold level crossing (black circles connected by dashed line) and the $2\pi/I_i(T_i)$ values (open circles connected by solid line representing the $\omega_{\text{int}}(t)$ function).

Let us first consider the IF model. It was demonstrated [6] that, in the high-frequency approximation, an IF ISI sequence represents a nonlinear transformation of the input signal

$$I_i \approx \theta/S_i, \quad S_i = S(T_i). \tag{2}$$

Since the highest Lyapunov index is invariant with respect to nonlinear transformations, the λ_1 value calculated for the I_i sequence must coincide with the results of calculation using the $S(t)$ signal. Our approach to calculating the Lyapunov index is essentially as follows [10, 11]. Once the IF ISI sequence is known, we may use Eq. (2) to obtain the sequence

$$\frac{1}{I_i} \approx \frac{1}{\theta}S_i = kS(T_i) \tag{3}$$

representing the values of the input signal multiplied by a certain constant k at the fixed time instants T_i. In order to pass to a signal with uniform time scale, the points $1/I_i(T_i)$ are interpolated by a smooth function $S_{\text{int}}(t)$, for example, by a cubic spline. This restores the linear transformation of the input signal to a certain approximation: $S_{\text{int}}(t) \approx kS(t)$ (Fig. 1b). Consequently, the $S_{\text{int}}(t)$ signal would retain both geometric and dynamic characteristics of the attractor corresponding to the input signal (external action). Evidently, this scheme is only valid within a certain approximation. However (see Fig. 2a), the λ_1 value calculated from the $S_{\text{int}}(t)$ signal by a method described in [12] coincides with the results of the λ_1 calculation proceeding directly from $S(t)$. By analogy with [6], the input signal was represented by a linear transformation of the first coordinate of a Rössler system in a chaotic mode: $S(t) = x(t) + C$, $\theta = 35$, $C = 40$.

Raising the threshold level leads to an increase in the average time interval $\bar{I}$ and, hence, a decrease in the accuracy of Eq. (2). Figure 2b shows the results of λ_1 calculation depending on the selection of constant C for the same test system (variation of the C value is equivalent to shifting the threshold level). As seen, the index remains virtually unchanged for $C > 30$. This corresponds to $\bar{I} < T_0/5$–$T_0/4$, where T_0 is the base period of oscillations of the $x(t)$ signal (cf. Fig. 2c). For smaller C values, the size of the time window occupied by the vector of state is greater than the signal correlation time, which hinders reliable determination of the dynamic characteristics of the external action (input signal) [8].

The DS reconstruction from a sequence of recovery times presents a more complicated problem. A possible approach to solving this task, proposed in our previous work [9], is as follows. First, a transition is performed from the time intervals I_i to the points $\omega(T_i) = 2\pi/I_i$ corresponding to the instantaneous frequency values averaged over the I_i intervals. Then, the $\omega(T_i)$ points are interpolated by a smooth function (a cubic spline) $\omega_{\text{int}}(t)$ to pass to a signal with the uniform time scale used in the attractor reconstruction. Using the resulting time dependence, it is possible to describe behavior of the average instantaneous frequency $\bar{\omega}^H(t)$ (Fig. 1c), while the reconstructed attractor retains the dynamic characteristics of chaotic oscillations in $S(t)$ (Fig. 2d). [For the TC model, the $S(t)$ signal was represented by the first coordinate $x(t)$ of the Rössler system.]

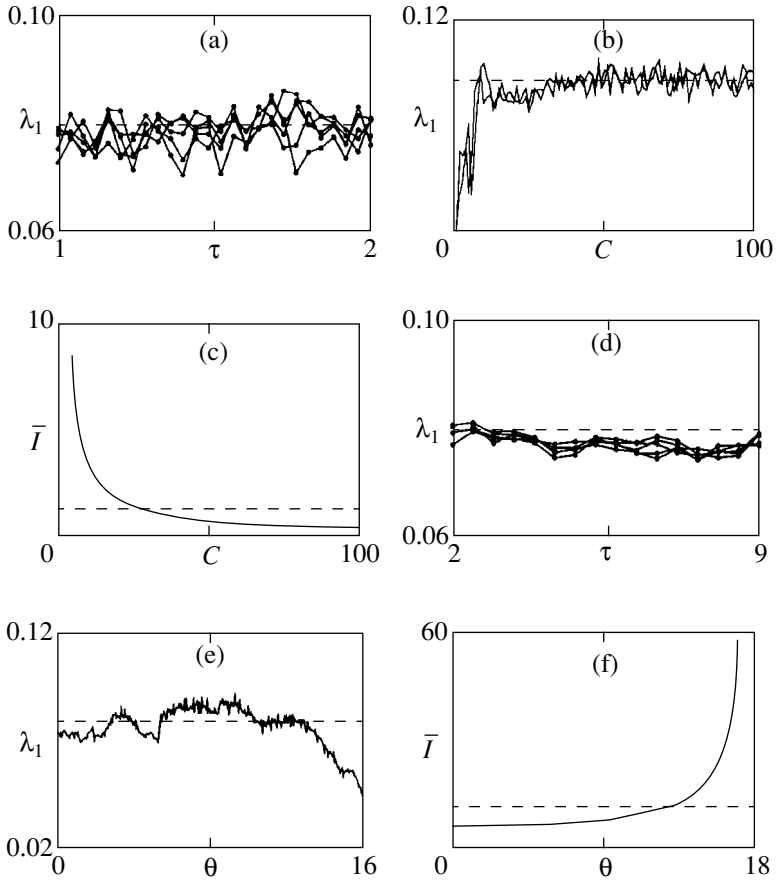

Fig. 2. (a, d) Plots of the highest Lyapunov index versus the delay time τ calculated for various dimensions of the embedding space using the (a) IF ISI and (d) TC ISI sequences for a Rössler system representing a source of chaotic oscillations (dashed lines show the λ_1 values calculated using the given system of equations); (b, e) plots of the highest Lyapunov index versus threshold level Θ calculated for the (b) IF and (e) TC models (in the former case, the threshold variation was modeled by equivalent change in the input signal shift *C*, see the text); (c, f) plots of the average time interval $\bar{I}$ versus threshold for the (c) IF (Θ modeled by *C*) and (f) TC models. The dynamic characteristics of the input chaotic oscillations can be determined provided that $\bar{I}$ does not exceed the characteristic time T_c indicated by the dashed line.

By analogy with the IF model, we have studied in detail dependence of the quality of reconstruction on the selection of the threshold level Θ. A shift of this threshold has a clear physical meaning. Indeed, assume that we have changed the input signal amplitude. From the standpoint of the DS theory, this would affect neither the geometry nor dynamics of the chaotic oscillations. At the same time, a change in the amplitude significantly modifies the structure of the TC ISI output sequence (i.e., the ISI distribution function and the recovery time transformation). These changes are so significant that it was previously considered impossible to estimate characteristics of the chaotic signal at large Θ (small-amplitude input signals) [7, 8]. However, as seen from Fig. 2e, the highest Lyapunov index is independent of the threshold, provided that $\bar{I}$ does not exceed a characteristic time scale T_c of the chaotic oscillations (in our case, the time of predictability $T_c \approx 1/\lambda_1$ [13]). Therefore, despite the inability to estimate the input set geometry [8], we may still calculate the dynamic characteristics using the ISI sequence. [Naturally, in speaking of the retained characteristics, we imply the results of approximate numerical experiments rather than of the rigorous mathematical calculation: the characteristics can be evaluated to within ≈±10%.]

The main conclusions from our investigation are as follows. The dynamic characteristics of a signal from small-scale dynamic system entering the neuron input can be determined from the output ISI sequence, provided that the average time interval does not exceed the characteristic time scale T_c. The time scales may be different for various mathematical models of spike generation: for the IF model, the T_c value does not exceed the time required for the correlation function to attain the first zero (for signals with clearly pronounced base frequency in the spectrum, this corresponds to a quarter of the base period); for the TC model, the characteristic time scale is markedly greater and equals approxi-

mately to the predictability time. In this work, we presented the results of calculations performed for the Rössler system. The results were confirmed by data of a series of experiments performed with various sources of chaotic oscillations. Thus, the dynamic characteristics of random oscillations determined from the output ISI sequence are retained upon linear transformations of the neuron input signal. For the restrictions formulated above, the accuracy of determining these characteristics is independent of the structure of the output sequence of spikes.

One of the authors (Pavlov) gratefully acknowledges the support from INTAS Foundation (grant no. YSF 99-4050). The work was also partly supported by a grant from the Royal Society of London.

REFERENCES

1. T. Sauer, Phys. Rev. Lett. **72**, 3911 (1994).
2. A. Longtin, A. Bulsara, and F. Moss, Phys. Rev. Lett. **67**, 656 (1991).
3. D. Pierson and F. Moss, Phys. Rev. Lett. **75**, 2124 (1995).
4. T. Sauer, in *Nonlinear Dynamics and Tine Series*, ed. by C. Culter and Kaplan, Fields Institute Communications (American Mathematical Society, Providence, 1997), Vol. 11, pp. 63–75.
5. F. Takens, in *Dynamical Systems and Turbulence. Lecture Notes in Mathematics* (Springer-Verlag, Berlin, 1981), pp. 366–381.
6. D. M. Racicot and A. Longtin, Physica D (Amsterdam) **104**, 184 (1997).
7. R. Hegger and H. Kantz, Europhys. Lett. **38**, 267 (1997).
8. R. Castro and T. Sauer, Phys. Rev. **55**, 287 (1997).
9. N. B. Janson, A. N. Pavlov, A. B. Neiman, and V. S. Anishchenko, Phys. Rev. E **58**, R4 (1998).
10. A. N. Pavlov, O. V. Sosnovtseva, E. Mosekilde, and V. S. Anishchenko, Phys. Rev. E **61** (2000) (in press).
11. A. N. Pavlov, E. Mosekilde, and V. S. Anishchenko, in *Stochaos: Stochastic and Chaotic Dynamics in the Lakes*, ed. by D. S. Broomhead, E. A. Luchinskaya, P. V. E. McClintock, and T. Mullin (American Institute of Physics, Melville, 2000), pp. 611–616.
12. A. Wolf, J. B. Swift, H. L. Swinney, and J. A. Vastano, Physica D (Amsterdam) **16**, 285 (1985).
13. J. Brindley and T. Kapitaniak, in *Chaotic, Fractal, and Nonlinear Signal Processing*, ed. by R. A. Katz (American Institute of Physics, Woodbury, 1996), pp. 605–611.

Translated by P. Pozdeev

Technical Physics Letters, Vol. 26, No. 8, 2000, pp. 675–677. Translated from Pis'ma v Zhurnal Tekhnicheskoĭ Fiziki, Vol. 26, No. 15, 2000, pp. 65–71.

The Laser-Induced Surface Evaporation

A. Yu. Ivanov and G. E. Skvortsov

St. Petersburg State University, St. Petersburg, 199164 Russia

Received March 24, 2000

Abstract—A special mode of laser action—the surface evaporation—has been experimentally studied on a large number of various materials. Characteristic features of the pure evaporation mode have been established, and some possible applications of the method for modifying surfaces and clean-cutting of biopolymers are indicated. *© 2000 MAIK "Nauka/Interperiodica".*

Interaction of a laser radiation with solid surfaces is considered in numerous publications (see review articles [1–3]). Despite the enormous amount of related data, some modes of this strongly nonequilibrium process have not been studied as yet. One such phenomenon is the anomalous scattering considered in the recent publication [4].

Below, we describe a special type of the laser surface treatment—the pure evaporation mode—underlying a number of technological operations. This mode is also of great interest as a typical example of pulsed resonance-like modes.

We will present the results of the experimental study of the laser-induced surface evaporation for various materials (metals, dielectrics, and biopolymers). Based on the qualitative analysis of this mode, we suggest a set of quantities to describe this mode and the experimental conditions of its implementation. Some possible applications of the mode are also indicated.

I. Consider the modes of surface treatment with the aid of a pulsed laser in terms of the laws of processes occurring in the corresponding systems [5].

The effect of a pulsed laser is characterized by the following quantities: the frequency ν and the wavelength λ of the laser radiation; the pulse duration δt and the pulse repetition period Δt; the power w [W] and the intensity (power density) j [W/cm^2] of the laser radiation; $j = w/a$, where a is the area of the illuminated spot on the surface.

The object is a surface described by the following set of structural factors: the coefficient of radiation absorption k, the characteristic times τ_s and lengths λ_s, the binding energy ε_s of a particle on the surface, and the characteristic intensity j_s of the absorbed radiation. All these structural factors depend on the radiation frequency and other quantities characterizing the laser radiation indicated above.

The laser-induced effect is determined by the penetration depth h, the area αa of the irradiated region, the excitation relaxation time τ_2, and the process duration τ_3.

The modes of the laser-induced processes are determined by a set of acting factors g and the corresponding structural factors $s(g)$ [5]. In accordance with the characteristics indicated above, this set of acting factors for a pulsed laser includes the following quantities:

$$G = \frac{g}{s[g]}: \Omega = \frac{\nu}{\nu_s}, \quad \Lambda = \frac{\lambda}{\lambda_s}; \quad T_1 = \frac{\delta t}{\tau_1}, \quad T_2 = \frac{\tau_2}{\tau_1}, \quad T_3 = \frac{\Delta t}{\tau_3}; \tag{1}$$

$$W = \frac{w}{w_s}, \quad w_s = \frac{\varepsilon_s}{\tau_1}, \quad J = \frac{j}{j_s}, \quad E = \frac{\omega \delta t}{\varepsilon_s}; \tag{2}$$

$$e = \frac{w \delta t}{ah} = j/v, \quad v = \frac{h}{\delta t}, \tag{3}$$

where v is the velocity of the evaporation front.

If the necessary data on the structure are lacking, it is expedient to use some special (critical) values of the acting factors g_c corresponding to transitions between various essentially different modes:

$$s(g) \longrightarrow g_c: \nu_s \longrightarrow \nu_c, \ \tau_1 \longrightarrow \tau_{1c}, \ \varepsilon_s \longrightarrow \varepsilon_c, \ldots . \tag{4}$$

Usually, the dynamic structural transitions take place in the vicinity of such particular values.

At present, several particular modes of laser-induced processes on the surface are known. The most intense of these modes is the anomalous scattering [4] taking place under the conditions $\delta t \sim 10^{-8}$ s, $10^3 < j < 10^7$. The second specific mode, which is considered in this article, is the pure laser-induced evaporation implemented under the conditions $\delta t \sim 10^{-8}$, $10^8 < j < 10^{10}$. At $j > 10^{12}$, the latter mode is transformed into a specific shock-wave mode described elsewhere [1].

In accordance with the above data, the threshold values are taken to be $j_{c1} = 10^3$, $j_{c2} = 10^8$, and $j_{c3} = 10^{12}$.

1063-7850/00/2608-0675$20.00

A number of specific modes can be obtained by combining the appropriate values of criteria (1)–(3)

$$\Omega, \Lambda \leqslant 1, \quad J \leqslant 1, \quad T \geqslant 1 \tag{5}$$

for the threshold values indicated above and for other known threshold values. Thus, more than thirty specific modes can be obtained for the above three threshold values of j with due regard for the frequency resonance $\Omega = 1$ and the relaxation "resonance" $T \approx 1$. Some of these modes are described in [6].

II. Now consider the conditions necessary for implementation of the pure evaporation mode, which provides intense material evaporation without changing the chemical composition in the irradiated region. This mode should necessarily be pulsed and resonance-like.

The first requirement should be met because, in most materials, the radiation with intensity exceeding 10^8 within the time $\delta t > 10^{-7}$ would initiate combustion [7].

The second requirement—the resonance-like character with respect to intensity—is imposed by the following limitations. At $j < 10^7$, the evaporation for time $\delta t \sim 10^{-8}$ is rather weak because of a low energy $e \cong j\delta t/\lambda = 2 \times 10^{-4} j < \rho\varepsilon_{s0}$, where $\varepsilon_{s0} \cong 10^4$ J/g is the tabulated average specific energy of evaporation. The j values exceeding 10^{10} lead to combustion. At $j \sim 10^9$, absorption should attain the maximum value [8]. Thus, in the general case, the evaporation mode is implemented within the range $10^8 < j < 10^{10}$. For each material, the range of intense pure evaporation is rather narrow, and the process is of the resonance-like nature.

The evaporation mode is more effective when evaporation is provided by a series of pulses. In this case, the material evaporated by the first pulse must go away so that the new pulse would directly interacts with the "open" surface rather than ionize the vapor. A number of experiments showed that the most appropriate pulse repetition frequency is 50–100 Hz. The velocity of laser-beam scanning of the surface was chosen in the range (2–4) mm/s. For a laser spot size of $\sim 10^{-3}$ cm, the number of acting pulses varied from three to six.

To provide for the clean-cutting of biopolymers, it is important to use a laser wavelength close to the wavelength of bound-water absorption $\lambda_s \approx 540$ nm. The condition of frequency (energy) resonance was satisfied by selecting laser radiation with the wavelength $\lambda = 530$ nm. In most experiments, we used this laser radiation and varied only its power.

III. Now consider the experimental results. The experiments were performed with the use of a solid-state Nd^{3+} : YAG laser (LTIP4-5 type) with the wavelength 530 or 1060 nm and a power of 10^6 W operating in the pulse-periodic mode with $\delta t = 2 \times 10^{-8}$ and $\Delta t =$ 0.01–0.02 s.

We studied the surfaces of various materials—metals (Al, Zn, Cu, Fe Ti, Mg), alloys, stainless steel, Duralumin, brass, dielectrics (C, S, P), various glasses, concrete, minerals (agate, jasper, lasurite, fluorite, nephrite, malachite, ruby, marble, etc.), plastics (textolite, organic glass, foam plastic, etc.), rubber, and biopolymers (paper, wood, fabrics, leather). The root-mean-square deviation of the surface roughness of these materials ranged from 0.007 to 100 μm.

The laser power in the experiments varied from 10^4 to 10^6. The beam spot at the normal beam incidence was usually $a = 3.1 \times 10^{-6}$ cm^2. The absorption coefficient $\bar{k}$ (averaged over the experiments) had the value 0.5. In this case, $j = 0.5w/a = 1.6 \times (10^9$–$10^{10})$. The evaporation depth under the action of one pulse ranged within $(1$–$4) \times 10^{-2}$ cm^2.

Using the above parameters, we obtained the following basic values for metals and biopolymers (averaged over the materials of one type).

For metals:

$$w = 2 \times 10^5, \quad h = 3 \times 10^{-2}, \quad v = 1.5 \times 10^6, \quad j = 3.2 \times 10^{10}, \quad e = 2.2 \times 10^4; \tag{6}$$

$$\text{Al: } \varepsilon = e/\rho_{\text{Al}} = 0.85 \times 10^4 \text{ J/g}, \quad \varepsilon_s = 1.14 \text{ eV}.$$

For wood:

$$w = 2 \times 10^4, \quad h = 10^{-2}, \quad v = 5 \times 10^5, \quad j = 3.2 \times 10^9, \quad e = 6.4 \times 10^3; \quad \varepsilon = 1.1 \times 10^4. \tag{7}$$

It should be noted that the energy of a particle detachment in the laser-induced evaporation mode is smaller than the specific evaporation heat (1.2×10^4) by a factor of 1.4. For biopolymers, the sublimation heat was not considered at all.

Being compared with the well-known thermal (combustion) mode, the evaporation mode is characterized by a number of distinctive features, namely:

1. Evaporation occurs without melting, i.e., directly from the solid phase.

2. The width and the depth of cutting are smaller than those provided by conventional methods, whereas the quality of cutting is higher.

3. No oxides or other compositional changes were detected in the evaporation regions (the exceptions are titanium, sulfur, and phosphorus).

4. All the cutting parameters (width, depth, and the rate of cutting) depend on the material and its roughness and can be controlled by a number of methods.

5. Precise layer-by-layer removal of a material is possible, including the "erasing" of a text printed on paper.

6. The quality of cutting is higher the more homogeneous the material is and is inversely proportional to the integrated reflection coefficient and the surface roughness.

7. Among a large number of readily evaporated materials, the exceptions are titanium, sulfur, and phosphorus, whose vapors are ignited almost simulta-

neously with the beginning of evaporation. Our attempts at obtaining high-quality glass cuts also failed: in the laser-induced evaporation mode, glasses start breaking in an irregular manner several hours upon cutting.

8. Usually, laser evaporation involving the interaction of a laser beam with the vapor plasma (without contact with the surface) is accompanied by sound generation.

With an increase of the deposited energy (radiation dose), the evaporation mode is changed to the well-known thermal mode.

IV. We should like to make some concluding remarks concerning the experiments and assess the technological possibilities provided by the laser evaporation mode.

Within the law of mode sequence [5], mode 3 (considered above) is intermediate between mode 2 (anomalous scattering [4]) and thermal-evaporation mode 4 preceding mode 5 described elsewhere [1–3].

Each of the above modes is characterized by the basic and accompanying dynamic structural transitions. Thus, mode 2 provides for the formation of a surface electromagnetic structure. Mode 3 is determined mainly by the evaporation (sublimation) transition. Mode 4 gives rise to the evaporation and ionization transitions, etc.

Since each structural transition necessarily includes an anomalous stage [9], the detailed study of each of these modes reveals some anomalies. In particular, for the laser evaporation mode, such an anomaly consists in the generation of sound, indicating a nonstationary (pulsating) character of the nonequilibrium evaporation.

An important property of the evaporation mode is the resonance-like character. It is expedient to determine a measure of this character using the relationship

$$G_r = \frac{1}{1 + r_{\pm}^2 (1 - G)^2}, \quad G = \frac{g}{g_c}, \tag{8}$$

where $r_{\pm}$ is the resonance degree at $g \gtrless g_c$.

A mode can be considered as resonance when Eq. (8) describes a rather narrow pulse, for example, if the conditions $r_{\pm} > 2$ are satisfied. According to this definition, the laser evaporation mode is a resonance-like mode with respect to the logarithmic intensity $G = \log(j/j_s)$, $j_s = 10^9$. The effective mode for each material is also of the resonance nature and should be refined experimentally.

The laser evaporation mode finds numerous practical applications. This treatment provides for the evaporative modification (cleaning, polishing, restoration) of various surfaces, precise clean-cutting of thin layers, and high-quality perforating. Another promising application is the use of the vapors formed during laser irradiation under the appropriate condensation conditions for obtaining various clusters, including nanoclusters. It is also possible to use this mode for obtaining various structural fullerene-like structures [10].

REFERENCES

1. S. I. Anisimov, A. M. Prokhorov, and V. E. Fortov, Usp. Fiz. Nauk **142** (3), 395 (1984) [Sov. Phys. Usp. **27**, 181 (1984)].
2. G. Chapter, Rev. Mod. Phys. **59** (3), 119 (1987).
3. S. I. Anisimov, Ya. R. Imas, and Yu. V. Khadyko, *Effect of High-Power Radiations on Metals* (Moscow, 1970).
4. A. Yu. Ivanov, Pis'ma Zh. Tekh. Fiz. **25** (16), 29 (1999) [Tech. Phys. Lett. **25**, 645 (1999)].
5. G. E. Skvortsov, Pis'ma Zh. Tekh. Fiz. **23** (6), 85 (1997) [Tech. Phys. Lett. **23**, 246 (1997)]; Pis'ma Zh. Tekh. Fiz. **23** (7), 23 (1997) [Tech. Phys. Lett. **23**, 261 (1997)]; Pis'ma Zh. Tekh. Fiz. **23** (10), 17 (1997) [Tech. Phys. Lett. **23**, 383 (1997)].
6. V. M. Akulin and N. V. Karlov, *Intense Resonance Interactions in Quantum Electronics* (Moscow, 1987).
7. Yu. I. Dymshits, Zh. Tekh. Fiz. **47** (3), 532 (1977) [Sov. Phys. Tech. Phys. **22**, 322 (1977)].
8. G. G. Vilenskaya and I. V. Nemchinov, Dokl. Akad. Nauk SSSR **186** (5), 1048 (1969) [Sov. Phys. Dokl. **14**, 560 (1969)].
9. G. E. Skvortsov, Pis'ma Zh. Tekh. Fiz. **25** (1), 81 (1999) [Tech. Phys. Lett. **25**, 35 (1999)].
10. J. M. Hunter, J. L. Fyc, and M. F. Jarrold, J. Chem. Phys. **3**, 1785 (1993).

Translated by L. Man

Technical Physics Letters, Vol. 26, No. 8, 2000, pp. 678–681. Translated from Pis'ma v Zhurnal Tekhnicheskoĭ Fiziki, Vol. 26, No. 15, 2000, pp. 72–79.

Measurement of Scintillator Parameters Using Pulsed X-ray Excitation

P. A. Rodnyĭ, S. B. Mikhrin, and A. N. Mishin

St. Petersburg State Technical University, St. Petersburg, 195251 Russia

Received February 26, 2000

Abstract—A setup for measurement of the major scintillator parameters, including decay time constants, light yield, and emission spectrum, has been developed. It consists of three main components: a small-size source of short X-ray pulses, a cryostat, and a registration system. The ultimate parameters characterizing the source are as follows: pulse duration, ~0.5 ns; repetition rate, 100 kHz; X-ray tube voltage, 30 kV; and current amplitude, 0.5 A. The registration system allows the measurements to be carried out in the 200–800 nm spectral range over the time intervals from 0.5 ns to 50 μs with resolution not worse than 0.1 ns. © *2000 MAIK "Nauka/Interperiodica".*

Measurements of the main scintillator parameters such as decay time constants, light yield, and emission spectrum conventionally employ excitation by gamma-quanta or by particles (electrons, protons, neutrons, etc.) [1]. Recently, pulsed X-ray radiation has also been used to study the luminescence and scintillation properties of wide-gap crystals [2]. This technique has obvious advantages. In comparison to gamma-quanta and heavy particles (α, n), X-ray pulses provide a more uniform and stable excitation of the bulk of a sample, which leads to a higher stability of the parameters of emitted light pulses. Excitation by electrons results in charging of sample surface and requires the object under study to be placed in vacuum. These problems do not arise when X-ray pulses are used. Looking for new scintillator materials, the researchers often have to deal with imperfect small-size samples, and intense X-ray pulses prove to be an indispensable tool in this situation. Experimental techniques based upon pulsed X-ray radiation are simple and reliable, which is especially valuable when a large series of specimens have to be examined [1, 2].

Scintillators are widely used in high-energy physics, positron emission tomography, computer-aided X-ray tomography, and other areas where high event count rates are encountered. Consequently, "fast" scintillators with nanosecond and subnanosecond emission times are to be employed. Only a limited number of such scintillators are now available (BaF_2, ZnO : Ga), and new materials capable of producing short scintillations are being actively searched for. Thus, there is a need in short (subnanosecond) exciting pulses.

Commercially available pulsed sources with two-electrode X-ray tubes (XRTs) [3] have a number of drawbacks: poor stability of the X-ray pulse parameters, low repetition rate, and a high anode voltage (~10^6 V). Fairly recently, three-electrode (controllable) XRTs came into use that are capable of producing stable-amplitude pulses with a ≥10 ns duration [4].

Short X-ray pulses can be obtained from an XRT equipped with a laser-excited photocathode [5]. Operating at an anode voltage of 30 kV, such a source can produce pulses with a ~100 ps duration. A significant disadvantage of this kind of sources is a very low amplitude of the XRT anode current (≤50 μA), with the result that the X-ray pulse energy absorbed by a sample only slightly exceeds the energy of a single gamma-quantum from a ^{60}Co source.

In this paper, we describe a source with a three-electrode XRT (30 kV, 0.5 A), which is capable of producing subnanosecond X-ray pulses at a repetition rate of up to 100 kHz. The source comprises the two main parts: an RTI2-0.05 three-electrode XRT and a modulator (Fig. 1, blocks *2* and *3*). The modulator, which consists of a GaAs LED–thyristor optocouple, delivers a control pulse with an amplitude of up to 290 V and a full width at half maximum (FWHM) of ~0.5 ns into a 50 Ω load [6]. In the present layout, the modulator is triggered by pulses from a G5-56 generator *1* (pulse amplitude, 10 V; pulse duration, 100 ns; repetition rate, 100 kHz) and energized by a power supply unit *6*. It is important to note that the compact semiconductor modulator is connected to the XRT grid–cathode assembly via a coaxial joint and forms a single block with the latter; this makes it possible to accomplish subnanosecond commutation [6]. The high voltage (up to 30 kV) is supplied to the XRT from source *4* with control block *5*. Bias supply unit *7* provides a constant negative voltage of 100–250 V at the XRT grid, which can also change the X-ray pulse duration to a small extent. The layout described is capable of producing short (0.5 ns) pulses of the anode current and the corresponding X-ray pulses. The latter are slightly broadened (by ~30%) with respect to the grid–cathode current pulses, whose

1063-7850/00/2608-0678$20.00 © 2000 MAIK "Nauka/Interperiodica"

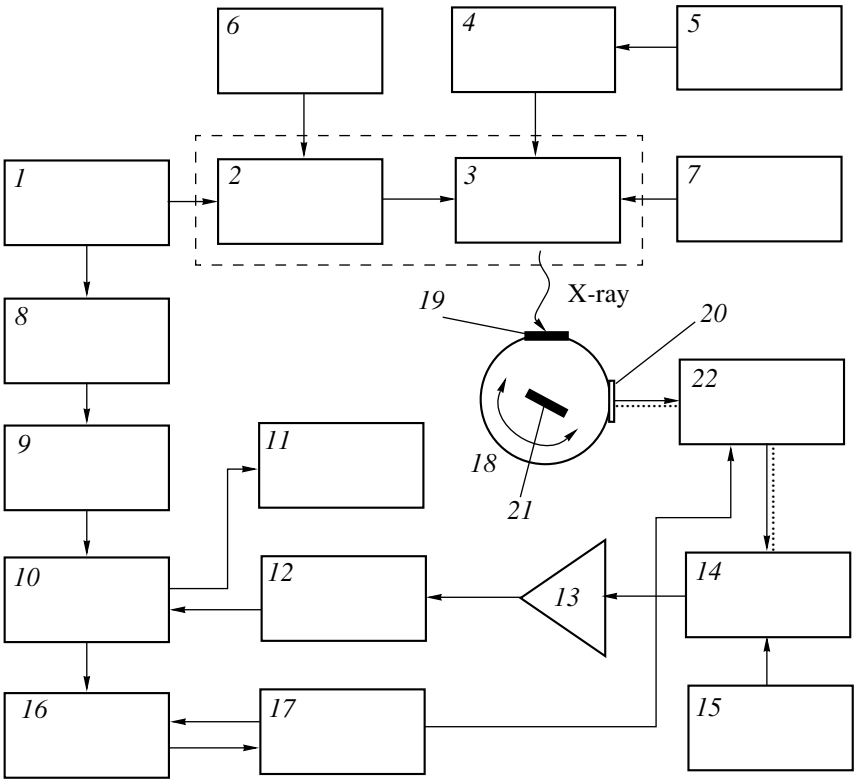

Fig. 1. Block diagram of the setup for measuring the scintillator parameters under pulsed X-ray excitation: (*1*) pulse generator; (*2*) modulator; (*3*) pulsed X-ray source; (*4*) high-voltage power supply unit; (*5*) control block; (*6*) modulator power supply unit; (*7*) bias source unit; (*8*) decoupling transformer; (*9*) START channel time-locking circuit; (*10*) time-to-amplitude converter; (*11*) frequency meter; (*12*) STOP channel time-locking circuit; (*13*) amplifier; (*14*) photomultiplier tube; (*15*) photomultiplier power supply unit; (*16*) analog-to-digital converter; (*17*) IBM PC; (*18*) cryostat; (*19*) beryllium cryostat window; (*20*) quartz cryostat window; (*21*) sample; (*22*) monochromator.

FWHM duration varies from 0.6 to 1 ns, depending on the bias voltage. Instability of the X-ray photon flux at the XRT axis is ~1% at an anode-current instability of 0.5%.

The source, comprising the XRT and the modulator, is designed as a cylinder 15 cm in length and 10 cm in diameter (including the lead shield). This unit can be easily mounted together with a photomultiplier tube (PMT) on an optical bench and matched with a cryostat in an experimental setup. The power consumption by the source (excluding the G5-56 generator) amounts to 50 W. When the tube is producing 0.5-A 1-ns pulses at repetition rate of 100 kHz, the average anode current equals ~25 μA, which is much lower than the maximum allowed average current of 500 μA. The 30 kV XRT operating voltage is also lower than the rated level (50 kV). To record a kinetic curve or a scintillator emission spectrum, the data are accumulated for several minutes. Thus, dissipative losses at the XRT anode in the course of the measurements are not high, and the unit does not require any special cooling.

Some of the components of this compact X-ray source are virtually identical to those used in the familiar 10 ns pulse sources, including the high-voltage supply unit, the control block, the insulation system for the high-voltage (anode) elements, and the radiation shield assembly around the working beam. These components are described in the literature [4, 7]. Note that, at equal operating voltages (30 kV), the maximum value of the anode current (0.5 A) in an XRT with thermionic cathode (RTI2-0.05) is 10^4 times higher than the corresponding value obtained in the tube with photocathode [5]. In the rated operating mode, the tungsten anode of RTI2-0.05 emits up to 10^7 X-ray photons per pulse with a mean energy of ~17 keV.

The sample under study is placed in a steel cryostat *18* (Fig. 1). In the region of the X-ray beam passage, the cryostat wall thickness equals 2 cm, which is sufficient to absorb the incident radiation completely. To prevent irradiation of the PMT detector by X-rays, the axes of the cryostat entrance beryllium window *19* (for the X-ray beam) and exit quartz window *20* (for the light flux) are arranged at a right angle to each other. The cryostat design allows the sample orientation with respect to these axes to be varied so as to optimize collection of the emitted light. The sample temperature can be varied from 80 to 600 K under a vacuum of 3×10^{-3} Torr; however, most of the measurements with new materials are performed at room temperature without evacuation of the cryostat volume.

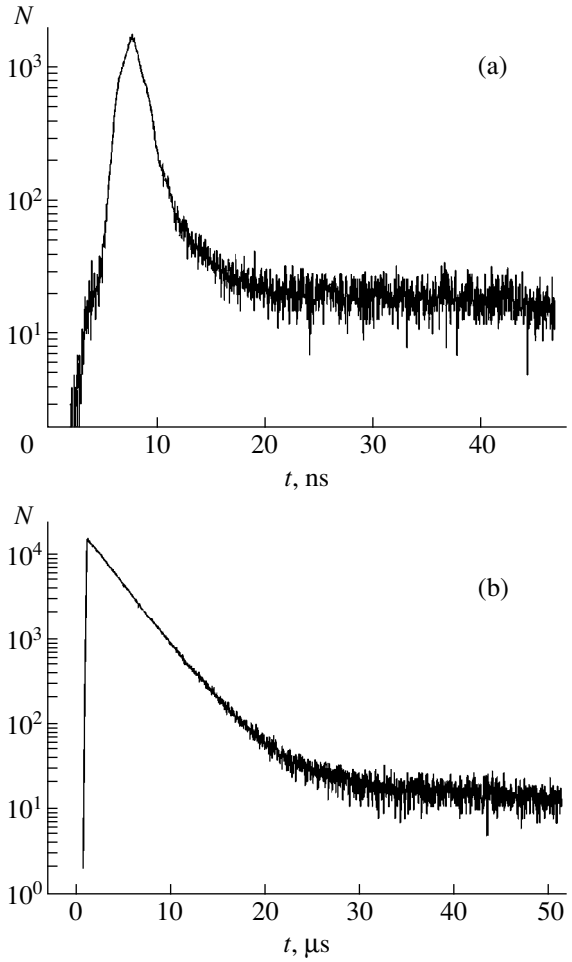

Fig. 2. Luminescence kinetics of (a) BaF_2 and (b) Gd_2O_2S : Pr measured using pulsed X-ray excitation. *N* is the number of pulses counted.

The sample (Fig. 1, *21*) mounted on a rod in the cryostat, is located at a distance of 6 cm from the X-ray beam entrance window. It can be estimated that an energy deposited by each X-ray pulse in a 1-cm^2-area sample (thick enough to completely absorb the incident X-ray radiation) is ~10^9 eV. Thus, in its action on the sample, such a short X-ray pulse is essentially equivalent to a gamma-quantum of ~10^9 eV energy. Possessing an energy efficiency of ~1%, the scintillator will emit ~3×10^6 optical photons per pulse.

A system used for registration of the emission from crystals under study, built within the CAMAC standard, is based on the START–STOP technique widely employed in physical experiments [8, 9]. The time-locking circuit (TLC) *12* provides for synchronizing the STOP channel to a definite point at the front edge of the single-electron pulses arriving from the PMT, which eliminates the effect of pulse amplitude fluctuations on the time resolution. Requirements to the START TLC unit *9*, operating with standard triggering pulses, are less stringent. The net error introduced by electronics in the time-domain measurements is less than 100 ps.

Let us consider how does the setup work. Synchronization pulses from the G5-56 generator *1* are passed to modulator *2*, the subnanosecond output pulses of which open the tube of the X-ray source *3*. Simultaneously, a constant bias voltage, which determines the anode current amplitude, is applied to the XRT grid from source unit *7*. The high-voltage power supply unit *4*, controlled by block *5*, provides up to 30 kV at the XRT anode. Modulator *2* is powered by a stabilized 500-V source *6*. The X-ray pulse enters cryostat *18* through the beryllium window *19* and hits the sample *21*. The light emitted by the sample leaves the cryostat through the quartz window *20* and, after being dispersed by monochromator *22*, enters the photomultiplier *14* supplied with high voltage from source *15*. A special small-size monochromator provides for the time-resolved emission spectra recording over a 200–800 nm range. The monochromator step motor is controlled by computer *17*.

In the study of samples with low light yield, the monochromator is not used and the sample emission goes directly to the PMT. The PMT output pulses are enhanced by amplifier *13* and passed through the STOP TLC unit *12* to enter the time-to-amplitude converter (TAC) *10*. In the other channel, the synchronization pulses are passed through the decoupling transformer *8* and the START TLC unit *9* to TAC *10*. The amplitude of the TAC output pulse is measured by a 12-bit analog-to-digital converter *16*, and the value obtained is stored by the computer *17* in a data file. Subsequent processing of the experimental data is carried out using the common application program packages. The frequency meter *11* is used in the layout adjustment. The light yield is determined by referencing the output signal obtained from the sample under study to the signal from a standard scintillator such as CsI : Tl.

This scheme operates stably when the load (i.e., the PMT single-electron pulse detection rate) does not exceed 10% of the excitation pulse repetition rate. At higher loads, two-photon events become important, which distorts the measurement results. To illustrate the performance of the setup described, we present the recorded luminescence kinetics of the well-known BaF_2 and Gd_2O_2S : Pr scintillators (Fig. 2). The decay time constants characterizing the fast and slow components in the BaF_2 emission (Fig. 2a), determined from these data, are 0.88 ± 0.02 and 850 ± 5 ns, respectively. Both values agree well with those found in the literature [10].

The luminescence kinetics of Gd_2O_2S : Pr shown in Fig. 2b exhibits, in contrast to the case of BaF_2, a single-exponent decay with a time constant of 3.05 ± 0.05 μs.

These experimental results demonstrate that, with the setup described, it is possible to carry out wide-dynamic-range measurements of the luminescence

kinetics over a large time interval (from 0.5 ns to 50 μs) with a time resolution of at least 0.1 ns.

REFERENCES

1. L. V. Viktorov, V. M. Skorikov, V. M. Zhukov, and B. V. Shul'gin, Izv. Akad. Nauk SSSR, Neorg. Mater. **27**, 1699 (1991).
2. P. A. Rodnyĭ, Appar. Metod. Rentgen. Anal. **39**, 152 (1988).
3. S. P. Vavilov, *Pulsed X-ray Techniques* (Énergiya, Moscow, 1981).
4. F. L. Gerchikov, *Controlled X-ray Radiation in Instrument Building* (Énergoizdat, Moscow, 1987).
5. S. E. Derenzo, W. W. Moses, S. C. Blankerspoor, *et al.*, IEEE Trans. Nucl. Sci. **41**, 629 (1994).
6. P. A. Rodnyĭ, B. R. Namozov, A. V. Rozhkov, and A. G. Ryzhkov, RF Patent No. 2054739, 1996.
7. V. G. Guk, A. A. Lobanov, and N. N. Skachkov, Élektron. Tekh., Ser.: Élektrovak. Gazorazryad. Prib. **2** (133), 37 (1991).
8. W. W. Moses, Nucl. Instrum. Methods Phys. Res. A **336**, 253 (1993).
9. F. L. Gerchikov, V. A. Gudovskikh, N. T. Danil'chenko, *et al.*, Pis'ma Zh. Tekh. Fiz. **6** (15), 911 (1980) [Sov. Tech. Phys. Lett. **6**, 394 (1980)].
10. M. Laval, M. Moszynski, R. Alemand, *et al.*, Nucl. Instrum. Methods **206**, 169 (1983).

Translated by M. Skorikov

Technical Physics Letters, Vol. 26, No. 8, 2000, pp. 682–685. Translated from Pis'ma v Zhurnal Tekhnicheskoĭ Fiziki, Vol. 26, No. 15, 2000, pp. 80–87.

Field and Input Admittance of a Vertical Magnetic Dipole Placed above a Plane Grid Screen

V. P. Akimov and L. A. Babenko

St. Petersburg State Technical University, St. Petersburg, 195251 Russia

Received March 23, 2000

Abstract—A solution describing the radiation field of a vertical magnetic dipole placed above a plane grid screen is presented. It is shown that both the solution and the related computational procedure can be substantially simplified using methods of virtual images and averaged boundary conditions. The obtained results can be used to calculate the parameters of electromagnetic screens involving metal grids. © *2000 MAIK "Nauka/Interperiodica".*

In order to obtain a unidirectional radiation from the simplest antennas (such as dipoles and loops) and arrays of such antennas, solid or grid metal screens are usually applied. In the case of a solid screen, the antenna characteristics can be very simply calculated using the mirror image method. Grid screens are not perfectly reflecting surfaces; therefore, in this case, the image method is inapplicable.

To calculate the radiation characteristics of antennas placed above grid screens, numerical methods are usually applied [1]. Such methods are rather time-consuming even for modern computing facilities. However, these problems can be solved using methods of averaged boundary conditions [2] and virtual images [3], which substantially simplify the computational procedure. This approach was successfully used [4, 5] to calculate the fields of vertical and horizontal electric dipoles placed above a plane metal grid.

Proceeding to the solution of the magnetic problem, consider Fig. 1, showing a vertical magnetic dipole of length L with dipole current I^m placed at height h above the surface of a plane wire grid (I) with square mesh. The mesh size is $a \ll \lambda$ (where λ is the radiation wavelength), the wire radius is $r_0 \ll a$, and the contacts between wires are perfect. For such parameters, the grid can be treated as an effective solid surface with averaged boundary conditions [2]. In order to determine fields in the upper and bottom half-spaces, introduce component $M_z = M$ of the magnetic Hertz vector satisfying the Helmholtz equation

$$(\nabla^2 + k^2)M_1(\mathbf{r}) = \frac{i}{\omega\mu_0} I^m L \delta(\mathbf{r} - \mathbf{z}_0 h), \quad z \geq 0, \quad (1)$$

$$(\nabla^2 + k^2)M_2(\mathbf{r}) = 0, \quad z \leq 0, \quad (2)$$

where $k^2 = \omega^2\varepsilon_0\mu_0$, ε_0 and μ_0 are the permittivity and permeability of free space, $\mathbf{r}$ are the coordinates of the observation point, and $\delta(\mathbf{r} - \mathbf{z}_0 h)$ is the Dirac delta.

Upon applying the Fourier transform in the XY-plane to Eqs. (1) and (2), we obtain

$$\tilde{M}_1'' + \gamma^2 \tilde{M}_1 = \frac{iI^m L}{\mu_0\omega}\delta(z - h), \quad z \geq 0, \quad (3)$$

$$\tilde{M}_2'' + \gamma^2 \tilde{M}_2 = 0, \quad z \leq 0, \quad (4)$$

where $\tilde{M}'' = \dfrac{d^2\tilde{M}}{dz^2}$, $\gamma^2 = k^2 - \alpha^2 - \beta^2$, α and β are the variables of the Fourier transform, and $\Im\mathrm{m}\gamma < 0$.

The structure of equations (3) and (4) coincides with that of equations describing a Z-directed transmission line with the propagation constant γ. Solutions to these equations can be written as

$$\tilde{M}_1 = Ce^{-i\gamma z} - \frac{I^m L}{2\gamma\omega\mu_0} e^{-i\gamma|z-h|}, \quad z \geq 0, \quad (5)$$

$$\tilde{M}_2 = De^{i\gamma z}, \quad z \leq 0. \quad (6)$$

The constants C and D are determined from the boundary conditions on the grid surface representing the continuity condition for the tangent components of the electric field intensity and the averaged boundary condition:

$$\mathbf{E}_{\tau_1} = \mathbf{E}_{\tau_2}\big|_{z=0}, \quad (7)$$

$$\mathbf{E}_{\tau_1} = i\eta\kappa\left(\mathbf{j}_\tau + \frac{1}{2k^2}\nabla(\nabla\mathbf{j}_\tau)\right)\Bigg|_{z=0}, \quad (8)$$

where $\eta = \sqrt{\dfrac{\mu_0}{\varepsilon_0}} = 120\pi$, $\kappa = \dfrac{a}{\lambda}\ln\dfrac{a}{2\pi r_0}$ is the grid parameter, and $\mathbf{j}_\tau = \mathbf{z}_0 \times (\mathbf{H}_2 - \mathbf{H}_1)$ is the averaged current density on the grid surface.

1063-7850/00/2608-0682$20.00

Taking into account that vectors **E** and **H** are related to the Hertz vector via relationships

$$\mathbf{E} = -i\omega\mu_0\nabla\times\mathbf{M}, \quad \mathbf{H} = k^2\mathbf{M} + \nabla(\nabla\cdot\mathbf{M}),$$

boundary conditions (7) and (8) can be written in terms of the Fourier images $\tilde{M}$ as

$$\tilde{M}_1 = \tilde{M}_2, \tag{9a}$$

$$\tilde{M}_1 = \frac{\eta}{\omega\mu_0}\kappa(\tilde{M}_1' - \tilde{M}_2'), \tag{9b}$$

where $\tilde{M}' = \dfrac{d\tilde{M}}{dz}$.

Using relationships (5), (6), and (9), we obtain

$$C = -A\frac{k}{k+2i\gamma\kappa}e^{-i\gamma h}, \quad D = A\frac{2i\gamma\kappa}{k+2i\gamma\kappa}e^{-i\gamma h},$$

$$A = -\frac{I^m L}{2\gamma\omega\mu_0}.$$

Now the Fourier images $\tilde{M}_1$ and $\tilde{M}_2$ can be written as

$$\tilde{M}_1 = A(e^{-i\gamma|z-h|} + R(\gamma)e^{-i\gamma(z+h)}), \quad z \geq 0, \tag{10}$$

$$\tilde{M}_2 = A(1 + R(\gamma)e^{i\gamma(z-h)}), \quad z \leq 0, \tag{11}$$

$$R(\gamma) = -\frac{k}{k+2i\gamma\kappa}. \tag{12}$$

Note that the first and the second terms in formula (10) describe the incident and reflected wave, respectively, and $R(\gamma)$ is essentially the reflection coefficient. In order to pass from the Fourier images to functions defined in the physical space, we should perform the inverse Fourier transform. We may choose, however, another way and derive an expression for the Hertz vector corresponding to the grid currents by considering some dummy source (image) similarly to the case of the perfectly conducting plane.

Assume that $R(\gamma)$ is the Laplace transform of function $f(s)$, that is,

$$R(\gamma) = \int_0^\infty f(s)e^{-\gamma}ds. \tag{13}$$

From relationships (12) and (13), it follows that

$$f(s) = \frac{ik}{2\kappa}e^{i\frac{k}{2\kappa}s}. \tag{14}$$

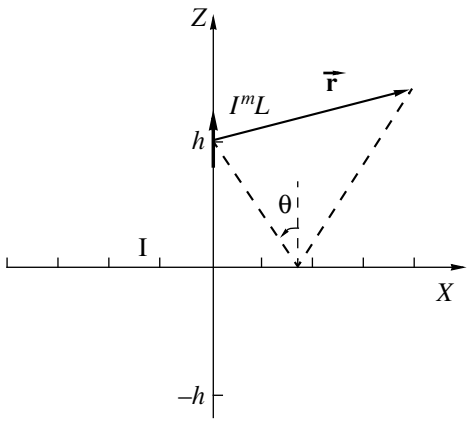

Fig. 1. Magnetic dipole above the grid screen.

Taking into account formulas (13) and (14), we can write expression (10) in the form

$$\tilde{M}_1 = A\left(e^{-i\gamma|z-h|} + \left(\int_0^\infty \frac{ik}{2\kappa}e^{i\frac{k}{2\kappa}s}e^{-\gamma s}ds\right)e^{-i\gamma(z+h)}\right) \tag{15}$$

$$= \tilde{M}_1^0 + \tilde{M}_1^1,$$

where $\tilde{M}_1^0$ and $\tilde{M}_1^1$ are the Fourier images of the Hertz vectors corresponding to the dipole and grid current, respectively.

In the physical space, the Hertz vector of the dipole field is determined by the expression

$$M_1^0(\mathbf{r}) = -\frac{iI^m L}{4\pi\mu_0\omega}G(\mathbf{r}-\mathbf{z}_0 h), \tag{16}$$

where $G(\mathbf{r}-\mathbf{z}_0 h) = \dfrac{e^{-ikd}}{d}$ is the free-space Green's function. By analogy with formula (16), we can represent M_1^1 as

$$M_1^1(\mathbf{r}) = -\frac{iI^m L}{4\pi\mu_0\omega}\frac{ik}{2\kappa}\int_0^\infty e^{i\frac{k}{2\kappa}s}G(\mathbf{r}-\mathbf{z}_0(-h+is))ds, \tag{17}$$

where **r** is the position vector determining coordinates of the observation point and $(-h + is)$ are the coordinates on the dummy source simulating the effect of the grid surface. Expression (17) can be treated as the Hertz vector of a virtual source placed in the complex space. This source is a semi-infinite linear magnetic dipole extended along the s-axis from 0 to ∞. The current of this source depends on the coordinate s on the imaginary axis and equals

$$I^{m'}(s) = -\frac{iI^m L}{4\pi\mu_0\omega}\frac{ik}{2\kappa}e^{i\frac{k}{2\kappa}s}. \tag{18}$$

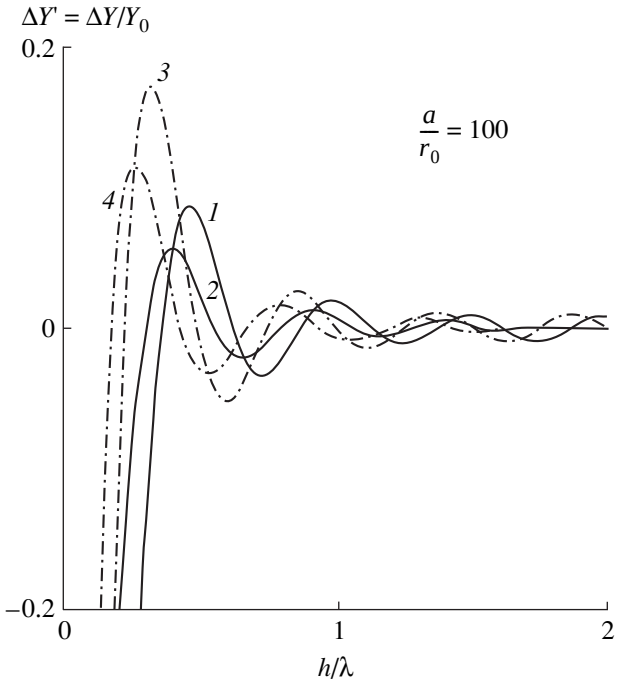

Fig. 2. The plots of (*1*) Re(ΔY') for $a/\lambda = 0.001$; (*2*) Re(ΔY') for $a/\lambda = 0.25$; (*3*) Im(ΔY') for $a/\lambda = 0.001$; and (*4*) Im(ΔY') for $a/\lambda = 0.25$.

Green's function in relationship (17) has the form

$$G(x, y, z, s) = \frac{\exp(-ik\sqrt{x^2 + y^2 + (z + h - is)^2})}{\sqrt{x^2 + y^2 + (z + h - is)^2}} = \frac{e^{-ikd}}{d};$$

that is, it involves the complex distance first introduced by Wait in transformation of the well-known Sommerfeld solution for a source located near an interface.

The integral appearing in expression (17) converges if, calculating it for a given complex distance d, we choose the branch with $\Im m d < 0$. Consider two limiting cases: (i) the grid is absent and (ii) the grid transforms to the perfectly conducting surface. If we assume that $r_0/a \longrightarrow 0$ as a result of decreasing radius of the grid wire, then evidently $\kappa \longrightarrow \infty$, which corresponds to "disappearance" of the grid surface. In this case, we obtain from Eq. (17) that $M_1^1(\mathbf{r}) \longrightarrow 0$; that is, the dipole is situated in the free space. If the grid density is large, that is, if $1/2\kappa \longrightarrow \infty$, then, performing partial integration in formula (17), we obtain that

$$M_1^1(\mathbf{r}) = \frac{iI^m L}{4\pi\mu_0\omega} G(\mathbf{r} + \mathbf{z}_0 h).$$

This expression corresponds to the Hertz vector of a magnetic dipole with opposite current placed at the mirror-symmetric (relative to the grid plane) point; that is, we come to the conventional mirror image method.

Thus, in order to determine the radiation field of a vertical magnetic dipole placed above the grid (for $z > 0$), we should add the field of the real dipole to that of its virtual image (18). The field in the bottom half-space can be determined in accordance with relationship (11).

If the observation point is located in the upper half-space ($z > 0$) at a large distance from both the dipole and the grid surface, then, passing to corresponding limits, we obtain a well-known relationship for the reflection coefficient of a plane *TE* wave from a grid with square mesh,

$$R^{TE} = -\frac{1}{1 + i2\kappa\cos\theta}.$$

Using the above technique and the method of induced magnetomotive forces, we can derive a relationship for determination of the relative variation of input admittance of the magnetic dipole related to the presence of grid screen:

$$\frac{\Delta Y}{Y_0} = -\frac{3}{4\pi\kappa} e^{-i4\pi h/\lambda} \int_0^\infty \left\{ \frac{1}{2\pi(2h/\lambda - i\tau)^3} + \frac{i}{(2h/\lambda - i\tau)^2} \right\} e^{\pi(i/\kappa - 2)\tau} d\tau, \quad (19)$$

where λ is the wavelength and $Y_0 = \frac{2\pi}{3}\sqrt{\frac{\varepsilon_0}{\mu_0}}(L/\lambda)^2$ is the radiation conductance of the magnetic dipole placed in the free space.

Formula (19) is well suited for calculations, since the integral is fast-convergent owing to the rapidly lowering magnitude of the integrand. Figure 2 presents the real and imaginary parts of the dipole input admittance as functions of h/λ for two values of a/λ.

As is well known, a physical implementation of the magnetic dipole is a loop of small radius b with electric current I^e. The magnetic current I^m on the dipole can be expressed in terms of the loop current as [6]

$$I^m = i\omega\mu_0 I^e S/L,$$

where $S = \pi b^2$ is the loop area.

Variation ΔZ_p in the loop input impedance related to the effect of grid screen can be expressed in terms of ΔY:

$$\Delta Z_p = \frac{\omega^2\mu_0^2 S^2}{L^2}\Delta Y \quad \text{or} \quad \frac{\Delta Z_p}{R_{0p}} = \frac{\Delta Y}{Y_0},$$

where $R_{0p} = Y_0\frac{\omega^2\mu_0^2 S^2}{L^2}$ is the input resistance of the loop placed in the free space [6].

In conclusion, it should be noted that the obtained results can be used to calculate the parameters of grid electromagnetic screens designed for the protection of physical installations and objects.

REFERENCES

1. J. R. Wait, *Antenna Theory* (McGraw-Hill, New York, 1969).
2. M. I. Kontorovich, M. I. Astrakhan, V. P. Akimov, and G. A. Fersman, *Electrodynamics of Network Structures* (Radio i Svyaz', Moscow, 1987).
3. I. V. Lindell, *Methods for Electromagnetic Field Analysis* (Clarendon, Oxford, 1992).
4. I. V. Lindell, V. P. Akimov, and E. Alanen, IEEE Trans. Electromagn. Compat. **EMC-28** (2), 107 (1986).
5. V. P. Akimov, in *Waves and Diffraction-90* (Akad. Nauk SSSR, 1990), Vol. 3, pp. 101–104.
6. G. T. Markov, *Antennas* (Gosénergoizdat, Moscow, 1960).

Translated by A. Kondrat'ev

Technical Physics Letters, Vol. 26, No. 8, 2000, pp. 686–688. Translated from Pis'ma v Zhurnal Tekhnicheskoĭ Fiziki, Vol. 26, No. 15, 2000, pp. 88–93.

The Barrier Operation Mode of an Electric-Discharge Galathea Trap

A. I. Morozov, A. I. Bugrova, A. S. Lipatov, V. K. Kharchevnikov, and M. V. Kozintseva

Kurchatov Institute of Atomic Energy, State Scientific Center of the Russian Federation, Moscow, Russia

Moscow Institute of Radio Engineering, Electronics, and Automatics, Moscow, Russia

Received March 22, 2000

Abstract—Experimental plasma parameters in an electric-discharge galathea multipole trap operating in a barrier mode ("discharge with mantle") at a magnetic field strength below 20 Oe are reported. The local plasma parameters exhibit saturation with increasing cathode emission current. The plasma energy lifetime τ_E and the "barrier" coefficient β are estimated. © *2000 MAIK "Nauka/Interperiodica"*.

Electric-discharge devices of a new type, called the multipole electric-discharge galathea traps (EDT-M), were suggested by Morozov and Bugrova. The first experimental results were obtained on a model device with quadrupole poloidal magnetic field created by two rings carrying currents passing in the same direction [1]. It was found that the system may operate in two modes featuring the discharge with "plasmid" or with "mantle." Since the plasma parameters under otherwise equal conditions were higher in the former mode, the discharge "with plasmid" was paid more attention both in [1] and in subsequent publications [2–4].

Later, it was understood that the character of the plasma configuration was determined primarily by the cathode position [5]. When the cathode is situated in the region of zero magnetic field, the system operates in the regime with "mantle," whereby the plasma (specifically, electrons generating an electric field keeping ions in the plasma region) is held in the trap by a magnetic barrier (Fig. 1a). Should the cathode be situated in a nonzero field, a discharge configuration with "plasmid" is observed (Fig. 1b) in which electrons are held mostly by the magnetic plugs. In this regime, only electrons penetrating through the plugs may reach the region of capture (to leave this region shortly after).

Figure 1 shows the computer-simulated particle trajectories illustrating the dynamics of electron motion in the two regimes. In accordance with the pattern of electron motion, the regime depicted in Fig. 1a was called [5] the "barrier" mode (B-mode) and that in Fig. 1b, the "plug" mode (P-mode).

Below, we report on the first results obtained for the EDT-M system operation in the B-mode. The experiments were performed on a quadrupole EDT-M device of the "string-bag" type described in [1]. The trap was operated with the working gas (xenon) flowing at a rate of $\dot{m} = 2$ mg/s under conditions of constant pumping, the residual air pressure in the chamber being $\sim(2–3) \times 10^{-4}$ Torr.

The magnetic field strength became zero at a point with the coordinates $r_0 = 17$ cm, $z = 0$, and a maximum barrier field was observed at $r_1 = 21.7$ cm, $z = 0$. The discharge was generated between an incandescent cathode placed in the zero-field position and the vacuum chamber walls. The gas was supplied via a tube to the region near the cathode. With the usual anode voltage ($U = 200$ V) applied in the absence of magnetic field, a "gas-jet" discharge was initiated between the cathode and the gas inlet tube with the discharge current J_2 close to the cathode emission current [6]. During the subsequent experiments, the cathode emission current was normalized to the J_2 value. The measurements were typically conducted at $J_2 = 200$ mA.

Once the magnetic field was switched on, a blue glow was observed all around the rings, showing virtually no visible attenuation with increasing distance from the cathode in the azimuthal direction. The measurements were carried out in a steady-state regime at a barrier field strength of $H_1 = 20$ Oe. This field held only electrons, whereas ions were kept by the electric field of electrons. Selection of the field strength was determined by the wish to avoid overheating the coils in the course of long-term operation.

A. Integral characteristics. In the barrier operation mode, the discharge current J_1 was virtually independent of the barrier field strength H_1, being determined primarily by the cathode emission current (i.e., by the J_2 value). As the gas supply rate grew from zero to a certain level $\dot{m}_*$, the discharge current increased from zero to $J_1 \sim J_2$.

B. Radial variation of the local plasma parameters. The values of n, T_e, and the ionization potential φ as functions of r were measured with the aid of probes. The results of these measurements revealed a (generally natural) tendency of the above quantities to saturation with increasing cathode emission current. The sat-

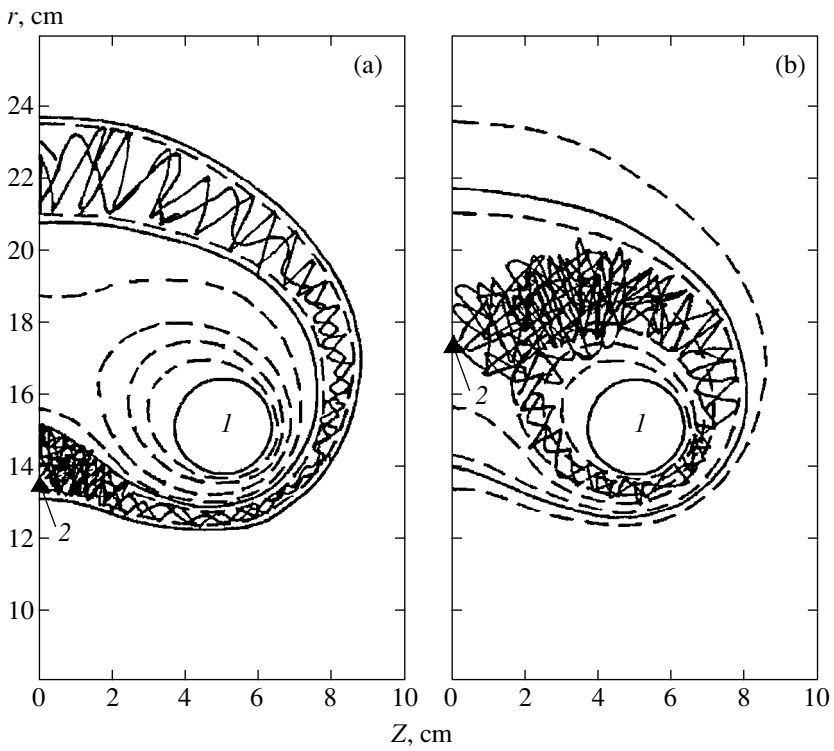

Fig. 1. Computer-simulated electron trajectories in an EDT-M trap operated in the (a) barrier and (b) plug modes: (*1*) cross section of plasma-surrounded coils; (*2*) cathode.

uration was reached for $J_2^* \approx 200$ and 300 mA in the P- and B-modes, respectively.

Figure 2 (dashed curves) shows the curves of $n(r)$, $T_e(r)$, and $\varphi(r)$ in the plane $z = 0$ observed in the P-mode (U = 200 V; J_1 = 200 mA; $\dot{m} \approx 2$ mg/s) and (solid curves) B-mode (U = 200 V; J_1 = 300 mA; $\dot{m} \approx 2$ mg/s). In the plug mode (see dashed curves), the plasma concentrates within a narrow ($\delta r \sim$ 2- to 3-cm) region at $r \approx$ 13.5 cm, where ions are kept in a potential well with a depth of $|\varphi_{min}| \sim 70$ eV and $T_e \sim 30$ eV, $n \sim 5 \times 10^{10}$ cm^{-3} at the center. In the barrier mode (solid curves), the plasma occupies a wider ($\delta r \sim$ 15 cm) region at $r \approx$ 17.5 cm with a potential well depth of $|\varphi_{min}| \sim 40$ eV and $T_{e\,max} \sim$15 eV, $n_{max} \sim 8 \times 10^{10}$ cm^{-3} at the center.

C. (r, z)-distribution of plasma parameters. We have measured the values of $n(r, z)$, $T_e(r, z)$, and $\varphi(r, z)$ in the barrier mode (U = 200 V, J_1 = 300 mA, and $\dot{m} \approx 2$ mg/s) with the aid of probes and determined the regions of approximately equal parameters (Fig 3). As seen, the maximum parameters ($T_{e\,max} \sim 20$ eV; $n_{max} \sim 9 \times 10^{10}$ cm^{-3}; $|\varphi_{min}|_{max} = 50$ eV) are reached at the points displaced from the plane $z = 0$ (where ions are kept in a potential well with a depth of $T_{e,0} = 15$ eV, $n_{e,0} = 8 \times 10^{10}$ cm^{-3}, and $|\varphi_{min}|_0 = 40$ eV).

This circumstance, together with non-equipotential character of the magnetic force lines, indicates that no

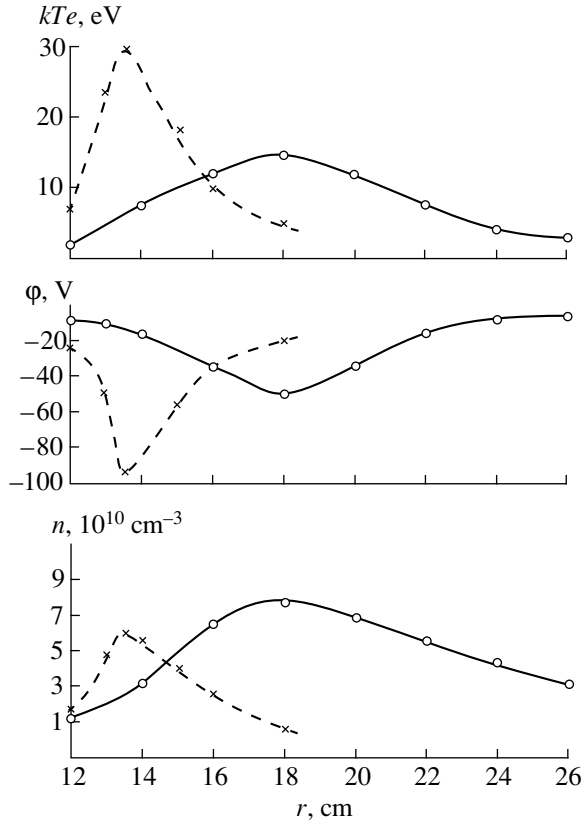

Fig. 2. Distribution of the plasma parameters in the central plane ($z = 0$) of an EDT-M trap operated in the (solid curves) barrier and (dashed curves) plug modes.

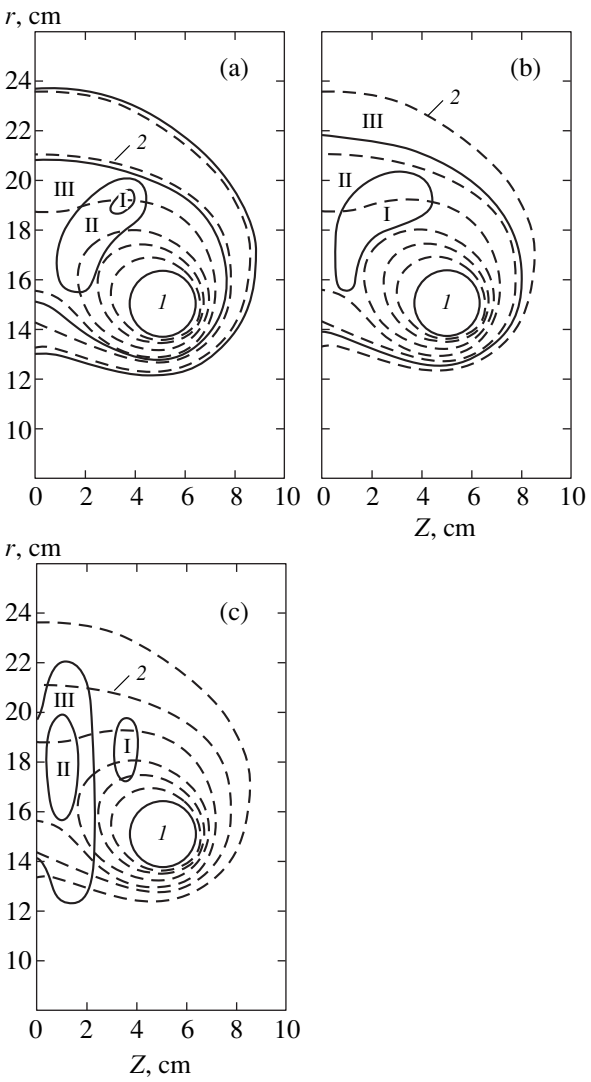

Fig. 3. Distribution of the plasma parameters (a) n_e, (b) T_e, and (c) φ over the (r, z) plane in the barrier operation mode: (a) I, 8.5×10^{10} cm^{-3} < n < 9×10^{10} cm^{-3}; II, 8×10^{10} cm^{-3} < n < 8.5×10^{10} cm^{-3}; III, 1×10^{10} cm^{-3} < n < 8×10^{10} cm^{-3}; (b) I, 15 eV < kT_e < 20 eV; II, 5 eV < kT_e < 15 eV; III, kT_e < 5 eV; (c) I, 45 eV < |φ| < 50 eV; II, 40 eV < |φ| < 45 eV; III, 10 eV < |φ| < 40 eV.

"Maxwellization" takes place because of a relatively short particle lifetime on the trap.

D. Estimates of β and τ_E. (a) The parameter β for a quadrupole EDT-M device of the "string-bag" type can be determined by different methods. The maximum local value is $(\beta_{loc})_{max} = \infty$. A more adequate characteristic is provided by the barrier coefficient β_0 defined by the formula

$$\beta_0 = \frac{8\pi nk(T_e + T_i)}{H_1^2}. \quad (1)$$

The effective ion temperature can be estimated from the known φ(r) and n(r) values by means of an "abelization" procedure. Under "weak" assumptions, we may assume $kT_i \approx 1/3|\varphi_{min}|$. Substituting T_e = 20 eV, n = 9×10^{10} cm^{-3}, and $|\varphi_{min}|$ = 50 eV into formula (1), we obtain $\beta_0 \approx 0.3$.

(b) The characteristic time of keeping the plasma energy (energy lifetime) τ_E is evaluated by the formula

$$\tau_E = \frac{\int \frac{3}{2} n\kappa(T_e + T_i)dV}{J_1 U}. \quad (2)$$

For the data of Fig. 3, this formula yields $\tau_E \approx 30$ μs, which is close to the value calculated by classical formula.

The authors are grateful to V.V. Savel'ev for computer simulation of the electron trajectories. The work was supported by the Ministry of Atomic Industry of the Russian Federation.

REFERENCES

1. A. I. Bugrova, A. S. Lipatov, A. I. Morozov, and V. K. Kharchevnikov, Pis'ma Zh. Tekh. Fiz. **18** (8), 1 (1992) [Sov. Tech. Phys. Lett. **18**, 242 (1992)].
2. A. I. Bugrova, A. S. Lipatov, A. I. Morozov, and V. K. Kharchevnikov, Pis'ma Zh. Tekh. Fiz. **18** (24), 54 (1992) [Sov. Tech. Phys. Lett. **18**, 815 (1992)].
3. A. I. Bugrova, A. S. Lipatov, A. I. Morozov, and V. K. Kharchevnikov, Fiz. Plazmy **19**, 1411 (1993) [Plasma Phys. Rep. **19**, 741 (1993)].
4. A. I. Morozov and V. V. Savel'ev, Usp. Fiz. Nauk **168** (11), 1153 (1998) [Phys. Usp. **41**, 1049 (1998)].
5. A. M. Bishaev, A. I. Bugrova, M. V. Kozintseva, *et al.*, in *Proceedings of the XXVI Zvenigorod Conference on Plasma Physics and CTR, Zvenigorod, 1999*, p. 82.
6. A. I. Bugrova, A. S. Lipatov, A. I. Morozov, and V. K. Kharchevnikov, Pis'ma Zh. Tekh. Fiz. **17** (19), 29 (1991) [Sov. Tech. Phys. Lett. **17**, 691 (1991)].

Translated by P. Pozdeev

Technical Physics Letters, Vol. 26, No. 8, 2000, pp. 689–693. Translated from Pis'ma v Zhurnal Tekhnicheskoĭ Fiziki, Vol. 26, No. 15, 2000, pp. 94–102.

Amorphous Shungite Carbon: A Natural Medium for the Formation of Fullerenes

V. A. Reznikov and Yu. S. Polekhovskiĭ

St. Petersburg State University, St. Petersburg, 199164 Russia

Received March 6, 2000

Abstract—A comparative analysis of data on the density, porosity, and intermolecular space of high-carbon shungites, graphite, glassy carbon, and C_{60} fullerite gave an estimate of the fullerene content in the shungite samples which agrees with the values obtained by electrochemical and polar solvent extraction methods. A low yield of fullerenes in the extracts obtained with nonpolar solvents is explained by the high polarity and large adsorption energy of fullerenes and related compounds. *© 2000 MAIK "Nauka/Interperiodica".*

The methods of C_{60} and C_{70} fullerene synthesis developed by the beginning of 1990s suggested that these compounds may be present in carbon-containing rocks. Indeed, shortly after the publication of reliable data on the physicochemical properties of C_{60} and C_{70}, these fullerenes were found in high-carbon shungites [1, 2]. These shungites still remain the only natural objects known to contain aromatic carbon-containing molecules. Up to now, no investigations were undertaken to determine the concentration, molecular composition, and distribution of fullerenes and/or their derivatives in shungites (Sh) with various structures of the carbon-containing substance (C_{sh}). This information is of value for elucidating the nature of C_{sh} and identifying the component responsible for the medical and ecological properties of Sh.

Filippov *et al.* [3] pointed out that there must be a relationship between the properties of shungite carbon C_{sh}, its fullerene-like structure, and the content of C_n fullerenes. Yushkin [4] suggested that a common mechanism may be responsible for the formation of C_{sh} and C_n. These hypotheses are justified provided that the concentration of fullerenes is related to the C_{sh} structure and correlated, at least in certain types of Sh, with the content of completely amorphized carbon phase [3, 5], the latter being the most probable initial material for the C_n synthesis.

Previously [6], we have presented evidence of a commercially significant C_n content (about 1%) in Sh-3. The purpose of this work was to perform a comparative analysis of some macrophysical properties of C_{sh}, its closest structural analog—glassy carbon (GC) [7, 8], and C_{60} fullerene, with a view to estimating the limiting content of C_n and elucidating a model of metamorphism in the shungite carbon structure.

For a carbon unit cell size of 1.0 Å [9] and a covalent atomic radius of C^0 = 0.77 Å [10], carbon atoms in C_{60} can be considered as C^+ ions surrounded by delocalized π-states (C^+e^-). Resonance excitation of a solvated C_{60} molecule in solution [11] must involve transitions into states with the electron affinity energy E_aC^+ evaluated [12] as $3E_aC^0$ = 3.81 eV. Taking into account the vibrational transitions in C_{60} (272, 496, and 776 cm^{-1} [11, 13]), this E_aC^+ value corresponds to the energy of the π-band maximum in the spectra of solutions. According to the quantum-chemical calculations [14], the energy position of the π-band maximum for a non-associated C_{60} molecule was evaluated as 3.43 eV, which is 65 meV below the electron work function [15]. The difference coincides, to within 3 meV, with the energy of "breathing" oscillations of the highly symmetric C_{60} molecule. Note also that 3.435 eV is the middle (arithmetic mean) value between E_aC^0 = 1.27 eV [10] and the ionization potential of C_{60} (5.6 eV), which confirms the above C_{60} model in the form of mutually bound C^+ ions surrounded by a cloud of π-electrons.

The non-associated C_{60} molecule admits the analogy between their delocalized π-electrons and the *s–d* electron states of small-size icosahedral metallic particles [9, 13]. For example, the ionization potential and the surface plasmon energy of Ag_{13} [16] virtually coincide with the corresponding values for C_{60}, while the maximum of the plasma absorption band of Ag_6 (considered as an elementary particle with metal bonds [17]) coincides with the calculated energy of the π-band maximum of the non-associated C_{60}. A difference between C_{60} and small metallic particles consists in (i) the form of the surface electron density distribution and (ii) the possibility of shape changing in the C_{60} carbon unit cell. The scattering of electromagnetic waves on these objects is determined by collective oscillations of the conduction electrons [18], while the plasma oscillations divide into π–σ- and π-states [9, 15, 19]. The π-states being localized upon adsorption on an electroneutral surface, the C_{60} molecule (as a solid particle)

1063-7850/00/2608-0689$20.00

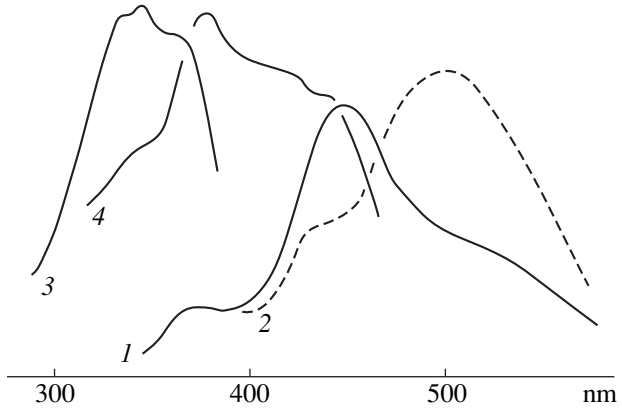

Fig. 1. Typical spectra of C_{60}: (*1*, *2*) luminescence (curve *2* illustrates a time variation of the emission spectrum); (*3*, *4*) luminescence excitation at (*3*) 410 and (*4*) 497 nm.

loses its metallic properties. In this case, an excited C_{60} particle with electron-acceptor properties must contain a bound electron-hole pair. Indeed, the luminescence spectra of C_{60} absorbed in a microporous glass or adsorbed on the surface of polymer molecules exhibit bands peaked at 365, 368, and 410, 433 nm shifted from the 361 and 407 nm bands in accordance with the frequencies of the characteristic vibrational states of C_{60} (Fig. 1).

The thermal stability of fullerenes, together with high electronegativity and polarizability of C_{60} [15, 19], allows this molecule to be considered as an adatom of large radius possessing the properties of elements of the VII group. For example, C_{60} is, like iodine, soluble in nonpolar solvents and has the values of ionization energy and E_a close to those of At [10].

Thus, C_{60} may exhibit, depending on the environment, both the individual molecular properties and the properties of metallic or semiconducting particles, or even halogen atoms. This accounts for the ability of C_{60} to form compounds with various types of chemical bonds, for the large energies of C_{60} adsorption on electron-donor surfaces, and for the effective solid-state interaction of C_{60} with ionic and/or molecular compounds [20].

A 10% decrease in the intermolecular distance in C_{60} crystals as compared to the interlayer spacing in graphite (3.35–3.36 Å) suggests that the π–π exchange interaction in this system is possible as well. A high mobility of C_{60} molecules near the position of equilibrium in the crystal lattice [13] allows us to assume that, when the carbon cell shifts from the equilibrium position, one of the neighboring molecules may act as a donor, and the other, as an acceptor of electron density. A shift of the π-states of the donor molecule to a low-energy level of the acceptor molecule corresponds to E_aC_{60} = 2.65 eV [13]. This model, in which the donor and acceptor are equivalent, can be applied to any pair of molecules. Therefore, the interaction between low-energy states and π-states of the acceptor molecule must be a fundamental energy characteristic of a C_{60} crystal. For the calculated mean energy of 3.435 eV, an equidistant value with respect to E_aC_{60} is 1.865 eV corresponding to the bandgap of C_{60} fullerite [9, 13]. This implies that the $2C_{60}$ dimer is an element of self-similarity in the fullerite structure, which may pass as a whole into solution to perform as the self-similarity element in the corresponding fractal aggregates [13].

In a non-associated C_{60} molecule, the electron shell thickness can be considered as corresponding to the thermodynamic equilibrium between the orbital and covalent radii of carbon atoms (1.39 Å). In this case, the ratio of the volume occupied by a carbon atom to the volume of a C_{60} molecule is $\cong$0.78. The same value is obtained for the density ratio of C_{60} fullerite (ρ = 1.697 g/cm^3) and graphite ($\cong$2.25 g/cm^3) calculated taking into account a difference in C–C bond lengths [5, 13]. For an equivalent surface filling of the entire C_{60} volume, the density (ρ) of fullerite increases to reach the ρ value for graphite. Therefore, the volume of the interlayer space in graphite is equivalent to the intermolecular volume in fullerite. A special feature of the C_{60} structure is the presence of pentahedra uniformly distributed over the carbon cell surface, whereby each carbon atom is shared by two hexagons and one pentagon. This implies that the pentahedra are formed as a result of self-organization in the excited C_{60} molecules.

A collective character of the self-organization of carbon molecules into an aromatic structure is indicated by coinciding energies of formation of the C_{60} molecules and π–σ-plasmons [13, 14]. It was also pointed out [13, 14] that the synthesis of fullerenes from C-clusters is an effective process provided that an energy released upon the contact of clusters amounts to a few eV, which is just the energy characteristic of the electron affinity of linear carbon molecules [21]. Therefore, the excited amorphized graphite-like clusters and chain molecules in a C_{sh} structure may form aromatic fullerene-like molecules. This is confirmed by a pyrolytic synthesis of fullerenes from chain hydrocarbons under conditions of weak interaction with environment in an oxygen-free atmosphere.

The samples of Sh-1 and GC exhibit, in addition to similar X-ray-amorphous structures and coinciding features in the 400–1600 cm^{-1} (see Fig. 2, curves *1* and *2*) range of the IR absorption spectra, close values of the strength characteristics, thermal expansion coefficients, heat capacity, and electric conductivity [5]. On the other hand, the thermal conductivity values differ 6–7 times. The low thermal conductivity of Sh-1 as compared to that of GC, with close values of most macrophysical characteristics, implies that the interphase boundaries may contain a considerable amount of heat-scattering centers. A middle (arithmetic mean) value

between the densities of graphite and C_{60} fullerite at 290 K is 0.02 g/cm^3 greater than the density of GC. This difference is related to a fully amorphized phase present in the GC structure [5], the density of which may be comparable with that of soot (ρ = 2.1–2.18 g/cm^3). Thus, the GC structure can be considered as a superposition of graphite-like packets (GLPs) with ultimate geometries of bent hexagonal layers.

The ratio of limiting values of the interplanar spacing in GLPs (3.65 and 3.41 Å for C_{sh} with globular and sheet morphology, respectively [3]) coincides with the density ratio of the corresponding types of Sh-1 (1.83–1.96 g/cm^3), which indicates that these packets are the main structural units of C_{sh}. A 2–7% increase in the interlayer spacing in GLP with respect to that in crystalline graphite corresponds to a decrease in the density down to ρ = 2.1–2.2 g/cm^3. This estimate does not take into account a possible change in the density within 2–4% due to a difference in interatomic distances between the C_{sh} and graphite structures, since the bending and small dimensions of GLPs necessarily imply the presence of carbon vacancies. For a C_{sh} structure porosity of 10–12% [5], the average density of GLPs correspond to the ρ value of Sh-1. A middle value between the densities of GLPs and C_{60} fullerite (1.9–1.95 g/cm^3) falls in the range of ρ values of Sh-1. For an average C-globule size of about 10 nm, the free volume of C-globules coincides with that of C_{60} molecules provided that the globules form a four-layer packet, which accounts for the fullerene-like structure of C_{sh} [3, 4, 22]. A smaller number of features in the IR spectrum of Sh-1 in comparison with the spectrum of GC (see Fig. 2, curves *1* and *2*) is indicative of a higher degree of order in the shungite carbon structure.

The density of C_{60} was estimated as ρ = 2.03 g/cm^3 [19]. Determined within the framework of the fullerene-like model, the interglobular porosity must fall within 30–35%, while the total porosity must be about 40%. A discrepancy between this estimate and the value (10–12%) presented above is eliminated if we assume that (i) a soot-like phase and/or C_n carbon phase is present in the inter- and intraglobular space and (ii) the GLPs are for the most part intercalated [8]. The latter assumption, like the hypothesis of a fullerene-like C_{sh} structure, is based upon the coincidence of the main spectral features observed in the 400–1500 cm^{-5} range for Sh-1 and C_{60} dimers in a KCl matrix [20] (Fig. 2, curves *2* and *3*). The IR spectrum of Sh-1 displays a Raman band of graphite at 1575–1580 cm^{-1}; the fact that this band is allowed in the IR spectrum is also related to the intercalation of monovalent electron-donor carbon atoms [23].

Considering GLPs as the walls of globules cannot explain the fact that the number of layers in the GLPs is odd before and even after the heat treatment of Sh samples [3]. A fractal character of the C_{sh} structure implies a mixed type of the interaction between GLPs and the absence of any pronounced GLP orientation. An evidence for the glassy structure of C_{sh} is provided by the coincidence of the Sh-1 density with that (ρ = 1.9 g/cm^3) of the melt of a mixture comprising chain and aromatic C-clusters [24]. In this context, the globular structure can be considered as resulting from an ordered mass rearrangement within a closed volume, beginning with nucleation of the graphite-like networks in the field of uniformly distributed catalytically active centers. A decrease in the number of crystallization centers corresponds to an increase in the size of GLPs and, hence, of the C-globules.

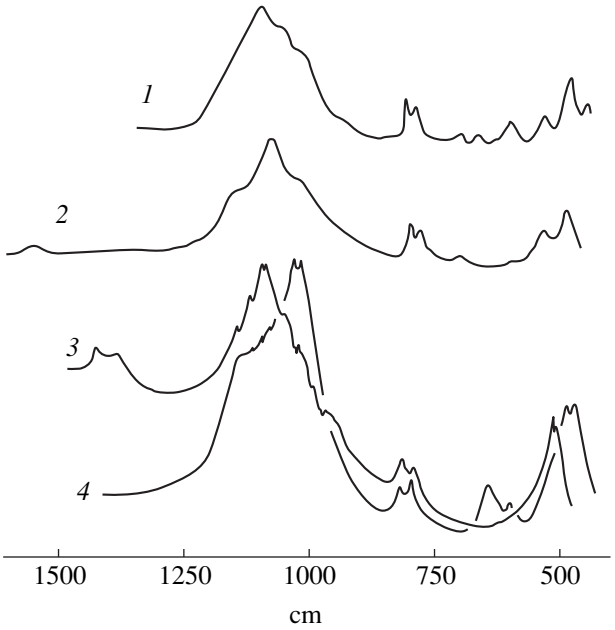

Fig. 2. IR absorption spectra: (*1*) glassy carbon; (*2*) shungite (Sh-1); (*3*) C_{60} in KCl matrix; (*4*) solid amorphized C_{60}-methylpyrrolidone phase.

In this model, the odd number of layers in the packet is a consequence of the primary monolayer nucleation; however, this does not exclude the possible nucleation of two layers and an even number of layers in the packet. Thus, GLPs can be considered as the elements of self-similarity in the fractal structure of C_{sh}. Assuming the precipitation-like accumulation of C-globules, the fractal dimensionality must fall within 2.3–2.5 D [25]. The interglobular porosity of this structure must be not lower than 20%. In our opinion, it is the total porosity level of C_{sh} that is the main evidence in favor of the recrystallization mechanism. The crystallization model of C_{sh} formation is confirmed by a filament (whisker) crystal structure of some shungite carbon samples [26]. Within the framework of the vapor–liquid–crystal mechanism [27], the filament crystal growth begins in a quasiliquid phase supplied with the mobile C-clusters, which makes possible the fullerene-like structure formation [28]. The growth of filament crystals require a sufficient free volume and a small number of primary

crystallization centers. The recrystallization process may not involve some part of the C-clusters. Thus, the main difference of the GLP formation in Sh is the closed space in which the process occurs, while the free volume formation provides conditions for the secondary recrystallization of weakly bound C-clusters into the final aromatic structures.

The fact that the ρ values of GC and Sh-1 can be obtained within the framework of the same GLP model implies that a difference between the calculated and measured densities of Sh-1 (0.03–0.07%) is related to the presence of either a C-phase with ρ = 1.6–1.66 g/cm^3 characteristic of the GC samples upon a high-temperature treatment [5] or fullerenes. The use of a macrophysical value for evaluating the total density of statistically distributed C_n molecules or their small-size aggregates is possible because the inter-pore space in C_{sh} is definitely smaller than the intermolecular volume in fullerite and in the adsorbed state of C_n. The existing notions about the shungite substance formation [3], as well as the presence of organic compounds, microorganisms, and water in the shungite samples, are inconsistent with the thermal mechanism of low-density C_{sh} phase formation.

As follows from the above considerations, the concentration of C_n in Sh samples with most disordered structure is estimated at 3–5 wt % of C_{sh}. This estimate is confirmed by observation of a resolved band at 1180 cm^{-1} in the IR spectrum of Sh-1 (see Fig. 2, curve *2*), which is a characteristic band in the spectrum of C_{60}. A similar band is observed in the spectrum of a solid amorphized C_{60}–methylpyrrolidone phase (see Fig. 2, curve *4*). At the same time, the spectra of this phase and Sh-1 contain, in contrast to the spectrum of C_{60}–KCl samples [29], no characteristic bands in the region of 1420–1430 cm^{-1}, which is most probably explained by the interaction of π-states in the major part of C_n with the matrix components. The common features observed in the IR spectra of Sh-1, GC, C_{60}–KCl_x, and ultradisperse graphite particles [30] reflect the presence of like structural groups of carbon atoms forming bent hexagonal layers [31].

According to the above estimates, there are 30–40 C_n molecules per globule, which allows the associative arrangement of these molecules in the free space of C_{sh}. This hypothesis is consistent with the calorimetric effects observed in the temperature intervals near 190–200, 235–245, and 280 K. For the samples of Sh-3 dehydrated in vacuum for 24 h at 280 K, the high-temperature maximum is observed 5–7 K below, and the low-temperature maximum, 5–7 K above the corresponding peaks for Sh-1. The high-temperature maxima are usually registered during the first DSC runs in the heating modes. These features allow us to assign the observed calorimetric features to processes in the ordered molecular aggregates with various relative concentrations of C_{60} and C_{70} molecules. The low-temperature maxima are attributed to changes in the vibrational mobility of C_{60} and C_{70} molecules, and the high-temperature maxima, to changes in the structure of C_{60} fullerite with a large admixture of C_{70} [32].

The calculated estimates of the content of C_n in Sh are confirmed by data on the extraction of thermoactivated Sh-1 samples with polar solvents capable of forming compounds containing donor–acceptor bonds with C_n. The samples obtained upon the thermal removal of hydrocarbons and solvent from the extracted bitumous phase exhibited crystallization of carbonaceous particles with a cubic and/or dendrite crystal habit. The X-ray diffraction data allowed these particles to be identified with $C_{60–70}$. The spectral features of the extracted carbon particles and their solutions also corresponded to the $C_{60–70}$ structure. The estimated mass of the isolated crystalline particles varied within 1.5–2.0 wt % of the Sh-1 sample, depending on the extraction conditions. The experimental data were indicative of the possible technological efficiency of using natural fullerenes extracted from shungites in medical and ecological applications.

REFERENCES

1. P. R. Buseck, S. J. Tsipurski, and R. Hettich, Science **257**, 215 (1992).
2. S. V. Kholodkevich, A. V. Bekhrenev, V. K. Donchenko, *et al.*, Dokl. Akad. Nauk **330** (3), 340 (1993).
3. M. M. Filippov, A. I. Golubev, P. V. Medvedev, *et al.*, *Organic Substances of Shungite-Bearing Rocks of Karelia* (Petrozavodsk, 1994).
4. N. P. Yushkin, Dokl. Akad. Nauk **337** (6), 800 (1994).
5. *Shungites of Karelia and Ways to Their Complex Use*, ed. by V. A. Sokolov and Yu. K. Kalinin (Petrozavodsk, 1976).
6. V. A. Reznikov, Yu. S. Polekhovskiĭ, and V. E. Kholmogorov, in *Carbonaceous Formations in Geologic History*, Abstracts of Papers (Petrozavodsk, 1998), pp. 71–72.
7. Yu. K. Kalinin, Zap. Vses. Mineral. O–va **119** (5), 1 (1990).
8. S. V. Kholodkevich and V. V. Pobochiĭ, Pis'ma Zh. Tekh. Fiz. **20** (3), 22 (1994) [Tech. Phys. Lett. **20**, 99 (1994)].
9. S. V. Kozyrev and V. V. Rotkin, Fiz. Tekh. Poluprovodn. (St. Petersburg) **27** (9), 1409 (1993) [Semiconductors **27**, 777 (1993)].
10. *Properties of Inorganic Compounds*, ed. by A. I. Efimov (Khimiya, Leningrad, 1983).
11. V. P. Belousov, V. P. Budtov, O. B. Danilov, *et al.*, Opt. Zh. **64** (12), 3 (1997) [J. Opt. Technol. **64**, 1081 (1997)].
12. V. A. Voll, Fiz. Tekh. Poluprovodn. (St. Petersburg) **29** (10), 2071 (1995) [Semiconductors **29**, 1081 (1995)].
13. A. V. Eletskiĭ and B. M. Smirnov, Usp. Fiz. Nauk **165** (9), 977 (1995) [Phys. Usp. **38**, 935 (1995)].
14. A. L. Chistyakov and I. V. Stankevich, Izv. Akad. Nauk, Ser. Khim., No. 9, 1680 (1995).
15. V. V. Afrosimov, A. A. Basalaev, and M. N. Panov, Zh. Tekh. Fiz. **66** (5), 10 (1996) [Tech. Phys. **41**, 412 (1996)].

16. Yu. I. Petrov, *Physics of Small Particles* (Nauka, Moscow, 1982).
17. V. A. Reznikov and A. V. Struts, Opt. Spektrosk. **73** (2), 355 (1992) [Opt. Spectrosc. **73**, 207 (1992)].
18. A. V. Klyuchnik, Yu. E. Lozovik, and A. V. Solodov, Zh. Tekh. Fiz. **65** (6), 203 (1995) [Tech. Phys. **40**, 633 (1995)].
19. Yu. M. Shul'ga and A. S. Lobach, Fiz. Tverd. Tela (St. Petersburg) **35** (4), 1092 (1993) [Phys. Solid State **35**, 557 (1993)].
20. V. A. Reznikov and A. A. Sukhanov, Pis'ma Zh. Tekh. Fiz. **25** (8), 45 (1999) [Tech. Phys. Lett. **25**, 313 (1999)].
21. L. N. Sidorov and O. V. Boltalina, Soros. Obrazov. Zh. **11**, 35 (1997).
22. V. V. Kovalevskiĭ, Zh. Neorg. Khim. **39** (1), 31 (1994).
23. V. I. Ivanov-Omskiĭ, A. A. Andreev, and G. S. Frolova, Fiz. Tekh. Poluprovodn. (St. Petersburg) **33** (5), 608 (1999) [Semiconductors **33**, 569 (1999)].
24. V. A. Polukhin and E. A. Kibanova, Zh. Fiz. Khim. **73** (3), 494 (1999).
25. J. Freder, *Fractals* (Plenum, New York, 1988; Mir, Moscow, 1991).
26. V. V. Kovalevski, A. N. Saphronov, and Ju. A. Markovski, Mol. Mater. **8**, 21 (1996).
27. E. I. Givargizov, *Growth of Filament and Platelike Crystals from Vapors* (Moscow, 1977).
28. V. A. Reznikov, T. É. Kekhva, and B. T. Plachenov, Pis'ma Zh. Tekh. Fiz. **16** (22), 1 (1990) [Sov. Tech. Phys. Lett. **16**, 847 (1990)].
29. A. A. Sukhanov and V. A. Reznikov, Pis'ma Zh. Tekh. Fiz. **25** (9), 56 (1999) [Tech. Phys. Lett. **25**, 363 (1999)].
30. Yu. S. Polekhovskiĭ and V. A. Reznikov, in *Ore Formation and Localization in Earth's Crust* (St. Petersburg State. Univ., St. Petersburg, 1999), pp. 123–147.
31. V. M. Loktev, Fiz. Nizk. Temp. **18** (3), 217 (1992) [Sov. J. Low Temp. Phys. **18**, 149 (1992)].
32. K. Kniaz, J. E. Fisher, L. A. Girifallo, *et al.*, Solid State Commun. **96**, 739 (1995).

Translated by P. Pozdeev

Technical Physics Letters, Vol. 26, No. 8, 2000, pp. 694–697. Translated from Pis'ma v Zhurnal Tekhnicheskoĭ Fiziki, Vol. 26, No. 15, 2000, pp. 103–110.

Pulsed EHF Superradiance Due to the Stimulated Scattering of a High-Power Pump Wave by a Counterpropagating Electron Bunch

N. S. Ginzburg, I. V. Zotova, A. S. Sergeev, R. M. Rozental', and M. I. Yalandin

Institute of Applied Physics, Russian Academy of Sciences, Nizhniĭ Novgorod, 603600 Russia

Institute of Electrophysics, Ural Division, Russian Academy of Sciences, Yekaterinburg, Russia

e-mail: radan@ief.intec.ru

Received February 4, 2000

Abstract—Stimulated scattering of a pump wave by an extended electron bunch counterpropagating with a relativistic translational velocity is studied theoretically. It is demonstrated that the realization of a superradiance regime ensures coherent emission of a short electromagnetic pulse with a frequency much higher than the pump frequency. © *2000 MAIK "Nauka/Interperiodica".*

1. In [1–5], pulsed superradiance (SR) due to different elementary mechanisms was theoretically studied. The process is essentially the coherent emission of an electromagnetic pulse by an electron bunch as a result of electron clustering. Although the bunch extends over several tens of wavelengths, the different parts emit in phase because the group velocity of the wave differs from the translational velocity of electrons so that the wave slips relative to the particles. Subnanosecond SR pulses have been experimentally generated in the microwave region [6–9] using the stimulated emission obtained by different methods including the cyclotron, Cherenkov, and undulator mechanisms. In connection, it is interesting to explore the possibility of producing ultrashort pulses during the stimulated Compton scattering of a high-power pump wave by a counterpropagating electron bunch. At relativistic electron velocities, the frequency of the scattered radiation must be much higher (due to the Doppler effect) than that of the pump wave.

This paper presents a theoretical analysis of the SR effect due to stimulated scattering from an electron bunch propagating along a uniform magnetic field in a smooth waveguide. Two simulation models are considered. The first model rests on the method of an averaged ponderomotive force used to describe the motion of electrons in the field of two electromagnetic waves. The second model employs direct numerical simulation using the particle-in-cell KARAT code.

2. Let us examine the scattering of a pump wave by an annular electron bunch of radius R_b and length b. The bunch propagates along a uniform transport magnetic field $\mathbf{H}_0 = H_0\mathbf{z}_0$ in a smooth circular waveguide of radius R. The fields of the incident and the scattered H-waves are represented in terms of the vector potentials:

$$\mathbf{A}_{i,s} = \mathrm{Re}\left\{\frac{A_{i,s}(z,t)}{k_{\perp i,s}}[\nabla_\perp \psi_{i,s}, \mathbf{z}_0]e^{i(\omega_{i,s}t - h_{i,s}z)}\right\}, \quad (1)$$

where the subscripts "i" and "s" refer to the incident and the scattered wave, respectively; $A_{i,s}(z, t)$ are slowly varying wave amplitudes; $\psi_{i,s} = J_{n_{i,s}}(k_{\perp_{i,s}} r)e^{in_{i,s}\phi}$ are the membrane functions of a round waveguide; $k_{\perp_{i,s}}$, $h_{i,s}$ are the transverse and longitudinal wavenumbers, respectively; and $n_{i,s}$ are the azimuthal numbers. Assume that the condition of combination-frequency wave matching is fulfilled:

$$\omega_s - h_s v_\parallel \approx \omega_i - h_i v_\parallel = \Omega. \quad (2)$$

At the same time, we suppose that the incident and scattered waves are well out of the cyclotron resonance with the electrons:

$$|\omega_{i,s} - h_{i,s}v_\parallel - \omega_H|T \gg 2\pi, \quad (3)$$

where $\omega_H = eH_0/m_0c\gamma_0$ is the gyromagnetic frequency, $\gamma_0 = (1 - v_0^2/c^2)^{1/2}$ is the relativistic mass factor, $v_\parallel$ is the longitudinal electron velocity, and T is the characteristic interaction time.

Assume that $A_s(z, t)$ is a slowly varying function of the longitudinal coordinate z and the time t and that the pump wave amplitude is fixed. Then, the stimulated

scattering of the pump wave by the bunch under conditions (2) and (3) obeys the equations

$$\left(\frac{\partial}{\partial z}+\frac{1}{v_{gr}}\frac{\partial}{\partial t}\right)a_s = if(t-z/\nu_\parallel)k_c a_i G I\frac{1}{\pi}\int_0^{2\pi} e^{-i\theta}d\theta_0,$$
$$\left(\frac{\partial}{\partial z}+\frac{1}{\nu_\parallel}\frac{\partial}{\partial t}\right)^2\theta = \mu k_c^2 \mathrm{Im}\{a_s a_i^* G^* e^{i\theta}\}, \quad (4)$$

where $a_{i,s} = eA_{i,s}/2m_0\gamma_0 c^2$ are the normalized wave amplitudes; $\theta = \omega_c t - h_c z$ is the time-dependent phase angle of electrons with respect to the combination-frequency wave; $k_c = \omega_c/c$, $\omega_c = \omega_s - \omega_i$ is the combination frequency; $h_c = h_s - h_i$ is the longitudinal wavenumber of the combination-frequency wave;

$$G = \frac{\Omega}{\beta_\parallel}\left\{\frac{J_{n_i+1}(k_{\perp i}R_b)J_{n_s+1}(k_{\perp_s}R_b)}{\Omega+\omega_H} + \frac{J_{n_i-1}(k_{\perp i}R_b)J_{n_s-1}(k_{\perp s}R_b)}{\Omega-\omega_H}\right\}e^{i(n_s-n_i)\phi}$$

is the electron–wave coupling coefficient; $\mu = \gamma_0^{-2}\beta_\parallel^{-3}$ is the clustering parameter; ν_{gr} is the group velocity of the scattered wave;

$$I = \frac{eJ_0}{m_0c^3}\frac{1}{2\gamma_0 h_s k_c R^2 N_s}$$

is the current parameter; J_0 is the beam current; $N_s = (1 - n_s^2/\nu^2)J_{n_s}^2(\nu)$ is the scattered-wave parameter with $\nu = k_{\perp s}R$ being a root of the $J'_{n_s}(x) = 0$ function; and $f(x)$ is an unperturbed profile of the bunch. Introducing new independent variables $\zeta = Ck_c z$, $\tau = (1/\beta_{gr} - 1/\beta_\parallel)^{-1}C\omega_c(t - z/\nu_\parallel)$ brings Eqs. (4) to the form

$$\frac{\partial a}{\partial\zeta}+\frac{\partial a}{\partial\tau} = f(\tau)\frac{i}{\pi}\int_0^{2\pi} e^{-i\theta}d\theta_0 \quad \frac{\partial^2\theta}{\partial\zeta^2} = \mathrm{Im}\{ae^{i\theta}\} \quad (5)$$

with the initial and boundary conditions

$$a|_{\tau=0} = a_0, \quad \theta|_{\zeta=0} = \theta_0 + r\cos\theta_0,$$
$$\left.\frac{\partial\theta}{\partial\zeta}\right|_{\zeta=0} = 0, \quad \theta_0 \in [0, 2\pi),$$

where $a = a_s a_i^* \mu G^*/C^2$, $C = (\mu I|a_i G|^2)^{1/3}$ is the gain, and the parameter r describes a small initial modulation of the bunch density.

The simulation was carried out for the values of parameters close to those selected for the forthcoming experiment with two synchronized RADAN accelerators [7–9] producing beams with nanosecond and subnanosecond pulse durations. One of the beams is used in a backward-wave oscillator to generate a 38-GHz E_{01} wave with a power of up to 60 MW. A waveguide transformer converts the output wave into an H_{11} pump wave that is transmitted to a waveguide carrying a subnanosecond electron bunch from the other accelerator. The transmission line comprises two quasioptical mirrors. The parameters of the forthcoming experiment are as follows: bunch current, 200 A; particle energy, 250 keV; pulse duration, 250 ps; bunch radius, 0.2 cm; transport magnetic field, 13 kOe; waveguide radius, 0.3 cm. The scattering is expected to occur in a wave with the same structure as that of the pump wave.

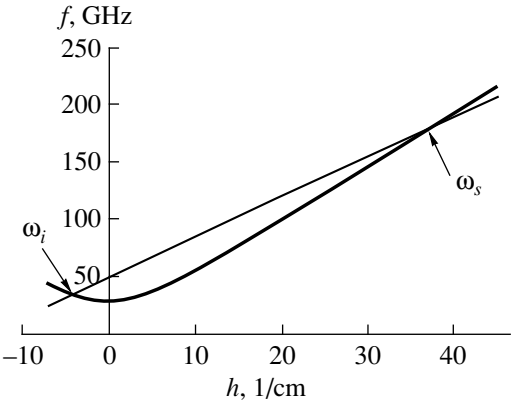

Fig. 1. Dispersion relation for the waveguide and the electron beam.

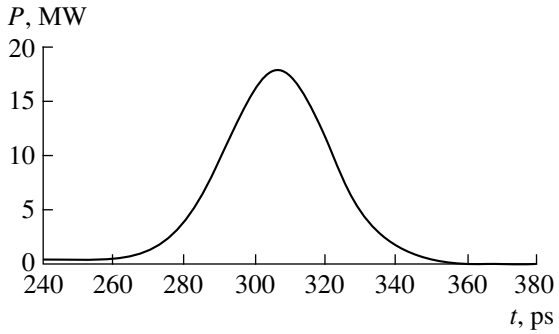

Fig. 2. The plot of scattered power vs. time.

The diameter of the waveguide for the scattering should be close to the cut-off value for the pump wave. This decreases the group velocity of the H_{11} pump wave so that its transverse electric field becomes stronger for a given power flux. (That is why the E_{01} wave is converted into the H_{11} wave.) As a result, electrons acquire a higher oscillation velocity. For example, if the waveguide radius is reduced from 0.4 to 0.3 cm, then the group velocity β_{gr}^i of the pump wave drops to about $\beta_{gr}^i \approx 0.5$ so that the electron oscillation velocity rises by a factor almost as large as 1.5 to reach $\beta_\perp \approx 0.13$. The dispersion relation plotted in Fig. 1 shows that the frequency of the scattered wave is about 170 GHz for the parameters selected. Figure 2 presents the results of

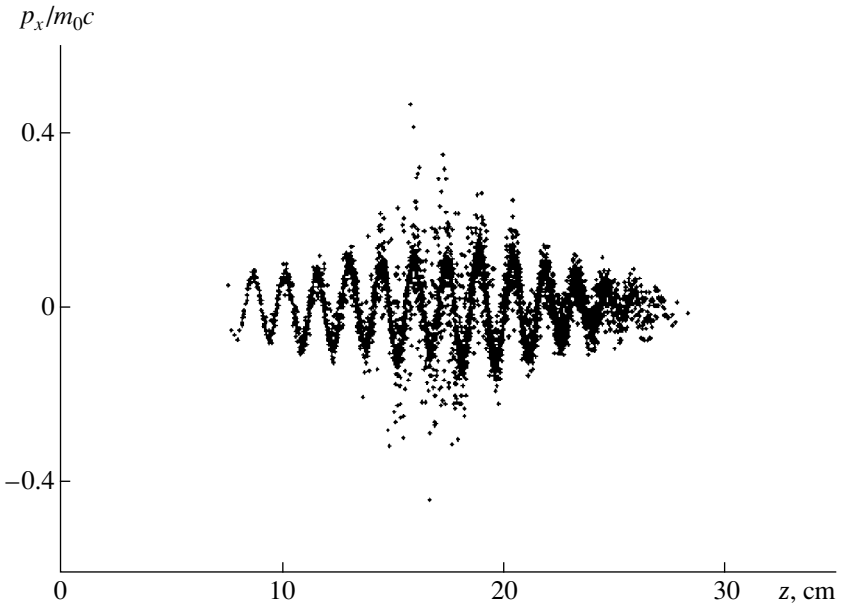

Fig. 3. Phase portrait of an electron bunch oscillating in a pump wave field.

simulation based on Eqs. (5). The scattered power is shown as a function of time for an interaction space length of 20 cm and a bunch duration of 250 ps. It is seen that duration of the scattered pulse is of the order of 100 ps and the peak power is 17 MW.

3. The possibility of superradiance due to the stimulated wave scattering was also supported by the particle-in-cell simulation using the KARAT code. The numerical experiment was carried out within the framework of a simplified plane two-dimensional model. The process was assumed to take place in a planar waveguide with a 38-GHz H_{01} pump wave. The computation was performed for a pumping power density of 100–150 MW/cm, a beam current of 200–500 A/cm, an electron energy of 200 keV, a transport magnetic field of 12 kOe, and a pump wave group velocity (β_{gr}) of about 0.5. These values correspond to those used with the first model. By contrast, the bunch duration was increased to 700 ps.

Figure 3 presents the phase portrait of a bunch oscillating in a pump field. Figure 4 displays the power waveform of the pulse and the spectrum of scattered radiation. It is seen that the spectrum is centered at 150 GHz and the peak power is about 1.5 MW. Also note that the peak power is lower than that obtained with the first model. The reason is that the second model is more realistic: it takes into account the scatter in electron positions, the effect of the space charge, etc.

To sum up, both models confirm the possibility of superradiance due to the stimulated wave scattering. In conclusion, note that the mechanism concerned works in the submillimeter band as well. Specifically, if the bunch energy is raised to 300 keV and pump frequency

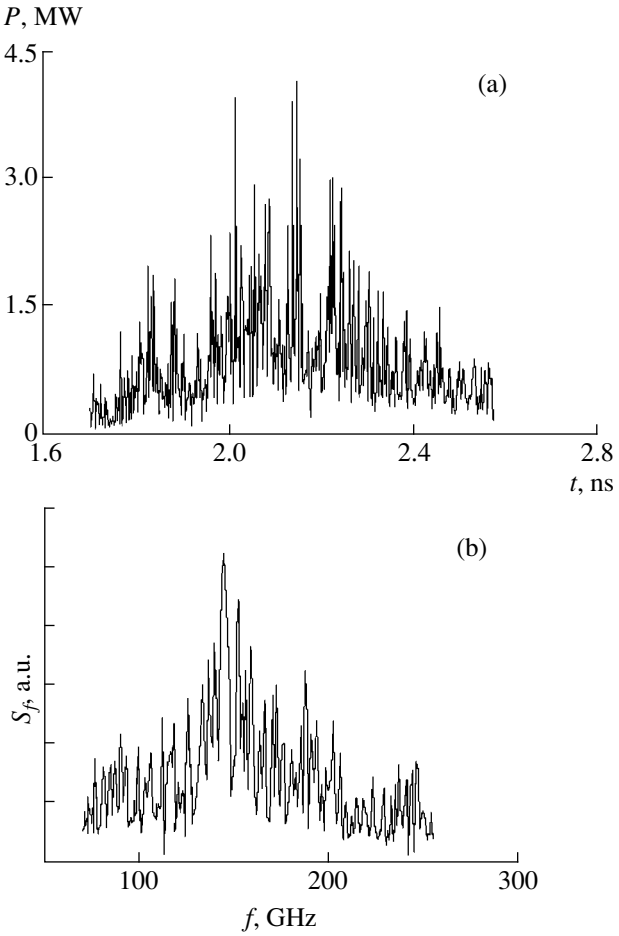

Fig. 4. Pulsed scattered radiation: (a) power waveform for $z = 0$; (b) power density spectrum. The data are obtained by a plane-model particle-in-cell simulation using the KARAT code.

is raised to 70 GHz, then the frequency of the scattered radiation will fall in the 400–500 GHz range.

This study was supported by the Russian Foundation for Basic Research (project no. 98-02-17308) and by the State Interdisciplinary Scientific-Technological Program, "Microwave Physics" section, project no. 1.13.

REFERENCES

1. R. Bonifacio, N. Piovella, and B. W. J. McNeil, Phys. Rev. A **44**, 3441 (1991).
2. N. S. Ginzburg, Pis'ma Zh. Tekh. Fiz. **14** (5), 440 (1988) [Sov. Tech. Phys. Lett. **14**, 197 (1988)].
3. N. S. Ginzburg, I. V. Zotova, and A. S. Sergeev, Pis'ma Zh. Éksp. Teor. Fiz. **60** (7), 501 (1994) [JETP Lett. **60**, 513 (1994)].
4. V. V. Zheleznyakov, V. V. Kocharovskiĭ, and Vl. V. Kocharovskiĭ, Izv. Vyssh. Uchebn. Zaved., Radiofiz. **29** (9), 1095 (1986).
5. N. S. Ginzburg, Yu. V. Novozhilova, and A. S. Sergeev, Pis'ma Zh. Tekh. Fiz. **22** (3), 39 (1996) [Tech. Phys. Lett. **22**, 359 (1996)].
6. N. S. Ginzburg, A. S. Sergeev, I. V. Zotova, *et al.*, Phys. Rev. Lett. **78** (12), 2365 (1997).
7. D. A. Jaroszynski, P. Chaix, and N. Piovella, Phys. Rev. Lett. **78** (9), 1699 (1997).
8. N. S. Ginsburg, A. S. Sergeev, Yu. V. Novozhilova, *et al.*, Nucl. Instrum. Methods Phys. Res. A **393**, 352 (1997).
9. N. S. Ginzburg, Yu. V. Novozhilova, A. S. Sergeev, *et al.*, Phys. Rev. E **60**, 3297 (1999).

Translated by A. Sharshakov

Technical Physics Letters, Vol. 26, No. 8, 2000, pp. 698–700. Translated from Pis'ma v Zhurnal Tekhnicheskoĭ Fiziki, Vol. 26, No. 16, 2000, pp. 1–7.

Remagnetization of a Circularly Anisotropic Amorphous Wire in an Alternating Magnetic Field

A. S. Antonov, N. A. Buznikov, and A. L. Rakhmanov

Institute of Theoretical and Applied Electrodynamics, Russian Academy of Sciences, Moscow, Russia

e-mail: andreyr@orc.ru

Received February 17, 2000

Abstract—Remagnetization of an amorphous ferromagnetic wire with circular anisotropy in an alternating longitudinal magnetic field was theoretically studied within the framework of a quasistationary approximation. A frequency spectrum of the emf generated in a probing coil wound on the wire was determined, and analytical expressions describing the dependence of the emf amplitude on the alternating magnetic field amplitude H_0 and the constant magnetic bias field value H_e were derived. The results can be applied to the development of weak magnetic field sensors. © *2000 MAIK "Nauka/Interperiodica".*

The interest of researchers in studying magnetically soft amorphous wires is related to their unique physical properties and good prospects for various technological applications. Investigations performed in the past decade showed evidence that the high-frequency impedance of these wires may exhibit a very large change in response to weak external magnetic fields, which was called the giant magnetic impedance effect [1–4]. This effect is now extensively investigated in the context of obtaining highly sensitive magnetic field sensors as well as magnetic recording media and devices. As for the magnetic field sensors, of considerable interest is the study of nonlinear remagnetization processes in amorphous ferromagnetic wires [5]. Indeed, use of the nonlinear effects may eliminate some undesirable phenomena such as hysteresis, metastable domain states, etc.

In this work, we have theoretically studied the remagnetization of an amorphous ferromagnetic wire with circular anisotropy in an alternating longitudinal magnetic field. A frequency spectrum of the emf generated in a probing coil wound on the wire was determined, and it was established that all harmonics are present in the spectrum provided that the amplitude of the alternating magnetic field exceeds a certain threshold level. The results confirmed a high sensitivity of the harmonic amplitudes V_k (k is the harmonic number) with respect to the constant magnetic bias field.

Consider an amorphous ferromagnetic wire with a diameter d in an alternating longitudinal magnetic field $H = H_e + \tilde{H}$, where H_e is the constant magnetic bias field and $\tilde{H} = H_0\sin(\omega t)$. The harmonic alternating component $\tilde{H}$ produces a change in the wire magnetization with time and, in accordance with the Faraday law, generates a circular emf V_φ in a coil wound around the wire. We will assume for simplicity that the skin effect in the wire is small and the alternating magnetic field is homogeneously distributed in the wire cross-section. The maximum frequency for which this approximation is valid can be estimated in the following way. A product of the specific conductivity of the amorphous film σ by the characteristic magnetic permeability $\tilde{\mu}$ usually does not exceed 10^{19} s^{-1} [6]. Then, the skin layer thickness $\delta = c(2\pi\sigma\tilde{\mu}\omega)^{-1/2}$ in a wire with $d \cong 10$ μm will exceed the diameter for the frequencies $f = \omega/2\pi$ below 10 MHz.

As is well known, the distribution of the easy anisotropic magnetization axes in amorphous ferromagnetic wires is controlled for the most part by the magnetostriction effect [5]. The magnetic properties of nonspun amorphous wires with negative magnetostriction constants are descried within the framework of a model assuming the presence of two regions in the wire: a central region (core) with homogeneous longitudinal magnetization and an outer shell with a circular direction of the magnetic anisotropy [1, 2, 5, 7–9]. In a wire with $d \cong 10$ μm, the core size is small and the contribution of this region to the total free energy of the wire can be neglected. For the sake of simplicity, we will additionally assume that the wire is single-domain, which is valid for sufficiently short samples (with a length not exceeding several centimeters) [5, 10, 11] in the shell of which no equilibrium domain structure can be realized because of the low magnetostriction constant.

Under these assumptions, the free energy of the wire is the sum of two terms representing the energies of magnetic anisotropy and the magnetic moment in the applied longitudinal field. Since the alternating field frequency is sufficiently small, the remagnetization process can be described within the framework of a

1063-7850/00/2608-0698$20.00

quasistationary approximation [12, 13], where the free energy density U has the following form:

$$U = (MH_a/2)\sin^2\theta - M(H_e + \tilde{H})\sin\theta. \quad (1)$$

Here, M is the saturation magnetization, H_a is the anisotropic field, and θ is the angle between the magnetic moment vector and the easy axis (circular direction). The emf V_φ generated in the probing coil is given by the formula

$$V_\varphi = -\frac{8\pi^2 N}{c}\int_0^{d/2}\frac{dM_z}{dt}r\,dr = -\frac{\pi^2 d^2 N}{c}\frac{dM_z}{dt}, \quad (2)$$

where N is the number of turns and $M_z = M\sin\theta$ is the longitudinal magnetization component. The latter quantity can be determined from the condition of minimum free energy:

$$M_z = \begin{cases}(M/H_a)[H_e + H_0\sin(\omega t)], & |H_e + \tilde{H}| < H_a,\\ \pm M, & |H_e + \tilde{H}| > H_a.\end{cases} \quad (3)$$

As can be seen from Eqs. (2) and (3), small amplitudes of the alternating field H_0 and the anisotropic field ($H_a < H_e$) lead to a linear response signal in the coil, containing only the first harmonic. For $H_0 > H_a - H_e$, the frequency spectrum of the emf signal will contain all harmonics. Introducing dimensionless harmonic amplitudes $v_k = cv_k/\pi d^2 NM\omega$ into Eqs. (2) and (3) and performing simple transformations, we obtain

$$v_1 = (H_0/H_a) \times [\tau_2 - \tau_1 + \sin(\tau_2)\cos(\tau_2) - \sin(\tau_1)\cos(\tau_1)],$$

$$v_k = \frac{H_0}{H_a}\left|\frac{\sin\{(k+1)\tau_2\} - \sin\{(k+1)\tau_1\}}{k+1} + \frac{\sin\{(k-1)\tau_2\} - \sin\{(k-1)\tau_1\}}{k-1}\right|, \quad k = 3, 5, \ldots, \quad (4)$$

$$v_k = \frac{H_0}{H_a}\left|\frac{\cos\{(k+1)\tau_2\} - \cos\{(k+1)\tau_1\}}{k+1} + \frac{\cos\{(k-1)\tau_2\} - \cos\{(k-1)\tau_1\}}{k-1}\right|, \quad k = 2, 4, \ldots,$$

where

$$\tau_1 = \begin{cases}-\pi/2, & H_0 - H_e < H_a,\\ -\arcsin\{(H_a + H_e)/H_0\}, & H_0 - H_e > H_a,\end{cases}$$

$$\tau_2 = \begin{cases}\pi/2, & H_0 + H_e < H_a,\\ \arcsin\{(H_a - H_e)/H_0\}, & H_0 + H_e > H_a.\end{cases} \quad (5)$$

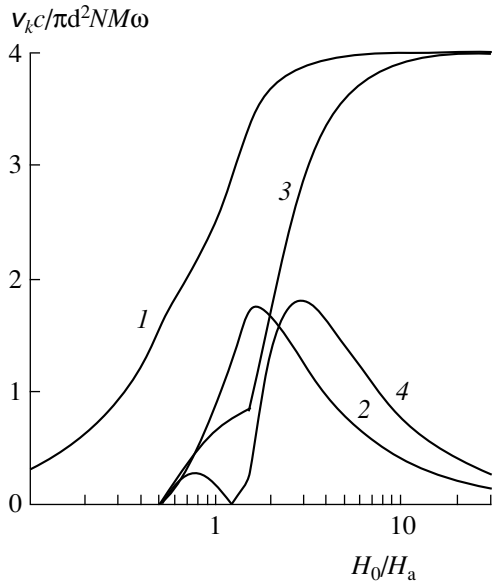

Fig. 1. The plots of harmonic amplitudes v_k versus alternating magnetic field amplitude H_0 calculated for $H_e/H_a = 0.5$ for $k = 1$ (*1*); 2 (*2*); 3 (*3*); 4 (*4*).

Figure 1 shows the plots of the first ($k \le 4$) harmonic amplitudes as functions of the alternating field amplitude H_0 calculated for a fixed magnetic bias field H_e by formulas (4) and (5). As seen, for $H_0 > H_a - H_e$, the frequency spectrum of the emf signal displays all harmonics. As the H_0 value increases, the odd harmonic amplitudes grow and the even harmonic amplitudes pass through a maximum and decay. As can also readily be shown using formulas (4) and (5), the dimensionless amplitudes of all odd harmonics asymptotically tend to a constant value ($v_k = 4$), while those of the even harmonics decrease proportionally to $8kH_a/H_0$.

Figure 2 shows the plots of the first harmonic amplitudes versus the magnetic bias field H_e calculated for a fixed amplitude of the alternating field H_0. As seen from these curves, the first harmonic dominates in the region of small H_e values. The contributions due to higher harmonics become significant when H_e increases to a sufficiently high level; however, the signal in the coil vanishes for $H_e - H_0 = H_a$ since no remagnetization takes place in the wire. Note that some harmonics are zero at intermediate values of the magnetic bias field amplitude (Fig. 2), which reflects a change in the phase of these harmonics by π.

For a nonlinear remagnetization regime to be established, the longitudinal magnetic field amplitude must exceed the anisotropic field strength in the wire during some part of the cycle of the alternating magnetic field variation. In this case, all harmonics will appear in the frequency spectrum of the emf generated in the probing coil. As seen from Fig. 2, the harmonic amplitudes are highly sensitive with respect to the constant magnetic bias amplitude H_e, which is an important characteristic

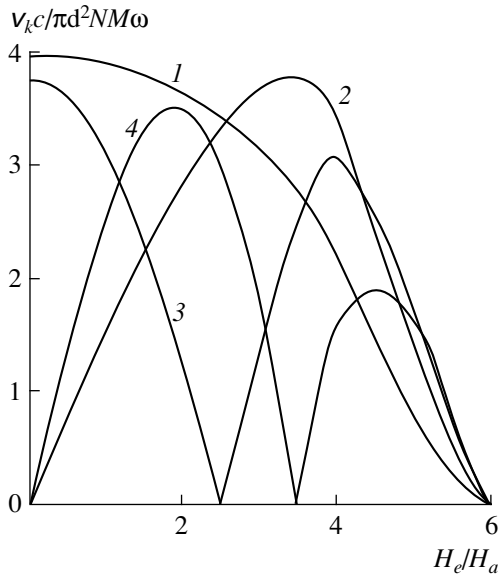

Fig. 2. The plots of harmonic amplitudes v_k versus magnetic bias field value H_e calculated for $H_0/H_a = 5$ and $k = 1$ (*1*); 2 (*2*); 3 (*3*); 4 (*4*).

for weak magnetic field sensors; for example, let us estimate the sensitivity of the second harmonic amplitude $|\partial V_2/\partial H_e|$ for a typical cobalt-based microscopic wire [14]. Assuming $d = 10$ μm, $M = 500$ G, $f = 5$ MHz, $H_a = 0.5$ Oe, and $H_0/H_a = 5$, $N = 100$, we obtain $|\partial V_2/\partial H_e| \approx 10^{-1}$ V/Oe. In conclusion, it should be noted that amplitudes of all the first harmonics are of the same order of magnitude. For this reason, the phenomenon of nonlinear remagnetization of an amorphous wire considered above may be of interest from the standpoint of developing magnetic-field-controlled frequency converters.

REFERENCES

1. K. Mohri, T. Kohzawa, K. Kawashima, *et al.*, IEEE Trans. Magn. **28** (5), 3150 (1992).
2. R. S. Beach and A. E. Berkowitz, Appl. Phys. Lett. **64** (26), 3652 (1994).
3. K. V. Rao, F. B. Humphrey, and J. L. Costa-Kramer, J. Appl. Phys. **76** (10), 6204 (1994).
4. J. Velazquez, M. Vazquez, D.-X. Chen, and A. Hernando, Phys. Rev. B **50** (22), 16737 (1994).
5. M. Vazquez and A. Hernando, J. Phys. D **29** (4), 939 (1996).
6. N. A. Usov, A. S. Antonov, and A. N. Lagar'kov, J. Magn. Magn. Mater. **185** (1–2), 159 (1998).
7. F. B. Humphrey, K. Mohri, J. Yamasaki, *et al.*, in *Proceedings of International Symposium on Magnetic Properties of Amorphous Materials* (Elsevier, Amsterdam, 1987), p. 110.
8. K. Mohri, F. B. Humphrey, K. Kawashima, *et al.*, IEEE Trans. Magn. **26** (5), 1789 (1990).
9. L. V. Panina, K. Morhi, T. Uchiyama, *et al.*, IEEE Trans. Magn. **31** (2), 1249 (1995).
10. N. A. Usov, A. S. Antonov, A. M. Dykhne, and A. N. Lagar'kov, Élektrichestvo, No. 2, 55 (1998).
11. A. S. Antonov, A. N. Lagar'kov, and I. T. Yakubov, Zh. Tekh. Fiz. **69** (3), 58 (1999) [Tech. Phys. **44**, 317 (1999)].
12. R. S. Beach, N. Smith, C. L. Platt, *et al.*, Appl. Phys. Lett. **68** (19), 2753 (1996).
13. A. S. Antonov, N. A. Buznikov, I. T. Iakubov, *et al.*, in *Proceedings of the Moscow International Symposium on Magnetism* (Mosk. Gos. Univ., Moscow, 1999), Part 2, p. 252.
14. M. Vazquez, J. M. Garcia-Beneytez, J. M. Garcia, *et al.*, in *Proceedings of the Moscow International Symposium on Magnetism* (Mosk. Gos. Univ., Moscow, 1999), Part 1, p. 259.

Translated by P. Pozdeev

Technical Physics Letters, Vol. 26, No. 8, 2000, pp. 701–704. Translated from Pis'ma v Zhurnal Tekhnicheskoĭ Fiziki, Vol. 26, No. 16, 2000, pp. 8–16.

Planar Free-Electron Lasers with Combined 1D/2D Bragg Mirror Resonators: A Theoretical Study

N. S. Ginzburg, A. S. Sergeev, N. Yu. Peskov, A. V. Arzhannikov, and S. L. Sinitskiĭ

Institute of Applied Physics, Russian Academy of Sciences, Nizhniĭ Novgorod, 603600 Russia

Institute of Nuclear Physics, Siberian Division, Russian Academy of Sciences, Novosibirsk, Russia

Received February 21, 2000

Abstract—The operation of a free-electron laser with a combined Bragg mirror resonator is studied theoretically. The resonator comprises a pair of planar Bragg reflectors with a two- and a one-dimensional relief pattern, respectively, and is closed in the transverse direction so as to ensure unidirectional outcoupling. It is demonstrated that this design provides for a possibility of obtaining spatially coherent radiation from a sheet electron stream with the cross size exceeding the wavelength by several orders of magnitude. © *2000 MAIK "Nauka/Interperiodica".*

1. Using sheet electron streams in free-electron lasers (FELs) seems to be a promising way for increasing output power, whereby the interaction space is developed in a transverse direction. It is now conceivable that a gigawatt output power level can be studied in the millimeter wave band, since high-current relativistic electron beams with a width of up to 150 cm and a power of up to 50 GW are already available [1, 2]. The main problem is the synchronization of waves from different parts of the stream. A two-dimensional (2D) distributed feedback has been suggested to solve the task [3, 4]. The feedback is effected by a 2D Bragg resonator comprised of a planar waveguide section with the inner surface having a double periodic relief pattern, the translation vectors being noncollinear. In contrast to a one-dimensional (1D) resonator with a corrugated inner surface, four partial waves are coupled in the 2D case, two of which propagate with the stream and in the opposite direction and the other two travel along the transverse axis, thus synchronizing radiation in the transverse direction. Reported in [4, 5], the analysis of the dynamics of such FELs showed that a steady-state single-frequency operation can be achieved with almost any stream width and that an increase in the system width results solely in longer transients, provided the optimum parameters are selected. On the other hand, the simplest configurations [3–5] suffer from the requirement that the system must be open in the transverse direction. As a result, the power has to be coupled out in two directions, whereas only unidirectional outcoupling is required in most cases. In [6], a way to ensure this was suggested whereby the resonator should be supplied with additional edge Bragg structures defecting the transverse power flows by 90° toward the electron stream. In our opinion, this resonator configuration is too complicated to be employed in pilot FELs with 2D distributed feedback. We think that effort should be made to design resonators closed in the transverse direction.

This paper analyzes the operation of a sheet beam FEL with a resonator comprising two dissimilar Bragg reflectors bearing 2D and 1D relief patterns (Fig. 1). Situated at the cathode (injector) end, the 2D reflector synchronizes the radiation in the transverse direction. At the collector end, it is sufficient to place a conventional 1D reflector to close the feedback loop. Both reflectors are closed in the transverse direction, but modest losses (e.g., ohmic) are still imparted to the input reflector for the sake of lasing stability. These losses have insignificant effect on the energy balance, provided that optimum parameters are selected. This means that the reflection coefficient of the output reflector is not too large and the radiation is amplified predominantly after the input reflector. Thus, the power is mostly emitted by the electron stream in the longitudinal direction and little is dissipated or scattered.

2. Let the input reflector have the following 2D relief pattern:

$$a = a_2 \cos(\bar{h}_2 z)\cos(\bar{h}_2 x), \tag{1}$$

where the pattern height $2a_2$ is assumed to be small. The pattern insures the coupling and mutual scattering of four partial waves

$$\mathbf{E} = \mathbf{E}_0 \mathrm{Re}([\mathcal{A}_+ e^{-ihz} + \mathcal{A}_- e^{ihz} + \mathcal{B}_+ e^{-ihx} + \mathcal{B}_- e^{ihx}]e^{i\bar{\omega}t}), \tag{2}$$

provided the propagation constant h satisfies the Bragg

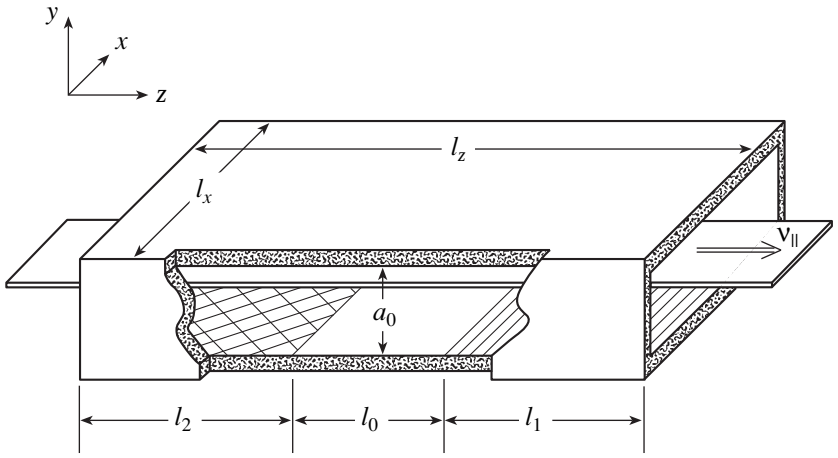

Fig. 1. Configuration of a planar FEL with a combined Bragg mirror resonator driven by a sheet relativistic electron beam. The input and the output reflector have a 2D and a 1D relief pattern, respectively.

resonance condition [3]:

$$h \approx \bar{h}_2. \tag{3}$$

In Eqs. (2) and (3), $\bar{h}_2 = \sqrt{2}\,\pi/d_2$, with d_2 being the period of the pattern; $\mathcal{A}_\pm(x, z, t)$ and $\mathcal{B}_\pm(x, z, t)$ are slowly varying functions; and $\bar{\omega} = 2\pi\bar{f} = \bar{h}_2 c$ is the Bragg frequency, which is chosen to serve as a carrier frequency. Allowing for excitation of the synchronous wave $\mathcal{A}_+$ by the electron stream, the mutual scattering of the partial waves by the pattern (1) is described by the following system of equations [7]:

$$\begin{aligned}
&\left(\frac{\partial}{\partial Z} + \beta_{gr}^{-1}\frac{\partial}{\partial \tau}\right)A_+ + i\alpha_2(B_+ + B_-) = F(X)J,\\
&\left(\frac{\partial}{\partial Z} - \beta_{gr}^{-1}\frac{\partial}{\partial \tau}\right)A_- + i\alpha_2(B_+ + B_-) = 0,\\
&\left(\frac{\partial}{\partial X} \pm \beta_{gr}^{-1}\frac{\partial}{\partial \tau}\right)B_\pm + i\alpha_2(A_+ + A_-) = 0.
\end{aligned} \tag{4}$$

The boundary conditions for Eqs. (4) are

$$\begin{aligned}
A_+\big|_{Z=0} = 0, \quad (B_+ + RB_-)\big|_{X=0} = 0,\\
(B_- + RB_+)\big|_{X=L_x} = 0,
\end{aligned} \tag{5}$$

where $R \le 1$ is the reflection coefficient of the cavity side walls for the $B_\pm$ waves. The dimensionless quantities in Eqs. (4) are defined as follows:

$$Z = zC\bar{\omega}/c, \quad X = xC\bar{\omega}/c, \quad L_{x,z} = l_{x,z}C\bar{\omega}/c,$$
$$\tau = tC\bar{\omega};$$

$(A_\pm, B_\pm) = (\mathcal{A}_\pm, \mathcal{B}_\pm)e\kappa\mu/\gamma mc\bar{\omega}C^2$; $\kappa \approx \beta_\perp/\beta_\parallel$ is the beam–wave coupling parameter; $\mu \approx \gamma^{-2}$ is the inertial bunching parameter [8]; γ is the relativistic mass factor of the electron beam; $\beta_\parallel$ is the translational electron velocity; β_{gr} is the group velocity of the waves;

$$C = \left(\frac{eI_0}{mc^3}\frac{\lambda^2\mu k^2}{8\pi\gamma a_0}\right)^{1/3}$$

is the Pierce gain parameter; I_0 is the beam current per unit width; a_0 is the cavity height (see Fig. 1); α_2 is the wave coupling parameter for the 2D pattern, which is proportional to a_2 [9]; and $F(x)$ is the electron stream density profile (see Fig. 1).

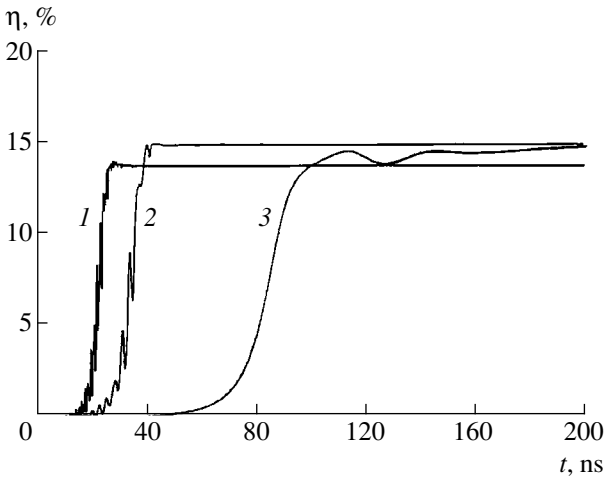

Fig. 2. Simulated turn-on transients in a combined1D/2D Bragg mirror FEL: the electronic efficiency vs. time at a cavity width l_x of (*1*) 20, (*2*) 70, or (*3*) 140 cm. Other parameter values are as follows: α_2 = (*1*) 0.08, (*2*) 0.04, or (*3*) 0.03 cm^{-1}; α_1 = (*1*) 0.1 or (*2*, *3*) 0.03 cm^{-1}; $\bar{f}$ = 75 GHz; $C = 6 \times 10^{-3}$; R = 0.95; l_2 = 18 cm; l_0 = 30 cm; l_1 = 10 cm; and $\Delta = -1.5$.

Like the smooth portion of the resonator, the output 1D reflector deals with two partial waves only:

$$\mathbf{E} = \mathbf{E}_0 \mathrm{Re}([\mathscr{A}_+ e^{-ihz} + \mathscr{A}_- e^{ihz}] e^{i\bar{\omega}t}). \quad (6)$$

These waves travel parallel and antiparallel to the translational beam velocity. The 1D Bragg pattern is defined as

$$a = a_1 \cos(\bar{h}_1 z), \quad (7)$$

where $\bar{h}_1 = 2\pi/d_1$ (with $2a_1$ and d_1 being the height and the period of the pattern, respectively). The waves are scattered if

$$h \approx \bar{h}_1/2. \quad (8)$$

The scattering is described by the equations

$$\left(\frac{\partial}{\partial Z} + \beta_{gr}^{-1}\frac{\partial}{\partial \tau}\right)A_+ + i\alpha_1 A_- = F(X)J,$$
$$\left(\frac{\partial}{\partial Z} - \beta_{gr}^{-1}\frac{\partial}{\partial \tau}\right)A_- + i\alpha_1 A_+ = 0, \quad A_-|_{Z=L_z} = 0, \quad (9)$$

where α_1 is the wave coupling parameter for the 1D pattern [9] and $l_z = l_2 + l_0 + l_1$ is the total cavity length (Fig. 1). In the smooth portion of the resonator, the amplification of the wave $\mathscr{A}_+$ obeys an equation similar to Eqs. (9) with a zero wave coupling parameter. The partial amplitudes $\mathscr{A}_\pm$ must be considered continuous at the boundaries between the resonator portions.

According to [8], the averaged particle motion in the field of synchronous wave $\mathscr{A}_+$ is described by the equation

$$\left(\frac{\partial}{\partial Z} + \beta_\parallel^{-1}\frac{\partial}{\partial \tau}\right)^2 \theta = \mathrm{Re}(A_+ e^{i\theta}) \quad (10)$$

subject to the boundary conditions

$$\theta|_{Z=0} = \theta_0 \in [0, 2\pi),$$
$$\left(\frac{\partial}{\partial Z} + \beta_\parallel^{-1}\frac{\partial}{\partial \tau}\right)\theta|_{Z=0} = \Delta, \quad (11)$$

where $\theta = \bar{\omega}t - h_z - h_w z$ is the instantaneous phase of electrons with respect to the synchronous wave, $\Delta = (\bar{\omega} - h v_\parallel - h_w v_\parallel)/\bar{\omega}C$ is the initial frequency detuning from wiggler synchronism at the carrier frequency, $h_w = 2\pi/d_w$, and d_w is the period of the wiggler. Having solved Eq. (10), one finds the electron current $J = \frac{1}{\pi}\int_0^{2\pi} e^{-i\theta}\, d\theta_0$ that excites the synchronous wave, this term entering into Eqs. (4) and (9). Note that Eqs. (4), (9), and (10) are written under the assumption that both the 1D and 2D Bragg resonance conditions (3) and (8) are met. This is obviously possible when $\bar{h}_2 = \bar{h}_1/2$, which in turn is satisfied if $d_2 = \sqrt{2}\, d_1$.

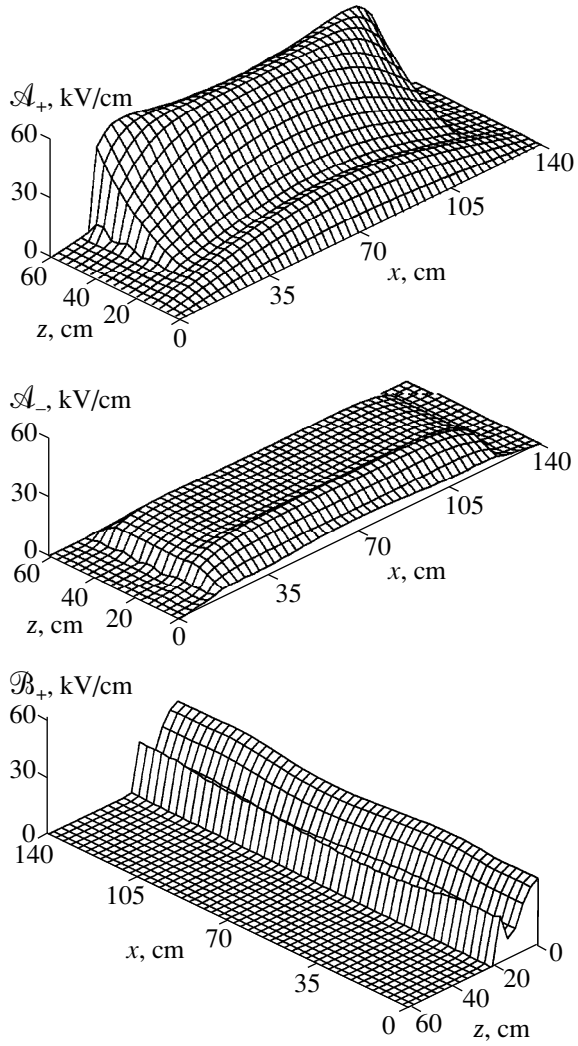

Fig. 3. Spatial distributions of the partial wave amplitudes $\mathscr{A}_\pm$ and $\mathscr{B}_+$ under steady-state FEL operation conditions. The parameter values are the same as for curve *3* in Fig. 2.

3. We carried out a simulation based on Eqs. (4), (9), and (10). The results are presented in Figs. 2 and 3. The parameter values were close to those of 4-mm-band FEL experiments conducted at the Institute of Nuclear Physics using the U-2 and U-3 accelerators [10, 11]. Specifically, we set the input (2D) reflector length at 18 cm, the output (1D) reflector length at 10 cm, the smooth portion length at 30 cm, and the cavity height at $a_0 = 1$ cm. The beam current per unit width was 1 kA/cm; the particle energy, 1 MeV; the wiggler period, 4 cm; and the particle oscillation velocity in the wiggler field, $\beta_\perp \approx 0.2$. Accordingly, the Pierce gain parameter was about $C \approx 6 \times 10^{-3}$.

Figure 2 depicts the electronic efficiency as a function of time for different widths of the interaction space. As seen, a steady-state FEL operation is possible. Note that the width was increased while simultaneously decreasing the wave coupling parameter, the

other dimensions being fixed. To obtain stable operation, a certain loss was imparted to the resonator for the $\mathcal{B}_{\pm}$ waves by setting the reflection coefficients of the input reflector at about 0.95 for the waves. This could be implemented by depositing an absorber onto the cavity side walls.

Figure 3 presents the spatial distributions of the partial wave amplitudes $\mathcal{A}_{+}$ and $\mathcal{B}_{\pm}$ under steady-state conditions for the case where $l_x = 140$ cm and the sheet relativistic electron beam occupies about 80% of the cavity width. In the beam region, $\mathcal{A}_{+}$ is seen to be almost uniform in the transverse direction. This ensures that all of the stream parts contribute the same power to the radiation and that the average efficiency is sufficiently high. Estimates of the partial power flows at the resonator ends (Fig. 3) indicate that the values of the reflection coefficients mentioned in the preceding paragraph have little or no effect on the energy balance, the resultant losses being within 1–2%. Under these conditions, the maximum output power of the FEL may reach 5–10 GW.

To sum up, the above analysis has demonstrated that using FELs with a combined Bragg resonator comprising two dissimilar planar reflectors with 2D and 1D relief patterns opens the way to obtaining a spatially coherent radiation from a sheet electron stream whose width exceeds the wavelength by several orders of magnitude. The resonator is closed in the transverse direction, thus ensuring unidirectional outcoupling.

REFERENCES

1. A. V. Arzhannikov, V. S. Nikolaev, S. L. Sinitsky, and M. V. Yushkov, J. Appl. Phys. **72** (4), 1657 (1992).
2. A. V. Arzhannikov, V. B. Bobylev, V. S. Nikolaev, *et al.*, in *Proceedings of the 10th International Conference on High-Power Particle Beams, San Diego, 1994*, Vol. 1, p. 136.
3. N. S. Ginzburg, N. Yu. Peskov, and A. S. Sergeev, Pis'ma Zh. Tekh. Fiz. **18** (9), 23 (1992) [Sov. Tech. Phys. Lett. **18**, 285 (1992)].
4. N. S. Ginsburg, N. Yu. Peskov, A. S. Sergeev, *et al.*, Nucl. Instrum. Methods Phys. Res. A **358**, 189 (1995).
5. N. S. Ginzburg, N. Yu. Peskov, and A. S. Sergeev, Opt. Commun. **112**, 151 (1994).
6. N. S. Ginzburg, N. Yu. Peskov, and A. S. Sergeev, Radiotekh. Élektron. (Moscow) **40** (3), 401 (1995).
7. N. S. Ginzburg, N. Yu. Peskov, A. S. Sergeev, *et al.*, Phys. Rev. E **160** (1), 935 (1999).
8. V. L. Bratman, G. G. Denisov, N. S. Ginzburg, and M. I. Petelin, IEEE J. Quantum Electron. **QE-19** (3), 282 (1983).
9. N. F. Kovalev, I. M. Orlova, and M. I. Petelin, Izv. Vyssh. Uchebn. Zaved., Radiofiz. **11** (5), 783 (1968).
10. M. A. Agafonov, A. Arzhannikov, N. S. Ginzburg, *et al.*, IEEE Trans. Plasma Sci. **26** (3), 531 (1998).
11. N. V. Agarin, A. V. Arzhannikov, V. B. Bobylev, *et al.*, in *Abstracts of the 21st International FEL Conference, Hamburg, 1999*, p. Mo-O-03.

Translated by A. Sharshakov

Technical Physics Letters, Vol. 26, No. 8, 2000, pp. 705–706. Translated from Pis'ma v Zhurnal Tekhnicheskoĭ Fiziki, Vol. 26, No. 16, 2000, pp. 17–21.

Electrical Properties of Thin $Ba_xSr_{1-x}TiO_3$ Films for Microwave Applications

S. V. Razumov and A. V. Tumarkin

St. Petersburg State Electrotechnical University, St. Petersburg, Russia

Received April 12, 2000

Abstract—Electrical properties of thin $Ba_xSr_{1-x}TiO_3$ films with variable composition were studied depending on technological parameters of the ion-plasma synthesis. © *2000 MAIK "Nauka/Interperiodica".*

In recent years, ferroelectric $Ba_xSr_{1-x}TiO_3$ (BSTO) films used in numerous applications have attracted the attention of researchers as possible materials for microwave devices [1, 2]. This interest is based on the strong dependence of the permittivity of BSTO films on the applied electric field strength, reliable operation of the BSTO-based microwave semiconductor devices at a field strength of up to ~40 V/μm and above [3], and a relatively low dielectric loss tangent of these materials in the microwave frequency range [4]. These properties make the BSTO films promising materials for the microwave devices such as varactors, phase-rotating devices, and tunable filters operating at room temperature [5].

From the standpoint of physical properties in the microwave frequency range, the most promising systems are offered by the BSTO films deposited onto sapphire and, especially, polycore substrates. However, now there is a need for ferroelectric films to combine a sufficiently strong field dependence of the permittivity with low microwave energy losses (at least, with a room-temperature loss tangent $\tan\delta < 0.01$ at 1 GHz). Creating such BSTO films presents a quite difficult task.

One of the most acceptable ways to obtain the BSTO films with perfect structure and high physical properties is offered by the ion-plasma deposition techniques. However, fabrication of the BSTO films with the properties acceptable for the microwave applications by the method of RF magnetron sputtering requires establishing a correlation between the main technological parameters of the film deposition process (including the synthesis temperature, working gas mixture composition, and target composition) and the electrical properties of the resulting BSTO films.

The purpose of this work was to study the properties of BSTO films obtained on single- and polycrystalline sapphire substrates by the RF magnetron sputtering of a ceramic target.

The sample films were prepared on a Leybold Z-400 technological magnetron system by the "on-axis" sputtering of 76-mm-diam ceramic targets of various compositions. The sputtered material was deposited either in pure oxygen or in a 50% O_2 + 50% Ar gas mixture at a total gas pressure of 8 Pa. The synthesis temperature was varied from 700 to 900°C. The RF discharge power was varied from 120 to 360 W. The electrical properties of the synthesized films were studied using planar capacitor structures with 0.35-μm-thick copper electrodes and an interelectrode gap width of ~7 μm. The electrical characteristics were measured at a frequency of 1 GHz and a voltage U applied to the capacitors varied from 0 to 300 V (E = 0–40 V/μm).

Figures 1a and 1b show the plots of the control ability factor $K = C_{max}(U)/C_{min}(U)$ versus the synthesis temperature for the films obtained by sputtering from $Ba_{0.8}Sr_{0.2}TiO_3$ and $Ba_{0.5}Sr_{0.5}TiO_3$ targets onto sapphire and polycore substrates. Figures 2a and 2b present the temperature dependences of the dielectric loss tangent for the same films. As seen from these data, both the control ability and the microwave losses of the films are determined to a considerable extent by the content of Ba in the deposit. In particular, the films produced by sputtering the $Ba_{0.8}Sr_{0.2}TiO_3$ target have a control ability factor of up to 2.5 at rather high losses ($\tan\delta = 0.04$ at $U = 0$ and above), which makes this material ineffective in the microwave frequency range.

More promising results were obtained for the films prepared from the $Ba_{0.5}Sr_{0.5}TiO_3$ target. These films exhibit a clear tendency of both the control ability factor and the dielectric loss tangent to increase with the synthesis temperature (Figs. 1a and 1b). However, the losses can be reduced by replacing pure oxygen with the O_2–Ar mixture, albeit at the expense of the control ability factor reduced to ~1.5. Apparently, the problem of obtaining BSTO films combining good control ability and low losses can be solved by compromising between the target composition (with the Ba and Sr contents not exceeding 0.5/0.5), a sufficiently high synthesis temperature, and the working gas mixture composition.

1063-7850/00/2608-0705$20.00

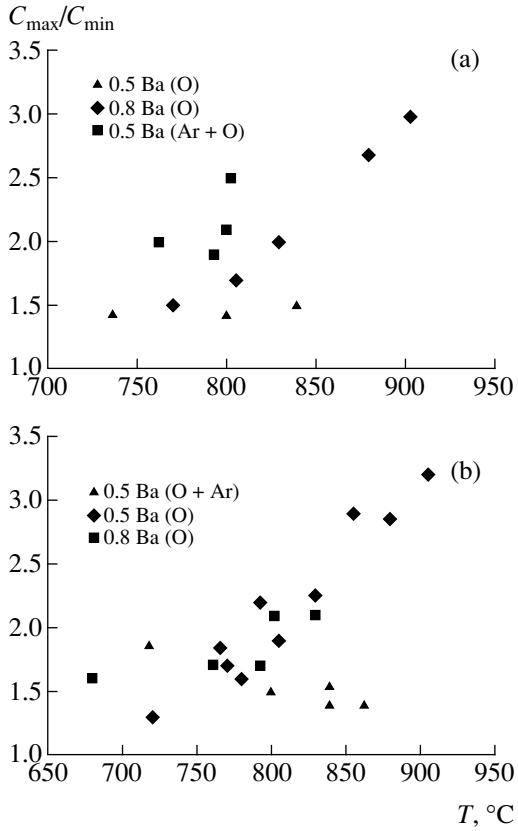

Fig. 1. Plots of the control ability factor versus temperature for various BSTO films deposited onto (a) sapphire and (b) polycore substrates.

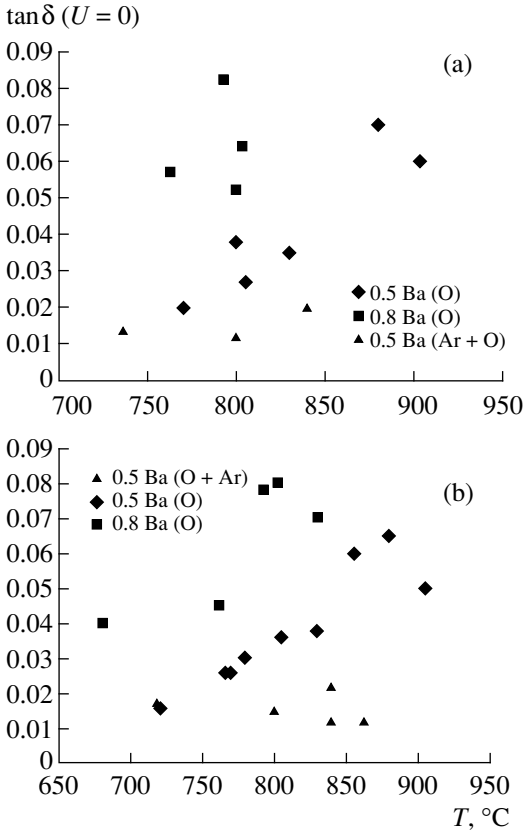

Fig. 2. Plots of the dielectric loss tangent versus temperature for various BSTO films deposited onto (a) sapphire and (b) polycore substrates.

Investigations of the film sample structure by X-ray diffraction showed that the films synthesized in the indicated temperature range contain blocks with the orientations (111), (110), and (100), their ratio depending on the synthesis temperature. We may suggest that a multiphase character of the films accounts for the rather high level of RF losses, although we failed to find any strict correlation between changes in the phase composition and the RF losses.

All the above considerations equally apply to the BSTO films deposited onto sapphire and polycore substrates, since no significant differences between the electrical properties of these films were observed.

Thus, we have demonstrated the possibility of controlling the electrical properties of BSTO films grown by method of RF magnetron sputtering on both single- and polycrystalline Al_2O_3 substrates. The obtained results determine the direction for further investigation of the synthesis of BSTO film combining a high control ability and low energy losses in the microwave frequency range.

REFERENCES

1. J. M. Ponds, S. W. Kirchoefer, W. Chang, *et al.*, Integr. Ferroelectr. **22**, 317 (1998).
2. F. Miranda, F. W. van Keuls, R. R. Romanofsky, and G. Subramanyam, Integr. Ferroelectr. **22**, 269 (1998).
3. Jaemo Im, O. Auciello, P. K. Baumann, *et al.*, Appl. Phys. Lett. **76**, 625 (2000).
4. J. D. Baniecki, R. B. Laibowitz, T. W. Shaw, *et al.*, Appl. Phys. Lett. **72**, 498 (1998).
5. A. B. Kozyrev, A. V. Ivanov, T. B. Samoilova, *et al.*, Integr. Ferroelectr. **24**, 297 (1999).

Translated by P. Pozdeev

Technical Physics Letters, Vol. 26, No. 8, 2000, pp. 707–709. Translated from Pis'ma v Zhurnal Tekhnicheskoĭ Fiziki, Vol. 26, No. 16, 2000, pp. 22–29.

A Thin-Layer Bichromated Gelatin for Holography Sensitive in the Red Spectral Range

N. M. Ganzherli, Yu. N. Denisyuk, S. P. Konop, and I. A. Maurer

Ioffe Physicotechnical Institute, Russian Academy of Sciences, St. Petersburg, 194021 Russia

Received December 16, 1999

Abstract—A variant of thin-layer optically sensitive material for holographic applications, based on a bichromated gelatin with glycerol and Methylene Blue dye additives, is suggested. The material is sensitive in the red spectral range, possesses the property of self-development, and provides for the possibility of the real-time reconstruction of holographic images. The bichromated gelatin is prepared using potassium bichromate. *© 2000 MAIK "Nauka/Interperiodica".*

Gelatin with chromate additives has been used as a medium for hologram recording since 1968 [1]. Previously, bichromated gelatin (BG) was known as a medium sensitive in the blue-green and ultraviolet spectral ranges. The task of expanding the spectral sensitivity range to the red, so as to provide for the holographic information recording using He–Ne laser radiation, is still important. Solving some practical tasks requires holographic media in the form of thin layers (with thicknesses from 100 μm to a few millimeters). Another requirement is the obtaining of self-developing layers, which would allow for the real-time image reconstruction.

According to [2], the intrinsic sensitivity of a bichromated gelatin in the red spectral range is very small (about 15–150 J/cm^2 for 10–30 μm thick layers). In order to increase the spectral range, the chromate-containing colloidal systems are doped with dyes possessing maximum absorption in the desired region. The main problem encountered in selecting such a sensitizer is related to the low solubility of many dyes in the presence of ammonium bichromate. For example, Methylene Blue tends to precipitate in the aqueous solutions of ammonium bichromate. However, most works devoted to the red sensitization of BG layers were performed with Methylene Blue (MB) [3–9]. The experimental data indicate that successful operation of the BG + MB system is possible provided that the solution pH is maintained on a level no lower than 9.0.

The first publication concerning the use of BG layers in a real-time operation mode not involving additional photochemical processing appeared in 1984 [9]. According to the data reported, undeveloped BG layers with a diffraction efficiency (DE) of 0.1–0.7% can be used for the optical data processing at an exposure of 200 mJ/cm^2. It was also pointed out that holding the BG layers for several hours in a humid atmosphere leads to some increase in the DE level.

The development of information recorded in a BG layer implies that water, one of the necessary components, has to be present in the composition at an amount sufficient to reveal the recorded image. Using sandwich structures with a BG layer confined in a closed volume between two glasses allows a certain amount of water to be retained in the layer upon gelation. In this case, a hologram is registered immediately in the water-saturated layer.

Previously [10–12], we have developed a thick-layer optically sensitive material based on a bichromated gelatin for the blue-green spectral range. The material was in the form of a 1–3 mm thick gel cast between two glasses. A certain amount of water retained in the layer allowed a real-time registration of the holograms. An obvious disadvantage of this thick-layer system was the limited lifetime of the holograms. In order to increase the water content in the BG layer, it was suggested to introduce a certain amount of glycerol to the emulsion composition [13, 14]. Glycerol may play a manyfold role in self-developing BG layers.

In addition to providing for the self-development process, this component increases the optical sensitivity and extends it toward the longwave spectral region. Moreover, glycerol acts as a plasticizer and increases the amount of water molecules capable of developing the recorded image due to the presence of hydrogen bonds. Self-developing bichromated gelatin layers containing up to 95% glycerol (relative to the dry gelatin weight) and having a thickness of 5–10 μm upon drying were described in [15]. It was established that an optimum content of free water providing a maximum sensitivity is reached in compositions containing 90–95% glycerol (relative to the dry gelatin weight).

Diffraction efficiency is the main holographic parameter characterizing a recording medium. Previously [16], we studied the holographic characteristics of glycerol-containing layers with MB additives, in which the BG was obtained using ammonium bichro-

1063-7850/00/2608-0707$20.00 © 2000 MAIK "Nauka/Interperiodica"

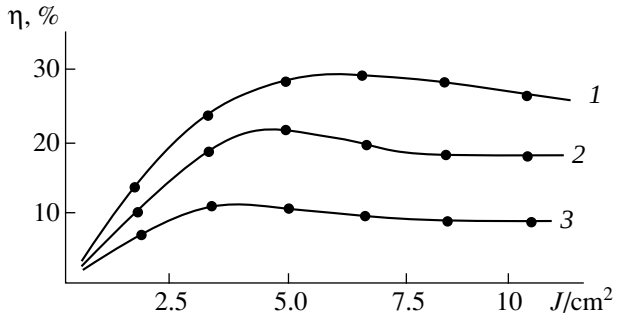

Fig. 1. The typical plots of diffraction efficiency η versus exposure for the holograms of two plane waves recorded in a symmetric scheme using an incident radiation power density of 54 mW/cm^2 in BG layers with various content of potassium bichromate (relative to the dry gelatin weight): (*1*) 60; (*2*) 40; (*3*) 20%.

mate.The sample layers with a thickness of 2 mm were prepared by in the form of gels between two glass plates. The MB precipitation was prevented by adding ammonia to pH 9. As long as ammonia did not evaporate from the glass-covered layers, MB did not precipitate. The sample holograms of two plane waves were recorded in a symmetric scheme using a He–Ne laser. The beam convergence angle corresponded to a spatial frequency of 100 mm^{-1}.

We have analyzed the DE as a function of exposure for various component concentrations. In particular, it was found that increasing the MB content leads to an increase in the absorption at 0.63 μm and a decrease in the optical transmission, which results in a drop of the DE of holograms. At the same time, increasing the concentration of ammonium bichromate to 50% (relative to the dry gelatin weight) increases the optical sensitivity and the maximum achievable DE level of the recorded gratings (DE reached 15% at a 10 mW/cm^2 power density of the incident radiation).

In some applications, it would be convenient to use layers with the open surface rather than sandwich structures confined between glass plates. However, as noted above, MB begins to precipitate as soon as pH decreases below 9.0. In the ammonium bichromate based layers described above, the pH was maintained by adding certain amounts of ammonia and keeping the samples closed upon gel casting. We have replaced ammonium bichromate with potassium bichromate, the other composition components and preparation features remaining the same. Ammonia was not added and the sample layers were open both during and after casting. In this way, we have succeeded in obtaining self-developing layers sensitive in the red spectral range. Both preparation and casting of these layers are much like the technology of obtaining self-developing BG layers sensitive in the blue range. Upon drying, the layer thickness varied from 100 μm to 2.2 mm.

The sample layers were prepared using the following procedure. A 10% gelatin solution was prepared and allowed to stand for 2 h at 25°C. To this solution was added glycerol (100% of the dry gelatin weight) and the mixture was treated for another 2 h at 40°C. Finally, potassium bichromate (at an amount of 20, 40, or 60% of the dry gelatin weight) and a necessary amount of a 0.5% MB solution (1 ml MB per 100 ml of the mixture) were added and the mixture was cast inside metal rings of certain thickness on glass substrates. Upon a 24-h gelation, during which the layer thickness somewhat decreased, the samples were ready for recording holograms.

We have studied the holographic characteristics of the sample BG layers upon recording the holograms of two plane waves in a symmetric scheme using a He–Ne laser operating at a wavelength of 0.63 μm. The convergence angle of the interfering beams was varied from 15° to 35°. We have also varied a power density of the recording radiation, the potassium bichromate content (20–60% of the dry gelatin weight), and the MB concentration. The holographic characteristics of the emulsions were measured 24 h after casting. The layer thicknesses varied from 0.6 to 2.2 mm.

Figure 1 shows the typical plots of DE versus exposure measured for the holograms studied. The optimum potassium bichromate concentration in layers with a thickness on the order of 1.3 mm was 60% (relative to the dry gelatin weight), for which the a maximum DE level of 29% was achieved. Increasing the potassium bichromate content above 60% led to a decrease in the DE value. The same effect was produced by increasing the MB concentration, which was explained by a drop in the sample layer transmission. In the course of drying, the sensitivity of sample layers gradually decreased and the DE level of holograms dropped. We have determined the DE of the holograms from two plane waves as a function of the spatial frequency of recorded gratings. It was established that the maximum DE gradually decreases with increasing spatial frequency, amounting to 26, 23, 18, 9, and 2% for the interfering beam convergence angles 17° (470 mm^{-1}), 20° (550 mm^{-1}), 25° (685 mm^{-1}), 30° (820 mm^{-1}), and 35° (955 mm^{-1}), respectively.

We have also studied the angular selectivity of three-dimensional (3D) holograms with respect to variation of the hologram reading angle. Figure 2a shows the corresponding DE plot for a hologram measured in a 1.37 mm thick layer by varying the angle of incidence of the reading beam at various time instants after the hologram recording. As seen, the DE level decreases with time as a result of degradation of the recorded holographic grating, which is explained by changes in structure of the gel-like medium containing a large amount of glycerol.

Previously [17], a simple expression was obtained that relates the angular selectivity δα of the 3D holo-

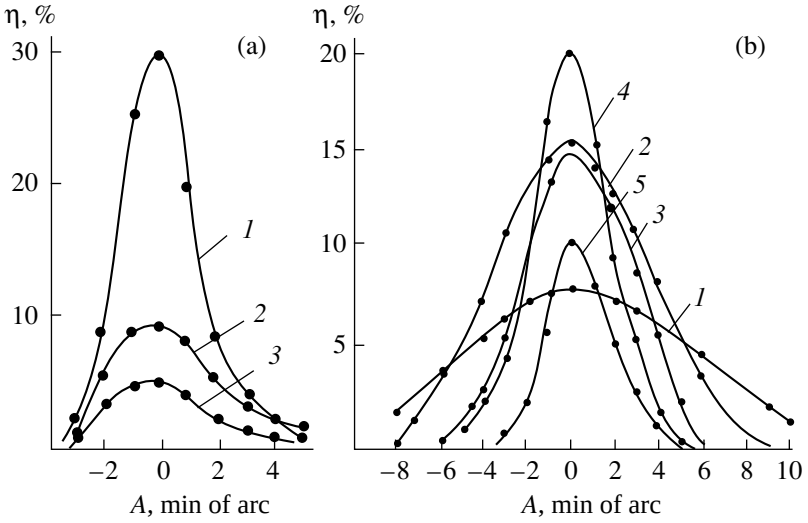

Fig. 2. The plots of diffraction efficiency η versus hologram reading angle *A* measured (a) at various times upon recording [*t* = 2 (*1*); 40 (*2*); 80 min (*3*)] in a 1.37 mm thick BG layer and (b) for BG layers of various thicknesses [*d* = 610 (*1*); 730 (*2*); 1020 (*3*); 1720 (*4*); 2140 μm (*5*)].

gram to the hologram thickness *d*, light wavelength λ, and the interfering beam convergence angle α:

$$\delta\alpha = \lambda/d\alpha.$$

Upon substituting the experimental values of $\delta\alpha = 5' = 0.0014$ rad, $\alpha = 15° = 0.259$ rad, and $\lambda = 0.63$ μm, we obtain an estimate of the sample thickness $d = 1.73$ mm. The table below presents the experimental values of δα and the maximum DE value η_{max} for BG layers of various thicknesses *d* (Fig. 2b) and the effective thicknesses *d*" calculated using the above formula:

δα, min	13.5	9	6.5	5	4	3.5
η_{max}, %	7.5	14.5	16	29	21	10
d, μm	610	730	1020	1370	1720	2140
d", μm	630	930	1310	1730	2200	2420

Taking into account the approximate character of the theoretical expression for the angular selectivity and uncertainty of the experimental δα and α values, the agreement between measured and calculated thicknesses can be considered as quite satisfactory. The proposed material, sensitive in the red spectral range, allows a real-time reconstruction of the recorded holographic image and, hence, can be used for investigating features of the hologram recording. The bichromated gelatin is cheap, simple in preparation, and ensures good reproducibility of results. The next task is to increase the lifetime of recorded holograms.

This work was supported by the Russian Foundation for Basic Research, project no. 99-02-18481.

REFERENCES

1. T. A. Shankoff, Appl. Opt. **7** (10), 2101 (1968).
2. C. Solano, R. A. Lessard, and P. C. Roberge, Appl. Opt. **24** (8), 1189 (1985).
3. T. Kubota, T. Ose, M. Sosaki, and K. Honda, Appl. Opt. **15** (2), 556 (1976).
4. T. Kubota and T. Ose, Appl. Opt. **18** (15), 2538 (1979).
5. R. Changkakoti, S. S. C. Babu, and S. V. Pappu, Appl. Opt. **27** (2), 324 (1988).
6. R. Changkakoti and S. V. Pappu, Appl. Opt. **28**, 340 (1989).
7. J. Blyth, Appl. Opt. **30**, 1598 (1991).
8. K. Wang, L. Guo, J. Zhu, *et al.*, Appl. Opt. **37** (2), 326 (1998).
9. S. Colixto and R. Lessard, Appl. Opt. **23** (8), 1989 (1984).
10. Yu. N. Denisyuk, N. M. Ganzherli, and I. A. Maurer, Pis'ma Zh. Tekh. Fiz. **21** (17), 51 (1995) [Tech. Phys. Lett. **21**, 703 (1995)].
11. Yu. N. Denisyuk, N. M. Ganzherli, and I. A. Maurer, Proc. SPIE **2688**, 42 (1996).
12. Yu. N. Denisyuk, N. M. Ganzherli, and I. A. Maurer, Opt. Spektrosk. **83** (2), 320 (1997) [Opt. Spectrosc. **83**, 320 (1997)].
13. V. P. Sherstyuk, A. N. Malov, S. M. Maloletov, and V. V. Kalinkin, Proc. SPIE **1238**, 218 (1989).
14. Yu. N. Vygovskiĭ, S. P. Konop, A. N. Malov, and S. N. Malov, Laser Phys. **8** (4), 901 (1998).
15. S. P. Konop, A. G. Konstantinova, and A. N. Malov, Proc. SPIE **2969**, 274 (1996).
16. Yu. N. Vygovskiĭ, P. A. Draboturin, A. G. Konop, *et al.*, in *Laser Application in Science and Technique* (Inst. Fiz. ILT Sib. Otd. Ross. Akad. Nauk, Irkutsk, 1997), pp. 149–159.
17. Yu. N. Denisyuk, Zh. Tekh. Fiz. **60** (6), 59 (1990) [Sov. Phys. Tech. Phys. **35**, 669 (1990)].

Translated by P. Pozdeev

Technical Physics Letters, Vol. 26, No. 8, 2000, pp. 710–712. Translated from Pis'ma v Zhurnal Tekhnicheskoĭ Fiziki, Vol. 26, No. 16, 2000, pp. 30–34.

Dissociation of Nitrogen Oxides under the Action of Pulsed Electron Beams

G. V. Denisov, Yu. N. Novoselov, and R. M. Tkachenko

Institute of Electrophysics, Ural Division, Russian Academy of Sciences, Ekaterinburg, Russia

e-mail: nov@iep.uran.ru

Received March 23, 2000

Abstract—The decomposition of nitrogen oxides NO_x in model gas mixtures ionized by microsecond pulsed electron beams was studied. The main decomposition mechanism is the dissociation of oxides caused by the interaction with atomic nitrogen. The final decomposition products are molecular oxygen and nitrogen. © *2000 MAIK "Nauka/Interperiodica".*

Smoky waste gases of thermal power plants contain a considerable proportion of toxic nitrogen oxides (NO and NO_2). The task of purification of the waste gases from toxic impurities has stimulated extensive investigations into the possibility of decomposing these impurities by electrophysical methods. These methods are based on the laws of chemical reactions in gases ionized under the action of various electric discharges and electron beams. In particular, these tasks were solved by using continuous-mode accelerators forming electron beams with a current density from 10^{-9} to 10^{-5} A/cm^2 [1–3]. This electron-beam treatment provides for a high degree (98–100%) of purification from nitrogen oxides, with the specific energy spent for the removal of one toxic molecule being 15–20 eV [4].

A mechanism for nitrogen oxide removal with the aid of continuous electron beams is sufficiently well studied (see, e.g., [5]). In the presence of water vapor, the electron-beam ionization leads to the formation of free radicals of the $O^{\bullet}$, $OH^{\bullet}$, and $O_2H^{\bullet}$ types. These radicals react with nitrogen oxides to form nitric acid. Upon adding ammonia, the acid forms an ammonium salt (NH_4NO_3) in the form of a solid powder trapped by filters. This purification mechanism, involving the formation of some product that has to be trapped and removed, implies a significant complication of the purification technology. Indeed, additional equipment (besides the electron accelerator and reaction chamber) is necessary for the supply of ammonia and the removal of powdered ammonium salts.

The elemental composition of nitrogen oxides coincides with that of pure air. In connection with this, the most economically efficient purification system is apparently that based on the nitrogen oxide conversion directly into molecular oxygen and nitrogen. The purpose of this work was to study the possibility of this conversion using a gas mixture modeling typical smoky waste gases.

The experiments were conducted on a setup comprising an electron accelerator; a plasmachemical reaction chamber; and a system providing preparation, admission, and monitoring of the gas mixture studied. The accelerator (analogous to that described in [6]) formed a pulsed electron beam with the following parameters: beam cross section, 10×100 cm; electron energy, 200 keV; pulse duration (FWHM), 5 μs; beam current density behind the output foil, 4.5×10^{-3} A/cm^2. The electron beam entered the reaction chamber with as volume of 12 dm^3.

A model gas mixture was prepared from pure molecular nitrogen (N_2), oxygen (O_2), and nitric oxide (NO) in a special mixer and then admitted to the plasmachemical reaction chamber, which was preliminarily evacuated and doubly washed with pure nitrogen. The gas mixture composition was as follows: nitrogen, 80–90%; oxygen, 0–20%, and nitric oxide, 100–1000 ppm. The qualitative and quantitative composition of the mixture was monitored using a TESTO-350 gas analyzer. The error of the concentration determination did not exceed 3%. Upon entering the plasmachemical chamber, the gas mixture was forced to flow over a closed loop during the entire experimental cycle. During circulation of the mixture without electron-beam irradiation, the NO component interacted with oxygen and exhibited the natural chemical oxidation to NO_2. After some time, when a dynamic equilibrium between nitrogen oxides was established, the gas mixture was treated with the electron beam. The treatment consisted in irradiating the gas by series of 50 electron-beam pulses.

Typical plots of the concentrations of nitrogen oxides [NO], [NO_2], and [NO_x] (where [NO_x] = [NO] + [NO_2]) versus the total number N of the electron-beam pulses are depicted in the figure. Curves *1*, *2*, and *4* were obtained for a gas mixture with an oxygen content of 10%, and curve *3* refers to a mixture free of oxygen.

1063-7850/00/2608-0710$20.00 © 2000 MAIK "Nauka/Interperiodica"

As seen, all the curves reflect gradual decrease in the corresponding oxide concentration with the total number of electron-beam pulses. This pattern differs from that reported [7] for mixture with the NO content above 1200 ppm, where decay in the NO_2 concentration with increasing N was preceded by an initial growth stage. Apparently, irradiation of a mixture containing a small amount of nitric oxide is either not accompanied by the oxidation to NO_2 or the amount of NO_2 formed is below the sensitivity level of the measuring instrument. It should be noted that experiments with oxygen-free gas mixtures containing small amounts of NO showed a decrease in the NO concentration without any NO_2 formation.

According to the commonly accepted notions about the free-radical mechanism of NO_x oxidation [5], a decrease in the concentration of nitrogen oxides in the mixture must be accompanied by the formation of nitric acid as the final reaction product; however, our experiments revealed the presence of nitric acid in very small, virtually trace amounts. This result is evidence that the mechanism of nitrogen oxide removal is not restricted to the oxidation process. Moreover, the electron-beam treatment of the oxygen-free mixture (see figure, curve *3*) was also accompanied by a decrease in the NO content.

A mechanism alternative to the free-radical nitrogen oxide reaction with the formation of nitric acid as the final product is offered by the NO_x dissociation yielding atomic species, followed by the formation of molecular nitrogen and oxygen. As is known, the energy of an electron beam injected into a nitrogen–oxygen mixture is spent not only for ionization and excitation of the mixture component but for the nitrogen dissociation as well. A calculation of the electron beam energy distribution in air performed by the Monte-Carlo method showed that the dissociation of molecular nitrogen by the direct electron impact mechanism takes about 2.5% of the total beam energy. Estimates showed that the concentration of atomic nitrogen formed upon the dissociation of N_2 molecules caused by the direct impact of high-energy electrons under our experimental conditions does not exceed 10^{12} cm^{-3}. The concentration of atomic nitrogen in the gas mixture may significantly increase at the expense of dissociative recombination of the N_2^+ ions. Our calculation showed that about 33.5% of the beam energy is spent the formation of these ions. The corresponding concentration of molecular nitrogen ions is ~10^{13} cm^{-3}. The dissociative recombination of N_2^+ leads to the formation of atomic nitrogen with a concentration of ~8×10^{13} cm^{-3}.

The subsequent reactions involving atomic nitrogen and impurity molecules and leading to a decrease in the concentration of nitrogen oxides are as follows:

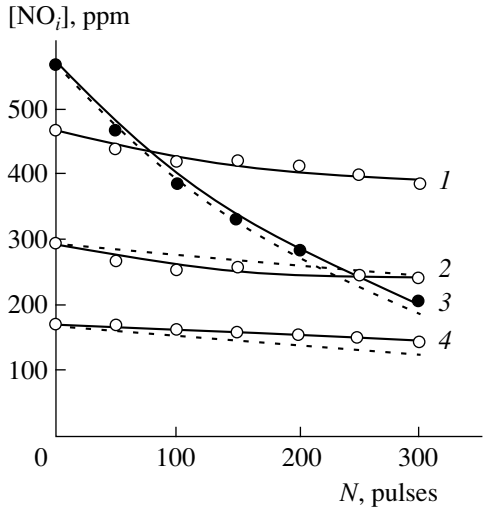

Plots of the concentration of nitrogen oxides [NO_i] ($i = 1, 2, x$) versus the number of electron-beam pulses for gas mixtures (*1*, *2*, *4*) containing 10% of oxygen and (*3*) free of oxygen: (*1*) NO_x; (*2*, *3*) NO; (*4*) NO_2. Solid lines connect the experimental points, dashed lines show the results of calculations.

$$N + NO \longrightarrow N_2 + O, \quad (1)$$

$$N + NO_2 \longrightarrow 2NO, \quad (2)$$

$$N + NO_2 \longrightarrow N_2 + 2O, \quad (3)$$

$$O + NO_2 = O_2 + NO. \quad (4)$$

The atomic oxygen and nitrogen form the corresponding molecular species. The results of calculation of the decreasing concentrations of nitrogen oxides according to Eqs. (1)–(4) are depicted in the figure by dashed lines. The calculations were performed using the reaction rate constants from [8]. As seen, Eqs. (1)–(4) rather satisfactorily describe the experimental dependences.

Thus, we have demonstrated that purification of the smoky waste gases from nitrogen oxides by using pulsed electron beams is based primarily on the mechanism of NO_x dissociation rather than oxidation. The dissociation reactions are most effective in the gas mixtures with a small oxygen content. The process of eliminating nitrogen oxides from the gas mixtures can be described as follows. The electron-beam irradiation of a gas mixture leads to the formation of N_2^+ ions, which exhibit dissociative recombination resulting in the formation of a sufficiently high concentration of atomic nitrogen. The interaction of atomic nitrogen with nitrogen oxides leads to their dissociation with the eventual formation of molecular oxygen and nitrogen. This mechanism of the toxic impurity elimination can be

used to develop a wasteless electrophysical technology for the purification of smoky waste gases.

This work was supported by the International Scientific-Technological Center, grant no. 271.

REFERENCES

1. S. Masuda, Pure Appl. Chem. **60** (5), 727 (1988).
2. E. L. Neau, IEEE Trans. Plasma Sci. **22** (1), 2 (1994).
3. N. Frank and S. Hirano, Radiat. Phys. Chem. **35**, 416 (1990).
4. J. C. Person and D. O. Ham, Radiat. Phys. Chem. **31** (1–3), 1 (1988).
5. A. A. Valuev, A. S. Kaklyugin, G. É. Norman, *et al.*, Teplofiz. Vys. Temp. **28** (5), 995 (1990).
6. K. A. Garusov, D. L. Kuznetsov, Yu. N. Novoselov, and V. V. Uvarin, Prib. Tekh. Éksp. **3**, 180 (1992).
7. G. V. Denisov, Yu. N. Novoselov, and R. M. Tkachenko, Pis'ma Zh. Tekh. Fiz. **24** (4), 52 (1998) [Tech. Phys. Lett. **24**, 146 (1998)].
8. V. N. Kondrat'ev, *Rate Constants of Vapor-Phase Reactions* (Nauka, Moscow, 1970).

Translated by P. Pozdeev

Technical Physics Letters, Vol. 26, No. 8, 2000, pp. 713–715. Translated from Pis'ma v Zhurnal Tekhnicheskoĭ Fiziki, Vol. 26, No. 16, 2000, pp. 35–40.

Optico-Acoustic Characterization of the Fractal Structure of Radiation from a Laser with Unstable Resonator

M. L. Lyamshev

Research Center of Wave Phenomena, Institute of General Physics, Russian Academy of Sciences, Moscow, 117942 Russia

e-mail: lyamshev@kapella.gpi.ru

Received March 28, 2000

Abstract—The thermooptical excitation of sound in a liquid by fluctuating laser radiation with sine-modulated intensity is studied theoretically. The intensity is randomly distributed over the beam cross section. It is assumed that the random processes are homogeneous and that the spatial spectrum of intensity fluctuations obeys a power fractal law. Possibilities for the optico-acoustic characterization of the fractal radiation structure of a laser with unstable resonator are discussed. © *2000 MAIK "Nauka/Interperiodica".*

Chaotic operation of lasers has attracted much attention in recent years. For example, Loskutov *et al.* [1] studied the routes to chaos and the properties of chaotic oscillation in an unstable resonator of a nonuniformly pumped fast-flow laser. A scheme of information chaos using an optical communications channel based on synchronized chaotic lasers with random pumping was considered in [2].

Key features of a nonlinear dynamic system can be described in terms of scaling and the correlation dimension or fractal dimension [3]. The scaling may occur in the emission harmonics of a plasma produced by intense laser radiation [4]. It was also demonstrated that the modal structure of the radiation from a laser with unstable resonator has a fractal character [5]. For a slit-aperture laser, the output intensity distribution was found to have a fractal dimension of $D = 1.6$. For a circular-aperture laser, the fractal dimension was evaluated at $D = 1.3$.

It was interesting to find out whether it is possible to examine the fractal structure of radiation of a laser with unstable resonator by optico-acoustic techniques. This study addresses the thermooptical excitation of sound in a liquid by laser radiation with sine-modulated intensity. The intensity fluctuations of the radiation are distributed in a random fractal fashion over the beam cross section. The effect of spatial and temporal laser intensity fluctuations on the excitation of sound in a liquid has already been studied in [6], but the charter of distribution was not specified.

Consider a laser beam incident on the interface between the atmosphere and a liquid which occupy the upper and the lower half-space, respectively. Let us define the Cartesian coordinates (x, y, z) in such a way that the origin lies on the interface and the z-axis is directed downward along the beam. The absorbed radiation produces thermal sources of sound in the liquid. According to [7], the laser-induced thermooptical sound excitation obeys the equation

$$(\Delta + k^2)\mu = i\frac{\kappa m\omega}{C_p}A\mu I(x, y)\exp(-\mu z). \qquad (1)$$

Here, p is the acoustic pressure; κ is the coefficient of volumetric expansion; C_p is the heat capacity; μ is the optical absorption coefficient; A is the transmission coefficient of the interface; m is the degree of intensity modulation; $I(x, y)$ is the intensity distribution over the beam cross section at the interface; and $k = \omega/c$, with c being the speed of sound in the liquid. We assume that $A = 1$. The time-dependent factor $\exp(-i\omega t)$ is then omitted.

The solution to Eq. (1) can be represented in the form [7]

$$p(r) = i\frac{\kappa\omega m}{C_p}\mu\int_\Omega I(x', y')\exp(-\mu z') \times \tilde{p}(x', y', z'/x, y, z)dx'dy'dz', \qquad (2)$$

where $\tilde{p}(r'/r)$ is the solution to the boundary-value problem of the diffraction of the field from a point source situated at the point r where the field $p(r)$ is to be determined. Let us consider $p(r)$ in the Fraunhofer region. Then, we have

$$\tilde{p}(r'/r) = \frac{\exp(ikr)}{4\pi r}\{\exp[-i(\alpha x' + \beta y' + \gamma z')] - \exp[-i(\alpha x' + \beta y' - \gamma z')]\}, \qquad (3)$$

where $\alpha^2 + \beta^2 + \gamma^2 = k^2$ and $r = (x^2 + y^2 + z^2)^{1/2}$.

Let the laser intensity distribution be a random function of the type $I(x, y) = I_0 f(x, y)$, where $\langle f(x, y)\rangle = 0$. Furthermore, assume that the random processes are homogeneous.

Upon substituting Eq. (3) into Eq. (2) and integrating the result with respect to z, we arrive at the following expression for the mean-square acoustic pressure $\langle |p(r)|^2 \rangle$:

$$\langle |p(r)|^2 \rangle = \frac{\kappa^2 \omega^2 m^2}{C_p^2} \frac{1}{4\pi^2 r^2} \frac{\mu^2 \gamma^2}{(\mu^2 + \gamma^2)^2} I_0^2 \sigma \times \int\limits_{\xi\,\eta} B(\xi, \eta) \exp[-i(\alpha\xi + \beta\eta)] d\xi d\eta, \quad (4)$$

where $B(\xi, \eta) = \langle f(x', y') f(x'', y'') \rangle$ is the normalized correlation function of intensity fluctuations; $\xi = |x' - x''|$; $\eta = |y' - y''|$; and σ is the area of the laser spot on the interface. Strictly speaking, the integration with respect to ξ and η is confined to the irradiated interface region. However, if $B(\xi, \eta)$ rapidly decreases within the beam cross section and $B(\infty) = 0$, then the integration can be extended to the interval from $-\infty$ to $+\infty$.

The properties of statistical fractals are often expressed in terms of structural functions (correlation functions) and their spectra. Remarkably, the functions represent power laws. This follows from the scale invariance of fractals [8].

In the context of statistical fractals related to the wave motion, an important characteristic is the power fluctuation spectrum having the form

$$G(q) \sim q^{\delta}, \quad (5)$$

where q is the wavenumber of spatial fluctuations. For objects with a fractal surface, the exponent δ is expressed as

$$\delta = D - 2d, \quad (6)$$

where D is the fractal dimension and d is the dimension of the embedding space.

Let us find the mean-square acoustic pressure in the case of a slit aperture extending along the x-axis. For this system, we can write

$$B(\xi, \eta) = B_1(\xi) B_2(\eta), \quad (7)$$

where $B_2(\eta) \approx 1$ (since the intensity fluctuations can be considered totally correlated in the transverse direction). For the longitudinal direction, the normalized correlation function is expressed as follows [9]:

$$B(\xi) = \frac{1}{2^{\nu - 1}\Gamma(\nu)} \left(\frac{\xi}{\xi_0}\right)^{\nu} K_{\nu}\left(\frac{\xi}{\xi_0}\right), \quad (8)$$

where $\Gamma(\nu)$ is the gamma function, $K_{\nu}(\xi/\xi_0)$ is the modified Bessel function of the second kind (also known as the Macdonald function), and ξ_0 is the longitudinal correlation radius of the intensity fluctuations. Note that $B(0) = 1$, $B(\infty) = 0$, and $B(\xi)_{\xi < \xi_0} \sim (\xi/\xi_0)^{\nu}$. This means that the correlation function has a power form and, hence, can be used for describing the fractal structure of laser intensity fluctuations.

Substituting Eqs. (7) and (8) into Eq. (4) and integrating the result, we obtain

$$\langle |p(r)|^2 \rangle = \frac{\kappa^2 \omega^2 m^2}{C_p^2} \frac{1}{4\pi^2 r^2} \frac{\mu^2 \gamma^2}{(\mu^2 + \gamma^2)^2} I_0 \sigma \eta_0 G(\alpha), \quad (9)$$

where η_0 is the laser spot size on the interface and $G(\alpha)$ is the spectral density of intensity fluctuations. The latter quantity is expressed as

$$G(\alpha) = \frac{\Gamma\left(\nu + \frac{1}{2}\right)}{\sqrt{\pi}\Gamma(\nu)} \frac{\xi_0}{(1 + \alpha^2 \xi_0^2)^{\nu + \frac{1}{2}}}. \quad (10)$$

If $\alpha\xi_0 > 1$, then $G(\alpha)$ obeys a power law (like any statistical fractal):

$$G(\alpha)_{\alpha\xi_0 > 1} \sim \alpha^{-(2\nu + 1)}. \quad (11)$$

Now, consider the case of a circular aperture. Here, Eq. (4) becomes

$$\langle |p(r)|^2 \rangle = \frac{\kappa^2 \omega^2 m^2}{C_p^2} \frac{1}{4\pi^2 r^2} \frac{\mu^2 \gamma^2}{(\mu^2 + \gamma^2)^2} I_0 \pi a^2 G(k_{\perp}), \quad (12)$$

where

$$G(k_{\perp}) = \int\limits_{-\infty}^{+\infty} B(\rho) \exp(-ik_{\perp}\rho) d\rho, \quad (13)$$

$k_{\perp}$ is the horizontal component of the wave vector $\mathbf{k}$, $k_{\perp}^2 = \alpha^2 + \beta^2$, $\bar{\rho} = |\rho' - \rho''|$, and a is the laser beam spot radius on the interface.

Let us write the correlation function $B(\rho)$ in the form of Eq. (8), where ξ is replaced by ρ and ξ_0, by ρ_0, the symbol ρ_0 denoting the correlation radius of intensity fluctuations.

For the spectral density $G(k_{\perp})$ defined by Eq. (13), we have

$$G(k_{\perp}) = \frac{\Gamma(\nu + 1)}{\sqrt{\pi}\Gamma(\nu)} \frac{\rho_0^2}{(1 + k_{\perp}^2 \rho_0^2)^{\nu + 1}}. \quad (14)$$

If $k_{\perp}\rho_0 > 1$, then

$$G(k_{\perp}) \sim k_{\perp}^{-2(\nu + 1)}. \quad (15)$$

To compute the acoustic field in the liquid, one has to evaluate ν for each particular case. Let us set the embedding space dimension $d = 2$ according to the numerical experiment reported in [5]. Then, Eqs. (5), (6), (11), and (15) imply that $\nu = 0.7$ for the slit aperture and $\nu = 0.35$ for the circular aperture. This computation also uses the fact that $D = 1.6$ and $D = 1.3$ for the two cases, respectively [5].

It follows from Eqs. (9)–(11) and (12)–(15) that the fractal structure of the radiation produced by a laser

with unstable resonator can be examined by optico-acoustic techniques. Indeed, assume that $\mu \ll k$, $k\sin\theta\xi_0 > 1$, and $kl \gg 1$ or that $k\sin\theta\rho_0 > 1$ and $ka \gg 1$, where l is the length of the slit aperture and a is the laser beam spot radius on the interface. Then, the mean-square sound pressure at a point of interest in the $x0z$-plane

$$\langle |p(r)|^2 \rangle \sim Cq^{\delta} \sim k^{\delta}, \tag{16}$$

where C is a constant determined by the parameters of the problem.

The exponent is expressed as

$$\delta = \frac{\log \langle |p(r)|^2 \rangle}{\log k}. \tag{17}$$

Varying the modulation frequency, one obtains the dependence $\delta = \varphi(k)$ and hence $D \sim \varphi(k)$.

This study was funded by the Russian Foundation for Basic Research, project no. 99-02-16334.

REFERENCES

1. A. Yu. Loskutov, A. V. Mushenkov, A. I. Odintsov, *et al.*, Kvantovaya Élektron. (Moscow) **29** (2), 127 (1999).
2. A. P. Napartovich and A. G. Sukharev, Kvantovaya Élektron. (Moscow) **25** (1), 85 (1998).
3. F. C. Moon, *Chaotic and Fractal Dynamics* (Wiley, New York, 1992).
4. V. P. Silin, Kvantovaya Élektron. (Moscow) **26** (1), 11 (1999).
5. G. P. Karman and J. P. Woerdman, Opt. Lett. **23** (24), 1909 (1998).
6. F. V. Bunkin, *Selected Works* (Nauka, Moscow, 1999).
7. L. M. Lyamshev, *Thermooptical Laser Sound Generation* (Nauka, Moscow, 1989).
8. M. Schroeder, *Fractals, Chaos, Power Laws* (Freeman, New York, 1990).
9. V. I. Tatarskiĭ, *Theory of Fluctuational Phenomena during the Sound Propagation in Turbulent Atmosphere* (Akad. Nauk SSSR, Moscow, 1959).

Translated by A. Sharshakov

Technical Physics Letters, Vol. 26, No. 8, 2000, pp. 716–717. Translated from Pis'ma v Zhurnal Tekhnicheskoĭ Fiziki, Vol. 26, No. 16, 2000, pp. 41–45.

Thermal Fluctuation Electromagnetic Field in the Medium as the Driving Force of Its Magnetosensitivity

Yu. A. Kartashov and I. V. Popov

North-West Correspondence Polytechnic Institute, St. Petersburg

Received July 23, 1999

Abstract—The so-called *kT* problem relating the magnetosensitivity and thermal oscillations of a condensed medium is solved. An external magnetic field acting upon a free charged particle occurring in a thermal fluctuation electromagnetic field inside the condensed medium gives rise to a rotational moment having the same direction for charged particles of the same sign. The rotational moment is proportional to the thermal energy *kT* and can substantially increase under the cyclotron resonance condition. © *2000 MAIK "Nauka/Interperiodica".*

Theories interpreting the magnetosensitivity of condensed media [1], including the biological ones [2], encounter a stumbling block known as the *kT* problem. The problem is that the potential energy of a magnetosensitive particle (molecule, atom, proton, etc.) in a magnetic field (MF) is very small in comparison with its thermal energy, even in the case of rather strong MFs.

This work attempts to solve this problem based on the concept of a thermal electromagnetic field (EMF) considered as the driving force of the charged particle motion. It is demonstrated that an external magnetic field gives rise to a rotational moment the direction of which is determined by the particle charge sign. This phenomenon is analogous to the effect of a weak electric field (EF) on charged particles in a conducting medium, adding a small drift velocity against the background of very large thermal velocities.

The motion of a particle (molecule, atom, proton, etc.) with the charge q and the mass m_0 in an EMF is described by the equation

$$m_0\frac{d\mathbf{V}}{dt} = -\frac{m_0}{\tau}\mathbf{V} + q\mathbf{V}\times\mathbf{B} + q\mathbf{B}, \qquad (1)$$

where $\mathbf{V}$ is the particle velocity, τ is its relaxation time in a given medium, $\mathbf{B} = \mathbf{B}_0 + \tilde{\mathbf{B}}$ ($\mathbf{B}_0$ and $\mathbf{B}$ are the constant and alternating components of the magnetic induction, respectively, $\mathbf{B}_0 \parallel \tilde{\mathbf{B}}$), and $\mathbf{E}$ is the equilibrium thermal fluctuation EF strength inside the medium.

In the spectral representation, a solution to Eq. (1) is as follows:

$$\tilde{\mathbf{V}} = \frac{q}{m_0}\exp\left(-\frac{t}{\tau} + i\frac{q}{m_0}\int_0^t B dt'\right)$$
$$\times\int_{-\infty}^{\infty}\tilde{e}(\omega)d\omega\left[\exp\left(i\omega t' + \frac{t'}{\tau} + i\frac{q}{m_0}\int_0^t B dt''\right)dt\right] \qquad (2)$$
$$+\tilde{V}_0\exp\left(-\frac{t}{\tau} - i\frac{q}{m_0}\int_0^t B dt'\right),$$

where the z axis of the Cartesian coordinates is parallel to $\mathbf{B}_0$; $\tilde{V} = V_x + iV_y$, $\tilde{V}_0$ is the value of $\tilde{V}$ at $t = 0$; and $\tilde{E} = E_x + iE_y = \int_{-\infty}^{\infty}\tilde{e}(\omega)\exp(i\omega t)d\omega$.

Consider a periodic MF. For $t \gg \tau$, the solution (2) can be rewritten as

$$\tilde{V} \simeq \frac{q}{m_0}\sum_{\nu,\, n=-\infty}^{\infty} b_n b_\nu^*\exp(-i\nu\Omega t)$$
$$\times\int_{-\infty}^{\infty}\tilde{e}(\omega)\frac{\exp[i(\omega + n\Omega)t]}{1/\tau + i(\omega + \Omega_c + n\Omega)}d\omega, \qquad (3)$$

where

$$\sum_{-\infty}^{\infty} b_n\exp(in\Omega t) = \exp\left(i\frac{q}{m_0}\int_0^t\tilde{B}dt'\right),$$

$\Omega_c = (q/m_0)B_0$ is the cyclotron frequency, and Ω is the MF oscillation frequency.

The ensemble-averaged z-component of a rotational moment due the Coulomb forces is given by the expression

$$\mathbf{M}_z = (\overline{\mathbf{r} \times q\mathbf{E}})_z = q(\overline{xE_y - yE_x}) = (q/2i)(\overline{\tilde{\rho}^* \tilde{E} - \tilde{\rho}\tilde{E}^*}), \quad (4)$$

where $\mathbf{r}$ is the particle radius-vector, $\tilde{\rho} = x + iy = \int \tilde{V}\, dt$, and the asterisk denotes complex conjugation.

Averaging in Eq. (4) with an allowance of the fluctuation–dissipation theorem [3] yields the expression

$$\overline{\tilde{e}^*(\omega)\tilde{e}(\omega')} = \frac{2}{3} g_E(\omega)\delta(\omega - \omega'),$$

where

$$g_E(\omega) = 3m_0\theta(\omega, T)/\pi q^2\tau,$$

$$\theta(\omega, T) = \hbar\omega/2 + \hbar\omega/[\exp(\hbar\omega/kT) - 1]$$

is the mean quantum oscillator energy. In order to simplify the mathematical transformations, below we assume that $\hbar\omega \ll kT$. Then, the rotational moment can be represented as

$$\overline{\mathbf{M}}_z = -\frac{2kT}{\tau}\left\{ \sum_{\nu,\, n = -\infty}^{\infty} b_n^* b_\nu \frac{\exp[-i(n-\nu)\Omega t]}{1/\tau - i(\Omega_c + \nu\Omega)} - \sum_{\nu,\, n = -\infty}^{\infty} b_n b_\nu^* \frac{\exp[i(n-\nu)\Omega t]}{1/\tau + i(\Omega_c + \nu\Omega)} \right\}. \quad (5)$$

In particular, in the case when only the stationary MF is operative ($b_n = \delta_{n0}$, where δ_{n0} is the Kronecker symbol), expression (5) is reduced to

$$\overline{M}_z = -\frac{2kT\Omega_c\tau}{1 + \Omega_c^2\tau^2}. \quad (6)$$

Note that the sign in Eqs. (5) and (6) indicates that the direction of $\overline{M}_z$ for the positively charged particles is opposite to that of $\mathbf{B}_0$. The above expressions show that either a periodic (at the frequency of the external MF) or stationary (when the alternating MF component is absent) rotational moment $\overline{M}_z$ proportional to the thermal energy kT acts upon a free charged particle. It follows from Eq. (5) that $\overline{M}_z$ substantially increases if the condition

$$\Omega_c + n\Omega = 0 \quad (7)$$

is met and the relaxation time is sufficiently large $\tau \gg 1/\Omega_c$. Expression (7) represents a condition of the experimentally observed cyclotron resonance [4].

The moment $\overline{M}_z$ generates rotational moments in the bond network of the medium (e.g., in the H-bond network), thus changing its structure. Since the moment is proportional to kT, the MF effect on the structure increases with the temperature (until the structure is destroyed by the fluctuation oscillations). Thus, there is no sense in the kT problem since there is no contradiction between thermal oscillations and magnetosensitivity of the medium. On the contrary, the magnetosensitivity is related to thermal oscillations.

Note that the rotational moment under consideration presumably accounts for the phenomenon of water magnetization [1] upon its motion in MF, since $\overline{M}_z$ decreases the turbulence microscale to change the adsorption and other properties of water. The phenomenon of the "water memory" [5] is possibly related to the effect of the rotational moments on a system exhibiting the Bjerrum defects. Since life on Earth appeared and evolved under the influence of the geomagnetic field, the $\overline{M}_z$ variation under the conditions of a hypomagnetic field may substantially perturb the organic life structure [6].

The allowance of an amplitude-modulated MF in Eqs. (2) and (4) yields a cyclotron resonance at the modulation frequency in agreement with the experimental observations [7].

It is clear that a thermal fluctuation MF also induces a rotational moment in the medium. In the general case, this moment is proportional to kT in a higher power than that in Eq. (5).

Note, finally, that a rotational moment acts upon a charged particle in a magnetic field regardless of the nature of forces causing oscillations of the particle.

REFERENCES

1. V. I. Klassen, *Magnetization of Aqueous Systems* (Khimiya, Moscow, 1982).
2. V. V. Novikov and M. N. Zhadin, Biofizika **39** (1), 45 (1994).
3. S. M. Rytov, *Introduction to Statistical Radiophysics* (Nauka, Moscow, 1966).
4. A. R. Liboff, S. D. Smith, and B. R. McLeod, in *Mechanistic Approaches to Interactions of Electric and Electromagnetic Fields with Living System* (Plenum, New York, 1987), p. 109.
5. M. V. Berezin, R. R. Lyapin, and A. M. Saletskiĭ, Preprint No. 21, MGU Fiz. Fak. (Moscow State University, Physical School, Moscow, 1988).
6. V. I. Kopanev and A. V. Shakula, *Effect of Hypomagnetic Field on Biological Objects* (Nauka, Leningrad, 1985).
7. W. R. Adey, Proc. IEEE **68** (1), 119 (1980).

Translated by A. Chikishev

Technical Physics Letters, Vol. 26, No. 8, 2000, pp. 718–720. Translated from Pis'ma v Zhurnal Tekhnicheskoĭ Fiziki, Vol. 26, No. 16, 2000, pp. 46–51.

Conical Waves Producing Longitudinal Power Flows

I. A. Kolmakov

Received September 29, 1999

Abstract—A conical electromagnetic wave converging to its axis is studied theoretically. It is demonstrated that the wave produces an intense self-accelerating flow of energy (momentum). Conical waves may find various applications such as in the acceleration of particles, the generation of high-power pencil beams, the transformation of simultaneously written spatial data into a time waveform, the measurement of flow rate, etc. It is noted that conical waves could set the stage for the manifestation of unknown properties of matter. © *2000 MAIK "Nauka/Interperiodica".*

This paper concerns an unexplored object of wave science: a conical wave (CW) converging to its axis. The gradient structure of such waves causes a progressive self-compression of the field near the axis (from the vertex to the base of the cone). In general, the process is accompanied by a motion accelerating in the longitudinal direction. This property enables one to produce an intense pencil flow of energy (momentum) by creating an appropriate distribution of electric current or acoustic pressure over the radiator aperture.

CWs may be acoustic or electromagnetic waves. It is conceivable that there may be CWs of some other nature. The CW radiator has the shape of a truncated cone that emits in the direction of its inward normal (so as to focus the CW). It is necessary that all points of the radiator surface emit simultaneously so that the wave vector be orthogonal to the CW front. In acoustics, this is achieved with electroacoustic (piezoceramic, etc.) radiators and the CWs can be visualized by the shadow or interference methods (see, e.g., [1, 2]). In the case of electromagnetic waves, the requirement of simultaneous emission calls for a specially designed radiator, and there seems to be no visualization techniques other than indirect ones. Nevertheless, theoretical studies revealed that there are general laws governing both acoustic and electromagnetic CWs. This fact may facilitate research into the general aspect as well as the electromagnetic aspect of the problem.

The present study concentrates on electromagnetic CWs, the notation being borrowed from [3]. It is pertinent to note that the velocity of an energy flow near the axis, which is dealt with in what follows, has nothing in common with the phase or group velocity of light. The energy flow arises because a CW acts as a conical plunger that both focuses and accelerates the wave energy in the direction of the CW axis. The figure sketches (*1*) a radiator and (*2*) a CW at the instant when the vertex of the cone is at the origin, the angle between the generatrix and the axis being denoted by θ_0. The arrows indicate the directions of the current density **j**, the fields **E** and **H**, and the wave vector **k**. On the conical surface of the CW, the magnitudes **E** and **H** are maximum. For the sake of simplicity, assume that **E** and **H** vary in a sinusoidal fashion in the direction of the inward normal l_n and that θ_0 is small.

Consider the focusing of the CW. While a CW equiphase surface is at a distance from the origin such that the energy flow produced by the compression has no effect, the velocity of the surface in the direction of l_n equals that of light, c; the velocity along the $0Z$-axis is $v_{0Z} = c/\sin\theta_0$; and the velocity of the intersection point of the radial plane and the equiphase surface is $v_{0R} = c/\cos\theta_0$. The "gradient" compression (see below) of the interior CW field arises in the vicinity of the origin and then spreads to distant CW regions. This adds to the velocity of the energy flow (mainly) along the $0Z$-axis: $v_Z = v_{0Z} = \text{const}$ at $Z = 0$, whereas $v_Z \geq v_{Z0}$ at $Z > 0$. Thus, the focusing of a CW is accompanied by the formation of a longitudinal self-accelerating flow of

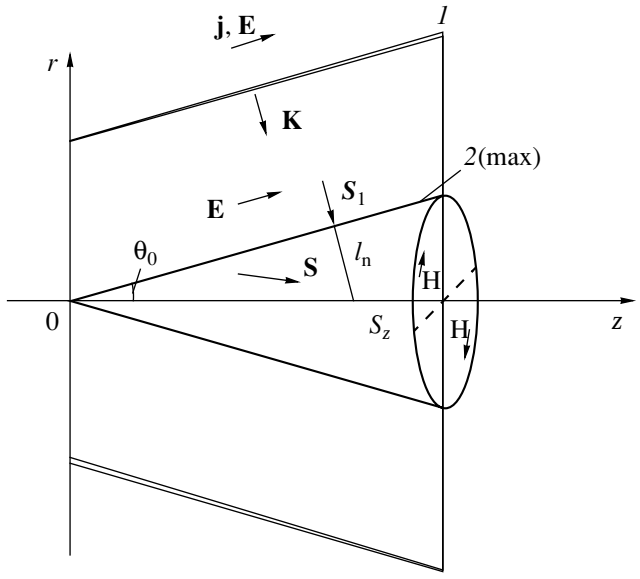

Figure.

1063-7850/00/2608-0718$20.00 © 2000 MAIK "Nauka/Interperiodica"

energy (momentum) near the 0*Z*-axis, with the flow velocity growing toward the 0*Z*-axis. A CW must have a gradient structure for the flow to be efficient, e.g., to have a sufficient duration. Specifically, the field must increase in going from the origin along the 0*Z*-axis and from the surface of field maximum (the conical surface in figure) toward the 0*Z*-axis.

Now, we outline how to solve the problem of a longitudinal CW field. The first is to find a CW field in the form of a harmonic wave traveling in the direction of l_n. This stage of evolution goes on before the interior CW region begins contracting. It is characterized by the relations $\mathbf{S}_1 \uparrow\downarrow l_n$ and $W_1 = S_1 c$, where $\mathbf{S}_1$ is Poynting's vector and W_1 is the energy density. Then, the field compression is described in terms of $\mathbf{S}$ and the energy flow velocity v with the initial condition in the form of expressions for $\mathbf{S}_1$ and W_1. Below, we present the fragments of a solution procedure to substantiate the above ideas and reproduce the necessary expressions.

Solving the first part of the problem reduces to treating a CW wave equation derived from Maxwell's equations in the cylindrical coordinates. The solution has the form

$$E_l = E_l(0)\sqrt{l_n L_n^{-1}}\exp\{-ik(L_n - l_n + ct)\};$$

$$H_\varphi = E_l(0)\cos 2\theta_0\sqrt{l_n L_n^{-1}} \times\{(2kL_n)^{-1}\sin[k(l_n - L_n - ct)] - \cos[k(l_n - L_n - ct)]\}, \quad (1)$$

where l designates the direction along and parallel to the cone; L_n are current values of the coordinates of the points in the interior region of the CW, counted in the direction of l_n; and l_n are the values of L_n on the boundary (i.e., on the cone surface). The components of the Maxwell's tension tensor are as follows:

$$\sigma_{ZZ} = (8\pi)^{-1}(E_Z^2 - E_R^2 - H_\varphi^2);$$
$$\sigma_{RR} = (8\pi)^{-1}(E_R^2 - E_Z^2 - H_\varphi^2);$$
$$\sigma_{RZ} = \sigma_{ZR} = (4\pi)^{-1}E_R E_Z; \quad (2)$$
$$\sigma_{\varphi\varphi} = (8\pi)^{-1}(H_\varphi^2 - E_R^2 - E_Z^2);$$
$$\sigma_{R\varphi}, \sigma_{\varphi R}, \sigma_{Z\varphi}, \sigma_{\varphi Z} = 0;$$

where E_R, E_Z, and H_φ are described by Eqs. (1) and (2). The field compression and the energy density are given by the formulas

$$|\mathbf{S}_1| = 2N_1 c\cos 2\theta_0\{(4kL_n)^{-1}\sin(2X) - \cos^2(X)\};$$
$$W_1 = N_1\{2\cos^2\theta_0\cos^2(X) + (2k_{L_n})^{-2}\cos 2\theta_0[\sin(X) - 4kL_n\cos(X)]\sin(X)\}, \quad (3)$$

where $N_1 = E_l^2(0)l_n(8\pi L_n)^{-1}$ and $(X) = (l_n - L_n - ct)$.

It is seen that Eqs. (1)–(3) completely define the CW field before the compression stage.

The second part of the problem is solved with the help of the energy and momentum conservation laws: $\partial T_i^k/\partial X^k = 0$. Let us integrate the corresponding equations over the region bounded by the conical surface, taking into account that, during the focusing, the region contracts with a speed equal to c. For example, S_Z in a three-dimensional space is found as follows:

$$\int \dot{S}_Z dV(t) = \oint\{\sigma_{ZR} df_R + R^{-1}\sigma_{Z\varphi} df_\varphi + \sigma_{ZZ} df_Z\}. \quad (4)$$

Deriving a solution obtained from Eq. (4), we have to integrate it using Eqs. (2) with respect to time subject to initial condition (3) for $t = 0$. Applying the mean-value theorem, we arrive at

$$\tilde{S}_Z = \frac{3cE_l^2(0)l_n}{8\pi\sin\theta_0}\left\{\frac{\cos 2\theta_0}{12kL_n^2}[1 - \cos[2k(l_n - L_n)]] + \frac{1}{r^2 z}\left\{ct[b_1] + \frac{c^2t^2}{2}[b_2] + \frac{c^3t^3}{3}[b_3] + \frac{c^4t^4}{2}[b_4]\right\}\right\}, \quad (5)$$

where

$$[b_1] = \frac{z}{\cos\theta_0} - r\left(1 + \frac{a_2}{2}\right) - \frac{a_2}{2}\left(l_n + \frac{1}{4k^2 r^0(2\cos\theta_0)^2}\right),$$

$$[b_2] = \frac{3(r - r^0)}{z\sin\theta_0}\left(1 + \frac{a_2}{2}\right) - \frac{6}{\sin\theta_0} - \frac{1}{\cos\theta_0}\left[1 + \frac{1}{2}\left(\frac{3a}{z\sin\theta_0}\left(l_n + \frac{1}{16k^2 r^0\cos\theta_0}\right) + 1 + \frac{l_n}{4r^0\cos\theta_0}\right)\right],$$

$$[b_3] = -\frac{3}{z\sin\theta_0}\left(1 + \frac{1}{\cos\theta_0} + \frac{a_2}{2}\right),$$

$$[b_4] = a_1 k^2\left(1 - \frac{3l_n}{z\sin\theta_0}\right)\cos\theta_0,$$

$$r^0 < r, \quad a_1 = (1 + \cos 2\theta_0)\cos 2\theta_0, \quad a_2 = \cos^2 2\theta_0.$$

Equation (5) indicates that $\tilde{S}_Z$ is proportional to r^{-2} and $\sin^{-1}\theta_0$. In the context of a linear approximation with respect to t, the flow density rapidly rises with time. Taking into account nonlinear terms reveals that the growth slows down to some extent after a time. The reason is that the integration procedure was linearized and, more importantly, that the amplitude was assumed to be uniform over the radiator surface. If one aims to produce an accelerating flow or at least to maintain a steady velocity, then the radiator field must increase

with Z (according to a certain law), as mentioned above.

The expression for $\tilde{S}_\varphi$ shows that the flow rotates about the $0Z$-axis. The rotation becomes more and more intense as r approaches zero. The component $\tilde{S}_R$ varies proportionally to $\cos^{-1}\theta_0$ so that $\tilde{S}_Z \gg \tilde{S}_R$ for small r. During the compression, $\tilde{S}_R$ first rises then drops, decreasing more rapidly than does $\tilde{S}_Z$. A more detailed description of CWs can be achieved with the help of numerical methods, whose algorithm is evident from the preceding. The velocity of the energy flow in the $0Z$-direction, defined by $v_Z^n = \tilde{S}_Z W^{-1}$, is expressed as follows:

$$v_Z^n = cE_l^2(0)(8\pi\tilde{W}\sin\theta_0)^{-1} \times \{l_n r^3 z(6kL_n^2)^{-1}\sin\theta_0\cos^2\theta_0 + 2rl_n\{f(t)\}\sin^2\theta_0\cos^{-1}\theta_0\}. \quad (6)$$

Here, $f(t)$ denotes the expression in braces appearing in Eq. (4). The expression for $\tilde{W}$ is omitted because it is rather cumbersome. It follows from Eq. (6) that v_z^n grows with time, since the denominator increases at a lower rate than does the numerator; all the comments on Eq. (5) apply to v_Z^n as well.

In conclusion, converging CWs may find applications in many areas. For example, they could be used for particle acceleration. (The advantages of CW acceleration over conventional approaches [4] has been demonstrated above.) The technique presented here could also serve to generate high-power pencil beams of electromagnetic radiation. Furthermore, it suggests the idea for a novel device that transforms data from the form of a spatial distribution (written simultaneously onto a CW equiphase surface) into the form of a time-dependent quantity. CWs offer a promising means of producing the echo effects [5], including a change in the radiation direction. Other potential areas of application are flowmeters [6], medicine, and some other technologies. Finally, CWs could set the stage for the manifestation of yet unknown properties or types of matter.

REFERENCES

1. S. A. Abrukov, *Shadow and Interference Methods for the Investigation of Optical Inhomogeneities* (Kazan. Univ., Kazan, 1962).
2. D. Holder and R. North, *Schlieren Methods* (H. M. Stationary Off., London, 1963; Mir, Moscow, 1966).
3. L. D. Landau and E. M. Lifshitz, *The Classical Theory of Fields* (Nauka, Moscow, 1973; Pergamon, Oxford, 1975).
4. A. N. Matveev, *Electrodynamics and Relativity Theory* (Vysshaya Shkola, Moscow, 1964).
5. I. A. Kolmakov and N. N. Antonov, Fiz. Plazmy **18** (10), 1372 (1992) [Sov. J. Plasma Phys. **18**, 708 (1992)].
6. I. A. Kolmakov, Pis'ma Zh. Tekh. Fiz. **25** (5), 53 (1999) [Tech. Phys. Lett. **25**, 189 (1999)].

Translated by A. Sharshakov

Technical Physics Letters, Vol. 26, No. 8, 2000, pp. 721–722. Translated from Pis'ma v Zhurnal Tekhnicheskoĭ Fiziki, Vol. 26, No. 16, 2000, pp. 52–56.

Pulsed High-Current Electron Beams Formed Without Vacuum

Yu. E. Kolyada

Azov State Technical University, Mariupol, Russia

Received November 30, 1999; in final form, March 10, 2000

Abstract—Microsecond pulsed electron beams were experimentally obtained under atmospheric pressure conditions in a high-current arc discharge channel of a plasma accelerator. © *2000 MAIK "Nauka/Interperiodica".*

Some applications involving electron beams, such as electron-beam processing, radiation-induced polymerization, modification of the surface properties of various materials, encounter the problem of extracting the beams into atmosphere. This is achieved by using either a thin metal foil separating the vacuum chamber of an accelerator from the atmosphere or a complicated scheme of differential pumping. However, good prospects in this respect are offered by methods of direct electron beam production under atmospheric conditions.

The formation of high-energy electrons by discharge in air was experimentally studied in [1–4], where the electron beam production was accompanied by the X-ray emission registered in the initial stage of the spark discharge development. The electron beam pulse duration was of the order of 10 ns in the range of kV voltages. The beam formation under these conditions was governed by the electron runaway effect [5, 6]. For a nonrelativistic electron, this phenomenon takes place provided that the retarding force is smaller than the electrostatic force of the external (accelerating) field. The retarding force is related to ionization losses and described by the well-known Bethe–Bloch formula:

$$F(\epsilon) = -\frac{n_0 e^4 Z}{8\pi\varepsilon_0^2}\ln\frac{2\epsilon}{I}, \qquad (1)$$

where e is the electron charge, ϵ is the kinetic energy of electron, n_0 is the concentration of gas molecules, Z is the atomic number, I is the average energy of inelastic losses, and ε_0 is the dielectric constant. The critical electric field strength, above which the acceleration (and runaway) of electrons takes place, is given by the formula

$$E_c = \frac{e^3 n_0 Z}{4\pi\varepsilon_0^2 2.72 I}. \qquad (2)$$

According to [6], this relationship can be conveniently presented as

$$\frac{E_c}{P} = 3.88\times 10^3\frac{Z}{I}, \qquad (3)$$

where the parameters E_c/P and I are measured in V/(cm Torr) and eV, respectively; in air, the inelastic loss factor can be taken equal to I = 15–80 eV.

In contrast to previous works dealing with nanosecond pulsed beams, this work was devoted to experimental investigation of the microsecond electron beams formed under the action of additional high-voltage pulses in a high-current arc discharge channel of an edge plasma accelerator operating under atmospheric pressure conditions.

Figure 1 shows a schematic diagram of the experimental system. The plasma accelerator (PU) depicted in the right-hand part of the scheme comprises a thick-wall dielectric tube (wall thickness, ~1 cm; internal

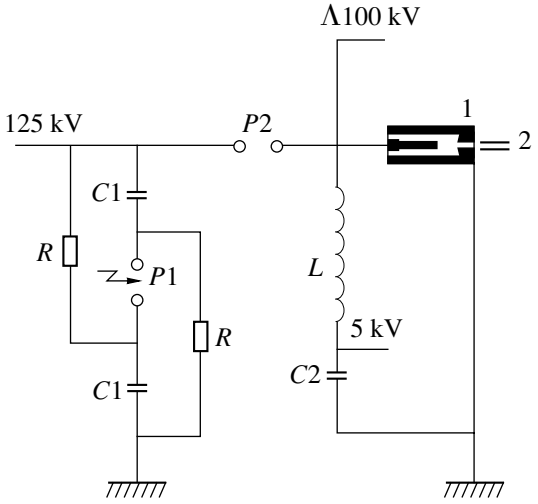

Fig. 1. A schematic diagram of the experimental system: (1) plasma accelerator; (2) electron beam; *C*2, capacitor bank (charge voltage, 5 kV; high-voltage start-up pulse amplitude, 100 keV); *L*, decoupling capacitor; *C*1, *R*, *P*1, *P*2, Marx generator (charging voltage, 125 kV).

1063-7850/00/2608-0721$20.00

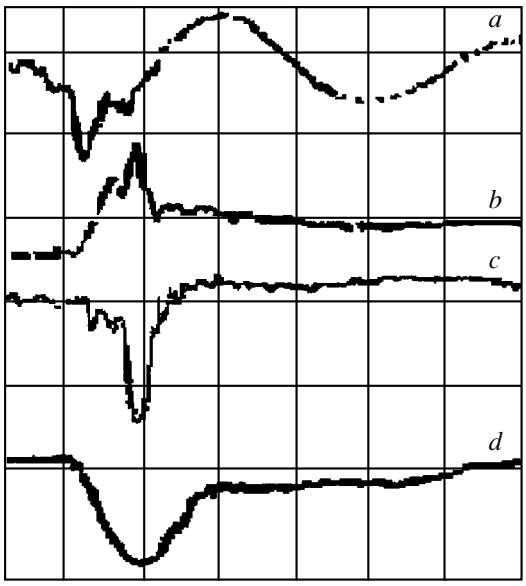

Fig. 2. Typical oscillograms of the (*a*) discharge current of the Marx generator, (*b*) voltage applied to the accelerating gap, (*c*) X-ray radiation pulse, and (*d*) microwave pulse in a 3–10 cm wavelength range. The oscillograph beam was swept at a rate of 5 μs/div with a sensitivity of 1 kA/div (for current) and 125 kV/div (for voltage).

diameter, 8 mm; length, 40 cm) with two (rod and ring) electrodes spaced by ~10 cm. The electric circuit was supplied from a capacitor bank with a capacitance $C2 = 1.5 \times 10^{-3}$ F operating at a working voltage of 5 kV. The design and operation of a similar accelerator scheme were described in detail [7]. A discharge between electrodes was initiated by high-voltage (~100 kV) start-up pulses with a base width of ~5 μs. The inductor coil with $L = 0.3$ mH prevented the starting pulses from penetrating into the capacitor bank. Upon the interelectrode gap breakdown, the capacitor bank produced a high-power discharge pulse with a duration of ~1.4 ms, whereby not less than 60% of the stored energy was converted into the plasma bunch energy.

A characteristic feature of this accelerator was that the high-power discharge formation and the dense plasma bunch injection into the ambient medium account for a pressure increase of up to 100 atm in the discharge channel. This pulse is followed by a depression-type wave, whereby the pressure at the pulse end may drop markedly below the atmospheric pressure level (1–5 Torr). At this instant, a negative high-voltage pulse was applied to the interelectrode gap from a two-stage Marx generator (see the left part of Fig. 1). The generator circuit parameters are as follows: $C1 = 0.64$ μF, $R = 48$ kΩ ($P1$ and $P2$ are the start-up and decoupling discharge gaps, respectively). The generator circuits charged by a voltage of 125 kV provided for a voltage pulse of ≤250 kV in the load (interelectrode gap). The inductance L prevented the starting pulses from penetrating into the circuit of capacitor bank $C2$. The high-voltage pulse acting upon the discharge gap of the plasma accelerator (occurring at this time instant at a reduced pressure) produced a pulsed electron beam.

Figure 2 shows typical oscillograms of the (*a*) discharge current of the Marx generator (measured with a Rogowsky coil), (*b*) voltage applied to the accelerating gap, (*c*) X-ray radiation measured by a crystal detector with multiplier phototube, and (*d*) microwave signal detected by a horn antenna in a 3–10 cm wavelength range. The oscillograph beam was swept at a rate of 5 μs/div with a sensitivity of 1 kA/div (for current) and 125 kV/div (for voltage). An analysis of the oscillograms shows that a microsecond pulsed electron beam is formed in the system with a beam current of ~1 kA and an electron energy of ~200 keV. The electron beam production is preceded by a high-power arc discharge in the accelerator channel, which heats the emitter (rod electrode) to a temperature close to the melting point. This probably accounts for excitation of the autothermoelectron emission.

Estimates of the E_c/P ratio by formula (3) suggest that the electron runaway effect can be manifested under the experimental conditions studied. Indeed, for a gas pressure in the discharge channel decreasing to 1–5 Torr during the plasma accelerator operation and an average electric field strength of ~20 V/cm in the gap, we obtain $E/p \sim (0.4–2) \times 10^4$ V/(cm Torr). In air, calculation by formula (3) yields $E_c/P = (0.8–3.5) \times 10^3$ V/(cm Torr), which is markedly lower than the level achieved in experiment.

Thus, the results of our investigation demonstrate the possibility of obtaining microsecond pulsed electron beams formed in a high-current arc discharge channel without vacuum.

The author is grateful to Ya.B. Faĭnberg for fruitful discussions and useful comments on the experiment planning and interpretation.

REFERENCES

1. Yu. L. Stankevich and N. S. Kalinin, Dokl. Akad. Nauk SSSR **177** (1), 72 (1967) [Sov. Phys. Dokl. **12**, 1042 (1968)].
2. R. C. Noggle, E. P. Kriger, and I. R. Way Land, J. Appl. Phys. **39** (10), 4746 (1968).
3. L. V. Tarasova, L. N. Khudyakova, T. V. Loĭko, and V. A. Tsukerman, Zh. Tekh. Fiz. **44** (2), 564 (1974) [Sov. Phys. Tech. Phys. **19**, 352 (1974)].
4. P. A. Bokhan and G. V. Kolbychev, Zh. Tekh. Fiz. **51** (9), 1823 (1981) [Sov. Phys. Tech. Phys. **26**, 1057 (1981)].
5. A. V. Gurevich, Zh. Éksp. Teor. Fiz. **39** (5), 1296 (1960) [Sov. Phys. JETP **12**, 904 (1960)].
6. Yu. D. Korolev and G. A. Mesyats, *The Physics of Pulse Breakdown in Gases* (Nauka, Moscow, 1991).
7. I. A. Glebov and F. G. Rutberg, *High-Power Plasma Generators* (Énergoatomizdat, Moscow, 1985).

Translated by P. Pozdeev

Technical Physics Letters, Vol. 26, No. 8, 2000, pp. 723–725. Translated from Pis'ma v Zhurnal Tekhnicheskoĭ Fiziki, Vol. 26, No. 16, 2000, pp. 57–62.

Dynamic Theory of Defects and Creep in Solids

Yu. V. Grinyaev and N. V. Chertova

Institute of Strength Physics and Materials Science, Siberian Division, Russian Academy of Sciences, Tomsk, 634055 Russia

Received December 20, 1999

Abstract—The dynamic equations of the field theory of defects are used to analyze the creep characteristics. A number of interesting results are obtained, of which some are consistent with the well-known experimental data, whereas others are quite new. In particular, the existence of a critical value of the applied stress and an unstable steady-state creep rate are established, which separate the stable and unstable creep modes and can be of great practical importance. *© 2000 MAIK "Nauka/Interperiodica".*

It is well known that a deformable solid is a complicated hierarchic system consisting of a large number of interacting structural elements that are considered on different scales [1]. The behavior of various hierarchic systems is a subject of synergetics [2], where various systems are studied on the micro-, meso-, and macrolevels. On the microscopic level, individual structural elements are considered by setting their positions, velocities, and the laws governing their interactions. On the mesoscopic level, the variables describing an ensemble of interacting structural elements are introduced. Finally, in order to describe the system on the macroscopic level, the initial mesoscopic level is used to develop the methods which would provide the prediction of macroscopic structures. In what follows, we consider the characteristics of deformation in solids during creep within the framework of the field theory of defects [3, 4] representing a mesoscopic description of the system. According to various physical theories [5, 6], the elementary creep processes in solids at moderate temperatures are provided mainly by dislocation motion. Using the dynamic equations of the field theory of defects,

$$\begin{aligned} B(\nabla \cdot I) &= -B(\alpha \overset{\times}{\cdot} I) - \rho \mathbf{V}^{\text{ext}}, \\ \nabla \cdot \alpha &= 0, \quad \nabla \cdot I = \frac{\partial \alpha}{\partial t}, \\ S\nabla \cdot \alpha &= -B\frac{\partial I}{\partial t} - S\left(\alpha \cdot \alpha - \frac{\delta}{2}\alpha^2\right) \\ &\quad - B\left(I \cdot I - \frac{\delta}{2}I^2\right) - \eta I - \sigma^{\text{ext}}, \end{aligned} \tag{1}$$

we arrive at the equation

$$B\frac{\partial I}{\partial t} + B\left(I \cdot I - \frac{\delta}{2}I^2\right) + \eta I + \sigma^{\text{ext}} = 0, \tag{2}$$

relating the velocity I of the defect flow to the externally induced stresses σ^{ext}, thus making it possible to study the creep phenomenon. In the above expressions, α is the dislocation-density tensor, $\mathbf{V}^{\text{ext}}$ is the velocity of elastic displacements, ρ is the density of the medium, η is the viscosity coefficient, B and S are the theory constants, and δ is the Kronecker symbol. The signs $(\times)$ and $(\cdot)$ indicate the vector and the scalar multiplication, the sign $(\overset{\times}{\cdot})$ corresponds to the vector multiplication with respect to the first indices and the scalar multiplication with respect to the second indices. Equation (2) is obtained under the condition that defects are uniformly distributed, so that the α, I field strengths are independent of the coordinates. According to [7], such a situation can be observed at the material yield stress, when single defects are randomly distributed over the material and cannot form any spatial structure. Since many of the experimental data on creep were obtained under tensile tests on rods [8–9], we consider here an equation of the uniaxial deformation. In terms of the dimensionless quantities $v = -(B/\eta)I_{11}$, $\tau = (\eta/B)t$, and $S = (B/\eta^2)\sigma_{11}$, this equation has the form

$$\frac{dv}{d\tau} = v^2/2 - v + S, \tag{3}$$

where v is the plastic deformation rate. At S = const (which corresponds to creep under a constant stress), we may use the stationarity condition

$$v^2/2 - v + S = 0 \tag{4}$$

to determine two rates of the steady-state creep:

$$v_1 = p = 1 + \sqrt{1-2S}, \quad v_2 = q = 1 - \sqrt{1-2S}. \tag{5}$$

Analyzing the plot (4) and the phase portrait (3), we see that the stationary state q is stable, whereas the state p is unstable. If the controlling parameter S approaches the value 1/2, the stable and the unstable stationary

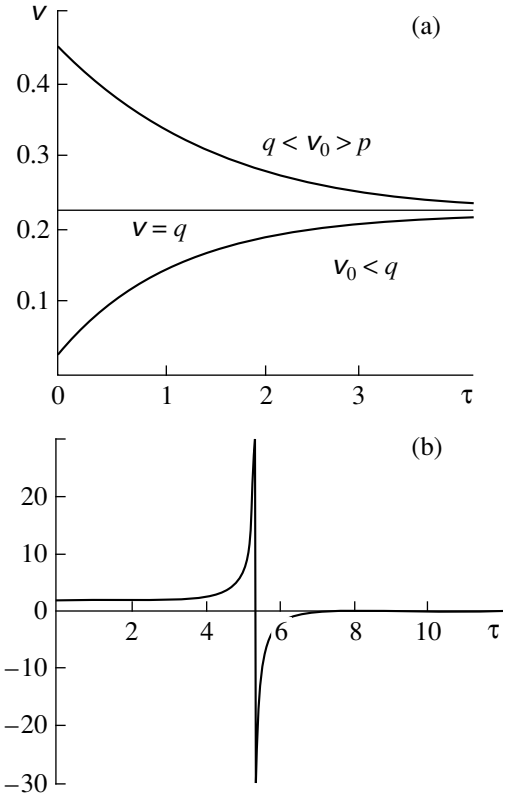

Fig. 1. Evolution of the creep rate at $S < S_*$: (a) $\nu_0 < p$ and (b) $\nu_0 > p$.

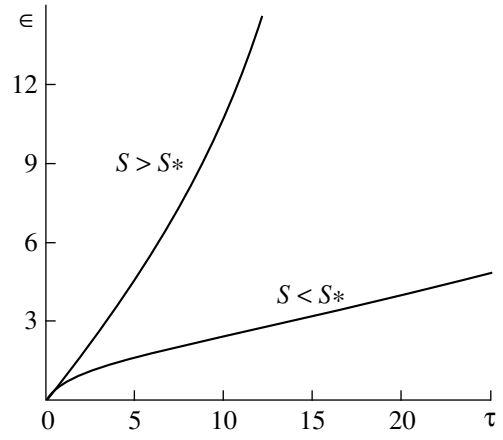

Fig. 2. Typical creep curves.

states approach one another and coincide at

$$S_* = 1/2, \tag{6}$$

whereas at $S > 1/2$, they both simultaneously disappear. At $S < S_*$, the solution to Eq. (3) has the following form:

$$\nu(\tau) = \frac{p - q[(\nu_0 - p)/(\nu_0 - q)]\exp[(p-q)\tau/2]}{1 - [(\nu_0 - p)/(\nu_0 - q)]\exp[(p-q)\tau/2]}. \tag{7}$$

Figures 1a and 1b show the strain rate curves illustrating the evolution at $S = 0.2$. At short times, the form of the function $\nu(\tau)$ is determined by the initial value ν_0 that can vary within three ranges: $0 < \nu_0 < q$, $q < \nu_0 < p$, and $\nu_0 > p$. Figure 1a shows the $\nu(\tau)$ curves obtained at ν_0 from the two first ranges. At $\nu_0 > p$ $\nu(\tau)$, the curve has a singularity (the denominator of the expression goes to zero, Fig. 1b), whence the time to the system failure (when the strain rate becomes infinite) is determined as

$$\tau_1 = [2/(p-q)]\ln[(\nu_0 - q)/(\nu_0 - p)].$$

At $S > S_*$, a solution to Eq. (3) can be written as

$$\nu(\tau) = \frac{\nu + \alpha^2}{\nu} + \left(\frac{\nu^2 + \alpha^2}{\nu}\right) \times \left(\frac{\cos(\alpha\tau/2)}{\cos(\alpha\tau/2) - \nu/\alpha\sin(\alpha\tau/2)}\right), \tag{8}$$

where $2\alpha = p - q$ and $\nu = 1 - \nu_0$. Obviously, the lifetime of a real system is limited by the condition

$$\cos(\alpha\tau/2) - (\nu/\alpha)\sin(\alpha\tau/2) = 0, \tag{9}$$

from which it follows that the time to failure equals

$$\tau_2 = (2/\alpha)\arctan(\alpha/\nu).$$

Usually, the experimental data on creep are represented in the form of a creep curve characterizing the change in deformation with time. Within the present approach, the corresponding dependences are obtained by integrating Eqs. (7) and (8) with respect to time. At $S < S_*$, the creep curve is described by the relationship

$$\varepsilon(\tau) = \varepsilon_0 + q\tau + 2\ln\left|(p-q)/[(p-\nu_0) - (q-\nu_0)\exp((p-q)\tau/2)]\right|, \tag{10}$$

and, at $S > S_*$, it has the form

$$\varepsilon(\tau) = \varepsilon_0 + \tau - 2\ln\left|\cos(\alpha\tau/2) - (\nu/\alpha)\sin(\alpha\tau/2)\right|. \tag{11}$$

Figure 2 shows the curves of stable and unstable creep obtained at $S = 0.15$, $\nu_0 = 0.7$ and $S = 0.55$, $\nu_0 = 0.8$, with $\varepsilon_0 = 0.0002$ in both cases.

The creep analysis based on the equation describing the evolution of a flow of defects showed that the character of the creep process is essentially dependent on the applied load S and the initial deformation rate ν_0. At a constant stress, the range of the stable creep is limited by the conditions $0 < S < S_*$ and $0 < \nu_0 < p$, where S_* is the critical stress and p is the unstable stationary deformation rate. The stress S_* allows us to introduce a limit of the stable creep determined by the material constants $\sigma^* = \eta^2/2B$. Beyond the stable creep limit ($\nu_0 > p$ or $S > S_*$), the time to system failure (τ_1, τ_2) decreases with an increase of the external load and the initial deformation rate.

The expressions obtained for the creep rate describe the well-known monotonic increase of the rate with stresses [8] and the fact that $q(S = 0) = 0$, which is also taken into account in constructing the phenomenological expressions for this quantity [9]. The typical creep curve has three regions. In the first region, the deformation rate gradually decreases down to the minimum value. In the second segment, the deformation rate remains constant. Finally, in the third region, the deformation rate increases again until the process is ended with the specimen failure. In our case, the curve $\varepsilon(\tau)$ at $S < S_*$ has only the stages of non-steady-state and steady-state creep, whereas the third segment is not described by this expression. However, the typical experimental creep curves were obtained under constant loading conditions. According to [8], in the case of constant stresses considered here, no creep acceleration can be observed until the very moment of specimen failure. The dependence $\varepsilon(\tau)$ at $S > S_*$ is described in [9], where it is also shown that the creep curve does not necessarily contain a region of decreasing deformation rate: upon a short period of deformation at a constant rate, the creep rate starts increasing. In fact, the whole diagram reduces to the third segment alone. The results obtained in our study indicate that at different values of the applied stress, all the three creep modes can be observed on the same specimen.

REFERENCES

1. V. E. Panin, V. A. Likhachev, and Yu. V. Grinyaev, *Structural Levels of Deformation in Solids* (Nauka, Novosibirsk, 1985).
2. H. Haken, *Advanced Synergetics: Instability Hierarchies of Self-Organizing Systems and Devices* (Springer-Verlag, New York, 1983; Mir, Moscow, 1985).
3. Yu. V. Grinyaev and V. E. Panin, Dokl. Akad. Nauk **353** (1), 37 (1997) [Phys. Dokl. **42**, 108 (1997)].
4. Yu. V. Grinyaev, N. V. Chertova, and V. E. Panin, Zh. Tekh. Fiz. **68** (9), 134 (1998) [Tech. Phys. **43**, 1128 (1998)].
5. A. H. Cottrell, *Dislocations and Plastic Flow in Crystals* (Clarendon Press, Oxford, 1953; Metallurgizdat, Moscow, 1958).
6. V. M. Rozenberg, *Creep in Metals* (Metallurgiya, Moscow, 1967).
7. N. A. Koneva and É. V. Kozlov, Izv. Vyssh. Uchebn. Zaved., Fiz., No. 2, 89 (1990).
8. L. N. Kachanov, *Theory of Creep* (Fizmatgiz, Moscow, 1960).
9. Yu. N. Rabotnov, *Mechanics of Deformed Solids* (Nauka, Moscow, 1979).

Translated by L. Man

Technical Physics Letters, Vol. 26, No. 8, 2000, pp. 726–728. Translated from Pis'ma v Zhurnal Tekhnicheskoĭ Fiziki, Vol. 26, No. 16, 2000, pp. 63–67.

A Single-Electron Transistor Model Based on a Numerical Solution of the Poisson Equation

I. I. Abramov and E. G. Novik

State University of Informatics and Radio Engineering, Minsk, Belarus

Received December 25, 1998; in final form, October 25, 1999

Abstract—A numerical model of a single-electron metal transistor is proposed based on a solution of the Poisson equation. The model provides a good agreement with experimental data on the current–voltage characteristics obtained at nonzero temperatures in the ambient medium. *© 2000 MAIK "Nauka/Interperiodica".*

At present, single-electron transistors (SETs) are conventionally simulated using semiclassical models [1]. A disadvantage in common for these models is that fitting to the experimental data is performed using parameters—capacitances and resistances of the tunneling junctions—that cannot be calculated. As a result, the models do not adequately reflect the structure design and physical properties of the SET materials, which hinder prediction of the electrical characteristics of final devices.

The purpose of this work was to elaborate a model based on the geometric and physical parameters of SETs.

An analysis of published data showed that most types of SETs can be described using a structural scheme depicted in Fig. 1 [2]. Below, we will also study the SET structures of this kind. Within the framework of the semiclassical approach, the current–voltage characteristics of SET structures can be calculated using a master equation [3]. According to this, currents passing the source and drain tunneling junctions obey the following relationship:

$$\begin{aligned}\partial\rho(n)/\partial t &= [\vec{I}_1(n-1) + \overleftarrow{I}_2(n-1)]\rho(n-1)\\ &+ [\overleftarrow{I}_1(n+1) + \vec{I}_2(n+1)]\rho(n+1)\\ &- [\vec{I}_1(n) + \overleftarrow{I}_1(n)]\rho(n) - [\vec{I}_2(n) + \overleftarrow{I}_2(n)]\rho(n).\end{aligned} \quad (1)$$

The total current through the SET structure is

$$\begin{aligned}I &= \sum_{n=-\infty}^{+\infty} \rho(n)(\vec{I}_1(n) - \overleftarrow{I}_1(n))\\ &= \sum_{n=-\infty}^{+\infty} \rho(n)(\vec{I}_2(n) - \overleftarrow{I}_2(n)).\end{aligned} \quad (2)$$

Here, $\vec{I}_1$ and $\overleftarrow{I}_1$ are the direct and reverse currents passing through the drain tunneling junction, respectively; $\vec{I}_2$ and $\overleftarrow{I}_2$ are the corresponding currents in the source tunneling junction; and $\rho(n)$ is the probability of finding n excess charge carriers on the "island" (see Fig. 1).

The values of voltage drops across the tunneling junctions are determined taking into account the results of calculation of the electrostatic potential distribution φ and the contact potential differences in the structure studied. Resistances of the tunneling junctions can be calculated using well-known relationships [4, 5].

Assuming that the magnetic field produces a negligibly small effect on the transistor operation, the electrostatic potential distribution φ can be determined from the Poisson equation

$$\nabla\varepsilon\nabla\varphi = -q_M, \quad (3)$$

where ε is the dielectric permittivity and q_M is the bulk

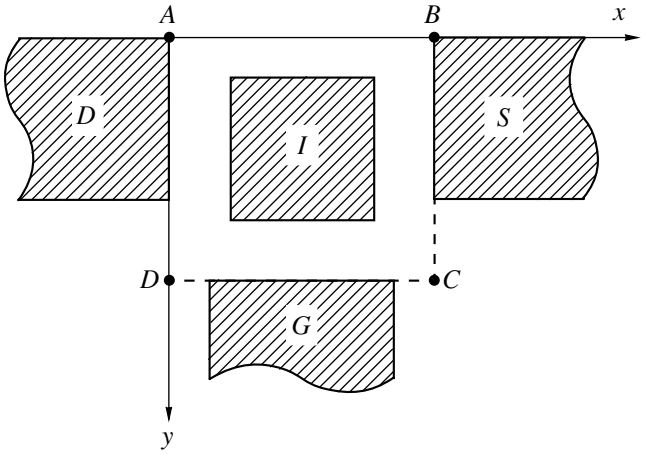

Fig. 1. Schematic diagram representing the proposed SET model: *D*, drain; *I*, "island"; *S*, source, *G*, gate.

1063-7850/00/2608-0726$20.00 © 2000 MAIK "Nauka/Interperiodica"

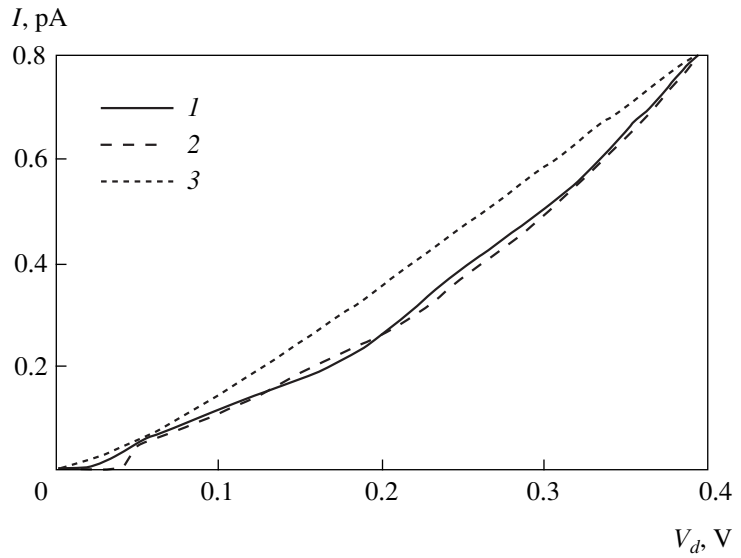

Fig. 2. Comparison of the experimental and calculated current– voltage characteristics: (*1*) experimental data; (*2*) proposed model; (*3*) MOSES program.

density of charge. Below, we also assume electroneutrality of the plasma at the "island" (except for the excess free charge carriers) and neglect charges in the dielectric. Therefore, q_M is determined only by the average density of excess charge carriers immediately on the "island." Under these assumptions, Eq. (3) can be solved in the active SET region between the source, drain, and gate (the two-dimensional region *ABCD* in Fig. 1). The boundary conditions are represented by the Dirichlet conditions at the contacts and the Neumann conditions at the free boundaries.

The finite-difference approximation of the Poisson equation (3) was formulated within the framework of the Tikhonov–Samarskiĭ approach [6]. All values were normalized using coefficients introduced in [6]. The system of linear algebraic equations obtained upon the finite-difference approximation was solved using a matrix trial method [7].

The proposed semiclassical two-dimensional numerical SET model was used as a base for a special computational program written in PASCAL adapted to an IBM PC/AT and included into a program package NANODEV intended for the modeling of nanoelectronic devices [8]. Using this program, we have calculated the current–voltage characteristics of a real metal SET [9] based on the Ti/TiO_x/Ti tunneling junctions operating at a nonzero temperature (T = 103 K). As seen from the data presented in Fig. 2, the results of calculations performed using the proposed model agree well with the experimental data. For comparison, Fig. 2 shows a curve calculated by the MOSES program [10]. Note that the time required for calculating a current–voltage characteristic is 3 min for our program and computer facilities versus 20 min for the MOSES program on a Pentium 200.

Let us analyze the factors responsible for the deviation from experiment observed for the results of calculations using both our numerical model and the MOSES model (based on the Monte-Carlo method) [10]. In the proposed model, the electrical characteristics are calculated using a two-dimensional potential distribution in the structure determined by solving the Poisson equation. In the well-known models [1, 10], the potential distribution is set according to a one-dimensional case, irrespective of the contact potential differences. Therefore, our model provides for a better agreement with experiment than the above models. Still, small deviation from the experiment can be explained by neglect of the parasitic effects in our model. Note, however, that these models are also not taken into account in the known semiclassical models.

Thus, we have developed a new semiclassical two-dimensional numerical model of a metal SET based on solving the Poisson equation. The model provides good agreement with experimental data on the current–voltage characteristics of SETs and can be used for predicting electrical characteristics of these devices.

The work was pertly supported by the Scientific-Technological Programs of the Republic of Belarus on Informatics, Low-Dimensional Systems, and Nanoelectronics.

REFERENCES

1. *Single Charge Tunneling: Coulomb Blockade Phenomena in Nanostructures*, ed. by H. Grabert and

M. H. Devoret (Plenum, New York, 1992), NATO ASI Ser., Ser. B: Phys., Vol. 294.
2. I. I. Abramov and E. G. Novik, Izv. Belarus. Inzh. Akad., No. 2 (6/2), 4 (1998).
3. K. K. Likharev, IEEE Trans. Magn. **MAG-23** (2), 1142 (1987).
4. J. G. Simmons, J. Appl. Phys. **34** (6), 1793 (1963).
5. H. Fukui, M. Fujishima, and K. Hoh, Jpn. J. Appl. Phys., Part 1 **36** (6B), 4147 (1997).
6. I. I. Abramov and V. V. Kharitonov, *Numerical Modeling of the Elements of Integrated Circuits* (Vysshaya Shkola, Minsk, 1990).
7. A. A. Samarskiĭ and E. S. Nikolaev, *Methods of Solving Network Equations* (Nauka, Moscow, 1978).
8. I. I. Abramov, I. A. Goncharenko, and E. G. Novik, Pis'ma Zh. Tekh. Fiz. **24** (8), 16 (1998) [Tech. Phys. Lett. **24**, 293 (1998)].
9. K. Matsumoto, M. Ishii, K. Segawa, *et al.*, Appl. Phys. Lett. **68** (1), 34 (1996).
10. R. H. Chen and K. K. Likharev, Appl. Phys. Lett. **72** (1), 61 (1998).

Translated by P. Pozdeev

Technical Physics Letters, Vol. 26, No. 8, 2000, pp. 729–733. Translated from Pis'ma v Zhurnal Tekhnicheskoĭ Fiziki, Vol. 26, No. 16, 2000, pp. 68–76.

Green's Tensor of the Maxwell Equations for a Planar Metal–Dielectric–Ferromagnet–Dielectric–Metal Sandwich Structure

V. E. Demidov and B. A. Kalinikos

St. Petersburg State Electrotechnical University, St.Petersburg, 197376 Russia

e-mail: eivt@eltech.ru

Received April 5, 2000

Abstract—Expressions for the dyadic Green's functions of the Maxwell equations for a planar metal–dielectric–ferromagnet–dielectric–metal sandwich structure are derived taking into account the electromagnetic retardation. © *2000 MAIK "Nauka/Interperiodica".*

Spin waves propagating in ferrite films and layered structures are widely applied in electrically tuned devices used for the processing of microwave signals [1]. Among these devices are filters, resonators, delay lines, suppressors of weak signals, convolvers, etc. Usually, the dispersion characteristics of spin waves propagating in ferromagnetic films and layered structures based on these films are calculated using the magnetostatic approximation, that is, neglecting the electromagnetic retardation. This substantially simplifies the form of dispersion equations and, in some cases, makes it possible to write these equations in an explicit form (see, for example, [2, 3]). Such an approach is justified when the permittivity of both the ferromagnetic film and the ambient space is small and the structure operates at moderate frequencies (below 10 GHz). Among the disadvantages of the magnetostatic approximation are substantial errors arising in attempts to calculate the parameters of such films in the millimeter wave band as well as in the case when the film is in contact with objects having a large permittivity.

In recent years, interest has revived in creating devices for the microwave signal processing based on ferroelectric materials with a large permittivity controlled by an applied static electric field (see, for example, [4]). Advantages of such devices are the high speed and small energy required for the electrical tuning. A similar mechanism can also be proposed to control dispersion characteristics of spin waves in structures involving contacting ferromagnetic and ferroelectric layers. In order to evaluate parameters of these structures, it is necessary to develop a theory of spin waves taking into account the electromagnetic retardation.

In the theory of normal spin oscillations and waves propagating in ferromagnetic films and layered structures based on these films, two approaches are usually applied. These approaches differ in methods of simultaneous integration of the magnetization equation and the Maxwell equations. In the first approach, expressions for components of the permeability tensor are obtained from the magnetization equation and are used in the solution of the Maxwell equations. In the second approach, the dyadic Green's functions of the Maxwell equations accounting for boundary conditions are first obtained and then used in solving the magnetization equation. As was shown in [2], the second approach (the method of dyadic Green's functions or Green's tensor) is more convenient, especially, in solving problems of the spectrum of spin waves with account of both the dipole–dipole and exchange interaction. In particular, the problem of the spectrum of spin waves and the problem of linear excitation of such waves in ferromagnetic films and layered structures were solved using this method [2, 3]. Another important advantage of the method of the dyadic Green's functions is that the first steps of calculations do not require linearization of the magnetization equation. This makes the second approach more suited to solve problems related to nonlinear spin waves (see, for example, [5]).

The dyadic Green's functions for the metal–dielectric–ferromagnet–dielectric–metal (MDFDM) planar sandwich structures were obtained previously [2]. However, the derivation was based on the solution of a magnetostatic equation system, which does not allow one to use these solutions for description of the structures involving layers with large permittivity, in particular, ferroelectric films.

The purpose of this work is to derive expressions for the dyadic Green's functions (Green's tensor) of a planar MDFDM sandwich structure on the basis of solution of the complete system of Maxwell equations involving vortex fields.

Consider a plane-parallel layer structure infinitely extended in the *YOZ* plane. The structure consists of an isotropic ferromagnetic film of thickness L separated on both sides from perfectly conducting screens by

1063-7850/00/2608-0729$20.00

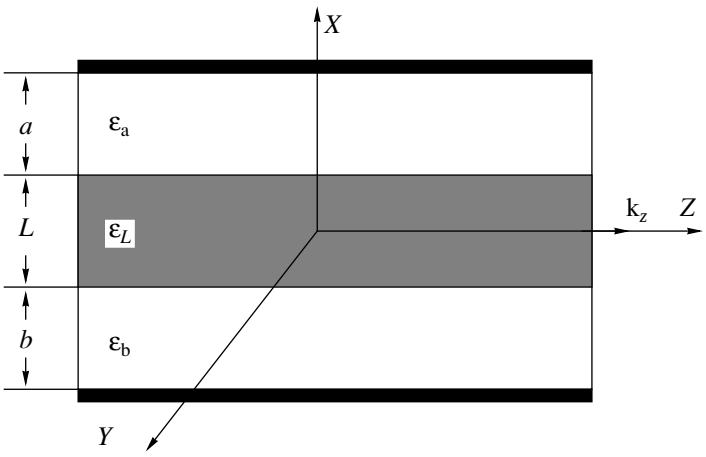

Geometry of the layered structure.

dielectric layers of thickness a and b, respectively. The ferroelectric film is described by variable magnetization $\mathbf{m}$ and permittivity ϵ_L, and the dielectric layers are described by permittivities ϵ_a and ϵ_b, respectively (see figure). The origin of coordinate system is placed on the middle plane of the ferromagnetic film.

Let us relate waves of the magnetic and electric field, $\mathbf{h} = \mathbf{h}_k(x)\exp(i(\omega t - k_z z))$ and $\mathbf{E} = \mathbf{E}_k(x)\exp(i(\omega t - k_z z))$ to the waves of variable magnetization $\mathbf{m} = \mathbf{m}_k(x)\exp(i(\omega t - k_z z))$. These relationships can be obtained from the complete system of Maxwell equations

$$\begin{aligned} \mathrm{rot}\,\mathbf{h} &= i\omega\epsilon_0\epsilon_r\mathbf{E}, \\ \mathrm{rot}\,\mathbf{E} &= -i\omega\mu_0(\mathbf{h} + \mathbf{m}), \\ \mathrm{div}\,\mathbf{h} &= -\mathrm{div}\,\mathbf{m}, \\ \mathrm{div}\,\mathbf{E} &= 0 \end{aligned} \qquad (1)$$

in the following form:

$$\mathbf{h}_k(x) = \int_{-L/2}^{L/2} \hat{G}_h(x, x'; k_z)\mathbf{m}_k(x')dx',$$

$$\mathbf{E}_k(x) = \int_{-L/2}^{L/2} \hat{G}_E(x, x'; k_z)\mathbf{m}_k(x')dx',$$

where $\hat{G}_h(x, x'; k_z)$ and $\hat{G}_E(x, x'; k_z)$ are the dyadic Green's functions of Eqs. (1).

It can be easily shown that system (1) splits into two independent equation systems for the components (E^x, h^y, E^z) and (h^x, E^y, h^z) of the electromagnetic field, respectively. The first triplet of the field components corresponds to transverse magnetic (*TM*) waves, whereas the second triplet corresponds to the transverse electric (*TE*) waves. It would suffice to know one of the components involved in each triplet, because the remaining components can be expressed in terms of these known values.

Let us choose components h_x and E_z as primary functions, since these components satisfy boundary conditions on the metal surfaces. These functions are determined from two second-order differential equations,

$$\frac{\partial^2}{\partial x^2}h_k^x - \gamma_i^2 h_k^x = -k_{0i}^2 m_k^x - \frac{\partial^2}{\partial x^2}m_k^x + ik_z\frac{\partial}{\partial x}m_k^z, \qquad (2)$$

$$\frac{\partial^2}{\partial x^2}E_k^z - \gamma_i^2 E_k^z = i\omega\mu_0\frac{\partial}{\partial x}m_k^y, \qquad (3)$$

where the parameter γ_i equals γ_a, γ_b, or γ_L, respectively, for each of the structure layers:

$$\gamma_L^2 = k_z^2 - k_{0L}^2, \quad k_{0L}^2 = \omega^2\epsilon_0\mu_0\epsilon_L,$$

$$\gamma_a^2 = k_z^2 - k_{0a}^2, \quad k_{0a}^2 = \omega^2\epsilon_0\mu_0\epsilon_a,$$

$$\gamma_b^2 = k_z^2 - k_{0b}^2, \quad k_{0b}^2 = \omega^2\epsilon_0\mu_0\epsilon_b.$$

The remaining components are connected with the primary ones via expressions

$$E_k^y = -\frac{\omega\mu_0}{k_z}(h_k^x + m_k^x),$$

$$h_k^z = -\frac{1}{i\omega\mu_0}\frac{\partial}{\partial x}E_k^y - m_k^z,$$

$$h_k^y = \frac{i\omega\epsilon_0\epsilon_i}{\gamma_i^2}\frac{\partial}{\partial x}E_k^z + \frac{k_{0i}^2}{\gamma_i^2}m_k^y,$$

$$E_k^x = \frac{k_z}{\omega\epsilon_0\epsilon_i}h_k^y.$$

Solving equations (2) and (3) in each layer, we obtain expressions for each of six components of the

electromagnetic field as functions of the variable magnetization. These expressions involve constants that can be obtained upon satisfying boundary conditions on the metal surfaces and layer interfaces.

Separating contributions from different components of the variable magnetization into corresponding components of the electromagnetic field, we obtain the final expressions for the Green's functions. In the ferromagnetic layer, these expressions take the following form:

$$G_h^{xx} = -\delta(x-x') - \frac{k_z^2}{\gamma_L \sinh(\gamma_L d)} \times \begin{cases} \sinh(\gamma_L x_b)\sinh(\gamma_L x_a') & x \geq x' \\ \sinh(\gamma_L x_a)\sinh(\gamma_L x_b') & x < x' \end{cases}$$

$$+ \frac{k_z^2}{\gamma_L N}\{\sinh(\gamma_L x_a')T_b G_3(x) + \sinh(\gamma_L x_b')T_a G_4(x)\},$$

$$G_h^{xz} = -\frac{ik_z}{\sinh(\gamma_L d)} \begin{cases} \sinh(\gamma_L x_b)\cosh(\gamma_L x_a') & x \geq x' \\ \sinh(\gamma_L x_a)\cosh(\gamma_L x_b') & x < x' \end{cases}$$

$$+ \frac{ik_z}{N}\{\cosh(\gamma_L x_a')T_b G_3(x) + \cosh(\gamma_L x_b')T_a G_4(x)\},$$

$$G_h^{zx} = \frac{ik_z}{\sinh(\gamma_L d)} \begin{cases} \cosh(\gamma_L x_b)\sinh(\gamma_L x_a') & x \geq x' \\ \cosh(\gamma_L x_a)\sinh(\gamma_L x_b') & x < x' \end{cases}$$

$$- \frac{ik_z}{N}\{\sinh(\gamma_L x_a')T_b G_1(x) + \sinh(\gamma_L x_b')T_a G_2(x)\},$$

$$G_h^{zz} = -\frac{\gamma_L}{\sinh(\gamma_L d)} \begin{cases} \cosh(\gamma_L x_b)\cosh(\gamma_L x_a') & x \geq x' \\ \cosh(\gamma_L x_a)\cosh(\gamma_L x_b') & x < x' \end{cases}$$

$$+ \frac{\gamma_L}{N}\{\cosh(\gamma_L x_a')T_b G_1(x) + \cosh(\gamma_L x_b')T_a G_2(x)\},$$

$$G_h^{yy} = \frac{k_{0L}^2}{\gamma_L \sinh(\gamma_L d)} \begin{cases} \cosh(\gamma_L x_b)\cosh(\gamma_L x_a') & x \geq x' \\ \cosh(\gamma_L x_a)\cosh(\gamma_L x_b') & x < x' \end{cases}$$

$$- \frac{k_{0L}^2}{\gamma_L N^y}\{\cosh(\gamma_L x_a')T_b^y G_1^y(x) + \cosh(\gamma_L x_b')T_a^y G_2^y(x)\},$$

$$G_E^{xy} = \frac{\omega\mu_0 k_z}{\gamma_L \sinh(\gamma_L d)} \begin{cases} \cosh(\gamma_L x_b)\cosh(\gamma_L x_a') & x \geq x' \\ \cosh(\gamma_L x_a)\cosh(\gamma_L x_b') & x < x' \end{cases}$$

$$- \frac{\omega\mu_0 k_z}{\gamma_L N^y}\{\cosh(\gamma_L x_a')T_b^y G_1^y(x) + \cosh(\gamma_L x_b')T_a^y G_2^y(x)\},$$

$$G_E^{yx} = \frac{\omega\mu_0 k_z}{\gamma_L \sinh(\gamma_L d)} \begin{cases} \sinh(\gamma_L x_b)\sinh(\gamma_L x_a') & x \geq x' \\ \sinh(\gamma_L x_a)\sinh(\gamma_L x_b') & x < x' \end{cases}$$

$$- \frac{\omega\mu_0 k_z}{\gamma_L N}\{\sinh(\gamma_L x_a')T_b G_3(x) + \sinh(\gamma_L x_b')T_a G_4(x)\},$$

$$G_E^{yz} = \frac{i\omega\mu_0}{\sinh(\gamma_L d)} \begin{cases} \sinh(\gamma_L x_b)\sinh(\gamma_L x_a') & x \geq x' \\ \sinh(\gamma_L x_a)\sinh(\gamma_L x_b') & x < x' \end{cases}$$

$$- \frac{i\omega\mu_0}{N}\{\cosh(\gamma_L x_a')T_b G_3(x) + \cosh(\gamma_L x_b')T_a G_4(x)\},$$

$$G_E^{zy} = -\frac{i\omega\mu_0}{\sinh(\gamma_L d)} \begin{cases} \sinh(\gamma_L x_b)\cosh(\gamma_L x_a') & x \geq x' \\ \sinh(\gamma_L x_a)\cosh(\gamma_L x_b') & x < x' \end{cases}$$

$$+ \frac{i\omega\mu_0}{N^y}\{\cosh(\gamma_L x_a')T_b^y G_3^y(x) + \cosh(\gamma_L x_b')T_a^y G_4^y(x)\}.$$

For layer a,

$$G_h^{xx} = -\frac{k_z^2}{\gamma_a N}\frac{\sinh(\gamma_a(x-a-L/2))}{\cosh(\gamma_a a)} \times (\sinh(\gamma_L x_a')D_b + \sinh(\gamma_L x_b')T_a),$$

$$G_h^{xz} = -\frac{ik_z\gamma_L}{\gamma_a N}\frac{\sinh(\gamma_a(x-a-L/2))}{\cosh(\gamma_a a)} \times (\cosh(\gamma_L x_a')D_b + \cosh(\gamma_L x_b')T_a),$$

$$G_h^{zx} = \frac{ik_z}{N}\frac{\cosh(\gamma_a(x-a-L/2))}{\cosh(\gamma_a a)} \times (\sinh(\gamma_L x_a')D_b + \sinh(\gamma_L x_b')T_a),$$

$$G_h^{zz} = -\frac{\gamma_L}{N}\frac{\cosh(\gamma_a(x-a-L/2))}{\cosh(\gamma_a a)} \times (\cosh(\gamma_L x_a')D_b + \cosh(\gamma_L x_b')T_a),$$

$$G_h^{yy} = \frac{k_{0L}^2}{\gamma_L N^y}\frac{\cosh(\gamma_a(x-a-L/2))}{\cosh(\gamma_a a)} \times (\cosh(\gamma_L x_a')D_b^y + \cosh(\gamma_L x_b')T_a^y),$$

$$G_E^{xy} = \frac{\omega\mu_0 k_z}{\gamma_a N^y}\frac{\epsilon_L\gamma_a}{\epsilon_a\gamma_L}\frac{\cosh(\gamma_a(x-a-L/2))}{\cosh(\gamma_a a)} \times (\cosh(\gamma_L x_a')D_b^y + \cosh(\gamma_L x_b')T_a^y),$$

$$G_E^{yx} = \frac{\omega\mu_0 k_z}{\gamma_a N}\frac{\sinh(\gamma_a(x-a-L/2))}{\cosh(\gamma_a a)}$$

$$\times(\sinh(\gamma_L x_a')D_b + \sinh(\gamma_L x_b')T_a),$$

$$G_E^{yz} = \frac{i\omega\mu_0\gamma_L}{\gamma_a N}\frac{\sinh(\gamma_a(x-a-L/2))}{\cosh(\gamma_a a)}$$

$$\times(\cosh(\gamma_L x_a')D_b + \cosh(\gamma_L x_b')T_a),$$

$$G_E^{zy} = -\frac{i\omega\mu_0}{N^y}\frac{\epsilon_L\gamma_a}{\epsilon_a\gamma_L}\frac{\sinh(\gamma_a(x-a-L/2))}{\cosh(\gamma_a a)}$$

$$\times(\cosh(\gamma_L x_a')D_b^y + \cosh(\gamma_L x_b')T_a^y).$$

For layer b,

$$G_h^{xx} = \frac{k_z^2}{\gamma_b N}\frac{\sinh(\gamma_b(x+b+L/2))}{\cosh(\gamma_b b)}$$

$$\times(\sinh(\gamma_L x_a')T_b - \sinh(\gamma_L x_b')D_a),$$

$$G_h^{xz} = \frac{ik_z\gamma_L}{\gamma_b N}\frac{\sinh(\gamma_b(x+b+L/2))}{\cosh(\gamma_b b)}$$

$$\times(\cosh(\gamma_L x_a')T_b - \cosh(\gamma_L x_b')D_a),$$

$$G_h^{zx} = -\frac{ik_z}{N}\frac{\cosh(\gamma_b(x+b+L/2))}{\cosh(\gamma_b b)}$$

$$\times(\sinh(\gamma_L x_a')T_b - \sinh(\gamma_L x_b')D_a),$$

$$G_h^{zz} = \frac{\gamma_L}{N}\frac{\cosh(\gamma_b(x+b+L/2))}{\cosh(\gamma_b b)}$$

$$\times(\cosh(\gamma_L x_a')T_b - \cosh(\gamma_L x_b')D_a),$$

$$G_h^{yy} = -\frac{k_{0L}^2}{\gamma_L N^y}\frac{\cosh(\gamma_b(x+b+L/2))}{\cosh(\gamma_b b)}$$

$$\times(\cosh(\gamma_L x_a')T_b^y - \cosh(\gamma_L x_b')D_a^y),$$

$$G_E^{xy} = -\frac{\omega\mu_0 k_z}{\gamma_b N^y}\frac{\epsilon_L\gamma_b}{\epsilon_b\gamma_L}\frac{\cosh(\gamma_b(x+b+L/2))}{\cosh(\gamma_b b)}$$

$$\times(\cosh(\gamma_L x_a')T_b^y - \cosh(\gamma_L x_b')D_a^y),$$

$$G_E^{yx} = -\frac{\omega\mu_0 k_z}{\gamma_b N}\frac{\sinh(\gamma_b(x+b+L/2))}{\cosh(\gamma_b b)}$$

$$\times(\sinh(\gamma_L x_a')T_b - \sinh(\gamma_L x_b')D_a),$$

$$G_E^{yz} = -\frac{i\omega\mu_0\gamma_L}{\gamma_b N}\frac{\sinh(\gamma_b(x+b+L/2))}{\cosh(\gamma_b b)}$$

$$\times(\cosh(\gamma_L x_a')T_b - \cosh(\gamma_L x_b')D_a),$$

$$G_E^{zy} = \frac{i\omega\mu_0}{N^y}\frac{\epsilon_L\gamma_b}{\epsilon_b\gamma_L}\frac{\sinh(\gamma_b(x+b+L/2))}{\cosh(\gamma_b b)}$$

$$\times(\cosh(\gamma_L x_a')T_b^y - \cosh(\gamma_L x_b')D_a^y).$$

The remaining components of the dyadic Green's functions are identically zero.

The above formulas involve the following designations:

$$G_1(x) = \cosh(\gamma_L(x+L/2))$$

$$+\frac{\gamma_L}{\gamma_b}\tanh(\gamma_b b)\sinh(\gamma_L(x+L/2)),$$

$$G_2(x) = -\cosh(\gamma_L(x-L/2))$$

$$+\frac{\gamma_L}{\gamma_a}\tanh(\gamma_a a)\sinh(\gamma_L(x-L/2)),$$

$$G_3(x) = \sinh(\gamma_L(x+L/2))$$

$$+\frac{\gamma_L}{\gamma_b}\tanh(\gamma_b b)\cosh(\gamma_L(x+L/2)),$$

$$G_4(x) = -\sinh(\gamma_L(x-L/2))$$

$$+\frac{\gamma_L}{\gamma_a}\tanh(\gamma_a a)\cosh(\gamma_L(x-L/2)),$$

$$N = \sinh(\gamma_L d)$$

$$\times\left\{\sinh(\gamma_L L)\left(1+\frac{\gamma_L^2}{\gamma_a\gamma_b}\tanh(\gamma_a a)\tanh(\gamma_b b)\right)\right.$$

$$\left.+\cosh(\gamma_L L)\left(\frac{\gamma_L}{\gamma_b}\tanh(\gamma_b b)+\frac{\gamma_L}{\gamma_a}\tanh(\gamma_a a)\right)\right\},$$

$$T_a = \sinh(\gamma_L a) - \frac{\gamma_L}{\gamma_b}\tanh(\gamma_b b)\cosh(\gamma_L a),$$

$$T_b = -\sinh(\gamma_L b) + \frac{\gamma_L}{\gamma_a}\tanh(\gamma_a a)\cosh(\gamma_L b),$$

$$D_a = \sinh(\gamma_L(a+L)) + \frac{\gamma_L}{\gamma_a}\tanh(\gamma_a a)\cosh(\gamma_L(a+L)),$$

$$D_b = \sinh(\gamma_L(b+L)) + \frac{\gamma_L}{\gamma_b}\tanh(\gamma_b b)\cosh(\gamma_L(b+L)),$$

$$x_a = x + a + L/2, \quad x_b = x - b - L/2,$$

$$d = a + b + L.$$

Elements G_i^y, N^y, T_i^y, and D_i^y can be obtained from elements G_i, N, T_i, and D_i using the following changes:

$$\frac{\gamma_L}{\gamma_a} \longrightarrow \frac{\epsilon_L\gamma_a}{\epsilon_a\gamma_L}, \quad \frac{\gamma_L}{\gamma_b} \longrightarrow \frac{\epsilon_L\gamma_b}{\epsilon_b\gamma_L}.$$

The obtained expressions for components of the dyadic Green's functions can be used in the solution of a wide spectrum of problems coupled with the investigation of both linear and nonlinear spin waves propagating in layered MDFDM structures of an arbitrary transverse geometry.

This work was supported by the Russian Foundation for Basic Research (project no. 99-02-16370) and the Ministry of General and Professional Education of the Russian Federation (project no. 97-8.3-13).

REFERENCES

1. J. D. Adam, D. M. Back, K. M. S. V. Bandara, *et al.*, *Physics of Thin Films. Thin Films for Advanced Electronic Devices* (Academic, New York, 1991).
2. B. A. Kalinikos, Izv. Vyssh. Uchebn. Zaved., Fiz. **24** (8), 42 (1981).
3. V. F. Dmitriev and B. A. Kalinikos, Izv. Vyssh. Uchebn. Zaved., Fiz. **31** (11), 24 (1988).
4. M. J. Lancaster, J. Powell, and A. Porch, Supercond. Sci. Technol. **11**, 1323 (1998).
5. M. P. Kostylev, B. A. Kalinikos, and H. Doetsh, J. Magn. Magn. Mater. **145**, 93 (1995).

Translated by A. Kondrat'ev

Technical Physics Letters, Vol. 26, No. 8, 2000, pp. 734–736. Translated from Pis'ma v Zhurnal Tekhnicheskoĭ Fiziki, Vol. 26, No. 16, 2000, pp. 77–82.

Effect of the Shock-Wave Treatment on the Dynamic Strength of 38KhN3MFA Steel

M. V. Sil'nikov, A. I. Mikhaĭlin, A. V. Petrov, Yu. I. Meshcheryakov, V. A. Ermolaev, N. S. Kochetova, and S. M. Usherenko

Special Materials Research and Production Corporation, St. Petersburg, Russia
Pulsed Processing Research and Production Corporation, Minsk, Belarus

Received October 19, 1999; in final form, March 17, 2000

Abstract—Effect of the shock-wave treatment on the dynamic strength of a 38KhN3MFA grade steel was studied in two different regimes—shock wave propagation and superdeep incorporation of ultrafine powder. In the first case, an increase in the dynamic strength is observed, related primarily to a decrease in the proportion of hard and brittle domains in the material as a result of the shock-wave action. The superdeep ultrafine powder incorporation produced no significant effects on the dynamic properties of steel. *© 2000 MAIK "Nauka/Interperiodica".*

The effects of shock waves on the properties of metals and alloys have always attracted the attention of scientists and technologists [1–4]. From the fundamental standpoint, this is a way to probe materials in the range of extremely high pressures and deformation rates, while researches are mostly interested in obtaining materials with high mechanical and technological properties not achievable for the other methods of processing. Although a considerable amount of experimental and theoretical information has been gained to the present concerning the effects of shock-wave action on the properties of solids, any new data in the field are still of great value.

The purpose of this work was to study the effects of two preliminary shock-wave treatment regimes on the dynamic strength of a structural alloyed steel of the 38KhN3MFA grade. The experiments were performed on cylindrical specimens with a diameter of 52 mm and a height of 10 mm, this shape being necessary for subsequent investigation of the dynamic mechanical properties of steel. In the first treatment regime, an explosion-initiated shock wave propagated through the specimens. In the second case, the same specimens were subjected to a triple joint action of a shock wave and a high-velocity (3000 m/s) dense (1–4 g/cm^3) jet stream of a mixture of ultrafine SiC and Ni powders. The time of material exposure to the particle flux was 100 μs. The background pressure in both cases was 10 GPa.

As is known [5, 6], the exposure of a metal to such a high-velocity jet stream results in penetration of the ultrafine particles to a very high material depth (up to a few millimeters). This leads to the formation of a modified composite layer representing a viscous matrix of the base material with incorporated solid powder particles, featuring the tracks of particle propagation. The tracks exhibit a complicated morphology, comprising a structureless zone of amorphized material, a region of strong fragmentation, and a domain of cellular dislocation structure. It was reported that the shock-wave treatment using a microparticle jet stream can modify the properties of materials, in particular, markedly increase the wear resistance of cutting instruments [6]. Simonenko *et al.* [7] proposed a model of particle capture and entraining by the shock-wave front, but the mechanism of superdeep penetration is still unclear. The two types of treatment were specially selected so as to allow us to separate the effect of the shock wave, accompanying the superdeep particle penetration, from a change in the material structure and properties related to the incorporation of powder in the material studied.

The dynamic strength was studied with the aid of a setup comprising a pneumatic light-gas gun and a differential laser interferometer. Nonplanarity of the striker and target at the moment of collision did not exceed 10^{-3} rad, and the collision velocity was 300–350 m/s. The interference signals were processed as described in [8] to obtain the target free surface velocity V and the velocity dispersion ΔV as functions of time. These data were used to determine the split velocity and split strength of the target material.

As seen from the data presented in Fig. 1, the split velocity $V = V_{max} - V_{min}$ of the 38KhN3MFA steel increased from 187 to 235 m/s for the specimens treated by the first method and to 248 m/s for the specimens subjected to the combined action of the shock wave and ultrafine powder. The split strength increased from 4.30 to 5.41 and 5.70 GPa. Thus, the main contribution to the dynamic strengthening is related primarily to the shock wave action.

In order to elucidate factors responsible for the increase in the dynamic strength of the 38KhN3MFA steel, we have studied the material structure by optical

1063-7850/00/2608-0734$20.00

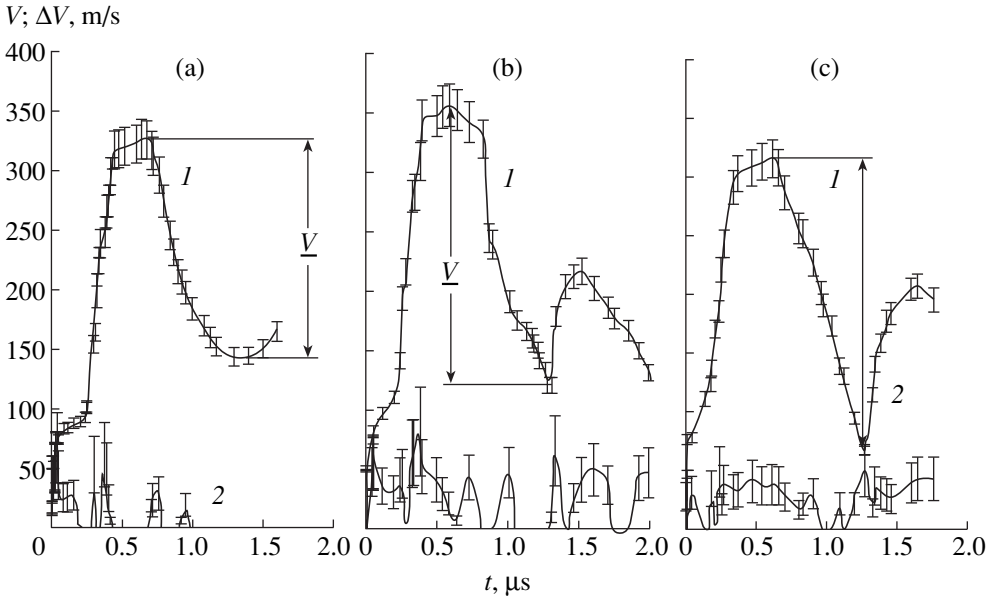

Fig. 1. Time variation of (*1*) the free surface velocity V and (*2*) the velocity dispersion ΔV for 38KhN3MFA steel specimens (a) in the initial state, (b) upon the shock-wave treatment and (c) upon the joint action of shock wave and dispersed particle incorporation.

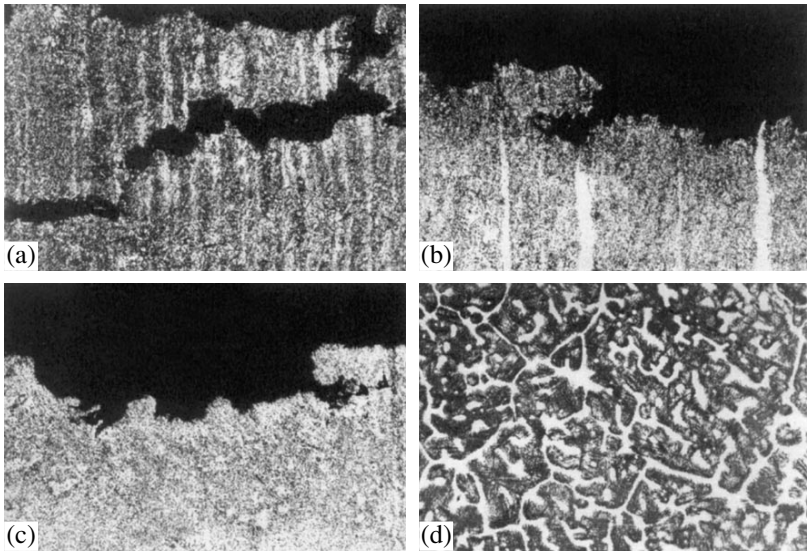

Fig. 2. Micrographs showing the morphology of 38KhN3MFA steel specimens (a, d) in the initial state, (b) upon the shock-wave treatment, and (c) upon the joint action of shock waves and incorporated ultrafine particles. The section plane is (a, b, c) parallel and (d) perpendicular to the rolling direction (magnification, ×100).

microscopy and measured the micro- and macrohardness at various points in the specimen cross section. Micrographs presented in Fig. 2 show that the region of split fracture in the initial specimens contains a considerable number of secondary cracks. The fracture surfaces also show an inhomogeneous band structure, which is also most pronounced in the initial state.

The bands are parallel to the rolling direction of a material from which the specimens were made (Fig. 2c). Along the axis perpendicular to the rolling direction, the structure of steel in both initial and treated states comprises the alternation of light and dark regions with dimensions corresponding to the band separation in Figs. 2a–2c. This fact is most clearly manifested in the initial specimen (Fig. 2d). No noticeable traces of the superdeep penetration of ultrafine particles were observed.

The microhardness of steel was markedly different in the light and dark regions, amounting to 473 and 321 HV50, respectively. Probably, the light bands cor-

respond to the regions of either increased carbon content or localized rolling deformation. In specimens upon the shock-wave treatment by both methods, the microhardness of bands remained the same, but the proportion of hard regions markedly decreased. As a result, the macrohardness of treated specimens decreased to 42 HRC (for both methods) against 45 HRC in the initial state. Thus, the increase in the dynamic strength of the 38KhN3MFA steel upon the shock-wave treatment of the type studied is due to a decrease in the proportion of hardest (and, probably, most brittle) component of the initially inhomogeneous material.

REFERENCES

1. J. Rinehart and J. Pearson, *Explosive Working of Metals* (Pergamon, Oxford, 1963; Mir, Moscow, 1966).
2. J. Rinehart and J. Pearson, *Behavior of Materials under Impulsive Loads* (Pergamon, Oxford, 1954; Inostrannaya Literatura, Moscow, 1958).
3. A. A. Deribas, *The Physics of Explosion Welding and Hardening* (Nauka, Novosibirsk, 1980).
4. P. Yu. Pashkov and Z. M. Gelunova, *The Effect of Shock Waves on Hardened Steels* (Volgograd, 1969).
5. V. G. Gorobtsov, K. I. Kozorezov, and S. M. Usherenko, Poroshk. Metall. (Minsk) **6** (1982).
6. K. I. Kozorezov, V. N. Maksimenko, and S. M. Usherenko, in *Selected Topics in Modern Mechanics* (1981), Part 1.
7. V. A. Simonenko, N. A. Skorkin, and V. V. Bashurov, Fiz. Goreniya Vzryva **27** (4), 46 (1991).
8. Yu. I. Meshcheryakov and A. K. Divakov, Preprint No. 25, Leningr. Filial Inst. im. A. A. Blagonravova Akad. Nauk SSSR (Leningrad Branch of the Blagonravov Inst. Acad. Sci. USSR).

Translated by P. Pozdeev

Technical Physics Letters, Vol. 26, No. 8, 2000, pp. 737–739. Translated from Pis'ma v Zhurnal Tekhnicheskoĭ Fiziki, Vol. 26, No. 16, 2000, pp. 83–88.

The Energy-Analyzing Properties of a Solenoid with a Screw Magnetic Axis

A. E. Dubinov and N. V. Kozlova

Sarov Physical Engineering Institute, Russian Federal Nuclear Center, Sarov, Russia

Received March 31, 2000

Abstract—The shape of a beam autograph in an electron energy analyzer with a screw magnetic axis was theoretically analyzed in a single-particle approximation. It is established that the autograph represents a flat smooth spiral involving inward with increasing energy and possessing self-tangency points. The dynamic range of the beam spectrum variation in the energy analyzer based on a screw-magnetic-axis solenoid is markedly greater as compared to that in an analogous system with toroidal magnetic field. © *2000 MAIK "Nauka/Interperiodica".*

At present, magnetostatic energy analyzers [1, 2] are the principal means of investigating the characteristics of high-current beams of charged particles. Of most interest are the energy analyzers based on solenoids conjugated with the magnetic systems of particle accelerators.

Previously [3, 4], we described an electron spectrometer based on implementing a toroidal solenoid. The principle of the electron beam energy determination in such a device is as follows. First, the analyzed part is cut from a beam with the aid of a thick diaphragm with a small hole. Then, the extracted part is passed along the curvilinear solenoid axis. As is known, electrons drifting in such a magnetic field deviate from the axis [5], the deviation being dependent on the longitudinal energy of electrons entering into the solenoid. Placing a transverse indicator plate (e.g., a photographic plate) at the solenoid output gives the so-called "beam autograph"—a curve every point of which corresponds to a certain energy. By analyzing of the intensity of blackening (optical density) at various points of the autograph, we may determine the energy spectrum of electrons.

However, it was found that the magnetic field configuration in this spectrometer has several disadvantages. First, solenoids with a toroidal magnetic field possess a rather narrow dynamic range for the energy measurements, limited from both above and below. These limitations are related to a special character of the charged particle motion in this magnetic field, which is well known from the analysis of similar motions in the toroidal thermonuclear traps. The limitation from below is related to the existence of an energy range in which the particles are "locally confined" and travel by the so-called "banana" trajectories [5]. The limitation from above becomes significant when the Larmor diameter exceeds the toroidal solenoid coil radius. Indeed, the energy spectra of electrons measured in the pulsed high-current direct-action accelerators [3, 4] exhibit no low-energy components, although the simplest analysis of the operation of these accelerators indicates that low-energy electrons must significantly contribute to the total energy spectrum. In other words, electrons with small energies are reflected by the magnetic field and cannot reach the photographic plate. Electrons with very large energies strike the analyzer chamber walls and are absorbed, thus also not reaching the plate.

Second, the autographs obtained on a photographic plate in a toroidal spectrometer exhibit nondifferentiable features of the reversal point type, hindering the analysis of the spectrum.

Below, we consider a different configuration of solenoid for the energy analyzer in which the magnetic axis has the form of a screw line (Fig. 1). This solenoid was considered previously [6] as the prototype of a thermonuclear trap with curvilinear magnetic axis.

The spatial distribution of magnetic field in a solenoid with the screw magnetic axis with a radius $r_0 = a/2$ can be approximately described in the cylindrical coordinates [6]:

$$\begin{pmatrix} B_r \\ B_\varphi \\ B_z \end{pmatrix} = \begin{pmatrix} \frac{1}{2}\varepsilon B_0\left(1 + \frac{3}{8}\varepsilon^2\frac{r^2}{a^2}\right)\sin\theta \\ \frac{1}{2}\varepsilon B_0\left(1 + \frac{1}{8}\varepsilon^2\frac{r^2}{a^2}\right)\cos\theta \\ B_0\left(1 - \varepsilon^2\frac{r}{2a}\right)\cos\theta \end{pmatrix},$$

where $\theta = \varphi - \alpha z$, $\alpha = \varepsilon/a$, and ε, a, and B_0 are constant quantities.

1063-7850/00/2608-0737$20.00

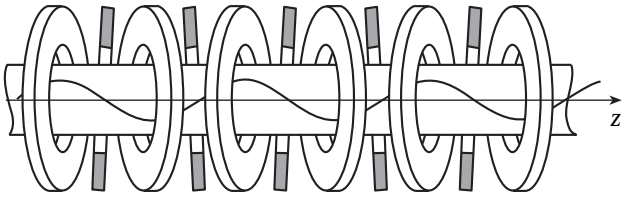

Fig. 1. Schematic diagram of a solenoid with a screw magnetic axis.

The shape of a beam autograph on a photographic plate can be calculated using a single-particle approximation. The equations of motion of a relativistic electron can be written in the following form [7]:

$$\frac{d}{dt}\begin{pmatrix} v_r \\ v_\varphi \\ v_z \end{pmatrix} = \begin{pmatrix} g_r + \dfrac{v_\varphi^2}{r} \\ g_\varphi - \dfrac{v_r v_\varphi}{r} \\ g_z \end{pmatrix},$$

where

$$\begin{pmatrix} g_r \\ g_\varphi \\ g_z \end{pmatrix} = \eta\gamma^{-1}\begin{pmatrix} v_\varphi B_z - v_z B_\varphi \\ v_z B_r - v_r B_z \\ v_r B_\varphi - v_\varphi B_r \end{pmatrix},$$

$\eta = e/m$ is the specific charge of electron (electron charge to mass ratio) and γ is the Lorentz factor (invariant in the given problem).

The above equations of motion were solved by the Runge–Kutta method; the error of the calculation was determined using the law of the total electron energy conservation ($v_r^2 + v_\varphi^2 + v_z^2 = \text{const}$).

Figure 2 shows an example of an autograph for a beam injected into solenoid along the *z*-axis, which was calculated for the following parameters: magnetic field $B_0 = 0.1$ T; $\varepsilon = 0.1$; electron transit distance $L = 0.3$ m; screw magnetic axis radius $r_0 = 0.1$ m.

It was found that the beam autographs have the shape of a smooth spiral involving inward, not possessing any nondifferentiable features hindering the data processing. However, the spiral exhibits a self-tangency point (Fig. 2b, point A) in the vicinity of which the beam energy spectrum processing encounters certain difficulties. As is readily seen, the dynamic energy range is limited neither from above (for $\gamma \longrightarrow \infty$, the curve in Fig. 2 involves toward the central point of the spiral autograph) nor from below (we failed to find "banana" trajectories even for an electron energy of 10 keV).

Thus, the results of our calculations demonstrated advantages of the energy analyzer with a screw magnetic axis, which possess a broader dynamic range for the energy measurements as compared to the analyzer with toroidal magnetic field. However, the autograph still contains points complicating the data processing. It should be also noted that the solenoid with a screw magnetic axis is smaller than its toroidal counterpart.

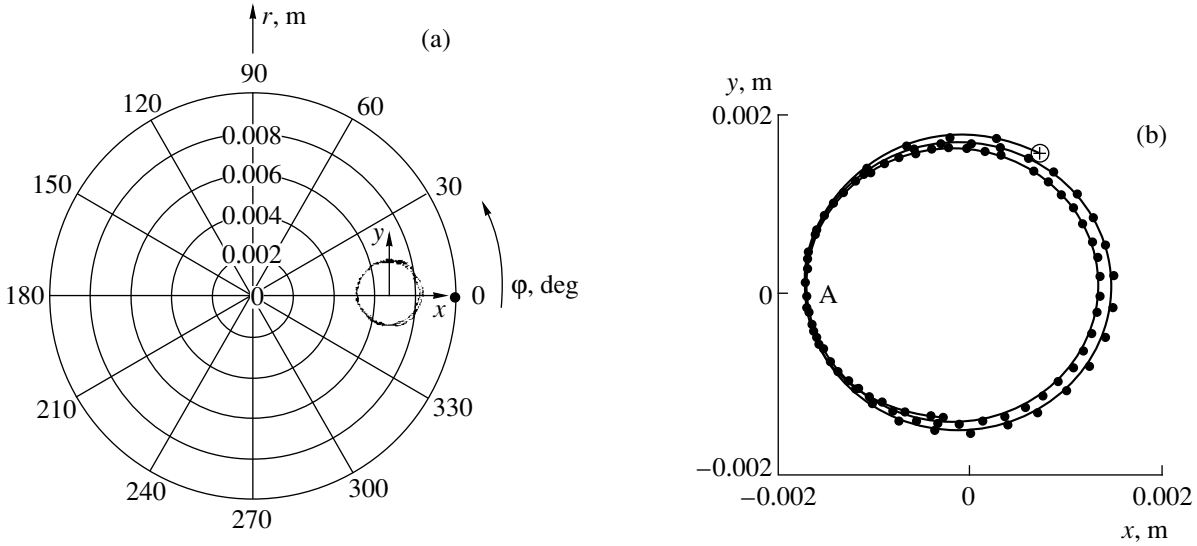

Fig. 2. An example of the beam autograph (a) plotted in the polar coordinates (the electron entrance point with the coordinates $r = 0.01$ m and $\varphi = 0°$ is indicated by the black circle) and (b) depicted on a greater scale in the local (x, y) coordinates (black circles corresponding to the energy varied from 100 to 300 keV at 2 keV point; open circle corresponds to 100 keV).

REFERENCES

1. A. I. Gerasimov, E. G. Dubinov, and B. G. Kudasov, Prib. Tekh. Éksp., No. 3, 31 (1971).
2. N. I. Tarantin, *Magnetic Static Analyzers of Charged Particles* (Énergoatomizdat, Moscow, 1986).
3. A. E. Dubinov, N. V. Minashkin, V. D. Selemir, *et al.*, in *Proceedings of 9th IEEE International Pulsed Power Conference, Albuquerque, 1993*, p. 708.
4. N. V. Stepanov, V. E. Vatrunin, and V. D. Selemir, in *Investigations into Plasma Physics: A Collection of Scientific Works*, ed. by V. D. Selemir and A. E. Dubinov (Russian Federal Nuclear Center–Institute of Experimental Physics, Sarov, 1998), p. 232.
5. Yu. N. Dnestrovskiĭ and D. P. Kostomarov, *Numerical Simulation of Plasmas* (Nauka, Moscow, 1993).
6. A. V. Georgievskij, V. E. Ziser, V. V. Nemov, *et al.*, Nucl. Fusion **14** (1), 79 (1974).
7. A. S. Roshal', *Modeling of Charged Particle Beams* (Atomizdat, Moscow, 1979).

Translated by P. Pozdeev

Technical Physics Letters, Vol. 26, No. 8, 2000, pp. 740–743. Translated from Pis'ma v Zhurnal Tekhnicheskoĭ Fiziki, Vol. 26, No. 16, 2000, pp. 89–96.

Nonparaxial Gaussian Beams: 2. Splitting of the Singularity Lines and the Optical Magnus Effect

A. V. Volyar and T. A. Fadeeva

Simferopol State University, Simferopol, Ukraine

Received November 23, 1999

Abstract—The Poynting vector field lines for the lowest modes of a nonparaxial Gaussian beam exhibit a number of loops and rings in the vicinity of the phase singularity lines (Airy's fringes), with negative energy fluxes present inside these loops and rings. The positions of these fluxes are nonsymmetric with respect to rotation about the optical axis. This asymmetry leads to a local splitting of the phase singularity lines, after which the beam cross section transforms from circular to elliptic. The asymmetry of the beam cross section can be eliminated by considering a superposition of circularly polarized even and odd modes. However, this approach only uniformly redistributes the negative energy fluxes in the azimuthal direction of the cross section, rather than completely eliminates these fluxes. Any small perturbation of the resulting symmetric beam gives rise to a unique phenomenon—the optical Magnus effect in the free space, whereby the beam intensity pattern rotates upon changing the circular polarization from right to left. This effect implies the presence of a spin–orbit coupling in the nonparaxial Gaussian beam propagating in the free space. © *2000 MAIK "Nauka/Interperiodica"*.

In the first part of this work,[1] we demonstrated that a linearly polarized nonparaxial low-order Gaussian beam may exist in the form of four modes, representing even (LP^{ev}) and odd (LP^{od}) waves with predominant *x*- or *y*-polarization. We have suggested that the linear polarization of modes is the factor accounting for a change in symmetry of the beam cross section in the region of transition from circular to elliptic shape (or vice versa) and, hence, for the vector field separation with respect to parity (in the general case, this assumption is really valid for unconfined waves subject to strong focusing [1, 2]). It should also be noted that the parity and polarization characteristics of a nonparaxial beam are subject to strict formal relationships. In particular, the *y*-electric polarization corresponds to an even mode and the *x*-magnetic polarization, to an odd mode. For the even modes, the electric field vector is parallel to the large semiaxis of the elliptic cross section, while the same condition holds in the odd modes for the magnetic field vector.

In additions, it was established that the axial energy flux near the focal plane may acquire negative values in the vicinity of the ring-shaped phase dislocations (Airy's fringes). The position of Airy's fringes, strictly confined by the focal plane in the single-mode states, can change for the mode superpositions of the $LP^{ev} \pm iLP^{od}$ types, where the (+) and (–) signs correspond to the position of fringes in front of or behind the focal plane. These unique phenomena, occurring in the free space, were related to the mutual asymmetry of electric and magnetic field and the presence of a special polarization direction. It might be expected that the above phenomena will not accompany a circularly polarized nonparaxial Gaussian beam possessing no special directions of this kind.

The purpose of this work was to study the vector properties of circularly polarized nonparaxial Gaussian beams propagating in the free space in the vicinity of the focal plane.

1. Let us consider a monochromatized low-order single-mode beam ($l = 0$) propagating in free space in the *z*-axis direction, representing a solution to the Maxwell equations. We will also require that this beam would transform into a paraxial Gaussian beam upon going to the paraxial approximation ($kz_0 \ll 1$, where z_0 is the Rayleigh length and $k_0 = 2\pi/\lambda$ is the wavenumber in vacuum) [2]. The Cartesian field components of this beam were tabulated in the first part of this work. We will use these components to form a circularly polarized (CP) field in the cylindrical $\{r, \varphi, z\}$ coordinate system by the following scheme: $CP_{ev}^{(\sigma)} \Rightarrow LP(e_y) + i\sigma LP(e_x)$ and $CP_{od}^{(\sigma)} \Rightarrow LP(h_y) + i\sigma LP(h_x)$ (here, $\sigma = \pm 1$ is the spirality factor determining the direction of rotation of the polarization vector):

$$CP_{ev}: e_r = \sigma(z + iz_0)F_1\exp(i\sigma\varphi),$$

$$e_\varphi = i(z + iz_0)F_1\exp(i\sigma\varphi), \quad e_z = \sigma\frac{\partial F_0}{\partial r}\exp(i\sigma\varphi),$$

$$h_r = (G_1 + r^2F_2)\exp(i\sigma\varphi), \quad h_\varphi = i\sigma G_1\exp(i\sigma\varphi),$$

$$h_z = -(z + iz_0)\frac{\partial F_1}{\partial r}\exp(i\sigma\varphi); \qquad (1)$$

[1] *Tech. Phys. Lett.* **26** (7), 573 (2000).

1063-7850/00/2608-0740$20.00 © 2000 MAIK "Nauka/Interperiodica"

$$CP_{\text{od}}: e_r = (G_1 + r^2F_2)\exp(i\sigma\varphi),$$
$$e_\varphi = i\sigma G_1\exp(i\sigma\varphi),$$
$$e_z = -(z + iz_0)\frac{\partial F_1}{\partial r}\exp(i\sigma\varphi).$$
$$h_r = -\sigma(z + iz_0)F_1\exp(i\sigma\varphi),$$
$$h_\varphi = -i(z + iz_0)F_1\exp(i\sigma\varphi),$$
$$h_z = -\sigma\frac{\partial F_0}{\partial r}\exp(i\sigma\varphi). \quad (2)$$

For brevity, Eqs. (1) and (2) are written in the CGS system of units, with wavenumbers expressed in the units of $k = 2\pi/\lambda$.

An analysis of these expressions shows that implementation of the circularly polarized basis and cylindrical coordinates cannot solve the problem of mutual symmetry of the electric and magnetic fields of the single-mode beam. In order to provide for the further symmetrization of the fields, we will use a superposition of even (1) and odd (2) modes constructed according to the scheme $CP^{(\sigma,\kappa)} \Rightarrow CP^{(\sigma)}_{(\text{ev})} + i\kappa CP^{(\sigma)}_{(\text{od})}$ (where $\kappa = \pm 1$ is the orbital index):

$$e_r = \{\sigma(z + iz_0)F_1 + i\kappa(G_1 + r^2F_2)\}\exp(i\sigma\varphi),$$
$$e_\varphi = i\sigma\{\sigma(z + iz_0)F_1 + i\kappa G_1\}\exp(i\sigma\varphi),$$
$$e_z = -i\sigma\frac{\partial}{\partial r}\{(z + iz_0)F_1 + i\kappa\sigma F_0\}\exp(i\sigma\varphi), \quad (3)$$
$$h_r = -\{\sigma(z + iz_0)F_1 + i\kappa(G_1 + r^2F_2)\}\exp(i\sigma\varphi),$$
$$h_\varphi = \kappa\sigma\{\sigma(z + iz_0)F_1 + i\kappa G_1\}\exp(i\sigma\varphi),$$
$$h_z = -i\sigma\kappa\frac{\partial}{\partial r}\{(z + iz_0)F_1 + i\kappa\sigma F_0\}\exp(i\sigma\varphi). \quad (4)$$

Now, the electric and magnetic fields are almost symmetric. In order to render these fields fully symmetric from the standpoint of the paraxial approximation, let us take into account that the second term in parentheses in the expressions for e_r and h_r is smaller than the first term by two orders of magnitude ($G_1 \gg r^2F_2$), the relationship being valid even under a weak condition of $kz_0 \geq 1$. This term reflects the deviation of the field

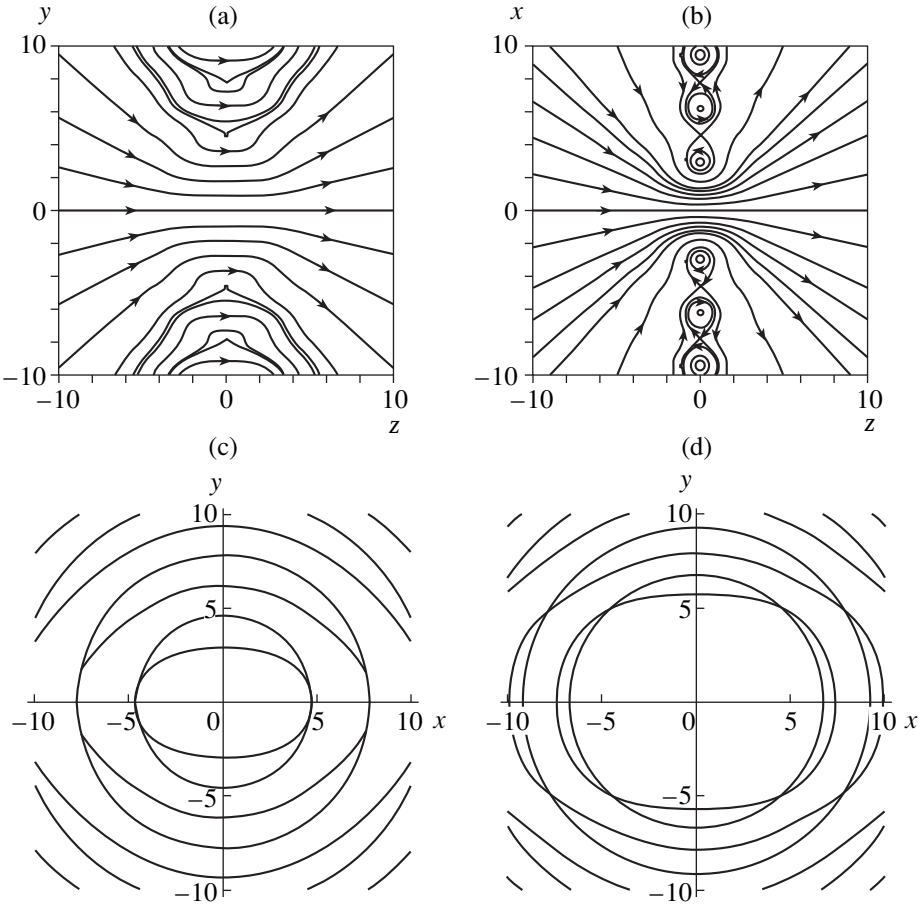

Fig. 1. Maps of the Poynting vector field lines for the even $LP(e_y)$ mode in the (a) $x = 0$ and (b) $y = 0$ planes and maps of the singularity lines $P_z(x, y, z) = 0$ of the same mode for (c) $kz_0 = 1$ and (d) $kz_0 = 5$ (all lengths expressed in units of $k = 2\pi/\lambda$).

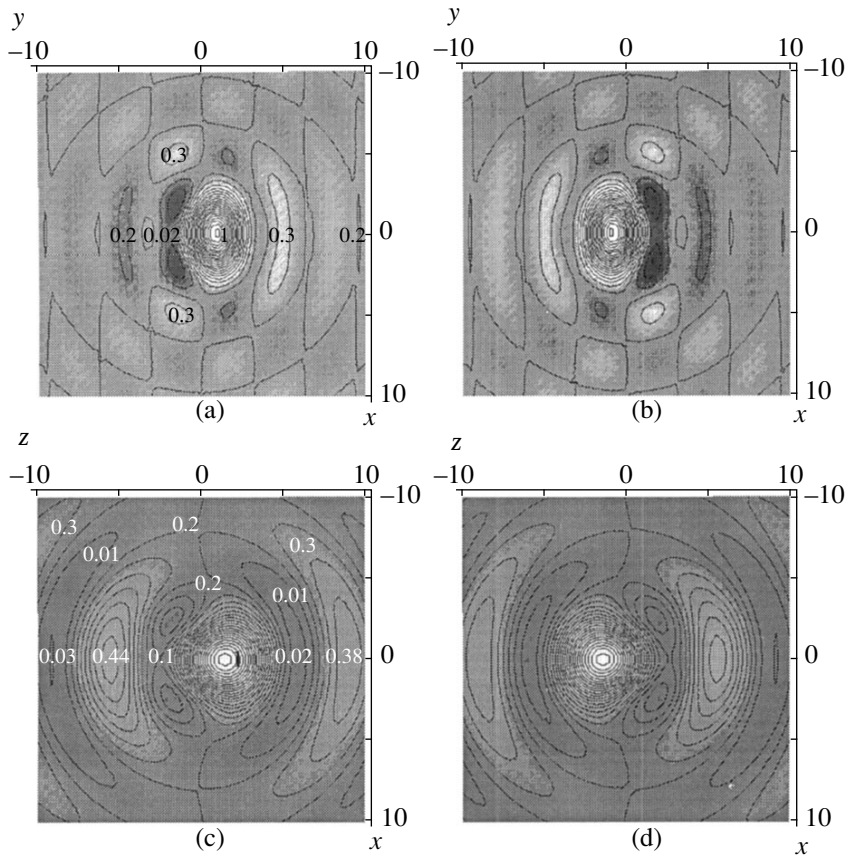

Fig. 2. Maps of the intensity levels for a superposition of the circularly polarized $CP^{(\sigma, \kappa)}$ mode and a plane monochromatic wave with the amplitude $a_0 = 1$ propagating along the optical axis ($\alpha = 0$) in the (a, b) *xy* and (c, d) *xz* planes for (a, c) $\sigma = 1$ and (b, d) $\sigma = -1$ ($kz_0 = 1$).

polarization from the circular type. In the paraxial approximation, the electric and magnetic fields must satisfy a relationship of the type $\mathbf{h}_t = \hat{z} \times \mathbf{e}_t$. Then, Eqs. (3) and (4) imply that

$$\sigma\kappa = 1. \quad (5)$$

The rigid relationship between the "spin" and "orbital" characteristics of the vector field is indicative of the presence of a spin–orbit coupling in the nonparaxial beam. In the following paper, we will attempt to strictly prove this statement in the case of nonparaxial optical vortices. Here, we will restrict the consideration to an illustrative interpretation of this phenomenon. It should be noted that we have checked the validity of the condition $\sigma\kappa = -1$ for the fields described by Eqs. (3) and (4) by computer simulation. It was found that these fields, albeit not representing travelling waves, form a special state of the "light droplet" type mentioned in the first part of this work.

Figures 1a and 1b show maps of the Poynting vector field lines for the even $LP(e_y)$ mode (see table in the first part of this work) in the $x = 0$ and $y = 0$ planes, respectively. Note the lack of symmetry in the field lines with respect to the $\pi/2$ rotation. This asymmetry is related to the negative energy fluxes in the *z*-axis direction. In Fig. 1a, the field lines in the vicinity of Airy's fringes in the $x = 0$ plane exhibit a singularity of the cusp type (no negative energy flux). At the same time, the ring and loop lines of the Poynting vector field in the orthogonal plane $y = 0$ (Fig. 1b) are indicative of the presence of negative energy fluxes.

The main part of the light flux is concentrated within a region at the focal plane with the coordinates $r < z_0$ and is projected onto the observation plane as a family of hyperbolas. In this region, lying in the vicinity of the optical axis and corresponding to the paraxial approximation, the field lines represent a family of straight generators of a one-sheet hyperboloid of rotation [4]. Note that the loop and ring trajectories are indicative of the presence of the sin–orbital coupling in the nonparaxial beam [5]. A comparison of the map of field lines in Fig. 1a to that reported for the wave energy flux behind a high-aperture microobjective lens [2, Fig. 4.21] shows good coincidence of the results obtained by different methods.

2. A remarkable feature is offered by inhomogeneous distribution of the negative energy fluxes and the related splitting of singularity lines. This effect resem-

bles the phenomenon of multiplicity of the atomic energy levels arising due to the influence of a microparticle spin. Figures 1c and 1d show families of the singularity lines ($P_z = 0$) of the $LP(e_y)$ mode, on which both real and imaginary parts of the transverse electric and magnetic field components simultaneously turn zero. The singularity lines of the $LP(e_x)$ mode will be merely rotated by $\pi/2$. Splitting of the singularity lines leads to a unique phenomenon—the optical Magnus effect for a single-mode beam in the free space. Let us consider this effect in some more detail.

The presence of the spin–orbit coupling implies a difference in the beam wavefunction response to the right-hand ($\sigma = 1$) and left-hand ($\sigma = -1$) circular polarizations. However, the fields (3) and (4) are symmetric with respect to rotation about the optical axis. In order to break the external symmetry, let us introduce a small perturbation in the form of a plane wave with the amplitude a_0, propagating at the angle α relative to the z-axis. The results of the small perturbation action upon the single-mode beams with the right-hand and left-hand circular polarizations in the focal plane are illustrated in Fig. 2. As seen from the intensity P_z distribution in the focal plane $z = 0$, the polarization switching from $\sigma = 1$ to $\sigma = -1$ results in the whole pattern rotation by the π angle.

The phenomenon of rotation of the speckle pattern in the field of radiation of an optical fiber upon changing the circular polarization direction is known as the optical Magnus effect [6]. This phenomenon is based upon the fundamental principles of interaction of radiation and medium with a gradient of the index of refraction. Our case presents a unique manifestation of the Magnus effect in the free space. Apparently, the role of the refractive index gradient is played by the gradient of the nonparaxial single-mode beam intensity. The possibility for observation of the transverse beam displacement by a distance of the order of half-wavelength in the focal plane of the lens was indicated by the results of approximate calculations [7]. Sadykov [8] substantiated the transverse shift of the focal spot within the framework of a geometric-optical approach.

At first glance, the transverse beam shift is not related to rotation of the intensity pattern. Nevertheless, a comparison of Figs. 2a and 2b indicates that the central spot, in which the major field intensity is concentrated, exhibits a transverse shift at a distance of $d \propto \lambda/2$ at the expense of rotation by π upon switching the circular polarization direction. It is important to note that, simultaneously with the transverse shift, the beam node exhibits a longitudinal shift by approximately the same distance (Figs. 2c, 2d). It would apparently be natural to relate the observed transverse shift to a difference in the propagation velocities of beams with orthogonal circular polarizations along the optical axis. However, this assumption is erroneous because the longitudinal Poynting vector component $\int P_z\, dS$, which is responsible for the group velocity, is the same for both orthogonal polarizations.

The authors are grateful to V.G. Shvedov for fruitful discussion.

REFERENCES

1. M. Born and É. Wolf, *Principles of Optics* (Pergamon, Oxford, 1969; Nauka, Moscow 1973).
2. S. Solimeno, B. Crosignani, and P. Di Porto, *Diffraction and Confinement of Optical Radiation* (Academic, Orlando, 1986; Mir, Moscow, 1989).
3. E. Abramochkin and V. Volostnikov, Opt. Commun. **125**, 302 (1996).
4. A. V. Volyar, T. A. Fadeeva, and V. G. Shvedov, Pis'ma Zh. Tekh. Fiz. **25** (5), 87 (1999) [Tech. Phys. Lett. **25**, 203 (1999)].
5. A. V. Volyar, V. Z. Zhilaĭtis, and V. G. Shvedov, Opt. Spektrosk. **86** (4), 664 (1999) [Opt. Spectrosc. **86**, 593 (1999)].
6. A. V. Volyar and T. A. Fadeeva, Pis'ma Zh. Tekh. Fiz. **23** (23), 59 (1997) [Tech. Phys. Lett. **23**, 927 (1997)].
7. N. B. Baranova, A. Yu. Savchenko, and B. Ya. Zel'dovich, Pis'ma Zh. Éksp. Teor. Fiz. **59** (4), 216 (1994) [JETP Lett. **59**, 232 (1994)].
8. N. R. Sadykov, Opt. Spektosk. **84** (2), 293 (1998) [Opt. Spectrosc. **84**, 250 (1998)].

Translated by P. Pozdeev

Technical Physics Letters, Vol. 26, No. 8, 2000, pp. 744–746. Translated from Pis'ma v Zhurnal Tekhnicheskoĭ Fiziki, Vol. 26, No. 16, 2000, pp. 97–102.

A New Phase Transition in Sodium Niobate

I. P. Raevskiĭ, L. A. Reznichenko, V. G. Smotrakov, V. V. Eremkin, M. A. Malitskaya, E. M. Kuznetsova, and L. A. Shilkina

Research Institute of Physics, Rostov State University, Rostov-on-Don, 344090 Russia

e-mail: smotr@ip.rsu.ru

Received March 28, 2000

Abstract—The temperature dependences of the dielectric constant ε of sodium niobate single crystals $NaNbO_3$ and sodium niobate-based $(Na,Li)NbO_3$ and $(Na,K)NbO_3$ solid solutions with low content of the second component have been studied. A weak anomaly observed in $\varepsilon(T)$ indicates a new phase transition in the vicinity of 150°C in $NaNbO_3$. The introduction of lithium or potassium into $NaNbO_3$ crystals increases the temperature of this transition. The X-ray powder diffraction data suggest that the new transition takes place between two rhombohedral phases. © *2000 MAIK "Nauka/Interperiodica".*

A large number of phase transitions (at present, their number amounts to six [1]) provided by the rotation of oxygen octahedra and by ordered ion displacements have attracted the attention of both theoreticians and experimenters to the antiferroelectric sodium niobate crystals ($NaNbO_3$) with a perovskite structure for about forty years. The studies of sodium niobate and sodium niobate-based solid solutions are also of great importance since they make the basis or are the components of various functional materials possessing piezoelectric, electrooptical, and pyroelectric properties and of materials used in capacitors, posistors, etc. [2–5]. Although it was stated that sodium niobate undergoes no phase transitions in the temperature range from –50 to 350°C [1], the temperature dependences of the electrophysical parameters of sodium niobate and sodium niobate-based solid solutions often showed weak anomalies [6–10] which could be associated, in particular, with some unknown (e.g., electric-field-induced or impurity-related) phase transitions.

Below, we describe the detailed study of dielectric and structural properties of sodium niobate and some sodium niobate-based solid solutions in the temperature range from 20 to 400°C. Since most of the phase transitions in sodium niobate are accompanied by very weak anomalies in the behavior of the dielectric constant ε [1], our studies were performed on single crystals providing much better observation of the anomalies in ε than the corresponding ceramics. $NaNbO_3$ single crystals and $(Na,Li)NbO_3$ and $(Na,K)NbO_3$ solid solutions with a low content of the second component were obtained by the method of mass crystallization in the Na_2CO_3–Nb_2O_5–B_2O_3 system [11] as colorless transparent 2-mm-long plates with a thickness ranging within 0.2–0.3 mm. The dielectric constant was measured during continuous heating or cooling at a rate of 2–3 K/min with the aid of a P5083 ac bridge in the 1–100 kHz frequency range. The Aquadag electrodes were applied onto the (001) faces of the grown crystals. The content of $LiNbO_3$ (1.5–2.5 mol %) and $KNbO_3$ (2–3 mol %) in the $(Na,Li)NbO_3$ and $(Na,K)NbO_3$ crystals was evaluated by comparing their structural parameters and the phase transition temperatures with the experimental values obtained for the ceramics and data reported for the corresponding solid solution crystals [12–14].

Figure 1 shows the $\varepsilon(T)$ curves for sodium niobate and $(Na,Li)NbO_3$ and $(Na,K)NbO_3$ crystals. In addition to the well-known anomalies in the regions of 240–270 and 350–360°C (corresponding to the well-known phase transitions) [1, 12–14], all the curves show weak anomalies in the vicinity of 150°C (for sodium niobate crystals) and 175–185°C (for the crystals of solid solutions). In fact, these anomalies have already been observed in a large number of crystals, including those synthesized under various conditions. Moreover, the temperatures of all the anomalies on the $\varepsilon(T)$ curves changed in a regular manner with the Li and K content in the solid solutions. Thus, it was possible to assume that the anomaly in $\varepsilon(T)$ in the vicinity of 150°C for sodium niobate was associated with a certain phase transition. It should also be emphasized that the analysis of published data on the properties of sodium niobate crystals and ceramics shows that weak anomalies of $\varepsilon(T)$ in the vicinity of 150°C have been repeatedly observed in various experiments [7–10]; however, they have been ignored and received no interpretation because of their low values in comparison with the features corresponding to the well-known phase transitions.

Despite the fact that the anomalies in $\varepsilon(T)$ revealed in our study are rather strongly smeared in comparison with anomalies associated with the well-known phase transitions, the temperatures of all these anomalies were almost independent of the measuring field frequency in the 1–100 kHz range. As is seen from Fig. 1,

the anomalies in $\varepsilon(T)$ corresponding to the well-known phase transitions are characterized by a pronounced temperature hysteresis (for the sake of clarity, the $\varepsilon(T)$ curve obtained in the cooling mode is shown only for the (Na,Li)NbO_3 crystals), whereas the temperature positions of the newly revealed weak anomalies in $\varepsilon(T)$ are almost independent of the mode: heating or cooling. The results obtained lead to the assumption that the character of the phase transition in the vicinity of 150°C in sodium niobate is close to a second-order phase transition.

The studies of the grown crystals in the polarized light showed that propagation of the phase fronts or changes in the extinction pattern take place only at temperatures in the 240–270 and 350–360°C regions, corresponding to the well-known phase transitions. Similar results were obtained earlier for $Na_{0.98}Li_{0.02}NbO_3$ crystals [12] together with a change in the slope of the temperature dependence of birefringence in the vicinity of 150°C indicating a possible phase transition.

The temperature dependences of the structural parameters of $NaNbO_3$ and $Na_{0.975}Li_{0.025}NbO_3$ powders synthesized by the method of solid-phase reactions showed no changes in the symmetry of the perovskite structure in the temperature range from 25 to 330–350°C. In the temperature range from 150 to 200°C (where the anomalies in $\varepsilon(T)$ were observed), only insignificant changes in the slope of the temperature dependences of the unit cell parameters *a*, *b*, and *c* and the angle β of the rhombohedrally distorted unit cell were recorded. In the vicinity of 270°C, (corresponding to the phase transition in $Na_{0.975}Li_{0.025}NbO_3$ accompanied by a pronounced anomaly in $\varepsilon(T)$), only rather weak changes in the slope of the temperature dependences of the unit cell parameters were observed. The results obtained are consistent with the structural data for $Na_{0.98}Li_{0.02}NbO_3$ powders [13] and lead to the assumption that the phase transitions in sodium niobate and the sodium niobate-based solid solutions (indicated by weak anomalies in $\varepsilon(T)$ in the vicinity of 150–200°C) take place between two rhombohedral phases.

Thus, the dielectric, optical, and structural studies and the analysis of the corresponding published data indicate that, in addition to the six well-known phase transitions in $NaNbO_3$, one more phase transition occurs in the vicinity of 150°C which is close to a second-order phase transition and is assumed to take place between two antiferroelectric rhombohedral phases. The existence of the phase transition in $NaNbO_3$ and sodium niobate-based solid solutions in the 150–200°C temperature range (which falls within the working interval of numerous functional sodium niobate-based materials) can produce a considerable effect on the temperature and temporal stability of various characteristics of these materials. This fact should necessarily be taken into account in designing new sodium niobate-based materials for various purposes. In particular, it is important to refine the corresponding temperature–

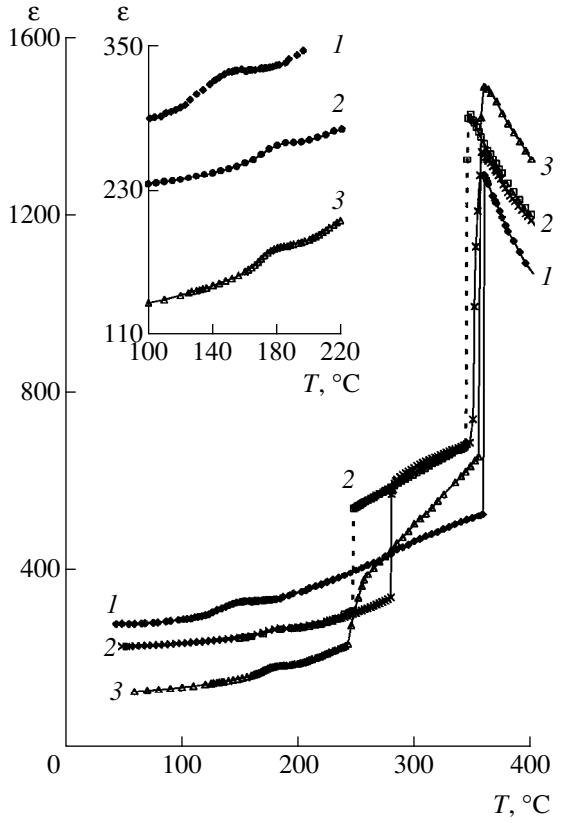

Fig. 1. Dielectric constant as a function of temperature, $\varepsilon(T)$, for (*1*) $NaNbO_3$ crystals and (*2*) (Na,Li)NbO_3 and (*3*) (Na,K)NbO_3 solid solutions with low content of the second component measured in the heating (solid lines) and cooling (dashed lines) modes at a frequency of 1 kHz.

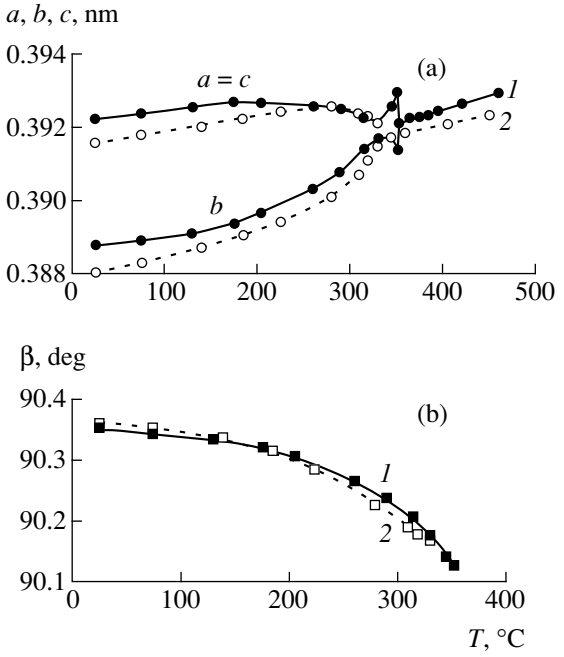

Fig. 2. Temperature dependences of the unit cell parameters of a rhombohedrally distorted perovskite-type structure of (*1*) $NaNbO_3$ and (*2*) $Na_{0.975}Li_{0.025}NbO_3$ powders.

composition phase diagrams of $NaNbO_3$-based solid solutions and the theoretical models which describe the sequence of phase transitions in $NaNbO_3$.

The study was supported by the Russian Foundation for Basic Research, project no. 99-02-17575.

REFERENCES

1. G. A. Smolenskiĭ, V. A. Bokov, V. A. Isupov, *et al.*, *The Physics of Ferroelectric Phenomena* (Nauka, Leningrad, 1985).
2. N. F. Borelly and M. Layton, IEEE Trans. Electron Devices **16** (6), 511 (1969).
3. P. Wang, T. Bai, Z. Chen, and M. Liu, J. Huazhong Univ. Sci. Technol. **16** (5), 123 (1988).
4. I. P. Raevskiĭ, L. A. Reznichenko, and M. A. Malitskaya, Pis'ma Zh. Tekh. Fiz. **26** (3), 6 (2000) [Tech. Phys. Lett. **26**, 93 (2000)].
5. A. Ya. Dantsiger, O. N. Razumovskaya, L. A. Reznichenko, and S. I. Dudkina, *High-Efficiency Piezoceramic Materials: Optimization of Search* (Paik, Rostov-on-Don, 1995).
6. V. A. Isupov, Izv. Akad. Nauk SSSR, Ser. Fiz. **22** (12), 1504 (1958).
7. N. N. Kraĭnik, Fiz. Tverd. Tela (Leningrad) **2** (4), 685 (1960) [Sov. Phys. Solid State **2**, 633 (1960)].
8. L. Pardo, P. Duran-Martin, J. P. Mercurio, *et al.*, J. Phys. Chem. Solids **58** (9), 1335 (1997).
9. K. Konieczny, W. Smiga, and C. Kus, Ferroelectrics **190**, 131 (1997).
10. K. Konieczny, Mater. Sci. Eng. B **60**, 124 (1999).
11. V. G. Smotrakov, I. P. Raevskiĭ, M. A. Malitskaya, *et al.*, Neorg. Mater. **16** (5), 1065 (1980).
12. A. Sadel, R. Von der Mühll, and J. Ravez, Mater. Res. Bull. **18**, 45 (1983).
13. A. Sadel, R. Von der Mühll, J. Ravez, *et al.*, Solid State Commun. **44** (3), 345 (1982).
14. M. Badurski and K. Stroz, J. Cryst. Growth **46**, 274 (1979).

Translated by L. Man

Technical Physics Letters, Vol. 26, No. 8, 2000, pp. 747–750. Translated from Pis'ma v Zhurnal Tekhnicheskoĭ Fiziki, Vol. 26, No. 16, 2000, pp. 103–110.

On the Possibility of Observing the Aharonov–Bohm Effect under Nonstationary Potential Conditions

A. G. Chirkov* and A. N. Ageev**

** St. Petersburg State Technical University, St. Petersburg, Russia*

*** Ioffe Physicotechnical Institute, Russian Academy of Sciences, St. Petersburg, 194021 Russia*

Received February 26, 2000

Abstract—Based on a theoretical analysis of the nonstationary excitation of a solenoid, it is demonstrated for the first time that vector potentials exist in the space outside the solenoid which can, in the general case, provide conditions for observation of the Aharonov–Bohm effect. *© 2000 MAIK "Nauka/Interperiodica".*

Since the first descriptions of the Aharonov–Bohm effect (ABE) [1–3], numerous theoretical and experimental works have been devoted to elucidating the nature of this phenomenon (see, e.g., [4, 5]). An original approach to observing this effect, not involving electron interactions with either magnetic or electric fields, consisted in realizing the situation where electrons would be moving in a region free of such fields. These conditions are most simply realized in the stationary regime; this is just the case that was studied until the beginning of 1990s. On the present-day level of technology, this regime was almost exhaustively studied in the experiments of Tonomura *et al.* [6].

Eventually, researchers turned to elucidating the possibility of the ABE manifestations in the case of nonstationary fields [7–10]. This expansion of the field of observation is very promising from the standpoint of experimental investigations, which may provide a deeper insight into the ABE nature. On the other hand, interpretation of the ABE observed under these conditions presents a more complicated task.

With a view to elucidating the ABE nature, the electromagnetic potentials are conveniently represented as the sums of two terms:

$$\mathbf{A} = \mathbf{A}^{\mathrm{f}} + \mathbf{A}^{0} \quad \text{and} \quad \varphi = \varphi^{\mathrm{f}} + \varphi^{0}, \tag{1}$$

where the superscript "f" indicates the potentials describing nonzero electromagnetic fields ("field" potentials) and superscript "0" refers to the potentials that, albeit corresponding to a solution of the Maxwell equations with boundary conditions, do not directly produce electromagnetic fields ("zero-field" or "excess" potentials). It should be noted that functions analogous to the zero-field potentials have been used for a long time in the mathematical physics. In particular, a zero-field vector potential appears (and is uniquely determined) in the problem of vector reconstruction from the given rotor and divergence a finite domain [11].

As is known [12], the zero-field potential can be represented in the following form:

$$\mathbf{A}^{0} = \operatorname{grad}\chi, \quad \varphi^{0} = -\frac{1}{c}\frac{\partial\chi}{\partial t}, \tag{2}$$

where χ is a differentiable function.

Note that the zero-field potentials are responsible for the ABE manifestations in all the works published so far dealing with the stationary case. This is related primarily to the circumstance that the ABE is observed in the "pure" form, whereby the shift of the interference bands is determined by the potentials rather than by the fields [13, 14]. On going to the nonstationary case, the question naturally arises as to whether a situation may take place whereby the zero-field potentials are created in a certain space region? In this context, the first point in analysis of the possibility of the ABE manifestations in the case of nonstationary fields must consist in determining the zero-field potentials. To our knowledge, this problem was not considered in the works published to date. As seen from the relationships determining fields through potentials,

$$\mathbf{B} = \operatorname{rot}\mathbf{A}, \quad \mathbf{E} = -c^{-1}\partial\mathbf{A}/\partial t - \operatorname{grad}\varphi, \tag{3}$$

the zero-field potentials exist only provided that $\varphi^0 \neq 0$, which implies that the Coulomb (radiation) gauge is inapplicable.

Let us consider the Maxwell–Lorentz equations describing, in the conventional notation, the electromagnetic field in a vacuum:

$$\operatorname{div}\mathbf{E} = 4\pi\rho, \quad \operatorname{rot}\mathbf{B} = \frac{4\pi}{c}\mathbf{j} + \frac{1}{c}\frac{\partial\mathbf{E}}{\partial t}. \tag{4}$$

Substituting expressions (1) and (3) into Eq. (4), we obtain equations determining the potentials:

$$\Box\varphi^{\mathrm{f}} + \frac{1}{c}\frac{\partial\Lambda^{\mathrm{f}}}{\partial t} + \Box\varphi^{0} + \frac{1}{c}\frac{\partial\Lambda^{0}}{\partial t} = -4\pi\rho, \tag{5a}$$

$$\Box \mathbf{A}^{\mathrm{f}} - \operatorname{grad}\Lambda^{\mathrm{f}} + \Box \mathbf{A}^{0} - \operatorname{grad}\Lambda^{0} = -\frac{4\pi}{c}\mathbf{j}, \qquad (5b)$$

where

$$\Box = \Delta - \frac{1}{c^2}\frac{\partial^2}{\partial t^2},$$

$$\Lambda^{\mathrm{f}} = \operatorname{div}\mathbf{A}^{\mathrm{f}} + \frac{1}{c}\frac{\partial \varphi^{\mathrm{f}}}{\partial t}.$$

Let us search for the $\mathbf{A}^{\mathrm{f}}$ and φ^{f} potentials in the form of solutions to inhomogeneous equations:

$$\Box \varphi^{\mathrm{f}} = -4\pi\rho, \qquad (6a)$$

$$\Box \mathbf{A}^{\mathrm{f}} = -\frac{4\pi}{c}\mathbf{j}. \qquad (6b)$$

Now, the terms containing zero-field potentials vanish identically by virtue of definition (2) and the Maxwell equations reduce to the Lorentz condition

$$\operatorname{div}\mathbf{A}^{\mathrm{f}} + \frac{1}{c}\frac{\partial \varphi^{\mathrm{f}}}{\partial t} = 0, \qquad (7)$$

involving only the field potentials rather than complete potentials. This makes superfluous the Strutton condition

$$\operatorname{div}\mathbf{A}^{0} + \frac{1}{c}\frac{\partial \varphi^{0}}{\partial t} \equiv \Delta\chi - \frac{1}{c^2}\frac{\partial^2 \chi}{\partial t^2} = 0.$$

Thus, within the framework of the scheme adopted for solving the Maxwell–Lorentz equations, Eq. (7) is a necessary part of the problem rather than merely a condition facilitating the solution. In the case when solutions of the nonlinear Eqs. (6) are expressed in terms of retarding potentials, the Lorentz condition (7) becomes the identical relation [15] and the remaining part of system (5) is satisfied by the zero-field potentials. Therefore, the nonzero field can be described by potentials satisfying Eqs. (6) with a necessary condition (7).

An example of a system featuring nonstationary zero-field potentials, presenting generalization of the stationary magnetostatic ABE, is offered by the nonstationary excitation of a cylindrical solenoid of infinite length with negligibly thin walls. In a cylindrical coordinate system (ρ, α, z) with the origin on the solenoid axis and the z-axis coinciding with the solenoid axis, the volume current distribution is described by the following equations:

$$j_\alpha(\rho, \alpha, z) = I_0\delta(\rho - R)\exp i(-n\alpha + \omega t), \qquad j_\rho = j_z = 0, \qquad (8)$$

where R is the solenoid coil radius and ω is the cyclic frequency of the current.

The nonzero vector potential components A_ρ and A_α have the following form (here and below, the harmonic time dependence is omitted) [16]:

$$A_\rho = \int_V j_\alpha(\boldsymbol{\rho}')\sin(\alpha - \alpha')G(\boldsymbol{\rho}, \boldsymbol{\rho}')dV', \qquad (9a)$$

$$A_\alpha = \int_V j_\alpha(\boldsymbol{\rho}')\cos(\alpha - \alpha')G(\boldsymbol{\rho}, \boldsymbol{\rho}')dV', \qquad (9b)$$

where $G(\boldsymbol{\rho}, \boldsymbol{\rho}') = -\frac{i\pi}{c}H_0^{(2)}(k|\boldsymbol{\rho} - \boldsymbol{\rho}'|)$ is the Green function of the Helmholtz equation [16], $H_0^{(2)}$ is the Hankel function, and $k = \omega/c$. Integrals entering into Eqs. (9) are readily calculated using an addition formula for the Hankel functions [16]:

$$H_0^{(2)}(k\sqrt{\rho^2 + R^2 - 2\rho R\cos(\alpha - \alpha')}) = \sum_{m=-\infty}^{+\infty} e^{-im(\alpha - \alpha')}\begin{cases} H_m^{(2)}(kR)J_m(k\rho), & \rho < R, \\ J_m(kR)H_m^{(2)}(k, \rho), & \rho > R. \end{cases} \qquad (10)$$

As a result, we obtain

$$A_\alpha = -\frac{i\pi^2 I_0 R}{c}e^{-in\alpha} \times \begin{cases} H_{n+1}^{(2)}(kR)J_{n+1}(k\rho) + H_{n-1}^{(2)}(kR)J_{n-1}(k\rho), & \rho < R, \\ J_{n+1}(kR)H_{n+1}^{(2)}(k\rho) + J_{n-1}(kR)H_{n-1}^{(2)}(k\rho), & \rho > R; \end{cases} \qquad (11a)$$

$$A_\rho = -\frac{\pi^2 I_0 R}{2c}e^{-in\alpha} \times \begin{cases} H_{n+1}^{(2)}(kR)J_{n+1}(k\rho) + H_{n-1}^{(2)}(kR)J_{n-1}(k\rho), & \rho < R, \\ J_{n+1}(kR)H_{n+1}^{(2)}(k\rho) - J_{n-1}(kR)H_{n-1}^{(2)}(k\rho), & \rho > R. \end{cases} \qquad (11b)$$

For $n = 0$ (i.e., in the absence of angular modulation), Eqs. (11) yield the following relationships:

$$A_\alpha = -\frac{2i\pi^2 I_0 R}{c}\begin{cases} H_1^{(2)}(kR)J_1(k\rho), & \rho < R, \\ J_1(kR)H_1^{(2)}(k\rho), & \rho > R \end{cases} \quad \text{and} \quad A_\rho = 0. \qquad (12)$$

In the stationary case ($\omega \longrightarrow 0$), these relationships lead to the known formulas $A_\alpha = J\rho/cR$ and $A_\alpha = JR/c\rho$ ($\rho > R$), where $J = 2\pi RI_0$ is the solenoid wall current per unit length). The only nonzero magnetic field component corresponding to potentials (12) has the following form:

(a) Alternating current

$$B_z = -\frac{2i\pi^2 I_0 Rk}{c}\begin{cases} H_1^{(2)}(kR)J_0(k\rho), & \rho < R, \\ J_1(kR)H_0^{(2)}(k\rho), & \rho > R; \end{cases} \quad (13)$$

(b) Stationary case

$$B_z = \frac{4\pi I_0}{c} \ (\rho < R), \quad B_z = 0 \ (\rho > R). \quad (14)$$

In accordance with Eqs. (1), let us divide into two parts the total vector potential in the space outside the solenoid coil so as to separate a term with zero rotor in Eq. (12). This can be done in a unique mode as follows:

$$A_\alpha = -\frac{2i\pi^2 I_0 R}{c}J_1(kR)H_1^{(2)}(k\rho) + \frac{4\pi I_0 R}{kc}\frac{J_1(kR)}{\rho} \equiv A_\alpha^{\mathrm{f}} + A_\alpha^0, \quad (15)$$

where A_α^{f} is the field potential component, A_α^0 is the zero-field potential component, and $H_1^{(2)}(k\rho) = H_1^{(2)}(k\rho) - 2i/\pi k\rho$. Separating the real parts of the potential components in Eq. (15), we obtain

$$\mathrm{Re}\,A_\alpha^{\mathrm{f}} = W\left\{\pi J_1(k\rho)\sin\omega t - \left[\frac{2}{k\rho} + \pi Y_1(k\rho)\right]\cos\omega t\right\}, \quad (16a)$$

$$\mathrm{Re}\,A_\alpha^0 = W\frac{2}{k\rho}\cos\omega t, \quad (16b)$$

where

$$W = \frac{2\pi I_0 R J_1(kR)}{c}$$

and Y_1 is the Neumann function.

The plots of A_α^{f} calculated according to Eqs. (16) at various time instants are depicted in the figure. An analysis of these curves indicates that situations are possible when electrons, travelling by certain trajectories and emitted at definite time moments, occur under the action of zero-field potentials only.

In the stationary case, $A_\alpha^{\mathrm{f}} = 0$ and $A_\alpha^0 = JR/c\rho$. Proceeding from the condition that the electric field is absent, we obtain the following expression for the scalar zero-field potential:

$$\varphi^0 = -\frac{4\pi i I_0 R}{c}J_1(kR)\alpha, \quad (17)$$

where α is the azimuthal angle. In the stationary case, $\varphi^0 = 0$.

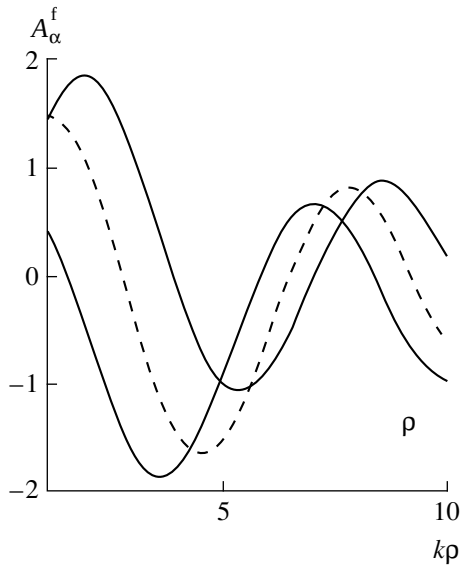

The field potential A_α^{f} calculated as function of the distance from solenoid $k\rho$ at three time instants corresponding to $\omega t = \pi/2$ [solid line, $\pi J_1(k\rho)$], $\omega t = \pi/4$ [dashed line, $0.25\pi\left(\pi J_1(k\rho) - \pi Y_1(k\rho) - \frac{2}{k\rho}\right)$], and $\omega t = 0$ [dotted line, $-\left(\pi Y_1(k\rho) + \frac{2}{k\rho}\right)$]. Calculated for $kr = W = 1$.

Note that, according to Eq. (15), there is a certain relationship between the solenoid coil radius and the wavelength of the electromagnetic field, determined by the roots of the equation $J_1(kR) = 0$, for which the fields outside the solenoid are zero. Under these nonstationary conditions, however, the zero-field potentials are also vanishing (a system of the closed waveguide type). The zero-field potentials are also vanishing for all $n \neq 0$.

In the general case, there are three situations in which the ABE can be observed in a nonstationary regime. These cases correspond to the de Broglie electron waves interacting with (i) zero-field potentials, (ii) both zero-field and field potentials, and (iii) field potentials only. The third case was considered in [7, 17] but still requires a deeper analysis. The ABE observed in the case of the de Broglie electron waves interacting with the field potentials is sometimes referred to as the Aharonov–Bohm quasi-effect.

Thus, we have demonstrated that zero-field potentials may exist in the space outside a solenoid excited in a nonstationary regime, which is a necessary but insufficient condition for manifestation of the Aharonov–Bohm effect.

REFERENCES

1. W. Franz, Verh. Dtsch. Phys. Ges. **20**, 65 (1939).
2. W. Ehrenberg and R. E. Siday, Proc. Phys. Soc. London, Sect. B **62**, 8 (1949).

3. Y. Aharonov and D. Bohm, Phys. Rev. **115**, 485 (1959).
4. S. Olariu and I. I. Popesku, Rev. Mod. Phys. **57**, 339 (1985).
5. M. Peskin and A. Tonomura, Lect. Notes Phys. **340**, 115 (1989).
6. A. Tonomura *et al.*, Phys. Rev. Lett. **56**, 792 (1986).
7. B. Lee, E. Yin, T. K. Gustafson, and R. Chiao, Phys. Rev. A **45**, 4319 (1992).
8. A. N. Ageev, Yu. M. Voronin, I. P. Demenchonok, and Yu. V. Chentsov, Pis'ma Zh. Tekh. Fiz. **22** (4), 25 (1996) [Tech. Phys. Lett. **22**, 144 (1996)].
9. G. Afanasiev and M. Nelhiebel, Phys. Scr. **54**, 417 (1996).
10. A. Vourdas, Phys. Rev. A **56**, 2408 (1997).
11. A. N. Tikhonov and A. A. Samarskiĭ, *Equations of Mathematical Physics* (Nauka, Moscow, 1953; Pergamon, Oxford, 1964).
12. M. G. Savin, *Lorentz Gauge Problems in Anisotropic Media* (Moscow, 1979).
13. D. H. Kobe, Ann. Phys. (N. Y.) **123**, 381 (1979).
14. T. H. Boyer, Phys. Rev. D **8**, 1679 (1973).
15. I. E. Tamm, *The Principles of Electricity Theory* (Nauka, Moscow, 1966).
16. G. T. Markov and A. F. Chaplin, *Excitation of Electromagnetic Waves* (Moscow, 1967).
17. A. N. Ageev, S. Yu. Davydov, and A. G. Chirkov, Pis'ma Zh. Tekh. Fiz. **26** (2000) (in press) [Tech. Phys. Lett. **26**, 392 (2000)].

Translated by P. Pozdeev